

The Simulation of Turbomachinery Flows at Arbitrary Mach Numbers and The Analysis of Leakage Flows in Shrouded Axial Turbines

Von der Fakultät Energie-, Verfahrens- und Biotechnik der
Universität Stuttgart zur Erlangung der Würde eines
Doktor-Ingenieurs (Dr.-Ing.) genehmigte Abhandlung

vorgelegt von
Jan Eric Anker
aus Karlsruhe

Hauptberichter: Prof. M. V. Casey, DPhil

Mitberichter: Prof. Dr.-Ing. E. Göde

Tag der mündlichen Prüfung: 22. April 2013

Institut für Thermische Strömungsmaschinen und
Maschinenlaboratorium der Universität Stuttgart

2013

Acknowledgment

The foundation for this thesis was laid during my position as a Research Associate at the Institute of Thermal Turbomachinery and Machinery Laboratory (ITSM) of University of Stuttgart. The work presented herein related to the study of leakage flow effects in shrouded axial turbines was funded by Forschungsvereinigung Verbrennungskraftmaschinen (FVV) in the framework of the projects Deckbandströmumseinfluss I-III, which is gratefully acknowledged.

First of all I would like to thank Prof. Michael V. Casey, the Director of ITSM, for supervising this thesis, many fruitful discussions, and for promoting my scientific work. His continuous interest in my research and his excellent guidance on turbomachinery flow physics was an inspiration and contributed significantly to the success of this thesis.

I would also like to express my gratitude to the late Prof. Heinz Stetter, the former Director of ITSM, for hiring me as a Research Associate and for his unwavering confidence in me. Furthermore, I would like to thank Dr. Joachim Messner, the former Vice-Director of ITSM, for ensuring that there always was sufficient funding for research and that the associates could present their work at international conferences.

My gratitude is also extended to Prof. Eberhard Göde for his support as a Commissary Director in the interim period before Prof. Casey was appointed as Director of ITSM. In addition, I would like to thank Prof. Göde for co-promoting this thesis.

Furthermore, I am obliged to the various members of the Supervising Committees of the aforementioned FVV projects for their constructive advice and guidance. Special thanks is due to the Chairmen of the first two projects, Dr. N. Vortmeyer and Dr. C. Mundo, for promoting the proposals for follow-on projects on leakage flow effects. I am also obliged to Dr. A. Jung, the Chairman of the third FVV project, for giving demanding, but constructive feedback and pushing for a very systematic study of the impact of the leakage flow in shrouded turbines.

In the context of the projects on leakage flow effects, I would additionally like to thank Dr. Jürgen F. Mayer, Head of the Section for Numerical Methods at ITSM, for his support in general matters and for his excellent reviews of the reports I wrote for FVV. His feedback, especially with regards to formal aspects, was very valuable. Furthermore, I am thankful that he gave me the freedom to develop numerical methods in the in-house flow solver ITSM3D during the FVV projects.

For their help in visualizing the leakage flow effects in Virtual Reality (VR), I would also like to thank Mr. Lars Frenzel and Dr. Uwe Wössner of the High Performance Computing Center Stuttgart (HLRS). The use of VR-visualization proved to be a very effective means to present results to the members of the Supervising Committee in the aforementioned FVV projects.

At this place I would like to thank Dr. Rüdiger Merz, who brought me to ITSM by hiring me as a Research Assistant (HiWi). His inspiring and opti-

mistic personality convinced me to carry out the MSc thesis in the Section for Numerical Methods at ITSM, which was the starting point in my career in Computational Fluid Dynamics (CFD). I learned a lot from him during his supervision and I am grateful to have had his advice and mentorship.

Furthermore, I owe many thanks to my former colleagues, students, and research assistants at the University of Stuttgart, who were supporting me in my work and personal development in numerous ways. In particular I would like to thank Mr. Holger Bauer, Mr. Francis Delhopital, Dr. Gerhard Eyb, Mr. Klaus Findeisen, Mr. Frank Fuchs, Mr. Peter Gerkens, Mr. André Gerlach, Mr. Wolfram Gerschütz, Mr. Michael Göhner, Mr. Steffen Kämmerer, Mr. Peter Kraus, Dr. Xandra Margot, Mr. Michael Rath, Mr. Dietmar Reiß, Mr. Markus Schatz, Mr. Andreas Seibold, Mr. Udo Seybold, Mr. Roland Sigg, Mr. Lutz Völker, and Mr. Volker Wittstock for their valuable collegial support, interesting discussions, productive collaborations and various memorable moments.

Of the students I was supervising when I was a Research Associate at ITSM, I would particularly thank Mr. Alexander Berreth, Mr. Jürgen Bosch, Mr. Reinaldo A. Gomes, Mr. Perttu Jukola, Mrs. Birthe Schrader, Mr. Alex Schulz, Mr. Senol Söğüt, and Mr. Christian Wölfel for the great collaboration on various CFD related topics. I want also to express my gratitude to Mr. H. C. Bauer for his help with interlibrary loans of literature and for sourcing various scientific literature and references.

I am indebted to my parents for their support during my studies. Last but not least, very special thanks go to my wife for her loving support and her encouragement while I was writing down this thesis.

Brussels, in July 2013

Jan E. Anker

Contents

Contents	iii
Nomenclature	ix
Abstract	xvii
Kurzfassung	xix
1 Introduction	1
1.1 Motivation	1
1.2 Literature survey	2
1.2.1 Leakage flow effects in shrouded axial turbomachinery	2
1.2.2 Methods for the simulation of turbomachinery flows at all speeds	5
1.2.3 Modeling of transitional and turbulent flows in turboma- chinery	11
1.3 Objectives of the present thesis	15
1.4 Outline of the present thesis	16
2 A baseline solution scheme	19
2.1 Governing equations	19
2.2 Discretization scheme and solution procedure	20
2.2.1 Spatial discretization	21
2.2.2 The necessity of adding artificial dissipation in a central scheme	23
2.2.3 The artificial dissipation scheme of Jameson, Schmidt and Turkel	23
2.2.4 Time-stepping scheme	25
2.2.5 Convergence acceleration techniques	26
2.2.6 Normalization of the flow equations	26
2.3 Boundary conditions	27
2.3.1 Inlet, outlet and mixing planes	27
2.3.2 Wall boundary conditions	27
2.3.3 Periodic boundary condition	28

3	A Mach number independent solution scheme	29
3.1	The time-derivative preconditioning scheme of Merkle	29
3.1.1	Eigenvalue scaling for convergence enhancement	31
3.1.2	Perturbation analysis for low Mach number flow	33
3.1.3	Robustness aspects	33
3.1.4	Scaling issues for low Reynolds number flow	34
3.2	Preconditioned discretization and solution scheme	35
3.2.1	Spatial discretization	36
3.2.2	Artificial dissipation	37
3.2.3	Time-stepping scheme	39
3.2.4	Calculation of the time step	39
3.2.5	Treatment of the initial and boundary conditions	39
3.2.6	The use of perturbed, normalized flow quantities	40
3.2.7	Implicit residual smoothing technique for preconditioned systems	40
3.3	Impact of preconditioning	41
3.3.1	Enhancement of the convergence rates	41
3.3.2	Accuracy preservation of the solution scheme for low Mach number flow simulations	42
3.4	Computational results	44
3.4.1	Inviscid flow over a bump	44
3.4.2	Flat plate	45
3.4.3	Supersonic flow through a row of wedges	45
3.4.4	Low-speed turbine	46
4	Low-diffusive discretization schemes	51
4.1	Scalar JST-scheme with TVD properties	51
4.2	JST-switched matrix dissipation	52
4.3	Strengths and weaknesses of JST-switched schemes	53
4.4	Scalar SLIP scheme of Jameson	54
4.5	Characteristic upwind scheme of Roe	57
4.5.1	Roe-averaging	58
4.5.2	Method adopted in the current work	58
4.6	Advected upstream splitting techniques	59
4.6.1	The AUSM+ scheme	60
4.6.2	Formulation of the AUSM+ scheme for a cell-vertex scheme	62
4.6.3	Preconditioned AUSM+-scheme	65
4.6.4	Robustness issues	69
4.7	Computational results	70
4.7.1	Ni-Bump test case	70
4.7.2	Flat plate laminar boundary layer	70
4.7.3	Supersonic flow through a row of wedges	72
4.7.4	Low-speed turbine	74

5	Development of a NRBC treatment for preconditioned systems	89
5.1	The Giles-Saxer approach	89
5.2	The Giles Condition	90
5.3	Quasi-three-dimensional steady-state NRBC	91
5.4	1D characteristic theory for imposing BCs	93
5.4.1	One-dimensional characteristic theory as a means to im- pose compatible boundary conditions	93
5.4.2	Axially subsonic inlet	95
5.4.3	Axially subsonic outlet	97
5.4.4	Axially supersonic inlet	98
5.4.5	Axially supersonic outlet	99
5.5	Implementation of the Q3D NRBC	99
5.5.1	Subsonic inflow boundary	100
5.5.2	Subsonic outlet boundary	103
5.5.3	Axially subsonic inlet or outlet boundaries in an overall supersonic flow	104
5.5.4	Axially supersonic inlet and outlet boundaries	105
5.5.5	Adjacent solid walls	105
5.6	Non-reflecting mixing planes	105
5.6.1	Coupling condition	106
5.6.2	Numerical implementation	106
5.7	Verification of the non-reflectivity	107
5.8	Comparison of developed and original NRBC	109
6	Analysis of leakage flow effects	115
6.1	Description of the shrouded turbine	115
6.2	Modeling of the shrouded turbine	116
6.2.1	Grids and boundary conditions	116
6.2.2	Numerical modeling	118
6.3	Validation of the computational results	118
6.4	Importance of the geometrical parameters of the labyrinth seal	124
6.5	Main flow - leakage flow interaction	124
6.5.1	The impact of the leakage flow on the main flow	124
6.5.2	Interaction between the potential field of the rotor and the cavity flow	125
6.5.3	Consequences of the leakage flow extraction on the sec- ondary flow field of the rotor	126
6.5.4	Consequences of the leakage flow re-injection on the sec- ondary flow field of the rotor	128
6.5.5	The impact of the presence of cavities on the formation of the secondary flow field	129
6.5.6	Impact of the Leakage Flow on the Secondary Flow Field in the Second Stator Row	130
6.6	Discussion of results	132
7	Summary and conclusions	135

A	Perturbation analysis	139
A.1	A preconditioning method for inviscid, low Mach number flow . . .	139
A.2	A preconditioning method for low Mach number, viscous flows . . .	143
A.3	Summary of the implications for the preconditioning parameters	147
B	Dispersion analysis	149
B.1	Governing equations and dispersion analysis	149
B.1.1	Dispersion analysis for ideal gas flow	151
B.1.2	Dispersion analysis for incompressible flow	151
B.2	Preconditioning for ideal gases	153
B.2.1	Wave speeds when time-derivative preconditioning is not applied	153
B.2.2	Wave speeds when low Mach number time-derivative preconditioning is applied	154
B.2.3	Wave speeds when low Reynolds number time-derivative preconditioning is applied	155
B.3	Preconditioning for incompressible flow	157
B.3.1	Wave speeds when time-derivative preconditioning for inviscid flows is applied	158
B.3.2	Wave speeds when time-derivative preconditioning for viscous dominated flows is applied	158
B.4	Implications of the dispersion analysis	160
C	Scaling of the artificial dissipation	163
C.1	Inviscid flows	163
C.2	Viscous dominated flows	166
D	Issues in low Mach number flow simulations	171
D.1	Singularity of the flow equations	171
D.2	Avoidance of round-off errors at low Mach numbers	172
D.3	Use of a perturbed temperature variable	174
E	Flux limiters	177
E.1	Monotonicity conditions and limiters	177
E.2	Limiter functions	180
E.3	Discussion of Jameson's SLIP and USLIP schemes	181
F	The Roe scheme for preconditioned systems	183
F.1	Conservative and non-conservative formulation	183
F.2	Use of conservative versus non-conservative variables	185
F.3	The principle of Roe-averaging	187
F.4	Eigenvector and absolute Jacobian matrices	189
G	Influence of geometry of the labyrinth seal	193
H	Numerical modeling of labyrinth seals	197

I Unsteadiness of leakage flow and necessary level of numerical modelling	199
Bibliography	203

Nomenclature

Latin symbols

a	Isentropic speed of sound
a_0	Constant in the CUSP scheme
A	Area, flux Jacobian
A_0	Measurement plane
B	Flux Jacobian
b_p	Factor in Roe's characteristic upwind scheme
c	Arbitrary wave speed
C	Flux Jacobian
$\mathbf{c}, c_i,$ $[u, v, w]$	Cartesian velocity vector
$c_{11}, c_{12},$ c_{21}	Factors in Roe's characteristic upwind scheme
c_{52}	Coefficient in the NRBC treatment
c_ϵ	Constant for determining the threshold value
c_p	Specific isobaric heat capacity
c_v	Specific isochore heat capacity
CFL	Courant-Friedrichs-Lewy number
d	Component of the artificial dissipation vector, quantity related to preconditioning
d_p	Quantity related to preconditioning
D	Determinant, mean diameter
D	Vector of the artificial dissipation
$ \mathcal{D} $	Absolute Mach number function (AUSM scheme)
e	Specific energy
E	Axial flux vector
E°	Kinetic energy
f	Weighting factor in the κ -scheme
F	Circumferential flux vector, general flux vector
G	Radial flux vector
h	Specific enthalpy, spanwise coordinate
H	Span, blade height, helicity
H	Vector of source terms, general flux vector
i	Grid index, summation index
\hat{i}	Imaginary unit, $\hat{i}^2 = -1$

I	Unity matrix
j	Grid index, summation index
J	Jacobian matrix
k	Grid index, user-defined scaling coefficient for the artificial dissipation, proportionality constant, wave number, summation index
\mathbf{k}	First vector in the system k, l, m of orthogonal vectors
k_λ	Thermal conductivity coefficient
l	Characteristic length, wave number, summation index
\mathbf{l}	Left eigenvector, second vector in the system k, l, m of orthogonal vectors
L	Reference length, limiter function, matrix of left eigenvectors
m	Scaled Mach number, wave number, summation index
\dot{m}	Mass flux
\mathbf{m}	Third vector in the system k, l, m
M	Mach number
$M_1, M_2,$ M_3	Measurement plane
MP	Midplane
\check{M}	Scaled Mach number to ensure pressure-velocity coupling (AUSM scheme)
\mathcal{M}	Mach number function (AUSM scheme)
$ \Delta\mathcal{M} $	Absolute Mach number function (AUSM scheme)
n	Fourier mode, summation index
\dot{n}	Rotational speed
\vec{n}	Direction vector, surface vector
N	Blade number, number of grid points in the circumferential direction (periodic nodes are only counted once per pitch)
$ \mathcal{N} $	Absolute Mach number function (AUSM scheme)
p	Static pressure
$\hat{\mathbf{p}}$	State vector (frequency domain)
P	Element of the limiter function of the SLIP scheme
\mathcal{P}	Element of the pressure sensor of the JST scheme, effective limiter of the SLIP scheme
$ \mathcal{P} $	Absolute Mach number function (AUSM scheme)
\mathbf{P}	Pressure flux vector (in the AUSM scheme)
Pe	Peclet number
Pr	Prandtl number
q	State variable
q_e	Exponent in the SLIP scheme
$\hat{\mathbf{q}}$	State vector (frequency domain)
\mathbf{Q}	State vector (conservative variables)
\mathbf{Q}_p	Vector of primitive state variables
\mathbf{Q}_v	Vector of viscous, primitive state variables
r	Radial coordinate, radius, ratio of successive

	slopes/differences, reaction
\mathbf{r}	Flux vector, contribution to the residual
R	Specific gas constant, matrix of right eigenvectors, residual, matrix of diffusive terms
Re	Reynolds number
s	Specific entropy, stages in the Runge-Kutta scheme, limiter, chord length, width of a gap/tip
s_{cl}	Clearance height
S	Surface, element of the limiter function of the SLIP scheme
t	Time, summation index
T	Absolute temperature
u	First component of the Cartesian velocity vector \mathbf{c}
V_∞	Axial velocity of the far-field
\hat{v}	Contravariant velocity component
\hat{V}	Volume weighted, contravariant velocity component
\check{V}	Cell volume (control volume)
\mathbf{U}	General state vector
v	Velocity, second component of the Cartesian velocity vector \mathbf{c}
\mathbf{v} ,	Velocity vector in an absolute frame
$[v_x, v_\phi, v_r]$	of reference (Cylindrical coordinates)
$\hat{\mathbf{v}}$,	Contravariant velocity vector in an absolute
$[\hat{v}_\xi, \hat{v}_\eta, \hat{v}_\zeta]$	frame of reference
V	Volume, velocity magnitude (absolute frame of reference)
V_l	Lower threshold for the eigenvalues corresponding to advective (linear) transport velocities
V_n	Lower threshold for the eigenvalues corresponding to acoustic (non-linear) transport velocities
V_r	Reference velocity
VNN	Von Neumann Number
w_x	Axial velocity component
w_ϕ	Circumferential velocity component
w_r	Radial velocity component
\mathbf{w} ,	Velocity vector in a relative frame
$[w_x, w_\phi, w_r]$	of reference (Cylindrical coordinates)
$\hat{\mathbf{w}}$,	Contravariant velocity vector in a relative frame
$[w_\xi, w_\eta, w_\zeta]$	of reference
W	Magnitude of the velocity vector in the relative system
\hat{W}	Volume weighted, contravariant velocity vector in the relative system
x	Axial distance, first Cartesian coordinate, length
y	Second Cartesian coordinate
z	Third Cartesian coordinate

Greek symbols

α	Thermal diffusivity coefficient, coefficient in the AUSM scheme, coefficient in the JST scheme, coefficient in the Runge-Kutta scheme, scaling factor for the dissipation
β	Coefficient in the AUSM scheme, quantity in the NRBC treatment
γ	Coefficient of the Runge-Kutta scheme, quantity in the NRBC treatment, isentropic coefficient
Γ	Preconditioning matrix
δ_{pc}	Preconditioning parameter
ϵ	Accuracy, tolerance, preconditioning parameter, perturbation parameter, threshold
ε	Resulting coefficient for the dissipation in the JST scheme
ϵ_{ijk}	Permutation tensor, three-dimensional Levi-Civita symbol
ϵ_m	Machine accuracy
ϵ_{rnd}	Round-off error
ζ	Third grid coordinate, loss coefficient
η	Second grid coordinate, normalized wall distance, similarity variable
Θ	Scaling factor in the JST scheme
κ	Factor in the scheme with the same name
λ	Eigenvalue
λ_{45}	Eigenvalue-based factor in the dissipation of the Roe scheme
Λ	Diagonal matrix of the eigenvalues
μ	Dynamic viscosity
ν	Pressure sensor, kinematic viscosity
σ	Condition number
σ_1, σ_2	Relaxation factors (NRBC)
σ_p	Factor in AUSM scheme
Ξ	Mach number related quantity
π	Number π , ratio between the circumference and the diameter of a circle
π	Dissipation vector (Roe scheme)
Π	Computational grid
ρ	Spectral radius
ϱ	Density
τ	Stress tensor
Υ	Mach number weighted conservative state vector
$\delta\Upsilon$	Difference of the surface weighted velocity vectors (Roe scheme)
ϕ	General state variable, characteristic variable, flow coefficient
Φ	State vector
χ	Constant for the artificial dissipation
ξ	First grid coordinate
ψ	General state variable, stage loading coefficient
Ψ	Limiter function
Ψ	State vector

ω	Angular frequency
$\boldsymbol{\omega}, \omega_i$	Vorticity vector
Ω	Angular speed of the rotating frame of reference
ω_{AUSM}	Scaling parameter of the AUSM scheme

Latin sub- or superscripts

0	Total quantity, quantity that is vanishing when preconditioning is shut off
(0)	Zeroth order
1	First component, related to equation 1
(1)	First order
(2)	Second order
3	Third component, related to equation 3
(4)	Fourth order
<i>a</i>	Outlet
adv	Advection part
apl	Applied
atd	Anti-diffusive
bc	Boundary condition
<i>c</i>	Convective
cal	Calculated by the flow solver
<i>CD</i>	Central difference term
cl	Clearance
comp	Compressible
<i>d</i>	Diffusive
<i>e</i>	Inlet related quantity, neutral (preconditioning matrix)
edi	Essentially diffusive
ex	Outgoing
<i>F</i>	Related to convective fluxes
<i>i</i>	Grid index, summation index, inner
in	Incoming
inv	Inviscid
incomp	Incompressible
is	Isentropic
<i>j</i>	Grid index, summation index
<i>k</i>	Grid index, summation index, dimensionless (preconditioning matrix)
<i>l</i>	Laminar, molecular, summation index, limiter
<i>L</i>	Left state, left eigenvector
lim	Limit
<i>m</i>	Summation index
<i>n</i>	Summation index
(<i>n</i>)	State at time step <i>n</i>

<i>o</i>	Outer
<i>p</i>	Derivative with respect to the pressure at constant temperature, isobaric, primitive, particular, pressure dissipation term
pc	Preconditioning related quantity
pgr	Pressure gradient
<i>r</i>	Radial component, reference quantity
rot	Rotor
<i>R</i>	Right state, right eigenvector
Roe	Roe average
<i>s</i>	Isentropic, summation index, non-reflecting in steady-state
(<i>s</i>)	State of the Runge-Kutta stage <i>s</i>
<i>S</i>	Surface weighted, related to sources
sec	Secondary
st	Stator
<i>t</i>	Turbulent, summation index
<i>T</i>	Derivative with respect to the temperature at constant pressure, transposed, temperature dissipation term
<i>x</i>	Axial component
<i>v</i>	Viscous
<i>V</i>	Volume weighted
<i>w</i>	Fin width

Greek sub- or superscripts

ϕ	Circumferential
ξ	Related to the first grid direction, derivative with respect to ξ
η	Related to the second grid direction, derivative with respect to η
ζ	Related to the third grid direction, derivative with respect to ζ

Symbolic superscripts and overbar symbols

+	Forward, positive part
-	Backward, negative part
^	Quantity related to the dual mesh, viscous control volume, contravariant
*	Normalized, critical, equidistantly distributed, system
†	Reference
'	Pseudoacoustic, scaled due to preconditioning, perturbed variable, local variation
"	Scaled due to preconditioning
-	Averaged, scaled quantity, anisotropically scaled, average interface value
~	Numerical value, perturbed quantity, normalized
^	Limited value, Fourier mode

Operators, functions and mathematical symbols

$\max()$	Maximum function
$\min()$	Minimum function
$\text{sign}()$	Signum function
$\mathcal{O}(\dots)$	In the order of
d	Total derivative
D	Substantial derivative, dissipation operator
δ	Variation
δ^+	Forward difference
δ^-	Backward difference
\ll	Much smaller than (one order in magnitude at least)
\gg	Much greater than (one order in magnitude at least)
Δ	Difference
∂	Partial derivative
\oint	Surfaceintegral
\int	Integral
\sum	Sum
$\text{Real}(\)$	The real part of a complex number
\ln	Natural logarithm
∞	Infinity
\forall	For all
\in	Is element of
\mathbb{C}	Set of imaginary numbers
\mathbb{N}	Set of natural numbers
\mathbb{R}	Set of real numbers
\mathbb{Z}	Set of integer numbers
$\sqrt{\quad}$	Square root
\cdot	Inner product
\wedge	Logical and
\vee	Logical or
$ \quad $	Absolute value of a scalar, determinant of a matrix
$\ \quad\ $	Euclidian norm of a vector
$[\quad]^T$	Transposition operator
∇	Gradient operator
$\text{Diag}(\dots)$	Diagonal matrix
\propto	Proportional to
\neq	Not equal
$:=$	Per definition equal to, set equal to
\approx	Approximately equal to
\equiv	Identically equal to
\times	Times

Conventions

The summation convention of Einstein

If not otherwise stated in the text, then the summation convention of Einstein is used for all sub- and superscripts i, j, k, l, p, q . According to this convention, a summation from 1 to 3 is to be performed if the same index appears twice in the same term. Example:

$$\frac{\partial \phi_i}{\partial x_i} = \sum_{j=1}^3 \frac{\partial \phi_j}{\partial x_j} = \frac{\partial \phi_1}{\partial x_1} + \frac{\partial \phi_2}{\partial x_2} + \frac{\partial \phi_3}{\partial x_3} = \frac{\partial \phi_x}{\partial x} + \frac{\partial \phi_y}{\partial y} + \frac{\partial \phi_z}{\partial z}$$

Abbreviations

1D	One-dimensional
1Dm	One-dimensional theory applied on the averaged state
1Dp	One-dimensional theory applied pointwise
3D	Three-dimensional
AUSM+	Enhanced Advection Upstream Splitting Method
CFL	Courant-Friedrichs-Lewy
CUSP	Convective Upwind Split Pressure
JST	Jameson-Schmidt-Turkel
JSTMatd	Jameson-Schmidt-Turkel Matrix-dissipation
LED	Local Extremum Diminishing
MUSCL	Monotone Upstream-centered Schemes for Conservation Laws
nonPC	Not preconditioned
NRPCBC	Non-reflecting boundary condition treatment for preconditioned systems
NRBC	Non-reflecting boundary condition
PC	Preconditioning
PCBC	Boundary condition treatment for preconditioned systems
Q3D	Quasi-three-dimensional
RPM	Rotations per minute
SLIP	Symmetric Limited Positive
TVD	Total Variation Diminishing
USLIP	Upstream Limited Positive
VNN	Von Neumann Number

Other conventions

- Non-transposed vectors are always column vectors and transposed vectors are always row vectors
- Formulas marked in **(bold face)** represent always a vectorial quantity

Abstract

In the present thesis a preconditioned solution scheme for the simulation of turbomachinery flow at arbitrary Mach numbers is presented. A time-derivative preconditioning technique is applied to an explicit, time-marching Navier-Stokes code, originally concipated for compressible, high-speed turbomachinery applications. Various aspects of the accurate simulation of incompressible or low Mach number, compressible flows are addressed. The preconditioning scheme is formulated for fluids with a general equation of state. As verified by several test cases, the use of preconditioning allows the code to simulate flows efficiently and accurately for all Mach numbers.

Four different dissipation schemes have been developed and adapted for the use in combination with preconditioning. It is shown how the robustness of Liou's improved Advection Upwind Splitting Method (AUSM+) scheme can be enhanced by controlling the anti-diffusive parts of the dissipative fluxes. The different dissipation schemes are assessed on several test cases in terms of accuracy, solution monotonicity, and robustness.

Since turbomachinery computations often are performed on truncated domains, a non-reflecting boundary condition (NRBC) treatment should be used. Because preconditioning alters the dynamics of the Navier-Stokes equations, the state-of-the-art NRBC treatment of Giles and Saxer can not be applied. For this reason, a new NRBC treatment for preconditioned systems and general equations of state is developed. The effectiveness of the novel treatment is demonstrated on two turbomachinery test cases.

After validation against available measurement data, the solution scheme is used for a computational study of the interaction of labyrinth seal leakage flow and main flow in an axial, low-speed turbine. The results are used to investigate leakage flow phenomena and their dependence on the geometrical parameters of the sealing arrangements. The most influential geometrical parameter, the clearance height, is varied between a vanishing and a realistic height to systematically identify the impact of the leakage flow on main and secondary flow as well as on the loss generation mechanisms.

The computational results show that the ingress of shroud leakage flow from the rotor significantly influences the main flow. The high swirl of the leakage flow causes a suction side incidence onto the following stator row and consequently leads to an amplification of the upper secondary channel vortex and increased losses.

The results imply that in order to reduce the losses in shrouded, axial turbines, the swirl of the reentering leakage flow should be corrected by constructive means. If this is technically infeasible, then the blades in the following blade row should be twisted to ensure a correct incidence and avoid flow separation. Since the computational results also show that not only the leakage flow but also the mere presence of cavities induce aerodynamic losses, the geometry of the inlet and outlet cavities must be considered with care in the design and optimization process of sealing arrangements for axial turbines.

Kurzfassung

In der vorliegenden Arbeit wird ein präkonditioniertes Lösungsverfahren zur Simulation von Turbomaschinenströmungen bei beliebigen Machzahlen vorgestellt. Das Präkonditionierungsverfahren wird in einem Navier-Stokes Code entwickelt, welcher ursprünglich für die Simulation von transsonischen Turbomaschinenströmungen konzipiert wurde. Verschiedene Gesichtspunkte für die genaue Berechnung von Strömungen mit geringen Geschwindigkeiten werden behandelt. Das Präkonditionierungsverfahren wird für Fluide mit einer generellen Zustandsbeschreibung formuliert. Mehrere Testfälle bestätigen, dass die Anwendung von Präkonditionierung eine genaue und effiziente Strömungsberechnung bei beliebigen Machzahlen ermöglicht.

Vier unterschiedliche Dissipationsverfahren werden entwickelt und für die Verwendung von Präkonditionierung angepasst. Dabei wird gezeigt, wie man die Robustheit der modifizierten Advection Upwind Splitting Method (AUSM+) von Liou durch eine gezielte Steuerung der antidiffusiven Terme der dissipativen Flüsse verbessern kann. Die Dissipationsschemen werden anhand mehrerer Testfälle hinsichtlich Robustheit, Genauigkeit und Monotonie des resultierenden Lösungsschemas untersucht.

Da die Berechnung von Turbomaschinenströmungen oft auf Rechengebieten mit kurzen Zu- und Abströmgebieten ausgeführt werden, sollte eine nicht-reflektierende Randbehandlung (NRRB) benutzt werden. Weil Präkonditionierung die Dynamik der zu integrierenden Erhaltungsgleichungen ändert, wurde im Rahmen der vorliegenden Arbeit eine NRRB für präkonditionierte Systeme und generelle Zustandsgleichungen entwickelt. Die Effektivität der neuen NRRB wird anhand zweier Turbomaschinentestfälle verifiziert.

Nach einer Validierung mit vorhandenen Messdaten wird das entwickelte Lösungsverfahren dazu benutzt, systematische numerische Untersuchungen der Interaktion von Deckbandleckage- und Hauptströmung in einer Niedergeschwindigkeitsaxialturbine durchzuführen. Die Spaltweite der Labyrinthdichtung wird variiert, um den Einfluss der Deckbandströmung auf Haupt- und Sekundärströmung sowie Verlustentstehung zu identifizieren.

Die Berechnungsergebnisse zeigen, dass die Leckageströmung der Rotorreihe einen signifikanten Einfluss auf die Hauptströmung hat. Der hohe Drall der wiedereintretenden Leckageströmung führt zu einer saugseitigen Fehlanströmung der nachfolgenden Leitradreihe und infolgedessen zu einer Verstärkung des oberen Kanalwirbels sowie zu einer Erhöhung der Verluste.

Die Ergebnisse legen nahe, dass der Drall der wiedereintretenden Leckageströmung durch konstruktive Maßnahmen korrigiert werden sollte, um Verluste zu minimieren. Alternativ sollte die nachfolgende Schaufelreihe gewunden werden, um eine Fehlanströmung infolge der Leckageströmung zu vermeiden. Da die Ergebnisse zeigen, dass nicht allein die Deckbandleckageströmung, sondern auch die bloße Präsenz von Kavitäten aerodynamische Verluste hervorrufen kann, sollte die Geometrie der Ein- und Austrittskammern der Labyrinthdichtung in die Design- und Optimierungsüberlegungen von Schaufelreihen mit Deckbandgeometrie einbezogen werden.

Chapter 1

Introduction

Turbomachines are the most common devices used in energy conversion processes and in aircraft propulsion so that the research and development in this discipline remains important. Current research objectives consist of developing propulsion and power systems having a higher efficiency and reliability, which simultaneously lead to lower emissions of pollutants and noise. To this end it is necessary to improve the understanding of the the interplay between the various physical phenomena in turbomachinery and how they can be influenced to optimize the overall performance of such devices.

1.1 Motivation

The anergy generated in turbomachinery can be attributed to various sources. Depending on the configuration the presence of wakes, secondary flow, boundary layers on blades and endwalls, the appearance of shocks and the occurrence of leakage flow may all contribute to the generation of losses.

The losses due to tip leakage flow represent a substantial part (typically a third) of the overall exergy losses generated in turbomachinery. The leakage flow leads to a reduction in the performance since a part of the flow bypasses the blade without exerting work and anergy is created through dissipation in the tip region. The leakage may also induce losses in performance in subsequent blade rows since it causes flow inhomogeneities after reentering the main flow.

The most obvious way to minimize exergy losses caused by leakage flow in turbomachinery, is to reduce the leakage mass flow by applying shrouds on the rotor tips and labyrinth seals between the rotating and non-rotating components. The reduction of the exergy losses through a minimization of the leakage flow is however technically limited. To be able to minimize the losses in efficiency incurred by the inevitable presence of leakage flow, it is important to understand the governing mechanisms when the leakage flow and the main flow are interacting.

The use of numerical simulations of fluid flows has become an important tool in the process of optimizing fluid machinery and in achieving insight in the flow physics of turbomachinery configurations. By employing Computa-

tional Fluid Dynamics (CFD) in the development process, the number of expensive experiments in testing facilities can be reduced.

The requirements on the numerical schemes are increasing for several reasons: The enhancement of the performance of computers, the competition in the energy and propulsion sector, and the demand for efficient energy conversion processes. The fluid dynamics software should deliver reliable and accurate predictions of the flow field, be robust, computationally efficient and easy to use. In this context it should be noted that the flow field encountered in turbomachinery is one of the most complicated in the field of fluid dynamics practice. The Mach number of the flow in turbomachinery can vary significantly within one single device. It would therefore be desirable to have a Navier-Stokes solver which is capable of simulating flow in turbomachinery accurately and efficiently at arbitrary Mach numbers.

In this thesis the Mach number independent simulation of turbomachinery flows with an arbitrary state description of the fluid is addressed. To be able to simulate incompressible, compressible, and transonic flows with one single solution algorithm, a time-derivative preconditioning method, non-reflecting boundary conditions, and low-diffusion discretization schemes are developed. The developed solution scheme is used to simulate and to numerically study the interaction between leakage and main flow in a $1\frac{1}{2}$ stage shrouded turbine. From the analysis, general conclusions concerning the impact of leakage flow on the main flow and the associated exergy loss mechanisms are drawn.

1.2 Literature survey and overview of state-of-the-art

This thesis concerns both the development of methods for the simulation of turbomachinery flows as well as the analysis of leakage flow and loss generation mechanisms in turbomachinery flows. In the following literature survey, modeling aspects and numerical issues will be treated separately from the physical analysis of turbomachinery flows.

1.2.1 Leakage flow effects in shrouded axial turbomachinery

The impact of tip clearance flow on the main flow and the associated exergy losses was extensively studied in the 1990s, which a plethora of publications on both experimental (e.g., [37, 127, 293]) and numerical (e.g., [22, 147, 151, 192]) studies in this field testifies. The interaction between the tip clearance flow and the main flow for turbomachinery rows with unshrouded blades is not comparable to the interaction of leakage flow and main flow in shrouded turbomachinery. In turbomachinery with free ending blade tips, the pressure difference between the suction and the pressure side of the blades causes a leakage flow over the blade tip whereas in shrouded turbomachinery the axial pressure difference over the blade row causes a part of the fluid to flow over

the shroud instead of passing through the blade channel. Except for effects due to friction, the leakage flow will not change its flow direction when passing over the shroud and will thus reenter in the main flow with a flow angle differing greatly from that of the main flow. The ingress of leakage flow in the main flow can cause complex flow effects and will in most cases be responsible for significant exergy losses.

The losses caused by leakage flow over shrouded blades can be minimized by reducing the leakage and much effort has been undertaken in this direction [223, 264]. Constraints on the design determine the minimum clearance that can be achieved. To minimize the leakage losses optimised sealing arrangements should be used. A further reduction of the losses due to shroud leakage effects can be obtained by controlling the interaction between the leakage flow and the main flow.

The first work on the impact of leakage flow on the main flow was conducted by Traupel [275], Kacker and Okapuu [138] and Denton [73]. These publications provide global correlations for losses caused by leakage flow, but they do not take into account that leakage flow effects not only result in entropy generation due to mixing but also can induce losses in subsequent blade rows due to the changes in the main flow field.

In recent years there has been a series of publications on the interaction of the leakage and the main flow in axial turbomachinery. The paper of Korschunov and Döhler [144] presents the effect of an artificially produced jet (which simulates leakage flow) entering the main flow at different angles on a following linear cascade. Pfau et al. [206] have examined the steady and unsteady interactions within the inlet seal cavity with a three step labyrinth seal on a rotor shroud both experimentally and numerically.

Attempts to optimize the geometry of the sealing arrangements, shroud, and the casing to minimize the losses incurred by the interaction between the leakage flow have been reported in several publications. Wallis et al. [292] have tried to reduce the aerodynamic losses due to mixing when the leakage flow reenters the main flow by applying turning bladelets on the shroud in a four stage turbine. Özdemir [197] and Klein [143] investigate the effect of shortening the shroud, so that the rotating blade row is only partially instead of fully covered by the shroud. Schlienger et al. [244] present the effects of labyrinth seal variation on multistage axial turbine flow but can not report any advantageous effect on the overall turbine efficiency. In contrast to that, by optimizing the shroud geometry, sealing arrangement, as well as the cavities and by additionally applying deflectors, Rosic et al. [232, 233] show that the exergy losses due to the presence of leakage flow can be significantly reduced. Both Peters [202] and Adami [3] show that the mixing losses caused by the ingress of leakage flow in the main flow can be reduced if the outer edge of the downstream wall of the outlet cavity is chamfered. Mahle [176] shows in a numerical study that a turning device close to the outlet of the labyrinth seal can lead to an increase of the overall efficiency of the turbine.

Both Wallis [292] and Gier et al. [96] have examined the contributions of different types of losses in a shrouded turbine. They found that not only

the leakage flow itself but also the presence of cavities is responsible for a substantial part of the generation of losses in an axial turbine. The effect of the presence of cavities on the secondary flow field was also investigated in the work of Anker et al. [15]. In the work of Rosic and Denton [231] and of Rosic et al. [232, 233] the influence of both the presence of leakage flow and cavities on the main flow and the losses in a 3-stage axial turbine is studied in detail and various loss mechanisms are identified. Apart from these publications, there are not many systematic studies on the influence of the leakage flow on the aerodynamics of axial turbines.

Numerous articles exist on modelling labyrinth seals in their effect on the rotordynamics of turbomachinery devices (e.g., [34, 55, 264, 272]) and on numerical modelling of the losses caused by leakage flow in throughflow codes or inviscid solvers (e.g., [77, 138, 162]). There are however only few studies on the numerical modelling of the labyrinth seals in 3D, turbulent simulations of multi-stage turbomachinery. The motivation for using a numerical model would be to avoid a full discretization of the details of the cavities and the labyrinth seals. Among others Hunter and Orkwis [122], Brown [45], Anker et al. [15], Rosic et al. [234], Gier et al. [95] have formulated simple numerical models to avoid a detailed discretization of labyrinth seals in their simulations. Even though the developed models capture important effects and are better used than not accounting for leakage flow at all, they need either to be calibrated with experimental data or results from detailed simulations to deliver accurate results. Anker et al. [15] furthermore show that the first and last cavity in a sealing arrangement need to be discretized as the flow field first is sufficiently homogeneous between the first and the last sealing fin to be modelled by simplified 1D approaches. For detailed predictions of the leakage flow effects, a full, geometrically complete discretization of the turbine, shroud and cavity geometry should be used.

In a series of projects funded by Forschungsvereinigung Verbrennungskraftmaschinen (FVV), the Chair of Steam and Gas Turbines (DGT) of the Ruhr-University Bochum and the Institute for Thermal Turbomachinery and Machinery Laboratory (ITSM) at University of Stuttgart, have collaborated to study the influence of the leakage flow in a $1\frac{1}{2}$ stage axial turbine with a labyrinth seal on the periphery of the moving row [6, 7, 9, 10, 13, 14, 19, 92, 202, 207, 208, 310]. In these projects extensive measurements with pneumatic five-hole probes and hot-wire anemometry were carried out together with steady-state and time-accurate simulations. Some of the earlier results have been presented in Wolter et al. [311], Peters et al. [203, 204], Giboni et al. [93, 94] and Anker et al. [11, 12, 15, 17].

The leakage flow interaction has only been studied in a few works using time-accurate measurement and simulations. The numerical and experimental work carried at ITSM (Anker et al. [10, 13, 15, 19]) and DGT (Peters, Giboni, Wolter, et al. [92–94, 204, 311]) in the aforementioned FVV projects address the temporal effects of the interaction between the leakage and the main flow. Using time-accurate measurements Schlienger et al. [244, 245] study the interaction between re-entering leakage flow and main flow in a

two-stage turbine. Adami et al. [3] apply an unsteady CFD approach to study the interaction between the leakage flow and the main flow.

The use of time-accurate experiments related to turbomachinery flow has the advantage over the application of stationary measurement techniques that both the temporal and circumferential variations in the flow field are resolved; both local unsteady effects as well as effects attributed to a varying flow field in a blade row that is moving relatively to another row can be traced. Analogously, the use of unsteady flow simulations has the advantage that interaction between the flow in the rotor and the stator can be simulated – the potential fields of the blades, the wakes and the flow are tracked from one blade row to the next and their temporal evolution can be simulated without any loss in accuracy. In time-accurate simulations the flow field at the computational interface between two adjacent blade rows are directly coupled as opposed to steady-state simulations where the blade rows are connected via mixing planes, where the flow field in adjacent blade rows are merely coupled over circumferentially averaged quantities.

In the numerical studies of ITSM mentioned above the periodically unsteady interaction between the leakage flow, secondary flow and the main flow is studied. As shown by the work of Anker et al. [15] by comparing time-averaged flow field of an unsteady simulation with the results of a steady-state simulation where mixing planes were used, the essential effects are still captured accurately even when steady-state simulations are carried out.

The results presented in this thesis contributes to the understanding of the interaction of leakage flow and main flow in axial turbomachinery. In this work a comprehensive study is carried out in which, by subtraction of the numerical solution for a vanishing and a realistic clearance height, the impact of the leakage flow on the main flow, the secondary flow and the loss generating mechanisms are explicitly identified. Attention is drawn to the effect that the leakage flow has on the flow field of the shrouded rotor row. In particular effects introduced by the interaction of the cavity flow and the main flow in the rotor are examined and different loss generating mechanisms are discussed.

1.2.2 Methods for the simulation of turbomachinery flows at all speeds

The rapid increase in computer performance has promoted the development and use of numerical methods in all technical and scientific disciplines. The rise in the computing power allows the use of models with increasing complexity and the use of finer numerical resolution of the dynamics of the systems modeled.

In this context, computational fluid dynamics (CFD) software has become an indispensable tool in many industrial sectors in which fluid flow is of concern. The application of CFD in the design process over the past three decades has led to a significant improvement in the performance of aircraft engines [119]. The design of modern turbines and compressors is unthinkable with-

out the help of CFD software; the effective use of CFD simulations is a key ingredient in the design of fluid machinery and aeronautic devices. The benefits of applying CFD range from shorter design cycles to better performance and reduced cost and weight [74, 134].

The flow in turbomachinery may be incompressible, subsonic, transonic, or supersonic. Many aircraft engines have mixed flows, in which all of these regimes are present in a single blade row. For this reason it would be advantageous to have a Navier-Stokes solver which is capable of simulating flow in turbomachinery accurately and efficiently over a broad Mach number range.

Historically, low speed flows were first solved using solution schemes that solve the Euler or Navier-Stokes equations for incompressible fluids. In the pseudo-compressibility approach introduced by Chorin [61], a pressure time derivative is introduced in the continuity equation, which makes the system of incompressible Navier-Stokes equations hyperbolic and provides a means of updating the pressure field [205, 230]. Alternatively for the simulation of incompressible or low Mach number flow, pressure-based methods [200] have been formulated, which are frequently applied in both academic and industrial flow solvers. In the pressure based methods, the momentum equations are solved in a segregated fashion applying the most current iterate of the pressure field. In a second step of each iteration, the pressure field is updated ensuring that continuity is fulfilled [87].

Since the time-dependent compressible Euler equations are hyperbolic, regardless whether the flow is sub- or supersonic, density-based time-marching schemes were developed in the context of transonic, external aerodynamic applications [32, 131] and later extended to viscous, internal turbomachinery applications [56, 265]. These methods proved to be very effective for the computation of high Reynolds number flows in the transonic and supersonic regimes. However, these schemes become inefficient and inaccurate at low Mach numbers due to the disparity of acoustic and the advective velocities for low speed flows. For this reason, the computation of low Mach number flow was dominated by solution procedures [61, 200] solving the incompressible Navier-Stokes equations for many years.

The application of time-marching methods could be extended to low Mach number compressible flow after it was realized that the difficulty in solving the compressible equations for low Mach number flow was attributed to the large disparity of the acoustic wave speed and the waves convected at particle speed. Low Mach number perturbation methods were the first techniques, which were used to alleviate these problems and to calculate low speed compressible flow [104, 187, 222].

Later, various local preconditioning procedures were developed in which the time derivatives of the compressible Euler and Navier-Stokes equations are altered to control the eigenvalues and to accelerate convergence [43, 59, 160, 276, 278, 290, 301]. D. Choi and Merkle [58, 59] were the first to formulate a preconditioning scheme for the full Euler equations for compressible, ideal gas flow. The scheme was later extended by Y.-H. Choi and Merkle [60] to the Navier-Stokes equations to also account for viscous effects. Weiss and

Smith adapted their method and introduced a pressure gradient sensor to increase the robustness of the resulting solution scheme [301]. Subsequently, Merkle et al. [188] extended the method for the simulation of fluid with general equations of state. Turkel [276] generalized the Pseudo-Compressibility approach of Chorin [61] and presented in his work a unified theory of preconditioned methods that can both be used for compressible and incompressible flows. The preconditioning methods of Merkle and Turkel are very similar and these methods have been devised by applying one-dimensional eigenvalue, dispersion, and perturbation analysis to equilibrate the propagation velocities to ensure a good conditioning of the flow equations [289].

Van Leer et al. [160, 173, 175] have developed an alternative preconditioning method which is based on a two-dimensional wave-front analysis of the Euler equations. In their approach the time-derivatives of the flow equations are not only scaled for low Mach number but also for supersonic flows. Their preconditioning method accounts for many design considerations (optimal eigenvector structure, flow angle insensitivities, clustering of numerical eigenvalues, et cetera) for inviscid, ideal gas flows [69, 158]. Their method was extended by Lee et al. [158, 159] to account for viscous effects. However, compared to the preconditioning method of Merkle, in their method viscous effects have been treated with less rigor. Furthermore, it is not evident how to extend the preconditioning method of van Leer to fluids described by a general thermal and caloric equation of state.

Common for all of the preconditioning methods mentioned above, is that the temporal terms in the equations to be solved are altered to facilitate the use of time-stepping methods and to enhance their convergence rates. The modification of the temporal terms to equilibrate the propagation speeds in the numerical solution process is not a restriction of the generality of preconditioning method; in the limit of a converged solution, the time derivatives disappear so that the changed dynamics of the equations does not affect the solution accuracy. When unsteady simulations are to be performed, the preconditioning method must be incorporated into a dual time-stepping scheme, where preconditioning is applied at the inner pseudo-time level, thereby not affecting the outer loop stepping through physical time [48, 286, 301]. Since the preconditioned Navier-Stokes equations are valid at all speeds, they have potential for providing uniform convergence over all Reynolds and Mach number regimes [159, 189].

Preconditioning is beneficial for multigrid schemes [69, 173] and improves convergence because it removes the inherent stiffness in the governing equations caused by the disparity in wave propagation speeds. The elimination of the stiffness is not only important in explicit schemes but also in implicit ones. Due to the presence of nonlinearities and factorization errors, implicit time-marching schemes require the use of a finite Courant-Friedrichs-Lewy (CFL) number which also make the convergence dependent on the dynamics of the flow equations.

For some solution schemes preconditioning also has the advantage that it ensures that the dissipative terms resulting from the discretization of the

inviscid fluxes are correctly scaling in the low Mach number limit. If applied without the use of preconditioning both the popular Roe- and the Jameson-Schmidt-Turkel schemes become not only inefficient but also inaccurate when the Mach number approaches zero [105, 287, 289, 291].

While preconditioning methods have become popular and are also used for the simulation of real gas [80, 188], inert multicomponent or multiphase [120, 121, 124, 164], reacting [33, 81, 91, 224, 241, 286, 300, 309], or cavitating flow [36, 54, 65, 84, 150, 195, 251], there are not many reports [51, 279, 298, 301] known to the author where preconditioning is used for simulating turbomachinery flow at low Mach numbers. None of the aforementioned papers discuss a proper treatment of boundary conditions in conjunction with turbomachinery applications. Moreover, only few authors have presented preconditioning schemes that can be used for the simulation of fluids with arbitrary equations of state in the context of turbomachinery simulations [24, 88, 108, 301].

In the last two decades much work in the CFD community has been attributed to the development of improved discretization schemes [44, 128, 168, 169, 267, 268, 270]. However, first in recent years the attention has been drawn to the development of classical dissipation [36, 196, 216, 279] and low diffusion schemes in conjunction with preconditioning [79, 141, 171, 199, 236]. In the last years there has also been an increasing interest in the development of discretization schemes that can be used for completely stagnating to supersonic flows and yield a dissipation that scales correctly in the limit of a vanishing Mach number [163, 167, 225, 237].

Whether the fluid flow is laminar, transitional, or turbulent, it is inherently unsteady in multi-stage turbomachinery. To resolve the interaction between the potential fields of blade rows moving relative to each other and the flow field in detail, time-accurate simulations have to be applied.

Even though computational resources have increased significantly over the last decades, unsteady flow simulations, even in the RANS context, are still very time consuming. Unsteady simulations, and the subsequent handling of large data sets and the associated post-processing require significantly more effort from the user than when a steady simulation is carried out. This is especially true for the simulation of multi-stage turbomachinery applications where the modelling of many subsequent blade rows is necessary. For these reasons steady-state stage calculations remain common practice in the industrial design process of turbomachinery.

When steady-state stage computations are to be performed, so-called mixing planes are utilized to couple different frames of reference and to transfer circumferentially averaged data from the computational domain of adjacent blade rows.

Since blade rows in turbomachinery can be closely spaced it is often necessary to impose inlet and outlet boundaries as well as mixing planes close to the blading in a region where the flow is far from being uniform. In order to ensure that physical waves can traverse the numerical boundaries without interacting with the flow field in the interior of the domain, so-called non-

reflecting boundary conditions (NRBC) have been developed.

The idea of NRBC is to ensure that every wave can leave the computational domain without causing reflections or spurious oscillations at the boundaries. This means that the boundary condition is transmissive for outgoing waves but suppresses all spatially varying distributions at the boundary that would correspond to modes of incoming waves. The basic theoretical concepts for constructing NRBC were developed in the 1970s [82, 83, 115, 145]. Since then a large number of publications have been issued on the topic of NRBC in many branches of engineering and applied mathematics [100]. Unifying and extending some of these theories, Giles [98, 99] formulated a method for the application of NRBC to the linearized 2D Euler equations.

In the literature many authors report the use of a boundary condition treatment based solely on Riemann invariants (e.g., [126]) or equivalently [66] a 1D characteristic boundary condition treatment based on the Euler equations (e.g., [211]). The principle of using characteristic theory is to separate the solution updates at the boundary into contributions from incoming and outgoing waves. This procedure is necessary to ensure that corrections of the boundary values, which are undertaken to meet the specified conditions, are compatible [117, 118] and that the corrections are propagated correctly into the interior of the computational domain. Lele and Poinso [211] have extended the characteristic boundary condition treatment to also account for viscous effects. Their method is often referred to as Navier-Stokes Characteristic Boundary Condition (NSCBC) treatment in the literature.

Whether or not it accounts for viscous effects, a disadvantage associated with the use of a one-dimensional characteristic theory for the treatment of boundary conditions is that these methods rely on the assumption that the flow at the boundaries can be regarded as locally one-dimensional. The single-dimensionality assumption has proven to perform well when the flow is almost aligned with the boundary; however distortions of the flow fields and reflections emerge when the flow does not cross the boundary perpendicularly or the flow is non-uniform in the transverse directions [247].

A further problem associated with the boundary condition treatment based solely on one-dimensional characteristic theory is related to the specification of spatially uniform boundary conditions. Giles and Saxer [242, 243] show that even if the characteristic variables at the boundary that are corresponding to outgoing waves are extrapolated from the interior, reflections will not be avoided if spatially constant distributions of flow variables are prescribed.

As shown by Seybold et al. [247, 248], the use of 1D characteristic treatment does not lead to reflections if a distribution of the flow variables is imposed, which corresponds to the solution one would obtain at the position of the current boundaries, if the computational domain would be extended up- and downstream, respectively. As noted by Denton [72], a physically sound boundary condition treatment for turbomachinery applications should impose desired values for averaged quantities but should allow a distribution of the flow variables in circumferential direction. Unfortunately, the use of a boundary condition treatment based on one-dimensional characteristic theory does

not allow an automatic prediction of a physical flow field distribution about a specified averaged value.

Yoo et al. [314, 315] achieved an improvement of the NSCBC type of boundary condition treatment by also accounting for transverse terms. This kind of boundary condition was further enhanced by Lodato et al. [170], who derived compatibility conditions at the edges and corners of the computational domain, where walls meet inlet or outlet boundaries. The inclusion of transverse terms allows for variations of the solution variables at the boundary and the resulting numerical treatment leads to non-reflecting boundaries. This method has been successfully applied in the context of Large Eddy Simulations of reacting flows but has not been adapted and tested for simulations of turbomachinery flow.

For steady-state simulations of turbomachinery flows Saxer and Giles [242, 243] devised a quasi-three-dimensional non-reflecting boundary condition treatment. In their approach, the solution at the boundary is decomposed into Fourier modes. The zeroth mode, which corresponds to the average solution, is treated according to standard one-dimensional characteristic theory and enables the user to specify the circumferential averages of certain flow field parameters at the boundary. The remaining harmonics of the solution at the boundary are altered to satisfy a condition derived by Giles basing on the linearized, two-dimensional Euler equations. This ensures that the variations corresponding to incoming (or reflected) waves are eliminated. In the quasi-three-dimensional approach of Saxer, the grid layers in the radial direction are treated independently, so that the Fourier decomposition of the state variables at the boundary is limited to the circumferential direction.

The quasi-3D (Q3D) steady-state NRBCs due to Saxer and Giles allows variations of the flow variables around an average value. In general they lead to a more physical prediction of the flow fields near the boundaries than when boundary conditions based merely on 1D characteristic theory are used [63, 247, 248].

In the derivation of the Q3D-NRBC it is assumed that the radial variations of the flow field are small compared to those in the pitchwise direction, so that this treatment may not always lead to a fully non-reflecting behavior of the boundaries. In addition, the Q3D-NRBC treatment requires the specification of the correct radial distribution of the boundary values. However, boundary values are often only known as average values for the whole boundary surface. Motivated by these limitations, the theory of Giles was extended to three dimensions by Anker and Seybold [21] and applied by Schrader [246]. In the publication of Anker et al. [20] it is shown that the developed steady-state, fully three-dimensional NRBC treatment outperforms the Q3D-NRBC in flow configurations where the flow is three-dimensional and periodicity exists in both lateral directions. The developed treatment applies a double Fourier expansion and when periodicity does not exist in both spanwise and circumferential direction, errors linked to Fourier decomposition are introduced, which significantly degrade the performance of this kind of boundary condition treatment.

It should be noted that Fatsis and van den Braembussche [86] also developed a three-dimensional non-reflecting boundary treatment for steady state flow simulations. However, their boundary condition treatment is approximate, whereas the theory developed by Anker and Seybold is exact within the linearized Euler equations. Imanari and Kodoma [125] have introduced a non-reflecting treatment for three-dimensional Euler equations by expanding the pressure field normal to the boundary into Fourier-Bessel series. They obtain a non-reflecting property by suppressing the perturbations that correspond to pressure waves leaving the domain. For the simulations of strut cascades they achieve good results, but their treatment is not general as they neglect the influence that vorticity and entropy waves have on the pressure perturbations. Fan and Lakshminarayana [85] solve partial differential equations in their three-dimensional boundary treatment for unsteady flows; however, the underlying theory contains several approximations and from their work it is not clear, whether or not their treatment leads to a fully non-reflecting boundary condition treatment.

Given the limitations of the 3D-NRBC treatment mentioned above, the Q3D-NRBCs of Saxer and Giles [242, 243] represent state-of-the-art for a boundary condition treatment for the simulation of turbomachinery applications. This boundary condition treatment has attained popularity and has been implemented in both research and commercial flow solvers [88, 123, 190, 210].

The treatment of one-dimensional boundary conditions in the context of time-derivative preconditioning schemes has been subject to several studies. Using a reflection analysis, Darmofal et al. [66, 67] have shown that a Riemann/Characteristic boundary condition treatment based on the unpreconditioned Euler equations are reflective when used with preconditioning. It is evident that the changed dynamics of the flow equations due to the use of time-derivative preconditioning must be accounted for when a characteristic boundary condition treatment is applied. How to concretely accommodate for the time-derivative preconditioning method in a boundary condition treatment based on Riemann invariants, or equivalently, on characteristic theory, has been addressed in various publications (e.g., [108, 277]), but to the knowledge of the author there has not been published any work on multidimensional non-reflecting boundary conditions for preconditioned systems and/or flows with general equations of state.

1.2.3 Modeling of transitional and turbulent flows in turbomachinery

The fluid flow encountered in turbomachinery devices is usually turbulent. Turbulent flows occur when the Reynolds number is larger than the critical one and a regular, laminar flow pattern collapses due to instability of the flow. In turbulent flow vortices are formed, which in a cascade process break up into successively smaller vortices until they are dissipated by viscous effects [116, 271]. The vortical motion in turbulent flows has a significant im-

impact on the averaged flow field, on the loss generation, and on separation and attachment of the flow over obstacles. Since the Navier-Stokes equations describe general flows, they can be used to simulate turbulent flow directly. Except for moderate low Reynolds numbers and simple geometries, a Direct Numerical Simulation (DNS) is computationally very expensive and practically not feasible due to the presence of vastly different length scales of the vortices [4, 212, 228]. An alternative approach, which demands less computational resources, is only to resolve the largest eddies and model the smallest ones. The so-called Large Eddy Simulation (LES) including the Detached Eddy Simulation (DES) techniques are increasing in popularity and have a strong predictive capability [40, 107, 119, 178]. These methods are used by research institutions for phenomenological studies [316] over aeronautical components, for the simulation of elementary flames, or for the computation of the reactive flow in combustors [181, 273].

Unfortunately, both a DES and a LES are computationally expensive since they require an unsteady simulation on meshes fine enough to resolve all the eddies in the main flow down to the inertial range, which for high Reynolds numbers can represent a formidable task. While a DES/LES is practically feasible for the aerodynamical study of isolated configurations, like the flow over wings or single turbomachinery blades, it is still far too expensive for being used for the simulation of complete turbomachinery stages.

To account for the influence of turbulence without resolving any of the turbulent eddies, statistical turbulence models have been developed. In these models the flow is simulated by solving the Reynolds-Averaged Navier-Stokes (RANS) equations in conjunction with a model for the Reynolds stresses [227], which describe the average influence of the turbulent eddies on the main flow. There are two different principal approaches for modeling the Reynolds stresses appearing in the RANS equations. In the most advanced Differential Reynolds Stress Modeling (DRSM) approaches [110–112, 135, 155, 259] a transport equation for each of the six different elements of the Reynolds stress tensor is solved as well as a transport equation for the dissipation rate of the turbulent kinetic energy [4, 53, 90, 212]. A computationally less expensive and a numerically more robust approach consists in modelling the Reynolds stresses as a function of the velocity gradients of the mean flow field. In the so-called eddy viscosity models the Boussinesq hypothesis [41] is applied, which assumes an analogy between the diffusive transport of momentum caused by the molecular and by the turbulent motion. In these models the influence of the turbulence on the main flow is effectively modelled by adding an eddy viscosity term to the molecular viscosity coefficient. In the simplest models the eddy viscosity is modelled via algebraic relations in dependence of the normalized wall distance, mean flow quantities as well as gradients of velocity and pressure. The oldest eddy-viscosity model is the mixing length model of Prandtl [214], in which the eddy viscosity is assumed to be proportional to the square of the mixing length and the norm of the velocity gradient. As detailed in Wilcox [306], modern algebraic turbulence models, e.g., the Cebeci-Smith [50, 255] and the Baldwin-Lomax [27] models repre-

sent extensions of this model by accounting for wall-damping [281], turbulent intermittency [64, 142] and Clausers [62] formula for the eddy viscosity in the defect layer. Algebraic turbulence models are robust and are for this reason still used [76]. These models are suited for attached flows with positive pressure gradients [306] or slightly negative pressure gradients as long as the flow does not separate [52]; for separated flows and/or flows with adverse pressure gradients only the Johnson-King [133] turbulence model is recommended [52, 183], which solves an ordinary differential equation for the maximum value of the shear stress. For complex, 3D flow configurations or flows with adverse pressure gradients, the use of so-called one- or two-equation turbulence models is preferable [52] in which respectively one- or two partial differential equations (PDE) are solved in addition to the RANS equations to model the effect of turbulence. Frequently applied one-equation models are the Baldwin-Barth [25, 26] and the Spalart-Allmaras turbulence model [258] as well as variants of the latter [240, 252, 257], which include effects due to rotation. Among the two-equation turbulence models, the $k-\varepsilon$ type (Standard [156, 157], Realizable [250], RNG [313]) and $k-\omega$ type (Modified Wilcox model [308]) are commonly applied in science and engineering. Contrary to the $k-\varepsilon$ turbulence models, the $k-\omega$ models do not need wall damping functions to correctly resolve turbulent boundary layers. However, $k-\omega$ models are very sensitive to the free stream values of ω [212]. In order to combine the advantages of both models, Menter [184] developed a model, which employs the original $k-\omega$ model of Wilcox [305] in the boundary layer and switches to the standard $k-\varepsilon$ model outside. Inspired by the Johnston-King model [133], Menter included in his Shear-Stress Transport (SST) model a modification of the definition of the eddy-viscosity, which accounts for the effect of the transport of the turbulent shear stress. In a comparative study on standard aerodynamic test cases, Bardina et al. [28] conclude that Menter's SST as well as the Spalart-Allmaras model outperform both the Standard $k-\varepsilon$ model of Launder and Sharma [156, 157] as well as Wilcox's original $k-\omega$ model. The Spalart-Allmaras and Menter's SST models are popular eddy-viscosity models and can now be regarded as a standard choice for industrial use [49].

In the context of the simulation and analysis of the leakage flow effects in shrouded axial turbines, Rosic et al. [232, 233] have been successful even though only a mixing-length approach for modeling the turbulence was used. Seybold [249] simulated the flow through the labyrinth seal in an axial turbine using various standard eddy-viscosity models ranging from the algebraic Baldwin-Lomax model to the $k-\omega$ SST model. Like in the work of Sögüt [256], which concerned the simulation of a complete shrouded axial turbine, no conclusion could be made in favour of any of the turbulence models used.

In the FLOMANIA project the performance of various one-equation, linear and non-linear two-equation models, DRSM, DES and LES models have been assessed by a large consortium on a range of different test cases including turbomachinery configurations [106]. In that collaborative assessment of turbulence models, it was found that the Spalart-Allmaras and the $k-\omega$ SST models perform well for predominantly attached, high Reynolds number flow.

For simpler, two-dimensional configurations non-linear two-equation models as well as DRSM models may lead to a better reproduction of the flow physics than the aforementioned models, even though not universally [49]. In the FLOMANIA project, it was furthermore concluded that all RANS based models, including DRSM, fail for complex, three-dimensional separating-reattaching flow. For such flows, acceptable results were only obtained when LES or hybrid LES-RANS approaches are used. These findings show that unless LES-based models are used, there is still considerable uncertainty associated with turbulence modeling for general flow configurations.

In order to accurately predict the losses in turbomachinery, not only the prediction of the effect of turbulence itself but also the accurate determination of the on-set and the extent of the laminar-turbulent transition is important [154, 266]. The accurate prediction of the boundary layer development and its interaction with the main flow is especially important for low-pressure turbines, where the flow often is transitional [152]. Despite the importance of transition modeling, compared to the development of statistical turbulence models for fully turbulent flow, the efforts that have been invested on developing models that reliably determine the laminar-turbulent transition of boundary layers are relatively low.

When turbomachinery flow is simulated using the RANS equations, a common method to account for the laminar-turbulent transition is to turn on the turbulence model at a predefined, given chord length (e.g., [136, 238]). A more advanced approach in the context of RANS simulations [213], consists in using empirical correlations [1, 180] for the determination of the transition onset location. None of these methods are predictive and the coupling of empirical correlations with RANS models can be challenging as some of these models require the determination of integral quantities like for instance the boundary layer thickness [154]. Some of these modeling approaches assume instantaneous transition at the onset location and thereby neglect the importance of the transitional region, which can lead to approximate results.

Transition can be predicted directly by applying low Reynolds models [307]; this method is however not regarded as a reliable means to predict the transition point or the extent of the transitional region [154, 239, 266, 295, 303]. The more general modeling approach is to solve for additional transport equations for states that are essential in the description of transitional flows (e.g., intermittency, laminar kinetic energy, or transition Reynolds number). Phenomenological models [57, 80, 296, 297] as well as correlation based models [260, 261, 266] have been developed. Transition modeling is a topic of active research [39] and current efforts are focused on developing models that do not need integral quantities and solely rely on local flow quantities [153, 185, 295–297].

In brief, whereas LES based models are quite promising for the accurate prediction of the fluid flow of aerodynamic configurations but are too expensive in terms of computational resources to be applied in practical turbomachinery simulations, the application of the computationally more efficient RANS models are connected with modeling uncertainties both for transitional

and fully turbulent flows.

While the improvement of RANS based turbulence models is important, a more pertinent issue for the simulation of low speed flows is to prevent that a wrong scaling of the dissipation terms or a numerically inconsistent boundary condition treatment are degrading the accuracy and the reliability of the solution scheme [6, 312]. Rather than to concentrate on devising and assessing RANS based turbulence models, which is a topic on its own, the development of an accurate, efficient, robust, and Mach number independent solution scheme is the focal point in the numerical part of this thesis. For this reason, issues related to modeling of turbulence will not be given much attention in later chapters of this thesis. The modeling method used in this work will be based on the algebraic approach developed by Merz [190] and Jung [136], which for the simulation of the attached flow through axial turbines has proven to be sufficiently robust and accurate for engineering purpose [149, 221] and can be used together with the time-inclination method of Giles [294] without the need for modifications.

1.3 Objectives of the present thesis

The aim of the present thesis is to contribute to the simulation and the analysis of turbomachinery flows.

On the numerical side, the goal of the present work is to develop a numerical scheme for the simulation of flows through multi-stage turbomachinery at arbitrary Mach number levels. It is required, that the solution scheme be robust, accurate and efficient and it be possible to simulate fluids obeying arbitrary thermal and caloric state equations.

The developments are to be based on an already existing density-based solution scheme for the simulation of high-speed flow developed by Merz [190], Krückels [147], Raif [221], Jung [136] and Bauer [30, 31]. The solution scheme should be low diffusive and be suited for the simulation of transonic flows containing strong shocks as well as large low Mach number regions so that the flow in arbitrary turbomachinery applications can be simulated accurately.

For the simulation of multi-stage turbomachinery the blade-rows can be situated close to each other and in the simulation of such configurations the inlet, outlet and the mixing planes may have to be positioned close to the blade rows, where the flow is inhomogeneous. To avoid that the numerical boundary treatment impairs the solution, a non-reflecting boundary condition needs to be developed, that is both suitable for the simulation of low Mach and transonic flows.

The second objective of the present thesis, is to use the developed solution scheme to simulate and analyse the flow in a $1\frac{1}{2}$ -stage, shrouded low-speed axial turbine situated at the University of Bochum [42]. The flow in this turbine is to be studied for a realistic clearance height of the labyrinth seal of the rotor row and the effect of the leakage flow on the main flow is to be investigated. Since the minimization of leakage flow is constructively limited

and the presence of leakage flow is thus inevitable, it is for the future design of turbomachinery components important to understand and identify the energy producing processes involved. The interaction between the cavity, leakage, secondary and main flow is a recent topic of interest and it is therefore important that a systematic study, which contributes to the comprehension of the physical phenomena and the loss generation taking place, be carried out.

1.4 Outline of the present thesis

The numerical methods developed in the current work are implemented in the ITSM3D flow solver. For this reason, the baseline solution scheme of that flow solver is described in Chapter 2. The chapter summarizes the discretization and solution scheme, which has been developed and applied successfully by Merz, Krückels and others for steady-state simulations of the flow through transonic turbomachinery devices [148, 191].

In order to be able to simulate flows at arbitrary Mach numbers with the density-based solution scheme used in ITSM3D, a time-derivative preconditioning technique is introduced. Chapter 3 describes the preconditioning method applied, its theoretical basis and the modifications introduced to make the method robust for practical simulations. Results from several verification and validation test cases confirm that the preconditioned solution scheme leads to Mach number independent convergence rates. The presented test cases show furthermore, that accurate solutions can be obtained for low Mach number, transonic, and supersonic flow conditions.

In order to obtain a solution scheme which is low diffusive, monotonicity preserving, and simultaneously leads to a sharp resolution of shocks, several upwind-biased artificial dissipation schemes were developed in the current work. These schemes are presented and assessed in Chapter 4. Since they were developed in the context of Merkle's time-derivative preconditioning scheme, they have been formulated for simulation of flows with a general equation of state. Results from several test cases show that the developed discretization schemes lead to less diffusive solutions than the baseline scheme and yield accurate and monotone solutions for both low and high Mach number flows.

In the current work, the quasi-three-dimensional non-reflecting boundary condition treatment of Giles and Saxer [242, 243] was extended to preconditioned systems and general equations of state. This extension was necessary since the use of time-derivative preconditioning alters the characteristic speeds of the governing equations. In addition, numerical tests showed that the use of the original boundary condition treatment of Giles and Saxer was neither robust nor did it lead to non-reflecting solutions when used in conjunction with the preconditioned solution scheme. The developed theory as well as the implementation details are described in Chapter 5. The presented results verify that the solutions obtained with the new boundary condition treatment are free of reflections for incompressible flows as well as for ideal gas flow at

arbitrary Mach numbers.

In Chapter 6 the low-diffusive, preconditioned solution scheme together with the developed non-reflecting boundary condition treatment is used to simulate the flow in $1\frac{1}{2}$ -stage axial turbine with shroud on the rotor row. By comparing the flow field for a realistic, a small and a vanishing clearance height, the influence of the leakage flow on the main and secondary flow is systematically investigated. The physical effects attributed to the interaction of leakage and main flow are discussed. In particular, effects introduced by the interaction of the cavity flow and the main flow in the rotor are examined and different loss generating mechanisms are discussed.

Chapter 2

A baseline Finite-Volume solution scheme for the Navier-Stokes equations

In the current work the flow solver ITSM3D was used for developing new schemes for the simulation of turbomachinery flows as well as for investigating the interaction between leakage and main flow in axial turbomachinery. As the name suggests the flow solver ITSM3D was developed at the Institute for Thermal Turbomachinery and Machinery Laboratory (ITSM) of University of Stuttgart. The baseline scheme, which is outlined in this chapter, was developed by Bauer [29], Jung [136], Krückels [146], Raif [221], and Merz [190], among others. The flow solver ITSM3D is used in the current work since it is computationally efficient and offers the use of non-reflecting inlet, outlet and mixing planes. With the time-inclination method of Giles, the flow solver can be used to simulate the rotor-stator interaction in axial turbomachinery for arbitrary pitch ratios [137].

2.1 Governing equations

For turbomachinery applications it is convenient to solve the Navier-Stokes equations in a cylindrical coordinate system that is aligned with the the rotational axis and rotates with the blade row. This choice of a coordinate system is the basis of the flow equations solved in ITSM3D as it naturally accounts for both the axis-symmetry as well as the angular motion of the turbomachinery geometry in an elegant fashion. The Navier-Stokes equations solved in ITSM3D are formulated for a $x - \phi - r$ coordinate-system, that is rotating with an angular speed Ω in a mathematical negative sense around the x -axis. These equations read as

$$\frac{\partial \mathbf{Q}}{\partial t} + \frac{\partial \mathbf{E}}{\partial x} + \frac{1}{r} \frac{\partial \mathbf{F}}{\partial \phi} + \frac{1}{r} \frac{\partial (r\mathbf{G})}{\partial r} + \mathbf{H} = \mathbf{0} \quad (2.1)$$

with

$$\mathbf{E} = \mathbf{E}_c - \mathbf{E}_v, \quad \mathbf{F} = \mathbf{F}_c - \mathbf{F}_v, \quad \mathbf{G} = \mathbf{G}_c - \mathbf{G}_v, \quad \mathbf{H} = \mathbf{H}_c - \mathbf{H}_v,$$

and

$$\begin{aligned}
\mathbf{Q} &= \begin{bmatrix} \varrho \\ \varrho w_x \\ \varrho w_\phi \\ \varrho w_r \\ \varrho e_0 \end{bmatrix}, \quad \mathbf{E}_c = \begin{bmatrix} \varrho w_x \\ \varrho w_x^2 + p \\ \varrho w_\phi w_x \\ \varrho w_r w_x \\ \varrho h_0 w_x \end{bmatrix}, \quad \mathbf{E}_v = \begin{bmatrix} 0 \\ \tau_{xx} \\ \tau_{\phi x} \\ \tau_{rx} \\ \tau_{xi} w_i + k_\lambda \frac{\partial T}{\partial x} \end{bmatrix}, \\
\mathbf{F}_c &= \begin{bmatrix} \varrho w_\phi \\ \varrho w_x w_\phi \\ \varrho w_\phi^2 + p \\ \varrho w_r w_\phi \\ \varrho h_0 w_\phi \end{bmatrix}, \quad \mathbf{F}_v = \begin{bmatrix} 0 \\ \tau_{x\phi} \\ \tau_{\phi\phi} \\ \tau_{r\phi} \\ \tau_{\phi i} w_i + k_\lambda \frac{1}{r} \frac{\partial T}{\partial \phi} \end{bmatrix}, \quad \mathbf{G}_c = \begin{bmatrix} \varrho w_r \\ \varrho w_x w_r \\ \varrho w_\phi w_r \\ \varrho w_r^2 + p \\ \varrho h_0 w_r \end{bmatrix}, \\
\mathbf{G}_v &= \begin{bmatrix} 0 \\ \tau_{xr} \\ \tau_{\phi r} \\ \tau_{rr} \\ \tau_{ri} w_i + k_\lambda \frac{\partial T}{\partial r} \end{bmatrix}, \quad \mathbf{H}_c = \frac{1}{r} \begin{bmatrix} 0 \\ 0 \\ \varrho w_r (w_\phi + 2\Omega r) \\ -\varrho (w_\phi + \Omega r)^2 - p \\ 0 \end{bmatrix}, \quad \mathbf{H}_v = \frac{1}{r} \begin{bmatrix} 0 \\ 0 \\ \tau_{r\phi} \\ -\tau_{\phi\phi} \\ 0 \end{bmatrix}.
\end{aligned}$$

In the baseline scheme in ITSM3D it is assumed that the fluid behaves as a caloric and thermal ideal gas, whereby the following state equations

$$p = \varrho RT, \quad \varrho e_0 = \frac{p}{\gamma - 1} + \frac{1}{2} \varrho [w_x^2 + w_\phi^2 + w_r^2 - (\Omega r)^2] \quad (2.2)$$

are used, where R represents the individual gas constant and γ the ratio of specific heats. The shear stresses are calculated assuming that the fluid behaves like a Newtonian fluid. The laminar viscosity μ_l is determined using Sutherland's law and turbulence is modelled applying the Baldwin-Lomax turbulence model, which is an algebraic model for the turbulent viscosity μ_t . It is assumed that the laminar and the turbulent Prandtl numbers are constant, i.e.,

$$\text{Pr}_l = 0.72, \quad \text{Pr}_t = 0.9 \quad (2.3)$$

respectively, so that the thermal conductivity k_λ can be calculated via the following relation:

$$k_\lambda = c_p \left(\frac{\mu_l}{\text{Pr}_l} + \frac{\mu_t}{\text{Pr}_t} \right). \quad (2.4)$$

2.2 Discretization scheme and solution procedure

The discretization- and solution scheme, that is applied in the flow solver ITSM3D is based on work of Jameson et al. [132]. In this scheme the spatial and temporal discretization are treated separately according to the method of lines. Correspondingly, the spatial and temporal discretization will in the following be described separately.

In the flow solver ITSM3D the Finite-Volume method is used for the spatial discretization of the flow equations. In this method, the physical space

is subdivided in finite volumes for which discrete balance equations are formulated for the conservation of mass, momentum and energy. These discrete equations approximate the integral average of the temporal change of the independent solution variables in each control volume. The use of an integral form ensures a conservation of the fluxes and admits weak solutions of the conservation equations; the latter property is important for capturing shocks in the simulation of transonic flows.

2.2.1 Spatial discretization

The conservative three-dimensional Navier-Stokes equations in cylindrical coordinates are discretized spatially using a cell-vertex Finite-Volume scheme. The computational domain is subdivided in curved hexahedral elements and the independent flow quantities are stored at the vertices of the elements. The volumes for discretization of the convective fluxes is formed by the eight hexahedral elements that share a node. With the assumption that the point of gravity of the resulting control volume is coinciding with the common corner point (i, j, k) and that the flow quantities are linearly distributed over the control volume $\check{V}_{i,j,k}$, the integral of the unsteady terms of the conservation equations can be approximated to

$$\int_{\check{V}_{i,j,k}} \frac{\partial \mathbf{Q}_{i,j,k}}{\partial t} dV \approx \check{V}_{i,j,k} \cdot \frac{\partial \mathbf{Q}_{i,j,k}}{\partial t} \quad (2.5)$$

with a second order accuracy. If the aforementioned assumptions are not met, the latter discretization is at worst of first order accuracy.

The surface integral of the convective fluxes and the volume integral of the convective sources are approximated through a discrete sum of fluxes and sources. The vector of the respective sums for each transport equation is called the convective residual vector \mathbf{R}_c . The corresponding sum resulting from the discretization of diffusive terms is called the diffusive residual vector \mathbf{R}_d . With the introduction of these residual vectors, the following semi-discrete form of the conservation equation is obtained

$$\frac{\partial \mathbf{Q}_{i,j,k}}{\partial t} = -\frac{1}{\check{V}_{i,j,k}} (\mathbf{R}_c + \mathbf{R}_d). \quad (2.6)$$

In ITSM3D the convective residual vector \mathbf{R}_c is calculated according to the method of Hall [109]. With this scheme the convective residual vector is calculated as

$$\begin{aligned} \mathbf{R}_{c,i,j,k} &= \sum_{m=1}^{24} (\bar{\mathbf{E}}_{c,m} S_{x,m} + \bar{\mathbf{F}}_{c,m} S_{\phi,m} + \bar{\mathbf{G}}_{c,m} S_{r,m})_{i,j,k} + \sum_{l=1}^8 (\bar{\mathbf{H}}_{c,l} V_l)_{i,j,k} \\ &= \sum_{m=1}^{24} (\mathbf{r}_{F,c,x,m} + \mathbf{r}_{F,c,\phi,m} + \mathbf{r}_{F,c,r,m})_{i,j,k} + \sum_{l=1}^8 (\mathbf{r}_{S,c,l})_{i,j,k} \end{aligned} \quad (2.7)$$

for each control volume $\check{V}_{i,j,k}$. The surface of the control volume $\check{V}_{i,j,k}$ is formed by the 24 outer surfaces \mathbf{S}_m of the eight cells V_l that surrounds the central node (i, j, k) , cf. Fig. 2.1.

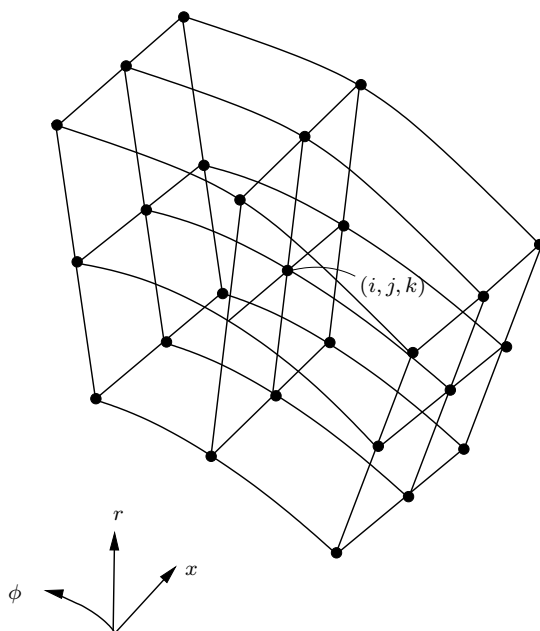


Figure 2.1: Control volume $V_{i,j,k}$ for the determination of the convective fluxes and sources

Through the assumption of a linear distribution of the state variables, the flux contribution of a face S_m is determined via an arithmetic averaging of the flux vectors at its four corners; for instance the axial component of the convective flux contribution $\mathbf{r}_{F,C,x,m}$ of the surface S_m calculates as

$$\mathbf{r}_{F,c,x,m} = \bar{\mathbf{E}}_{c,m} S_{x,m} = \frac{1}{4} (\mathbf{E}_{c,m,1} + \mathbf{E}_{c,m,2} + \mathbf{E}_{c,m,3} + \mathbf{E}_{c,m,4}) S_{x,m}, \quad \forall m = 1, \dots, 24. \quad (2.8)$$

Similarly, the specific contribution $\mathbf{r}_{S,c,l}$ of the convective source terms $\mathbf{H}_{c,l}$ of a hexahedral element V_l to the convective residual is calculated by an arithmetic averaging of the source terms of the eight corners $i = 1, \dots, 8$:

$$\mathbf{r}_{S,c,l} = \frac{1}{8} V_l \sum_{i=1}^8 \mathbf{H}_{c,l,i}. \quad (2.9)$$

A cell-vertex scheme has the advantage over a cell-centered scheme that the fluxes can be determined directly without the need for interpolation. Furthermore, for a cell-vertex scheme the boundary conditions can be applied without extrapolation of the states. According to Rossow [235], cell-vertex schemes have the advantage that they possess a second order accuracy on smooth meshes and a first order accuracy on distorted meshes. On smooth meshes cell-centered schemes also possess a second order accuracy, but they exhibit a zero order accuracy on distorted meshes.

In order to determine the residuals \mathbf{R}_D of the diffusive contributions, it is necessary to calculate the gradients of the velocities and the temperature. In ITSM3D the diffusive residuals are calculated according to the approach

of Radespiel and Rossow [217], which exhibits a second order accuracy on smooth grids and a first order accuracy on distorted meshes. This accuracy is achieved by calculating the gradients on the dual mesh by simultaneously accounting for the skewedness and curvilinearity of the grid. A detailed description of the scheme for the computation of the diffusive contributions can be found in the work of Radespiel and Rossow [217] as well as in the thesis of Merz [190].

2.2.2 The necessity of adding artificial dissipation in a central scheme

The finite-volume scheme described above applies a central discretization. Since numerical dissipation is not inherent to this type of discretization, an odd-even decoupling of the states of successive nodes may occur if no artificial dissipation is introduced in the scheme. In the baseline scheme in ITSM3D artificial dissipation D is added to the convective and diffusive residuals in the following manner:

$$\frac{\partial \mathbf{Q}_{i,j,k}}{\partial t} = -\frac{1}{\check{V}_{i,j,k}} (\mathbf{R}_c + \mathbf{R}_d + D). \quad (2.10)$$

The artificial dissipation terms are calculated in such a way, that they damp high frequency oscillations but leave the waves that extend over many grid nodes undamped. The damping of the high frequency oscillations in the solution is important due to the non-linear terms in the momentum equations. Through these terms energy can be transferred from long to short waves. If no mechanism is dissipating the energy of the low frequency waves, these may reach a sufficient amplitude that the scheme becomes unstable even if it were stable for the linearized flow equations. The laminar and the turbulent viscosity in the flow simulations damp the high frequency oscillations. However, except in regions of low cell Reynolds numbers, this damping is only effective for frequencies that are higher than those which can be resolved on a practical mesh for RANS computations, wherefore artificial dissipation is indispensable not only for inviscid but also for viscous flow computations.

2.2.3 The artificial dissipation scheme of Jameson, Schmidt and Turkel

The artificial dissipation applied in ITSM3D is based on the work of Jameson, Schmidt, and Turkel (JST) [132] and is constructed of a combination of second and fourth order differences of the solution vector. Applying a grid conformal $\xi - \eta - \zeta$ coordinate system, the artificial dissipation $D_{i,j,k}$ related to the control volume $\check{V}_{i,j,k}$ reads as

$$D_{i,j,k} = \left(-D_{\xi}^{(2)} + D_{\xi}^{(4)} - D_{\eta}^{(2)} + D_{\eta}^{(4)} - D_{\zeta}^{(2)} + D_{\zeta}^{(4)} \right) \mathbf{Q}_{i,j,k}. \quad (2.11)$$

The second and fourth order dissipation operators are defined as

$$D_\xi^{(2)} = \delta_\xi^- (\bar{\rho}_\xi^V \varepsilon^{(2)})_{i+1/2,j,k} \delta_\xi^+ \quad (2.12)$$

and

$$D_\xi^{(4)} = \delta_\xi^- (\bar{\rho}_\xi^V \varepsilon^{(4)})_{i+1/2,j,k} \delta_\xi^+ \delta_\xi^- \delta_\xi^+, \quad (2.13)$$

respectively, with the forward and backward difference operators δ_ξ^+ and δ_ξ^- for the ξ -direction given by

$$\delta_\xi^+ \psi_{i,j,k} := \psi_{i+1,j,k} - \psi_{i,j,k}, \quad \delta_\xi^- \psi_{i,j,k} := \psi_{i,j,k} - \psi_{i-1,j,k}. \quad (2.14)$$

The scaling factor $\bar{\rho}_\xi^V$ can be determined isotropically by a simple addition of the volume weighted spectral radii for all grid directions

$$\bar{\rho}_{\xi,i+1/2,j,k}^V = \rho_{\xi,i+1/2,j,k}^V + \rho_{\eta,i+1/2,j,k}^V + \rho_{\zeta,i+1/2,j,k}^V. \quad (2.15)$$

The scalar formulation of the artificial dissipation in Eq. (2.11) with the isotropic scaling factors in Eq. (2.15) was originally developed for the solution of the Euler equations with meshes having an aspect ratio close to unity. For the solution of the RANS equations for typical turbomachinery applications meshes with large aspect ratios are used. To avoid that the stretching of the grids does not lead to excess dissipation, the anisotropic scaling factors of Radespiel et al. [218] are used in ITSM3D. For instance for the ξ direction, the anisotropic scaling factor is calculated as

$$\bar{\rho}_{\xi,i+1/2,j,k}^V = (\Theta_\xi \cdot \rho_\xi^V)_{i+1/2,j,k}, \quad (2.16)$$

where the weighting factor Θ_ξ is defined as

$$\Theta_\xi = 1 + \max \left(\frac{\rho_\eta^V}{\rho_\xi^V}, \frac{\rho_\zeta^V}{\rho_\xi^V} \right)^\alpha \quad \text{with} \quad \alpha = \frac{1}{2}. \quad (2.17)$$

The coefficients $\varepsilon^{(2)}$ and $\varepsilon^{(4)}$, which appear in the equations (2.12) and (2.13), are dependent on the pressure gradient and control the amount of the second and fourth order dissipation. These coefficients are determined by

$$\varepsilon_{i+1/2,j,k}^{(2)} = k^{(2)} \max(\nu_{\xi,i-1,j,k}, \nu_{\xi,i,j,k}, \nu_{\xi,i+1,j,k}, \nu_{\xi,i+2,j,k}) \quad (2.18)$$

and

$$\varepsilon^{(4)} = \max(0, k^{(4)} - \varepsilon_{i+1/2,j,k}^{(2)}) \quad (2.19)$$

with the pressure sensor

$$\nu_{\xi,i,j,k} = \left| \frac{p_{i-1,j,k} - 2p_{i,j,k} + p_{i+1,j,k}}{p_{i-1,j,k} + 2p_{i,j,k} + p_{i+1,j,k}} \right|. \quad (2.20)$$

The fourth order dissipation ensures stability and convergence of the solution in regions where the gradients are small. Since the fourth order dissipation

leads to overshoots in the solution near shocks, this part of the dissipation is shut off gradually with increasing activation of the second order dissipation. To avoid that the accuracy of the central discretization scheme is not globally degraded, the second order dissipation is only activated locally in regions where the pressure sensor ν detects large variations in the pressure.

The constants $k^{(2)}$ and $k^{(4)}$ are defined by the user; typical values are $1/2$ and $1/64$, respectively. The dissipation operators for the η - and ζ -direction are defined in analogous fashion as the operators defined in the equations (2.12) and (2.13) for the ξ -direction.

2.2.4 Time-stepping scheme

The semi-discrete Navier-Stokes equations (2.10) represent a system of first order ordinary differential equations with respect to time. In ITSM3D a five-stage, explicit Runge-Kutta scheme is used for the time-integration of this system of differential equations. This scheme has the property of being effective in damping high frequency errors and is according to Mavriplis [179] very efficient in combination with a multigrid technique.

In the Runge-Kutta scheme that is used in ITSM3D the dissipative and the diffusive terms are not calculated on each stage, which significantly reduces the computational overhead. Furthermore, this so-called hybrid Runge-Kutta scheme has the advantage over the classical one, that for the same maximal Courant-Friedrichs-Lewy number CFL_{max} it possesses a higher value for the maximal stable von Neumann number VNN_{max} , which adds stability to a solution scheme for viscous flow. For a detailed discussion of the performance and the computational costs of various hybrid Runge-Kutta schemes, the reader may refer to the work of Merz [190].

The hybrid Runge-Kutta that is used in ITSM3D was devised by Radespiel and Swanson [219] and reads as

$$\begin{aligned} \mathbf{Q}_{i,j,k}^{(0)} &= \mathbf{Q}_{i,j,k}^{(n)}, \\ \mathbf{Q}_{i,j,k}^{(s)} &= \mathbf{Q}_{i,j,k}^{(0)} - \alpha_s \frac{\Delta t}{\tilde{V}_{i,j,k}} \left(\mathbf{R}_c^{(s-1)} + \mathbf{R}_d^{(0)} + \sum_{t=1}^s \gamma_{st} \mathbf{D}_{i,j,k}^{(s-1)} \right), \quad s = 1, 2, \dots, 5 \\ \mathbf{Q}_{i,j,k}^{(n+1)} &= \mathbf{Q}_{i,j,k}^{(5)} \end{aligned} \tag{2.21}$$

with

$$\mathbf{R}_c^{(s-1)} = \mathbf{R}_c(\mathbf{Q}^{(s-1)}), \quad \mathbf{R}_d^{(0)} = \mathbf{R}_d(\mathbf{Q}^{(0)}), \quad \mathbf{D}^{(s-1)} = \mathbf{D}(\mathbf{Q}^{(s-1)}) \tag{2.22}$$

and the coefficients

$$\begin{aligned} \gamma_{11} = \gamma_{21} = 1, \quad \gamma_{22} = 0, \quad \gamma_{31} = \gamma_{41} = \frac{11}{25}, \quad \gamma_{32} = \gamma_{42} = 0, \quad \gamma_{33} = \gamma_{43} = \frac{14}{25}, \\ \gamma_{44} = 0, \quad \gamma_{51} = \frac{154}{625}, \quad \gamma_{52} = 0, \quad \gamma_{53} = \frac{196}{625}, \quad \gamma_{54} = 0, \quad \gamma_{55} = \frac{11}{25}, \\ \alpha_1 = \frac{1}{4}, \quad \alpha_2 = \frac{1}{6}, \quad \alpha_3 = \frac{3}{8}, \quad \alpha_4 = \frac{1}{2}, \quad \alpha_5 = 1. \end{aligned} \tag{2.23}$$

The state vector in the grid point (i, j, k) at the beginning and the end of a time step n are thereby denoted by $\mathbf{Q}_{i,j,k}^{(n)}$ and $\mathbf{Q}_{i,j,k}^{(n+1)}$, respectively.

It should be noted that when an explicit integration scheme is used, that the differential equations (2.10) are physically decoupled from each other, if the time step is chosen too large. This leads to an unstable integration; – to ensure a stable integration it is necessary that the domain of dependence of each node in the computational fields be larger than the physical one. The maximum time step that according to linear theory allows a stable integration of the Navier-Stokes equations calculates according to Merz [190] to

$$\Delta t_{\max} = \frac{\text{CFL}_{\max}}{\rho_{\xi} + \rho_{\eta} + \rho_{\zeta} + 4 \cdot \max(4/3 \cdot \nu, \alpha) \cdot \frac{\text{CFL}_{\max}}{\text{VNN}_{\max}} [(\nabla \xi)^2 + (\nabla \eta)^2 + (\nabla \zeta)^2]}. \quad (2.24)$$

The maximum stable CFL and von Neumann number of the hybrid scheme used in ITSM3D are given by

$$\text{CFL}_{\max} = 4, \quad \text{VNN}_{\max} = 9, \quad (2.25)$$

respectively.

With the aforementioned discretization and solution scheme the coupled systems of ordinary differential equations (2.10) are integrated starting from an initial guess of the solution and constant boundary conditions until a maximum number of time steps have been carried out or a steady state has been reached, for which the temporal derivatives and consequently the residuals vanish. The use of the unsteady Navier-Stokes equations for the simulation of steady state flow problems, in which the time is only used as an iteration variable, has the advantage over the solution of the corresponding steady state equations, that it is possible to use a single solution scheme for the simulation of steady transonic flows, since the unsteady Navier-Stokes equations always exhibit a hyperbolic-parabolic character irrespective whether the flow is sub- or supersonic.

2.2.5 Convergence acceleration techniques

The convergence of the explicit solution scheme of the flow solver ITSM3D is accelerated using a multiple-grid technique, the implicit residual smoothing technique of Radespiel et al. [218], and a local time stepping procedure. A detailed description of the various convergence enhancement techniques implemented in ITSM3D can be found in the thesis of Merz [190].

2.2.6 Normalization of the flow equations

In order to minimize round-off errors in the unpreconditioned solution schemes in ITSM3D the flow quantities are normalized with the inlet total pressure $p_{0,e}$, the total inlet temperature $T_{0,e}$, a characteristic length l_r (usually the

chord of the first stator) and the specific gas constant R . For a detailed description of the normalization procedure, the reader may refer to the work of Merz [190].

2.3 Boundary conditions and their numerical treatment

The solution of the Navier-Stokes equations (2.1) requires the specification of conditions for the states at the boundaries of the computational domain. In the following, the boundary conditions and their numerical treatment in steady-state simulations of turbomachinery applications are described.

2.3.1 Inlet, outlet and mixing planes

At the inlet- and outlet boundaries as well as at the mixing planes where the stator and rotor blocks are coupled via circumferential averaged quantities, a boundary condition treatment based on the work of Giles [98] and Saxer [242] is applied. With their non-reflecting boundary condition treatment, it is possible to carry out computations on truncated domains where the boundaries of the computational domain are lying close to the blades without obtaining spurious reflections at the boundaries.

In ITSM3D the user has to specify the radial distribution of the total pressure, the total temperature, and the flow angles. At the outlet boundary the radial distribution of the static pressure has to be given. If the flow is axially supersonic, then the user has also to specify the Mach number distribution at the inlet. In this case, the specification of the static pressure at the outlet boundary can be omitted.

At the mixing planes, the coupling of the circumferential averaged flow quantities is carried out such that the mass, the momentum and the energy are conserved over the interface.

2.3.2 Wall boundary conditions

On solid walls the so-called no-slip condition is used, which implies that the fluid at the wall is not moving relative to it. The walls in ITSM3D are either treated as adiabatic or as isothermal. In the former case, the temperature in the nodes on the walls are determined from the condition that the temperature gradient on the wall vanishes. For isothermal walls, the temperature in the nodes at the walls follow from the boundary condition. In either of the aforementioned cases, the pressure at the wall is variable and is determined by the flow solver in dependence on the flow field in the interior.

2.3.3 Periodic boundary condition

The use of periodic boundary conditions for the simulation of turbomachinery flow can lead to a drastic reduction of the computational time as well as the memory requirements. In the case that the inflow in the configuration is rotationally symmetric and mixing planes are used to couple the simulated flow field between the rotor- and the stator rows, it is sufficient to discretize one single blade channel in each row instead of the full annulus.

The periodic boundary conditions in ITSM3D are realised by a direct coupling of the state variables via the use of ghost cells, which are constructed by an angular extension of the grid. At the periodic boundaries, not only the independent state variables but also the second order differences are copied into the layer of phantom cells, such that the nodes on the periodic boundaries can be treated in the same fashion as the nodes in the interior of the domain.

Chapter 3

Development of a Mach number independent solution scheme

The baseline scheme presented in the previous chapter is efficient for transonic flow computations. For the simulation of turbomachinery with large regions of low Mach number flow, the scheme becomes inefficient due to the disparity in the speed of sound and the convection velocities. To ensure that the density based solution scheme is efficient independently of the Mach number level of the flow, time-derivative preconditioning must be used.

In the current work the time-derivative preconditioning scheme of Merkle and coworkers was introduced in the flow solver ITSM3D. This chapter describes the Merkle preconditioning scheme and its implementation in ITSM3D. In addition, issues related to the simulation of flow in the low Mach and low Reynolds number limit are addressed. The performance of the developed scheme for the simulation of turbomachinery flow is assessed and it is shown that with this scheme accurate flow computations can be carried out efficiently at arbitrary Mach numbers.

3.1 The time-derivative preconditioning scheme of Merkle

The principle of preconditioning is to modify the dynamics of the Navier-Stokes equations such that the disparities in the transport velocities are reduced and that the different physical processes can evolve at the same rate.

The propagation velocities of the various processes can in principle be altered by either scaling the convective or the unsteady terms. However, in order to avoid the introduction of unnecessary source terms and to obtain a solution scheme that ensures global flux conservation, it is important to use the original, unscaled conservative flux vectors as given in Eq. (2.1). Thus, when preconditioning methods are used, the dynamics of the governing equations are always changed by multiplying the vector of the time-derivatives of the independent variables by an appropriate matrix.

The idea of time-derivative preconditioning is to alter the dynamics of the

time-stepping procedure but not necessarily to change the resulting solution. If the scaling of the artificial dissipation is not altered, the residuals representing the sum of convective, diffusive, and dissipative fluxes are identical for the preconditioned and the unpreconditioned scheme. Thus, in the limit of a converged solution, the flow fields obtained with a preconditioned and an unpreconditioned solution scheme are the same.

When preconditioning is applied, it would be possible to use the conservative state vector $\mathbf{Q} = [\rho, \rho w_x, \rho w_\phi, \rho w_r, \rho e_0]$ as a set of independent variables. In the preconditioning scheme of Merkle, the vector of the primitive, viscous variables $\mathbf{Q}_v = [p, w_x, w_\phi, w_r, T]^T$ is used instead of the conservative ones, since this set of variables can be used for describing constant density flow. Furthermore, for constant density flow this choice of solution variables results in the artificial compressibility method of Chorin [61] if an appropriate preconditioning matrix is used [301]. The choice of the viscous, primitive variables is also convenient when fluids with arbitrary equations are to be simulated, since it is easier to calculate the density ρ and the specific enthalpy h from \mathbf{Q}_v than to calculate the temperature T and pressure p from \mathbf{Q} [188]. The preconditioned solution scheme developed in the current work, can handle all kinds of thermal and caloric state equations, which can be written in the following form

$$\rho = \rho(p, T), \quad h = h(p, T). \quad (3.1)$$

With the choice of \mathbf{Q}_v as solution vector, the derivation of the preconditioning matrix begins by transforming the independent variables in Eq. (2.1) from the vector of conservative variables \mathbf{Q} to the vector of viscous, primitive variables $\mathbf{Q}_v = [p, w_x, w_\phi, w_r, T]^T$ as follows:

$$\frac{\partial \mathbf{Q}}{\partial \mathbf{Q}_v} \frac{\partial \mathbf{Q}_v}{\partial t} + \frac{\partial \mathbf{E}}{\partial x} + \frac{1}{r} \frac{\partial \mathbf{F}}{\partial \phi} + \frac{1}{r} \frac{\partial (r\mathbf{G})}{\partial r} = \mathbf{H}, \quad (3.2)$$

where the Jacobian $\frac{\partial \mathbf{Q}}{\partial \mathbf{Q}_v}$ is given by

$$\frac{\partial \mathbf{Q}}{\partial \mathbf{Q}_v} = \begin{bmatrix} \rho_p & 0 & 0 & 0 & \rho_T \\ w_x \rho_p & \rho & 0 & 0 & w_x \rho_T \\ w_\phi \rho_p & 0 & \rho & 0 & w_\phi \rho_T \\ w_r \rho_p & 0 & 0 & \rho & w_r \rho_T \\ h_0 \rho_p - & \rho w_x & \rho w_\phi & \rho w_r & h_0 \rho_T + \\ (1 - \rho h_p) & & & & \rho h_T \end{bmatrix}. \quad (3.3)$$

The indices p and T represent the isothermal derivative with respect to the pressure and the isobaric derivative with respect to the temperature, respectively; i.e., h_T is the specific heat capacity at constant pressure.

To ensure uniform, efficient convergence over all Mach numbers, the physical Jacobian is replaced with the preconditioning matrix Γ_v , so that the following equations

$$\Gamma_v \frac{\partial \mathbf{Q}_v}{\partial t} + \frac{\partial \mathbf{E}}{\partial x} + \frac{1}{r} \frac{\partial \mathbf{F}}{\partial \phi} + \frac{1}{r} \frac{\partial (r\mathbf{G})}{\partial r} = \mathbf{H} \quad (3.4)$$

have to be solved. As first proposed by Merkle et al. [188], fluids with a general equation of state can be dealt with when Γ_v is chosen as

$$\Gamma_v = \begin{bmatrix} \varrho'_p & 0 & 0 & 0 & \varrho'_T \\ w_x \varrho'_p & \varrho & 0 & 0 & w_x \varrho'_T \\ w_\phi \varrho'_p & 0 & \varrho & 0 & w_\phi \varrho'_T \\ w_r \varrho'_p & 0 & 0 & \varrho & w_r \varrho'_T \\ h_0 \varrho'_p - h'_p & \varrho w_x & \varrho w_\phi & \varrho w_r & h_0 \varrho'_T + \varrho h'_T \end{bmatrix} \quad (3.5)$$

in a form analogous to the physical Jacobian $\frac{\partial \mathbf{Q}}{\partial \mathbf{Q}_v}$. The preconditioning matrix Γ_v differs from the Jacobian $\frac{\partial \mathbf{Q}}{\partial \mathbf{Q}_v}$ only by the change of the partial derivatives ϱ_p , ϱ_T , h_T and $1 - \varrho h_p$, which represent physical properties, by the respective artificial terms ϱ'_p , ϱ'_T , h'_T , and h'_p . In the following sections, it will be shown how these quantities can be chosen to ensure well-conditioned flow equations at all Mach numbers.

3.1.1 Eigenvalue scaling for convergence enhancement

The eigenvalues of the linearized unsteady Euler equations for the ξ -direction of a grid-conformal, curvilinear ξ - η - ζ coordinate system read as

$$\begin{aligned} \lambda_{\xi,1,2,3} &= \hat{w}_\xi, \\ \lambda_{\xi,4,5} &= \frac{1}{2} \hat{w}_\xi \left(1 + \frac{d}{d'} \right) \pm \frac{1}{2} \sqrt{\hat{w}_\xi^2 \left(1 - \frac{d}{d'} \right)^2 + 4 \frac{\varrho h_T}{d'} (\nabla \xi)^2} \end{aligned} \quad (3.6)$$

with

$$d = \varrho h_T \varrho_p + \varrho_T (1 - \varrho h_p), \quad d' = \varrho h_T \varrho'_p + \varrho'_T (1 - \varrho h_p) \quad (3.7)$$

if the parameters h'_T and h'_p with $h'_T := h_T$ and $h'_p := h_p$ have been set to their respective unscaled counterpart [6, 9]. The term

$$\hat{w}_\xi = w_x \xi_x + w_\phi \xi_\phi + w_r \xi_r \quad (3.8)$$

represents the contravariant velocity component along the grid direction ξ with w_x , w_ϕ and w_r representing the relative velocity components in the cylindrical system. When preconditioning is not used, $d = d'$, and the last two eigenvalues should equal the propagation velocities of the pressure waves. From this reasoning it follows that the isentropic speed of sound is given by

$$\left(\frac{\partial p}{\partial \varrho} \right)_s \equiv a^2 = \frac{\varrho h_T}{\varrho_T (1 - \varrho h_p) + \varrho \varrho_p h_T} = \frac{\varrho h_T}{d}, \quad (3.9)$$

as can also be derived directly by means of basic thermodynamic relations [19, 47]. Consequently, the ratio $\varrho h_T / d'$ may be interpreted as the square of the artificial speed of sound a'^2 . In order to avoid eigenvalue stiffness caused by the disparity between acoustic and convective velocities for subsonic flows, this artificial speed of sound is reduced to the convective reference velocity V_r according to

$$a' = \sqrt{\frac{\varrho h_T}{d'}} := V_r. \quad (3.10)$$

The convective reference velocity is oriented after the norm of the local velocity vector according to

$$V_r = \min(\|\mathbf{w}\|, a), \quad (3.11)$$

where $\mathbf{w} = [w_x, w_\phi, w_r]$ represents the relative velocity vector. By combining Eqs. (3.7) and (3.10) the following prescription for the preconditioning parameter ϱ'_p results:

$$\varrho'_p = \frac{1}{V_r^2} - \frac{1 - \varrho h_p}{\varrho h_T} \varrho'_T. \quad (3.12)$$

The convective reference velocity V_r is limited by the sonic speed, so if the other preconditioning parameters are set to their corresponding physical values, at supersonic speed the preconditioned flow equations (3.4) revert to the unscaled Navier-Stokes equations (2.1). Preconditioning is not necessary at supersonic velocities, since density based schemes are efficient at these conditions.

In the incompressible limit the energy equation of the unscaled Navier-Stokes equations is decoupled from the continuity and momentum equations. This property is also desirable for the preconditioned system of flow equations, which is the reason why the preconditioning parameter ϱ'_T should be scaled proportional to its physical counterpart ϱ_T . In the solution scheme presented here ϱ'_T is set according to

$$\varrho'_T = \delta_{pc} \cdot \varrho_T, \quad (3.13)$$

where the parameter δ_{pc} is defined by the user. For the choice $\delta_{pc} = 0$ or for the case of incompressible flow, the preconditioning matrix is regular for all reference speeds ($V_r > 0$) as long as the density and the heat capacity take on physical values ($\varrho, h_T > 0$), as shown in the work of Anker et al. [7, 9]. In the case that the parameter δ_{pc} is set to a non-vanishing value, it should be noted that the regularity of the preconditioning matrix for compressible fluids can not longer be guaranteed for all finite reference speeds. However, for ideal gases the preconditioning matrix first gets singular for supersonic values of the reference speed V_r if the parameter δ_{pc} is bounded by unity. Thus, by bounding the reference velocity V_r by Eq. (3.11) and limiting the parameter δ_{pc} to the range $\delta_{pc} \in [0, 1]$ the regularity of the preconditioning matrix can be ensured for ideal gas flow.

With the preconditioning parameter ϱ'_p determined according to Eq. (3.12) it can be shown by combining the Eqs. (3.6), (3.9), (3.10) that the condition number σ for ideal gas flow tends to $\sigma = \frac{|1+\sqrt{5}|}{|1-\sqrt{5}|} \approx 2.62$ for $\|\mathbf{w}\| \rightarrow 0$ independently of the choice of the preconditioning parameter δ_{pc} .

For an incompressible fluid with $\varrho = \text{const.}$ the sonic speed is infinite and the time derivatives in the continuity equation vanish. By preconditioning the Navier-Stokes-Equations (2.1) using the matrix given in Eq. (3.5) and setting the reference velocity to $V_r = \|\mathbf{w}\|$, temporal derivatives of the pressure are added to the continuity equation. For the special case of $V_r = \sqrt{2} \cdot \|\mathbf{w}\|$ the preconditioning results in the artificial compressibility approach of Chorin [61]. This choice leads to the condition number of $\sigma = 2$ independently of the magnitude of the flow speed. The physical values $\varrho_T = \varrho_p = 0$ that cause the

sonic velocity in incompressible fluids to be infinite are replaced with the artificial properties ϱ'_p and ϱ'_T when preconditioning is used. This replacement makes time-marching solution schemes practically feasible for compressible, low Mach number as well as for incompressible flow.

3.1.2 Perturbation analysis for inviscid, low Mach number flows

Instead of performing an eigenvalue analysis for finding suitable values for the preconditioning parameters, a perturbation analysis of the inviscid flow equations for low Mach numbers may be carried out as demonstrated in Appendix A. The analysis presented there shows that in order to ensure a proper balance between the temporal and the convective terms in the flow equations for low Mach numbers, the physical quantity ϱ_p should be replaced with a scaled quantity ϱ'_p given by

$$\varrho'_p = k_{\text{inv}}/u^\dagger{}^2, \quad (3.14)$$

with u^\dagger as a representative velocity scale (e.g., the norm of the local velocity vector). Other physical properties (e.g., ϱ_T , h_T , $1 - \varrho h_p$) need not to be changed in order to achieve a well-conditioned system of inviscid flow equations.

3.1.3 Robustness aspects

In order to prevent singularities at solid walls, not $\|\mathbf{w}\|$, but the maximum of $\|\mathbf{w}\|$ and $V_{\text{lim}} = \epsilon_{\text{lim}} \cdot a$ is used as reference velocity for subsonic flows, where ϵ_{lim} is typically set to 10^{-5} . As will be shown later in this chapter, preconditioning yields a significant enhancement of the convergence rates at low Mach numbers. However, as first discussed by Darmofal and Schmid [68], preconditioned systems show an increased sensitivity to pressure fluctuations and are unstable in the presence of pressure fluctuations that are large compared to the dynamic pressure, especially in the initial phase of a simulation. One approach devised by Weiss et al. [299] to handle this sensitivity is to introduce the term $V_{\text{pgr}} = \epsilon_{\text{pgr}} \sqrt{\delta p / \varrho}$ and to limit the lower bound of the pseudo-acoustic speed a' in the case that the spatial pressure variations δp are larger than the potential dynamic pressure variations. For the case of a compressible, inviscid fluid the pseudo-acoustic velocity is calculated according to

$$a' = V_r = \min[a, \max(\|\mathbf{w}\|, V_{\text{lim}}, V_{\text{pgr}})]. \quad (3.15)$$

In the present work this modification was adopted with the pressure variation δp taken as the maximum pressure variation over a control volume and $\epsilon_{\text{pgr}} \in [0.1, 2]$. To further increase the robustness, the reference velocity V_r at a node i was in the current work determined as the maximum of the reference velocity $V_{r,i}$ of the local node i and the corresponding values $V_{r,j}$ in the surrounding nodes $j = 1, \dots, N_j$:

$$V_r = \min[a, \max(V_{r,i}, V_{r,n})], \quad V_{r,n} = \max_{j=1, \dots, N_j} (\|\mathbf{w}\|_j, V_{\text{lim},j}, V_{\text{pgr},j}). \quad (3.16)$$

The procedure of looping over neighbouring nodes may be repeated; in the current work it was found that accounting for the immediate neighbours already leads to a very robust scheme. This result is confirmed by Venkateswaran et al. [285], who also report a significant gain in the robustness by applying this method.

Because the instability of a preconditioned scheme in the presence of large pressure fluctuations is due to non-linear effects, Venkateswaran et al. [284, 288] suggest to embed the preconditioning scheme in an implicit-implicit dual time-stepping procedure, in which preconditioning is only applied at the inner level where the linearized flow equations are solved. They claim to achieve robustness of the solution scheme without employing the aforementioned pressure switch. Since an explicit Runge-Kutta scheme was used in the current work, this method of attaining robustness was not considered.

3.1.4 Scaling issues for low Reynolds number flow

With the preconditioned solution scheme presented so far, inviscid flows can be calculated efficiently at arbitrary Mach numbers. However, as recognized by Choi and Merkle [59] additional modifications are necessary for obtaining an efficient scheme for viscous flows. Even though flows in turbomachinery configurations usually have high Reynolds numbers where it could be anticipated that the dominant characteristics controlling the solution of the Navier-Stokes equations are the same as those of the Euler equations, the Reynolds numbers of the cross stream directions in the boundary layers may still be small.

In the following the modifications necessary for calculating diffusion dominated flow efficiently will be described. The extension of the preconditioning method to viscous flows assumes that the Mach number as well as its square is lower than the Reynolds number (i.e., $M/\text{Re} \ll 1$ and $M^2/\text{Re} \ll 1$), which is the case for most technical applications. In the case of high Mach numbers and low Reynolds numbers, the viscous effects must be accounted for in a different manner in order to ensure a good conditioning of the flow equations (cf. Appendix B).

Using perturbation analysis for viscous, ideal gas flows, it is shown in Appendix A that the preconditioning parameter ϱ'_T should be limited by

$$\varrho'_T \leq \varrho_r \text{Re}/T_r \quad (3.17)$$

in order to prevent the temporal derivative of the temperature from becoming dominant in the continuity equation. T_r and ϱ_r represent a reference temperature and reference density, respectively. In the present work this preconditioning parameter was not scaled in dependence of the Reynolds number and the inviscid prescription $\varrho'_T = \delta_{\text{pc}} \varrho_T$ according to Eq. (3.13) was also used for the viscous case. A combination of Eqs. (3.13) and (3.17) leads to the following condition for the preconditioning parameter δ_{pc} :

$$\delta_{\text{pc}} \leq \frac{\varrho_r}{\varrho_T T_r} \text{Re}. \quad (3.18)$$

This restriction can be met for all flow conditions by setting the parameter δ_{pc} to zero. A variation of this parameter from $\delta_{pc} = 0$ to $\delta_{pc} = 1$ did not prove to have significant influence on the computation of high Reynolds, adiabatic flow with the preconditioned solution scheme in ITSM3D. The results presented in the current work were obtained with the preconditioning parameter δ_{pc} set to unity.

According to Merkle [186], and as also shown in Appendix A, a scaling of the energy equation by setting $h'_T = h_T/\text{Pr}$ is appropriate if the Prandtl number deviates largely from unity. Since most fluids encountered in turbomachinery applications have Prandtl numbers in the order of unity, this modification was not adopted in the present work.

As shown in Appendix A by employing a perturbation analysis, the temporal term in the continuity equation balances the convective term for viscous dominated flows provided that

$$\varrho'_p = k_v \text{Re}^2 / V_r^2 \quad (3.19)$$

holds [186], with k_v as a proportionality constant having a magnitude in the order of unity. Furthermore, as shown in Appendix B by means of a dispersion analysis for low Reynolds number flow, this prescription of the preconditioning parameter ϱ'_p leads to a good conditioning of the flow equations both for compressible and incompressible flows, when the other preconditioning parameters h'_p and h'_T are set to their physical values and the preconditioning parameter ϱ'_T simultaneously is set to its physical counterpart or to zero.

Using a Fourier stability analysis [289], it can be shown that the proper Reynolds number to use in Eq. (3.19) is the cell-Reynolds number, $Re_{\Delta x} = v\Delta x/\nu$. The cell-Reynolds number can be incorporated and viscous effects can be accounted for by limiting the reference velocity V_r by the velocity scale of diffusion of momentum V_{vis} given by $V_{\text{vis}} = \nu/\Delta x$ in the following manner:

$$V_r = \min(a, \max(\|\mathbf{w}\|, V_{\text{lim}}, V_{\text{pgr}}, V_{\text{vis}})). \quad (3.20)$$

The introduction of the cell-Reynolds number shows that whether or not low Mach preconditioning is used, depends on both the flow field and the grid resolution. An inspection of Eq. (3.20) shows that the introduction of the diffusion velocity scale V_{vis} may reduce the inviscid preconditioning. When active, the low Reynolds number scaling causes the convective terms to be stiff, but since in this case the viscous terms dominate, the convective fluxes are negligible and do not inhibit the convergence.

3.2 Discretization and solution scheme for the preconditioned Navier-Stokes equations

In this section the method for solving the preconditioned Navier-Stokes equations (3.4) is described. Since the developed preconditioned solution scheme is

based on the scheme that was described in Chapter 2 for solving of the original, unpreconditioned Navier-Stokes equations, this description is kept short and focuses on the differences between the schemes.

3.2.1 Spatial discretization

In the solution scheme used, the preconditioned equations (3.4) are solved in the integral form

$$\int_V \Gamma_v \frac{\partial \mathbf{Q}_v}{\partial t} dV + \oint_A (\mathbf{E} r d\phi dr + \mathbf{F} dx d\phi + \mathbf{G} r dx d\phi) + \int_V \mathbf{H} dV = 0, \quad (3.21)$$

where V represents the content of an arbitrary control volume and A represents its surface. The convective and the diffusive fluxes are in principle determined as in the original scheme; minor differences are only due to the use of a different set of independent solution variables. In the original scheme the temperature and the pressure must be determined from the conservative state vector $\mathbf{Q} = [\rho, \rho w_x, \rho w_\phi, \rho w_r, \rho e_0]^T$; due to the implemented functionality in ITSM3D of simulating ideal gas flows with a temperature-dependent heat capacity, the temperature is determined iteratively. In the preconditioned solution scheme, the viscous, primitive state variables are used as independent solution variables and are consequently directly available. In this scheme, the elements of the conservative state vector \mathbf{Q} must be determined from the elements of the vector $\mathbf{Q}_v = [p, w_x, w_\phi, w_r, T]$ of primitive state variables. This determination can be carried out directly even for general equations of state, since Merkle's preconditioning scheme requires the user to specify the density and the enthalpy as explicit functions of the pressure and the temperature.

Similar to the original scheme, the temporal term in the preconditioned Navier-Stokes equations is discretized assuming that the distribution of the primitive viscous state variables are linearly distributed over the control volumes. With the preconditioning matrix $\Gamma_{v,i,j,k}$ calculated as function of the state vector $\mathbf{Q}_{v,i,j,k}$ in the central node (i, j, k) of the control volume, it follows that the discretization

$$\int_{\check{V}_{i,j,k}} \Gamma_{v,i,j,k} \frac{\partial \mathbf{Q}_{v,i,j,k}}{\partial t} dV \approx \check{V}_{i,j,k} \cdot \Gamma_{v,i,j,k} \frac{\partial \mathbf{Q}_{v,i,j,k}}{\partial t} \quad (3.22)$$

is of second order accuracy in cases where the central node of a control volume $\check{V}_{i,j,k}$ coincides with the center of gravity.

With the sum of the convective fluxes \mathbf{R}_c , the sum of the diffusive fluxes \mathbf{R}_d and the artificial dissipation vector \mathbf{D} , the semi-discrete, preconditioned Navier-Stokes equations can be written as

$$\Gamma_v \frac{\partial \mathbf{Q}_v}{\partial t} \Big|_{i,j,k} = -\frac{1}{\check{V}_{i,j,k}} (\mathbf{R}_c + \mathbf{R}_d + \mathbf{D})_{i,j,k}. \quad (3.23)$$

The convective residual vector \mathbf{R}_c and the diffusive residual vector \mathbf{R}_d are calculated in the same manner for the preconditioned Navier-Stokes equations as for the unpreconditioned ones using the discretization techniques of

Radespiel and Rossow [217] and Hall [109], respectively. The techniques for calculating the convective and the diffusive residuals were already described in Chapter 2 and will be omitted here. In the following only the calculation of the artificial dissipation is described.

3.2.2 Artificial dissipation

Like in the solution and discretization scheme for the unscaled Navier-Stokes equations (cf. Chapter 2), the artificial dissipation vector \mathbf{D} in the preconditioned, baseline solution scheme is calculated according to the approach of Jameson et al. [132] using a blend of second and fourth order differences:

$$\mathbf{D}_{i,j,k} = (-D_\xi^2 + D_\xi^4 - D_\eta^2 + D_\eta^4 - D_\zeta^2 + D_\zeta^4) \mathbf{Q}_{v,i,j,k}. \quad (3.24)$$

When time-derivative preconditioning is used, the differences are constructed in dependence of the primitive, viscous state variables $\mathbf{Q}_v = [p, w_x, w_\phi, w_r, T]^T$ instead of differences of the vector $\mathbf{Q} = [\rho, \rho w_x, \rho w_\phi, \rho w_r, \rho e_0]^T$ of conservative state variables. The second and fourth order difference operators employ the preconditioning matrix Γ_v ; for the ξ -direction these are defined as

$$D_\xi^{(2)} = \delta_\xi^- \left(\bar{\rho}_\xi^V \varepsilon^{(2)} \Gamma_v \right)_{i+1/2,j,k} \delta_\xi^+, \quad D_\xi^{(4)} = \delta_\xi^- \left(\bar{\rho}_\xi^V \varepsilon^{(4)} \Gamma_v \right)_{i+1/2,j,k} \delta_\xi^+ \delta_\xi^- \delta_\xi^+. \quad (3.25)$$

The respective difference operators D_η and D_ζ for the η - and ζ -directions are defined analogously.

For the simulation of low Mach number flows, it would also be possible to construct the artificial dissipation using differences of the conservative variables. However, for low Mach number flows it is easier to avoid round-off errors (cf. Appendix D.2) and ensure smoothness of the simulated flow field if the vector of primitive, viscous variables are used to construct artificial dissipation, as the gradient of these variables is the driving force for the convective and diffusive fluxes in the flow [71]. In the case of incompressible flow, the use of differences of the conservative variables to construct the artificial dissipation would not be suitable, as the density differences vanish identically. As shown in Appendix C, the incorporation of the preconditioning matrix and the use of the spectral radii of the preconditioned system ensures that the artificial dissipation scales correctly in the limit of low Mach numbers both for inviscid and viscous flow.

The formulation of the artificial dissipation used in the Eqs. (3.24) and (3.25) above is conservative [278]; with this method of constructing the artificial dissipation, flows with an arbitrary Mach number level can be simulated. As demonstrated in the work of Anker et al. [17] as well as in subsequent sections of this chapter, the resulting scheme can be used to simulate transonic flows and accurately capture the shocks as well as reliably predict low Mach number flow. It should be noted that the dissipation operators of the preconditioning scheme in Eq. (3.25) through the presence of a matrix-vector product are computationally more costly than the dissipation operators in Eqs. (2.12)

and (2.13) of the original scheme; the computational overhead of the conservatively formulated dissipation corresponds approximately to the additional costs of a matrix-dissipation scheme.

If conservativity of the solution scheme can be sacrificed, which is something that could be done for purely subsonic flows, then the dissipation vector \mathbf{D} can be determined through Eq. (3.24) with the difference operators defined as

$$D_{\xi}^{(2)} = \delta_{\xi}^{-} \left(\bar{\rho}'_{\xi}{}^V \varepsilon^{(2)} \right)_{i+1/2,j,k} \delta_{\xi}^{+}, \quad D_{\xi}^{(4)} = \delta_{\xi}^{-} \left(\bar{\rho}'_{\xi}{}^V \varepsilon^{(4)} \right)_{i+1/2,j,k} \delta_{\xi}^{+} \delta_{\xi}^{-} \delta_{\xi}^{+} \quad (3.26)$$

instead of the computationally more expensive operators defined in Eq. (3.25). If these nonconservative dissipation operators are used, then the artificial dissipation should first be added to the residuals \mathbf{R}_c and \mathbf{R}_d after they have been multiplied with the inverse preconditioning matrix Γ_v^{-1} ; the use of a non-conservative dissipation scheme leads to the following system of semi-discrete equations

$$\frac{\partial \mathbf{Q}_{i,j,k}}{\partial t} = -\frac{1}{\tilde{V}_{i,j,k}} \left[\Gamma_v^{-1} (\mathbf{R}_c + \mathbf{R}_d) + \mathbf{D} \right]_{i,j,k}, \quad (3.27)$$

which are to be integrated forward in time.

Like in the solution scheme for the unscaled Navier-Stokes equations, the scaling factors $\bar{\rho}'_{\xi_{i+1/2,j,k}}{}^V$ for the artificial dissipation are given as

$$\bar{\rho}'_{\xi_{i+1/2,j,k}}{}^V = \rho'_{\xi_{i+1/2,j,k}}{}^V \left\{ 1 + \max \left[\left(\frac{\rho'_{\eta_{i+1/2,j,k}}{}^V}{\rho'_{\xi_{i+1/2,j,k}}{}^V} \right)^{1/2}, \left(\frac{\rho'_{\zeta_{i+1/2,j,k}}{}^V}{\rho'_{\xi_{i+1/2,j,k}}{}^V} \right)^{1/2} \right] \right\} \quad (3.28)$$

in dependence of the volume weighted spectral radii $\rho'_{\xi}{}^V$, $\rho'_{\eta}{}^V$, and $\rho'_{\zeta}{}^V$ according to a suggestion of Martinelli [177] and Radespiel et al. [218]; the corresponding factors for the η - and ζ -direction are defined in an analogous fashion. In contrast to the original scheme, the spectral radii $\rho'{}^V$ of the preconditioned Euler equations are used rather than the volume weighted spectral radii ρ^V of the unscaled Euler equations. For example, the spectral radius for the ξ -direction, which is used for scaling of the artificial dissipation, is determined as

$$\rho'_{\xi}{}^V = \frac{1}{2} \|\mathbf{w} \cdot \mathbf{S}_{\xi}\| \left(1 + \frac{d}{d'} \right) + \frac{1}{2} \sqrt{\|\mathbf{w} \cdot \mathbf{S}_{\xi}\|^2 \left(1 - \frac{d}{d'} \right)^2 + 4 \frac{\rho h_T}{d'}} \quad (3.29)$$

instead of

$$\rho_{\xi}^V = \|\mathbf{w} \cdot \mathbf{S}_{\xi}\| + a \cdot \|\mathbf{S}_{\xi}\|, \quad (3.30)$$

which is the spectral radius used in the original scheme. As discussed in Appendix C it is necessary to use the spectral radius of the preconditioned equations to ensure a correct magnitude of the artificial dissipation in the limit of low Mach and Reynolds numbers.

The factors $\varepsilon^{(2)}$ and $\varepsilon^{(4)}$ for controlling the artificial dissipation are calculated in the same way as in the original scheme, i.e., they are determined according to Eqs. (2.18) and (2.19).

3.2.3 Time-stepping scheme

The semi-discrete system of preconditioned Navier-Stokes equations (3.23) are integrated with the five-stage, hybrid, explicit Runge-Kutta scheme of Radespiel and Swanson [219]

$$\begin{aligned}
 \mathbf{Q}_{v_{i,j,k}}^{(0)} &= \mathbf{Q}_{v_{i,j,k}}^{(n)}, \\
 \mathbf{Q}_{v_{i,j,k}}^{(s)} &= \mathbf{Q}_{v_{i,j,k}}^{(0)} - \alpha_s \frac{\Delta t}{\tilde{V}_{i,j,k}} (\Gamma_v^{(s-1)})^{-1} \left[\mathbf{R}_c^{(s-1)} + \mathbf{R}_d^{(0)} + \sum_{t=1}^s \gamma_{st} \mathbf{D}^{(s-1)} \right]_{i,j,k}, \\
 \mathbf{Q}_{v_{i,j,k}}^{(n+1)} &= \mathbf{Q}_{v_{i,j,k}}^{(5)}
 \end{aligned} \tag{3.31}$$

where $s = 1, \dots, 5$ denotes the stage number. The coefficients α_s, γ_{st} ; $s = 1, \dots, 5$; $t \leq s$ are the same as those for the unpreconditioned flow equations and are given in Eq. (2.23).

In contrast to the Runge-Kutta scheme given in Eq. (2.21) for the integration of the unscaled Navier-Stokes equations, the sum of the residuals in the preconditioned integration scheme given in Eq. (3.31) is multiplied with the inverse of the preconditioning matrix Γ_v . The inverse preconditioning matrix Γ_v^{-1} is determined as a function of independent solution $\mathbf{Q}_v^{(s-1)}$, which is present at the beginning of Runge-Kutta stage s .

3.2.4 Calculation of the time step

The size of the maximum stable time-integration step Δt_{\max} for the system of preconditioned Navier-Stokes equations (3.4) is calculated as

$$\Delta t_{\max} = \frac{\text{CFL}_{\max}}{\rho'_\xi + \rho'_\eta + \rho'_\zeta + 4 \cdot \max(4/3 \cdot \nu, \alpha) \cdot \frac{\text{CFL}_{\max}}{\text{VNN}_{\max}} [(\nabla \xi)^2 + (\nabla \eta)^2 + (\nabla \zeta)^2]}, \tag{3.32}$$

analogous to the relation (2.24) for the maximum allowable time step for the unpreconditioned Navier-Stokes equations [18].

3.2.5 Treatment of the initial and boundary conditions

For the steady state numerical simulation of turbine flows, six different types of boundaries have to be considered: Inlet, outlet, non-rotating and rotating walls, periodicity and mixing planes.

Solid walls are treated as isothermal and the no-slip condition is applied for viscous flows. When inviscid flows are simulated or a symmetry plane is needed, slip-walls can be defined instead.

In all of the calculations presented in this paper, the wall temperature is set to the total temperature at the inlet boundary. Periodicity in the pitch-wise direction is ensured using phantom cells that keep copies of the periodic values such that the points on these boundaries can be treated like interior points.

At the inlet and outlet boundaries and at the mixing planes a non-reflecting post-correction method is used. The boundary conditions used represent an extension of the work of Giles [98] and Saxer [242] to preconditioned systems with arbitrary equations of state and the essential elements of the developed theory are presented in Chapter 5.

3.2.6 The use of perturbed, normalized flow quantities

In order to minimize round-off errors in the unpreconditioned solution scheme in ITSM3D the flow quantities are normalized as previously described in Chapter 2.2.6. Since the preconditioned solution can handle incompressible fluids and fluids with general state equations, the isobaric heat capacity c_p is used for normalization rather than the specific gas constant. As for the unpreconditioned scheme, also the inlet total pressure temperature $p_{0,e}$, the total inlet temperature $T_{0,e}$ and a characteristic length l_r are used as reference quantities for the normalization.

When the preconditioned solution schemes in ITSM3D are used, the so-called perturbed, normalized quantities

$$\tilde{p}^* = \frac{p - p_{0,e}}{p_{0,e}} = p^* - 1, \quad \text{and} \quad \tilde{T}^* = \frac{T - T_{0,e}}{T_{0,e}} = T^* - 1 \quad (3.33)$$

are used as independent solution variables as this does not spoil the mantissa for storage of the nearly constant part of the pressure and the temperature (cf. Appendix D).

To also avoid round-off errors linked to the calculation and use of the enthalpy, the enthalpy at the inlet is used as reference condition.

Gradients and differences (artificial dissipation) are directly calculated by means of the perturbed and normalized variables. However, state functions as well as the preconditioning matrix are determined in function of the absolute quantities p^*, T^* , which are obtained from the perturbed variables by incrementation, i.e., $p^* = \tilde{p}^* + 1, T^* = \tilde{T}^* + 1$.

To address the singularity problem outlined in Section D.1, the pressure should be normalized with a reference value for the dynamic pressure. This was not done in the current work; however with the use the normalization and perturbation procedure described in this section, low Mach number flow ($M = 10^{-4}$) could be accurately calculated using a single precision (4 Byte) representation of floating numbers.

3.2.7 Implicit residual smoothing technique for preconditioned systems

In order to accelerate the convergence of the unscaled Navier-Stokes equations to steady state, an implicit residual smoothing technique with variable coefficients [177, 218] was implemented in the flow solver ITSM3D by Merz [190]. The implicit residual smoothing technique used in conjunction

with preconditioning is the same as for the original scheme with the exception that the smoothing coefficients now are calculated as functions of the spectral radii of the preconditioned system instead of those of the unscaled Navier-Stokes equations.

3.3 Preconditioning and its impact on the efficiency and accuracy of a solution scheme

The use of time-derivative preconditioning schemes can lead to a dramatic enhancement in the efficiency and a significant improvement of the accuracy of the solution scheme at low Mach numbers. In this section, both of these beneficial aspects will be discussed.

3.3.1 Enhancement of the convergence rates

Preconditioning generally leads to enhanced convergence rates for low Mach number flows. The reason for this can be found in the improved damping of the errors as well as in the increase in the maximum allowable time-steps due to eigenvalue clustering. In the following these effects will be discussed separately.

By effectively setting the numerical speed of sound a' to the norm $\|\mathbf{w}\|$ of the relative velocity vector for convective dominated flows, the maximum allowable time step for low Mach number flow can be increased substantially. To show this, one-dimensional inviscid flow is assumed. In this case, the maximum allowable time step Δt_{\max} for an explicit unpreconditioned scheme can be estimated as

$$\Delta t_{\max} = \text{CFL}_{\max} \cdot \Delta x / \rho \quad (3.34)$$

where CFL_{\max} represents the maximum stable CFL number of the integration scheme and $\rho = \max_i |\lambda_i|$ represents the spectral radius of the flux Jacobian of the linearized flow equations. The slowest modes of the solution are transported with a speed that corresponds to the value of the smallest eigenvalue of the system of linearized Euler equations. Thus, in explicit time-stepping schemes for which the maximum stable integration time step is limited by the CFL condition given in Eq. (3.34), the number of time steps needed to convect the slowest modes through the computational domain is directly related to the condition number $\sigma = \max_i |\lambda_i| / \min_i |\lambda_i|$. For the unscaled Euler-equations the condition number is given by

$$\sigma = (a + \|\mathbf{w}\|) / \|\mathbf{w}\| = (1 + M) / M, \quad (3.35)$$

which for low Mach numbers can be approximated to $\sigma \approx 1/M$. Thus, if preconditioning is not used and if the effect of numerical damping is not strong,

the number of iterations required to converge a simulation of the Euler equations goes beyond all bounds as the Mach number tends to zero.

If time-derivative preconditioning is used, then the numerical speed of sound a' is oriented after the convection speed. With $a' = \|\mathbf{w}\|$ the maximum allowable time step $\Delta t'_{\max}$ can be estimated as $\Delta t'_{\max} = \text{CFL}_{\max} \cdot \Delta x / \|\mathbf{w}\|$. Consequently, the ratio of the maximum allowable time step with and without the use of preconditioning can be determined to

$$\Delta t'_{\max} / \Delta t_{\max} = (a + \|\mathbf{w}\|) / (a' + \|\mathbf{w}\|) = \frac{1}{2}(a + \|\mathbf{w}\|) / \|\mathbf{w}\|, \quad (3.36)$$

which for low Mach numbers can be approximated to $\Delta t'_{\max} / \Delta t_{\max} \approx \frac{1}{2} \frac{1}{M}$. Thus, for low Mach number flows, the maximum allowable time step when preconditioning is used is significantly larger than when preconditioning is not used.

Implicit solution methods are known to be less sensitive to stiffness of the governing equations than their explicit counterparts. For unconditionally stable integration schemes there is no limit in the maximum stable CFL number, wherefore the stiffness nominally should not affect the number of iterations needed for convergence of the flow equations. It should be noted that the unconditional stability of an integration scheme usually refers to a property given for the solution of linear flow equations. For non-linear problems, the solution can only be found iteratively using finite CFL numbers. Thus, also for implicit schemes, the stiffness and the disparity of the wave propagation speeds of the governing equations matter.

The possibility to use a larger time step, enhances the convergence speed assuming the damping of errors is not impaired by the use of larger time steps. The use of time-derivative preconditioning has in fact a clearly positive effect on the damping rates both on explicit and implicit schemes as shown by Buelow [46], Venkateswaran and Merkle [289] by carrying out a von Neumann analysis of the solution scheme. As furthermore shown by Lynn [173] and van Leer [174] by analysing the Fourier footprints, preconditioning has the effect of clustering the eigenvalues of the discretized equations. Numerical tests show that the clustering of eigenvalues leads to a significant enhancement of the error damping properties of a given multigrid scheme.

3.3.2 Accuracy preservation of the solution scheme for low Mach number flow simulations

Several discretization schemes, among them the JST, Roe, and the AUSM+ discretization schemes degrade in accuracy for low Mach numbers if applied in their original form. By the use of a perturbation analysis, it is shown in Appendix C, that the original JST scheme for the solution of the unpreconditioned Navier-Stokes equations leads to a wrong scaling of the artificial dissipation for low Mach number inviscid or viscous flows. Using the normalized flow equations as a basis for the analysis, it is shown that in the case of low Mach number flow (under inviscid or high Reynolds number flow conditions),

the artificial dissipation D_1 added to the continuity equations scales in the order of the Mach number ($D_1 = \mathcal{O}(M)$) whereas the artificial dissipation $D_{2,3}$ added to the momentum and the energy equation scales inversely proportional to the Mach number ($D_{2,3} = \mathcal{O}(1/M)$). Ideally, the amount of artificial dissipation added to each of the flow equations should scale in the order of unity independently of the Mach and Reynolds number level. The wrong scaling of the artificial dissipation leads for low Mach number flows to an odd-even decoupling of the pressure field, which manifests itself in unphysical wiggles in the pressure field of a computation, as can be seen in Fig. 3.4a, where the simulated pressure field for a low speed test rig obtained with the original JST scheme are shown. At the same time, the excess amount of artificial dissipation that is added to the momentum and the energy equations degrades the accuracy of the solution. The effect of this can be seen in Fig. 3.5, where the circumferentially averaged flow velocities computed with (PC) and without (NonPC) the use of preconditioning are compared for the aforementioned low speed test rig.

However, if preconditioning is used and the scaling factor of the artificial dissipation is based on the spectral radius of the preconditioned equations, the artificial dissipation scales in the order of unity in terms of normalized flow equations independently of the Mach number level of the simulated flow ($D_{1,2,3} = \mathcal{O}(1)$). The result of a correct scaling for the test case discussed above can be seen in Fig. 3.4b. The use of time-derivative preconditioning leads to a correct scaling of the artificial dissipation added to the continuity equation and consequently to a smooth simulated pressure field. Furthermore, since the addition of excess dissipation to the momentum and the energy equation is avoided, the accuracy of the results are improved. This is shown in Fig. 3.5, where it is visible that the preconditioned scheme is able to resolve secondary flow effects, while the original scheme is not.

As demonstrated in Appendix C, for low Reynolds number flow both the use of the original scheme as well as inviscid preconditioning leads to a wrong scaling of the artificial dissipation. In the case of low Reynolds number flow, the artificial dissipation terms first scale correctly when the preconditioning method properly accounts for viscous effects.

3.4 Computational results

3.4.1 Inviscid flow over a bump

To demonstrate that the preconditioned solution scheme is able to calculate a configuration efficiently and accurately over a broad Mach number range, results from the computation of the Ni-Bump [226] test case are presented in the following. In this test case the internal inviscid, two-dimensional flow through a parallel channel having a 4.2 % thick circular bump on the lower wall is considered. The computational grid is shown in Fig. 3.1 and consists of $177 \times 3 \times 21$ grid points. In all simulations conducted, the scalar JST dissipation scheme was used.

The calculations were initialized by a flow field which was gained using the non-preconditioned solution scheme for an isentropic outlet Mach number of $Ma_{is,a} = 0.59$. All simulations were run until machine zero of the continuity residual was reached. Table 3.1 shows the isentropic Mach numbers for which the calculations were performed with (PC) and without (NonPC) preconditioning and the number of iterations N that were necessary for achieving a drop in the residuals by 5 orders in magnitude.

In the case of an isentropic outlet Mach number of $Ma_{is} = 0.85$ the original boundary values of the test case [226] were prescribed and the flow is transonic. The solutions obtained with the original and the preconditioned scheme are plotted in Figs. 3.2a and 3.2b, respectively. The calculated flow fields are nearly identical, which shows that the shock capturing property of the original scheme is retained when preconditioning is used. For this case, the original scheme is faster than the preconditioned one.

When the preconditioned scheme was used at the other Mach number cases, a drop in the residual by five orders of magnitude was always achieved within 7650 iterations. As expected, the necessary number of iterations using the original scheme increases with decreasing Mach number. However, a more serious problem that arises when using the original scheme, is the deterioration of accuracy with decreasing Mach number.

In Figs. 3.3a and 3.3b the Mach number distributions obtained with the different schemes for the case of an isentropic Mach number of $Ma_{is} = 0.037$ are compared; it is apparent that the original scheme is much more diffusive than the preconditioned scheme, since the former produces a long tail after the Bump with reduced Mach numbers in the solution. Furthermore, in contrast to the nearly symmetrical flow solution obtained with the preconditioned scheme the Mach number lines of the flow field simulated with the non-preconditioned solution are tilted in streamwise direction. Obviously, the accuracy of the solution scheme is only preserved at low Mach numbers when preconditioning is used.

$Ma_{is,a}$	N (PC)	N (NonPC)
0.013	6480	13290
0.037	7330	8930
0.084	7650	8930
0.850	5210	4090

Table 3.1: Number of iterations N needed for a residual drop by five orders of magnitude in the Ni-Bump case in dependence of the isentropic Mach number $Ma_{is,a}$

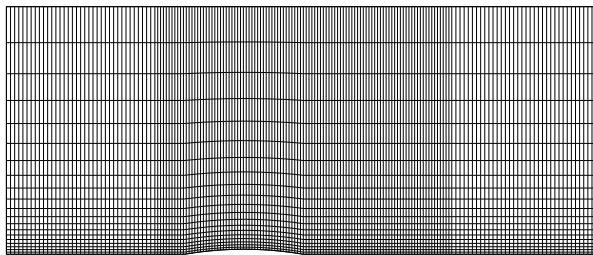


Figure 3.1: Computational grid for the Ni-Bump test case

3.4.2 Flat plate

In Chapter 4.7.2 a comparison of the performance of various low diffusion schemes are shown for the case of a viscous flow over a flat plate ($Ma_{is,a} = 0.136$). A comparison of the results for the JST dissipation scheme with and without preconditioning clearly shows that preconditioning improves the results (cf. Fig. 4.6).

The different dissipation schemes used in conjunction with preconditioning for the simulation of the flat plate test case presented in detail in Chapter 4.7.2 lead to comparable convergence rates; for a CFL-number of $CFL = 1$ all schemes achieve a residual drop of 4 orders in magnitude within 4,000-5,000 iterations. In contrast to this, the non-preconditioned solution scheme needs 30,000 iterations for obtaining the same residual drop. Even though one iteration with the preconditioned solution scheme can consume up to 25 % more CPU-time than the non-preconditioned one, it is clear that preconditioning not only enhances the accuracy of the solution but has also the potential of substantially increasing the computational efficiency of a given solution scheme at low Mach numbers.

3.4.3 Supersonic flow through a row of wedges

In Chapter 4.7.3 results of the simulation of the supersonic flow through a row of wedges are shown. As shown by comparing the pressure field (cf. Fig. 4.11), the difference in the results obtained using the JST scheme with and without preconditioning are marginal; the use of time-derivative preconditioning

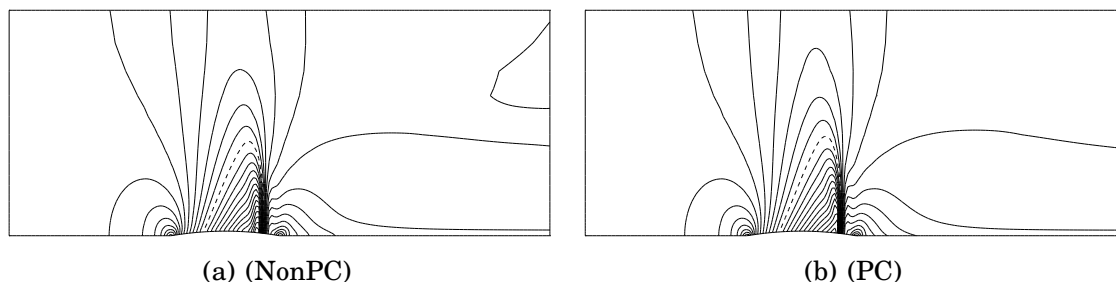


Figure 3.2: Calculated Mach number contours ($\Delta Ma = 0.025$) of the transonic Ni-Bump test case ($Ma_{is} = 0.85$) using the non-preconditioned (NonPC) and the preconditioned (PC) JST-scheme

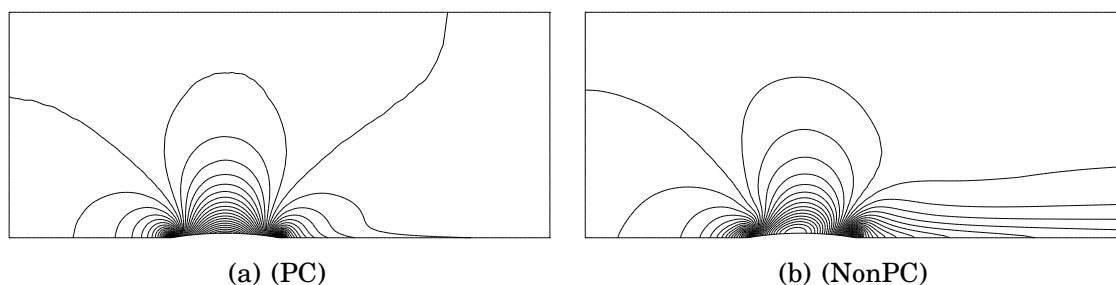


Figure 3.3: Calculated Mach number contours ($\Delta Ma = 0.0002$) of the subsonic Ni-Bump test case ($Ma_{is} = 0.037$) using the non-preconditioned (NonPC) and the preconditioned (PC) JST-scheme

does not in any way impair the shock capturing properties of the JST-scheme. Thus, when preconditioning is used, both low Mach number flow and supersonic flow can be simulated accurately.

3.4.4 Low-speed turbine

In order to verify that the presented scheme is able to simulate low-speed multistage turbomachinery efficiently, in this section results from the simulation of the flow in a 1.5 stage axial air turbine are presented. In this low-speed test case, the Mach number ranges from $Ma = 0.05 - 0.15$ in the main flow. It will be shown that on coarse grids the secondary flow effects are only captured when preconditioning is used.

The turbine considered is operated in a test rig at the Ruhr-Universität Bochum where extensive steady-state measurements have been carried out [6, 9]. For a detailed description of the test case, the reader is referred to Chapter 6 of this thesis. In this section, the configuration is simulated for a clearance height of $s_{cl} = 1$ mm and a rotor speed of $n = 500$ rpm.

The 1.5 stage axial turbine was discretized using a block-structured grid. The numerical grids used consist of 327,000 grid points in total; the first stator was discretized using $61 \times 25 \times 33$ nodes.

All calculations were conducted with a CFL-number of $CFL = 1.5$ and run until the mass flow rates had reached constant values. The fluid was modelled

as an ideal gas in the simulations applying the original, unpreconditioned solution scheme. In the simulations using the preconditioned solution scheme the fluid was modelled either as incompressible ($\rho = \text{const}$) or as an ideal gas.

Using preconditioning, three multiple-grid levels, and an impulsive start, convergence of the mass flow rates was achieved within 4000 iterations independent of the fluid model used. However, when preconditioning was not used, about 12000 iterations were needed in order to obtain convergence.

In Figs. 3.4a and 3.4b the static pressure contours of the solution computed with the original (NonPC) and the preconditioned scheme (PC) are plotted in the azimuthal plane at midspan, respectively. Since the simulated flow fields obtained with the preconditioned scheme are qualitatively independent of the fluid model applied, only the flow field where the fluid was modeled as ideal gas is shown. The original, non-preconditioned solution scheme produces unphysical wiggles in the solution, especially at the leading and trailing edges of the blades. In addition, the isobars of the computed flow field are not perpendicular to the boundary layers. Previous work showed that using finer grids leads to smoother isobars in the main flow. The use of a finer grid does not alleviate the problem of solution decoupling in the boundary layers. With a finer discretization of the boundary layer, the Mach number of the nodes lying next to the wall decreases, whereby the low Mach number deficiencies in the neighbourhood of the wall become pronounced. In contrast to this, the preconditioned scheme produces smooth and physical solutions in all regions of the flow.

In Fig. 3.5 the calculated circumferentially averaged axial and circumferential velocities in the plane M2 (located 30 mm behind the rotor) are compared to measurement data. As seen by the circumferentially averaged axial velocities, both the preconditioned scheme and the original one underpredict the axial velocities. While a mass flow of 13.04 kg/s was measured, the preconditioned scheme predicts a mass flow of 12.53 kg/s and 12.61 kg/s for the compressible and the incompressible case respectively, whereas in the simulation with the original scheme a mass flow rate of 12.24 kg/s was obtained. The measured circumferentially averaged velocities in M2, depicted in Fig. 3.5a, reveal that there is a reduced mass flow in the hub region of the rotor, since the hubside passage vortex causes an overturning of the main flow. While the preconditioned solver captures the tendencies of the secondary flow, the original scheme completely fails to reproduce the secondary flow effects. Furthermore, in the casing region in M2, where the leakage flow enters the main flow, the preconditioned solver predicts the averaged circumferential velocities fairly well, cf. 3.5b.

From the findings of Volpe [291] and from previous work of the present author [16], it is known that by using enough grid points and lowering the artificial damping parameter $k^{(4)}$ from 0.03 to $k^{(4)} = 0.015$ compensates for some of the deficiencies of using a non-preconditioned code for the simulation of low Mach number flows. However, the use of 3.2 Mio. grid points as in a previous work of the author [16] instead of the 327,000 grid points used here, is not practicable when taking into account that the original scheme exhibits

a slower convergence rate. The results presented here clearly show the need for preconditioning when simulating low Mach number flow in multistage turbomachinery.

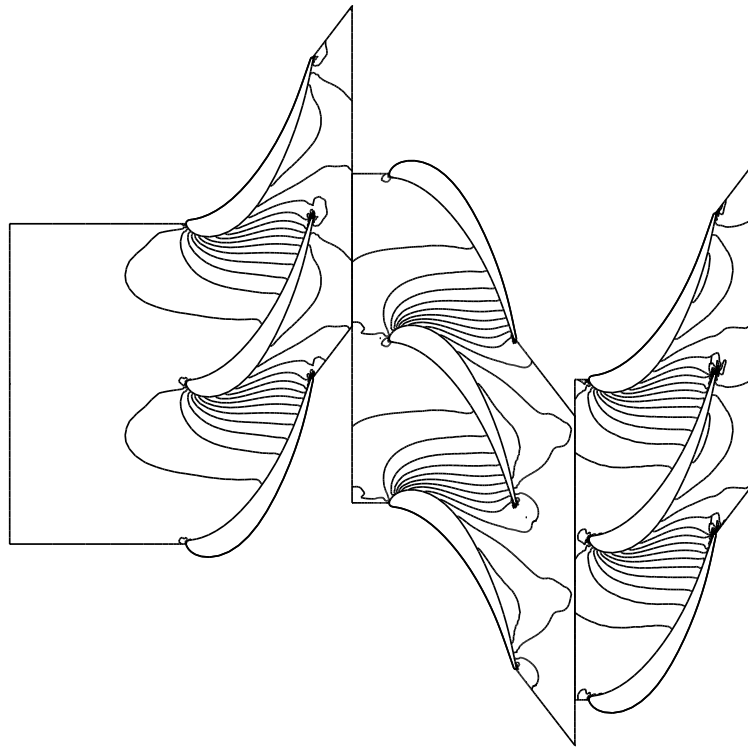
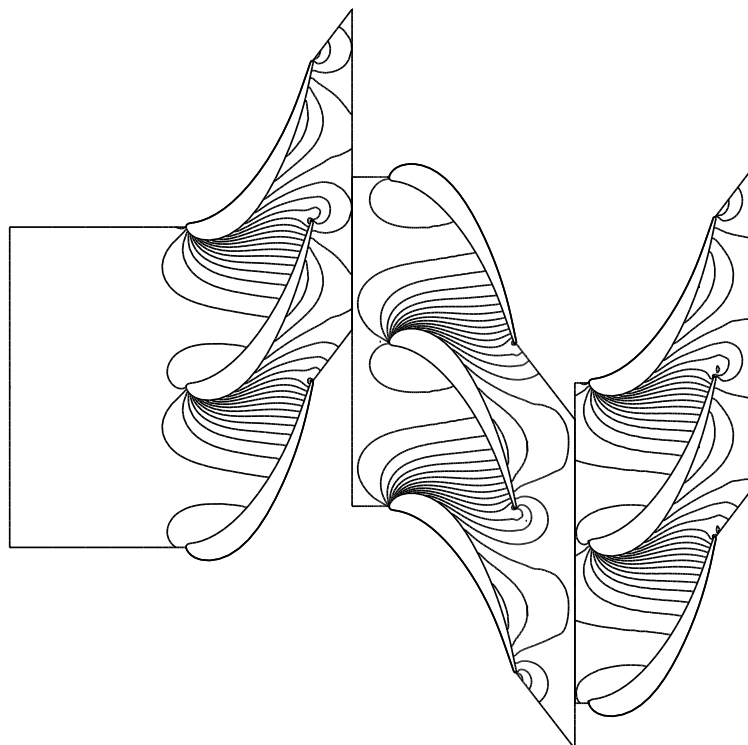
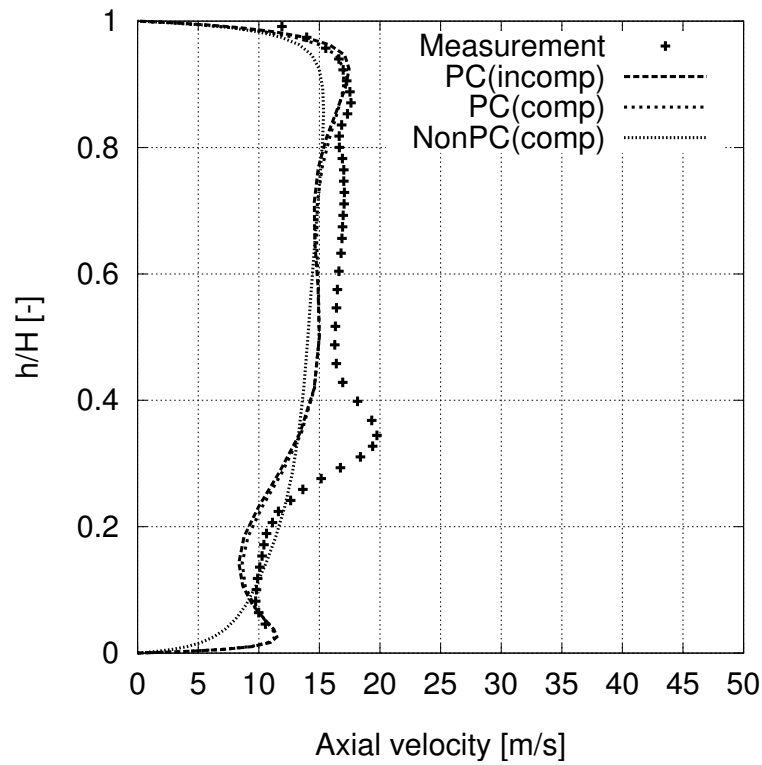
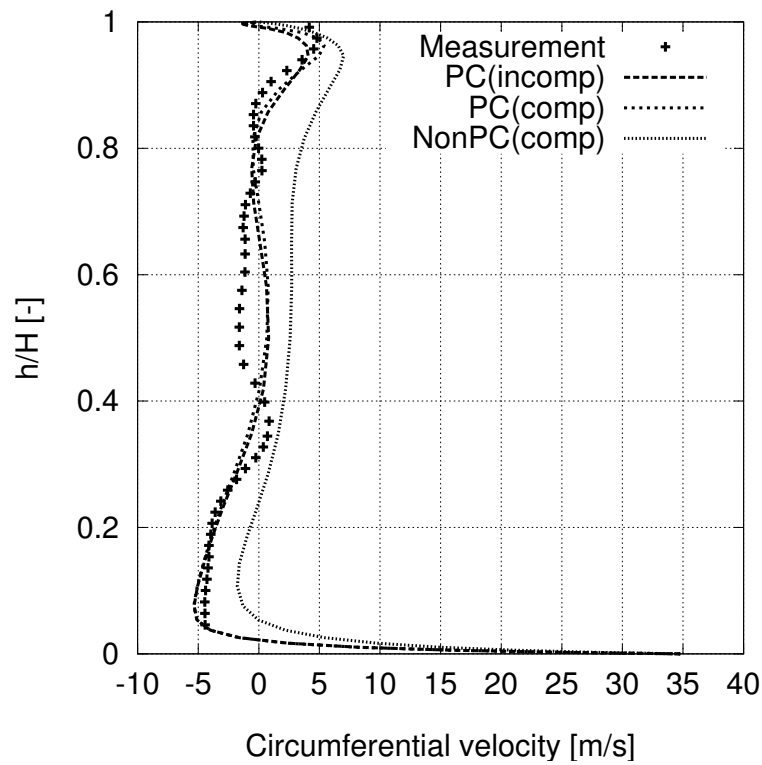
(a) NonPC, $\varrho = p/RT$ (b) PC, $\varrho = p/RT$

Figure 3.4: Lines of constant pressure of the flow field in the low-speed turbine computed with the preconditioned (PC) and the original scheme (NonPC)



(a)



(b)

Figure 3.5: Circumferentially averaged velocities over the relative channel height h/H in the measurement plane M2 (30 mm behind rotor) of the low-speed turbine

Chapter 4

Development of low-diffusive discretization schemes for preconditioned systems

The baseline solution scheme in ITSM3D applies a central discretization of the fluxes. To stabilize the solution scheme and to damp numerical oscillations, the artificial dissipation technique of Jameson, Schmidt and Turkel (JST) [131] is applied, which uses a blend of second and fourth order differences of the solution variables. This solution scheme is robust and suited for the simulation of transonic flows through turbomachinery [147, 190]. To improve the overall solution scheme and to ensure an accurate resolution of the flow field at arbitrary Mach numbers without numerical overshoots of the state variables, various alternative dissipation schemes have been implemented in the flow solver ITSM3D as a part of the current work.

In this chapter the schemes developed for the construction of the artificial dissipation are described and their extension to preconditioning are discussed. Common for the formulated dissipation models is that they can be applied for the simulation of fluids with arbitrary equations of state at all flow speeds.

4.1 Scalar JST-scheme with TVD properties

The scalar dissipation scheme of Jameson, Schmidt and Turkel (JST) is the baseline scheme in ITSM3D and was described in the previous chapters. It is a popular scheme since it is conceptually simple and very robust. However, in its original formulation it does not ensure monotonicity of the solution and causes overshoots in the state variables in the vicinity of shocks, contact discontinuities and boundary layers. The overshoots of the flow solution near shocks can be avoided using the improved pressure switch developed by Swanson and Turkel [268], which reads as:

$$\nu_{\xi,i,j,k} = \frac{|p_{i-1,j,k} - 2p_{i,j,k} + p_{i+1,j,k}|}{(1 - \chi)P_{\text{JST}} + \chi P_{\text{TVD}} + \epsilon_d}, \quad (4.1)$$

with

$$\begin{aligned} P_{\text{JST}} &= |p_{i+1,j,k} + 2p_{i,j,k} + p_{i-1,j,k}|, \\ P_{\text{TVD}} &= |p_{i+1,j,k} - p_{i,j,k}| + |p_{i,j,k} - p_{i-1,j,k}|, \end{aligned} \quad (4.2)$$

and $\epsilon_d = 10^{-5}$, where the parameter $\chi \in [0, 1]$ is specified by the user. By setting the parameter χ to $\chi=0$ the original pressure switch is obtained, and with $\chi=1$ the solution scheme should, according to Swanson and Turkel [268], obtain the property of being Total Variation Diminishing (TVD).

4.2 JST-switched matrix dissipation

Even if the use of preconditioning reduces the level of the artificial dissipation in the momentum equations of the Navier-Stokes equations at low Mach numbers, the accuracy of the solution scheme can be improved further by applying a matrix formulation of the dissipation. While the matrix dissipation formulation in conjunction with preconditioning proposed by other authors are limited to incompressible flow [51] or ideal gas mixtures [263], the scheme presented in the following is formulated without any limiting assumption regarding the state equation of the fluid.

In contrast to the scalar scheme of Jameson et al. [131], in which the spectral radius of the flux Jacobian is used for scaling the dissipation terms of each equation, in the matrix dissipation approach each component of the dissipation vector is in effect scaled individually. Formally, the matrix dissipation formulation is obtained from the scalar scheme by simply replacing the volume weighted spectral radii $\bar{\rho}'_{\xi}{}^V$ in Eq. (3.26) with the volume weighted absolute Jacobian matrix $|\bar{A}_{\Gamma,\xi}^V|$, so that the second and fourth difference operators are calculated according to

$$\begin{aligned} D_{\xi}^{(2)} &= \delta_{\xi}^{-} (\Gamma_v |\bar{A}_{\Gamma,\xi}^V| \varepsilon^{(2)})_{i+1/2,j,k} \delta_{\xi}^{+}, \\ D_{\xi}^{(4)} &= \delta_{\xi}^{-} (\Gamma_v |\bar{A}_{\Gamma,\xi}^V| \varepsilon^{(4)})_{i+1/2,j,k} \delta_{\xi}^{+} \delta_{\xi}^{-} \delta_{\xi}^{+}. \end{aligned} \quad (4.3)$$

The volume-weighted absolute Jacobian is defined as

$$|\bar{A}_{\Gamma,\xi}^V| = L_{\Gamma,\xi}^{-1} \cdot |\bar{\Lambda}_{\xi}^V| \cdot L_{\Gamma,\xi} \quad (4.4)$$

with L_{ξ} as the matrix of left eigenvectors for the Jacobian of the inviscid flux vector in ξ -direction and

$$|\bar{\Lambda}_{\xi}^V| = \text{Diag.} (|\bar{\lambda}_{\xi,1}^V|, \dots, |\bar{\lambda}_{\xi,5}^V|) \quad (4.5)$$

as the corresponding diagonal matrix of the absolute, volume-weighted, anisotropically scaled eigenvalues. The applicable eigenvectors and the product of the absolute Jacobian with the difference vector $\delta \mathbf{Q}_v$ are given in Appendix F.

As indicated by the use of overbar-quantities in the Eqs. (4.3) to (4.5), in order to increase the robustness of the matrix dissipation scheme, the volume-weighted eigenvalues are scaled anisotropically in the same way that the spectral radii were scaled in the scalar scheme.

Near stagnation points and sonic lines, some of the eigenvalues of the Jacobian $|\bar{A}_{\Gamma,\xi}^V|$ approach zero. To avoid vanishing dissipation terms for such situations, the elements of the diagonal eigenvalue matrix are limited as suggested by Swanson and Turkel [268] as follows:

$$\begin{aligned} |\bar{\lambda}_{\xi,1,2,3}^V| &= \Theta_\xi \cdot \max(V_l \sigma_\xi^V, |\lambda_{\xi,1,2,3}^V|), \\ |\bar{\lambda}_{\xi,4,5}^V| &= \Theta_\xi \cdot \max(V_n \sigma_\xi^V, |\lambda_{\xi,4,5}^V|), \end{aligned} \quad (4.6)$$

with σ_ξ^V as the volume weighted spectral radius and Θ_ξ as the coefficient for anisotropic scaling, which is defined in Eq. (2.17). Brodersen [44] has tested the influence of the parameters V_l, V_n for a matrix dissipation scheme for the unpreconditioned Navier-Stokes equations; as a good compromise between stability and robustness he suggests that these parameters should be set to 0.3 and 0.4, respectively. In the current work these proposed values were adopted.

It should be noted that if all eigenvalues were equal, the corresponding Jacobian matrix $|\bar{A}_{\Gamma,\xi}^V|$ would be a diagonal matrix. Since three eigenvalues are equal and the remaining two only differ by the sign of the pseudoacoustic velocity, the resulting product of the Jacobian matrix and the first or third order differences is not very complex, cf. Appendix F where the product $|\bar{A}_{\Gamma,\xi}^V| \cdot \delta \mathbf{Q}_v$ is given. In agreement with the findings of Brodersen, the matrix dissipation scheme only results in a negligible overhead in CPU-time per time step compared to the scalar dissipation.

4.3 Strengths and weaknesses of JST-switched schemes

The scalar and the matrix-dissipation JST-schemes are simple, they are robust [254] and have been implemented in a variety of flow solvers (e.g., [23, 108, 126, 201, 279]).

Both the scalar and the matrix JST-switched dissipation schemes exhibit deficiencies due to the use of a blend of second and fourth order differences of the solution variables for the dissipation terms. For instance, in the matrix dissipation scheme the differences $(\delta \mathbf{Q}_v)_{i+1/2,j,k} = \mathbf{Q}_{v,i+1,j,k} - \mathbf{Q}_{v,i,j,k}$ are scaled with the absolute Jacobian $|A_\xi|_{i+1/2,j,k}$ for building the second order difference dissipation terms. If the absolute Jacobian is calculated from the Roe-average states of the left "L" (i, j, k) and right "R" ($i+1, j, k$) side of the interface and an appropriate central discretization of the convective fluxes is used, the result is a first order upwind scheme. Thus, the second order difference dissipation terms are physically motivated, but when activated, they lead to a degradation of the order of accuracy of the solution scheme. The fourth order difference dissipation terms on the other hand are only numerically motivated. The idea of the fourth order difference dissipation is merely to prevent odd-even decoupling and to stabilize the central difference scheme. The third order differences $\delta^3 Q_{v,i+1/2} = Q_{v,i+2} - 3Q_{v,i+1} + 3Q_{v,i} - Q_{v,i-1}$ for the construction of

the dissipation based on the fourth order differences are also scaled with the Jacobian $|A_\xi|_{i+1/2,j,k}$. This Jacobian is calculated as a function of the state variables in the nodes left and right of the interface at $i + 1/2, j, k$. Thus, not every state contributing to the third order differences is taken into account and these terms lack a clear physical motivation. However, these terms have the advantage that for appropriate values of the scaling parameter $k^{(4)}$ they do not degrade the second order accuracy of the central differencing scheme.

Jameson [129, 130] has proposed an alternative artificial dissipation model which combines the advantages of the second and fourth order difference dissipation used in the JST scheme, leads to second order accuracy in smooth regions of the flow and in addition has the property of providing essentially monotone solutions. Such a scheme can be obtained when the dissipative flux is constructed by using only the left and right states of the cell interfaces. In order to attain a scheme which exhibits a second order accuracy, the left and right states of the intermediate points are extrapolated from nearby data. To obtain monotonicity of the scheme, appropriate limiters are used. This scheme is the topic of the following section.

4.4 Scalar SLIP scheme of Jameson

As an alternative to the JST-switched schemes Jameson [129] proposed the scalar SLIP scheme, that is computationally and conceptually simple and yet leads to monotone solutions. In the scalar SLIP scheme the dissipation vector $\mathbf{d}_{i+1/2}$ associated with the flux at the interface between the nodes i and $i + 1$ is calculated as follows

$$\mathbf{d}_{\xi,i+1/2} = \frac{1}{2} \alpha_{i+1/2}^V (\mathbf{Q}_{i+1} - \mathbf{Q}_i). \quad (4.7)$$

Jameson suggests setting the coefficient α^V to the absolute value of the minimum eigenvalue of the linearized flux Jacobian A :

$$\alpha^V = \min_k \hat{\lambda}_k^V, \quad \text{and} \quad \hat{\lambda}_k^V = \begin{cases} |\lambda_k^V|, & \text{if } \lambda_k^V \geq \epsilon, \\ \frac{1}{2} \left(\epsilon + \frac{\lambda_k^V{}^2}{\epsilon} \right), & \text{if } |\lambda_k^V| < \epsilon, \end{cases} \quad (4.8)$$

with ϵ as a positive threshold proportional to the speed of sound a that prevents the scheme from admitting stationary expansion shocks that would violate the entropy condition. Tweedt et al. [279] suggest a similar formulation for the dissipation in which they also account for cell stretching.

When preconditioning is used, the formulation for the dissipation in Eq. (4.7) should be substituted with the following formulation

$$\mathbf{d}_{\xi,i+1/2,j,k} = \frac{1}{2} (\Gamma_v \alpha'^V)_{i+1/2,j,k} (\mathbf{Q}_{v,i+1,j,k} - \mathbf{Q}_{v,i,j,k}), \quad (4.9)$$

where Γ_v represents the preconditioning matrix of Merkle, \mathbf{Q}_v the vector of primitive, viscous variables, and the scaling factor α' defined like α in Eq. (4.8)

but based on the eigenvalues of the preconditioned system. The resulting dissipation vector for the ξ -direction is given by

$$\mathbf{D}_{\xi,i,j,k} = \mathbf{d}_{\xi,i+1/2,j,k} - \mathbf{d}_{\xi,i-1/2,j,k}. \quad (4.10)$$

The corresponding terms \mathbf{D}_η and \mathbf{D}_ζ for the η - and ζ -direction are defined analogously. The complete dissipation vector $\mathbf{D}_{i,j,k}$ for the control volume $\tilde{V}_{i,j,k}$ is determined by

$$\mathbf{D} = \mathbf{D}_\xi + \mathbf{D}_\eta + \mathbf{D}_\zeta. \quad (4.11)$$

In the following, only the dissipation in the ξ -direction will be considered and the j and k indices will be omitted in the notation for the sake of simplicity.

The discretization scheme formulated so far leads to a scheme which is of first order accuracy. To reduce the amount of artificial dissipation and to attain a scheme of second order accuracy, Jameson [129, 130] suggests using either a symmetric or a upstream limited positive (SLIP / USLIP) one-dimensional reconstruction procedure. With this procedure, the diffusive flux is formed by the reconstructed states $\mathbf{Q}_{i+1/2,L}$ and $\mathbf{Q}_{i+1/2,R}$ at the interfaces of the dual mesh instead of the values in the neighbouring nodes, \mathbf{Q}_i and \mathbf{Q}_{i+1} , respectively. The former states are obtained by interpolation of nearby data from the left and the right side of the interface. This interpolation procedure is subject to limiters to preserve monotonicity in a similar manner to the reconstruction of the solution in Van Leer's Monotone Upstream-centered Schemes for Conservation Laws (MUSCL) [282].

When the SLIP-procedure is applied, each of component of the state variable vector $\mathbf{Q}_v = [q_v^1, \dots, q_v^5]^T$ at the interface $i + 1/2$ is determined by

$$\begin{aligned} q_{v,i+1/2,L}^k &= q_{v,i}^k + \frac{1}{2}L(\Delta q_{v,i-1/2}^k, \Delta q_{v,i+3/2}^k), \\ q_{v,i+1/2,R}^k &= q_{v,i+1}^k - \frac{1}{2}L(\Delta q_{v,i-1/2}^k, \Delta q_{v,i+3/2}^k), \end{aligned} \quad \forall k = 1, \dots, 5 \quad (4.12)$$

with $\Delta q_{v,i+1/2}^k = q_{v,i+1}^k - q_{v,i}^k$ and the SLIP limiter defined as

$$L(\phi_1, \phi_2) = \frac{1}{2}P(\phi_1, \phi_2)(\phi_1 + \phi_2), \quad P(\phi_1, \phi_2) = 1 - \left| \frac{\phi_1 - \phi_2}{|\phi_1| + |\phi_2| + \epsilon_l} \right|^{e_q}, \quad (4.13)$$

where e_q is a positive power. To obtain a higher order dissipation scheme, the components of the extrapolated state vectors $\mathbf{Q}_{v,i+1/2,L}$ and $\mathbf{Q}_{v,i+1/2,R}$ at the left and the right side of the interface $i + 1/2$ are calculated according to Eqs. (4.12) and (4.13). Then the diffusive flux for the ξ -direction is determined as

$$\mathbf{d}_{\xi,i+1/2,j,k} = \frac{1}{2}(\Gamma_v \alpha^V)_{i+1/2,j,k} (\mathbf{Q}_{v,i+1/2,j,k,R} - \mathbf{Q}_{v,i+1/2,j,k,L}) \quad (4.14)$$

instead of the prescription in Eq. (4.9). However, in the case that the limiter function L returns zero, the last formulation in Eq. (4.14) becomes equivalent to the first order formulation in Eq. (4.9).

In the current work the parameter e_q of the SLIP limiter given in Eq. (4.13) was set to $e_q = 2$. Inspired by the work of Venkatakrishnan [283] on limiters for unstructured grids, the threshold value ϵ_l to prevent the denominator from

getting zero for vanishing differences ϕ_1 and ϕ_2 of the state variables was defined as

$$\epsilon_l = c_\epsilon \|\Delta x\|^{3/2}, \quad c_\epsilon \in [1, 5], \quad (4.15)$$

where $\|\Delta x\|$ represents the grid spacing length. If ϕ_1 and ϕ_2 have opposite signs (which is the case for an extremum), then $P(\phi_1, \phi_2)$ vanishes and the left and right states are simply taken without extrapolation, thereby locally reducing accuracy of the scheme to first order and preventing overshoots of the solution variables.

As discussed by Jameson the presence of the threshold quantity ϵ_l in the SLIP limiter (4.13) relaxes the Local Extremum Diminishing (LED) property of the scheme. With the introduction of the threshold quantity the scheme preserves its second order accuracy at smooth extremes, leads to a faster convergence rates, and it decreases the likelihood of limit cycles in which the limiter interacts unfavorably with the corrections of the solution scheme [129].

It should furthermore be noted that to achieve a local extremum diminishing scheme other limiter-functions $L(\phi_1, \phi_2)$ than the one given in Eq. (4.13) can be used. Jameson [129] shows that any limiter fulfilling the properties

$$\begin{aligned} P1 : \quad L(\phi_1, \phi_2) &= L(\phi_2, \phi_1), & P2 : \quad L(\alpha\phi_1, \alpha\phi_2) &= \alpha L(\phi_1, \phi_2), \\ P3 : \quad L(\phi_1, \phi_1) &= \phi_1, & P4 : \quad L(\phi_1, \phi_2) &= 0 \quad \text{if } \phi_1 \cdot \phi_2 < 0, \end{aligned} \quad (4.16)$$

leads to a LED scheme, if used in conjunction with the reconstruction and dissipation scheme described above by Eqs. (4.12) and (4.14). Thus, as a substitute for the SLIP limiter defined in Eq. (4.13) one of the following well-known limiters

$$\begin{aligned} L(\phi_1, \phi_2) &= S(\phi_1, \phi_2) \cdot \min(|\phi_1|, |\phi_2|), \\ L(\phi_1, \phi_2) &= S(\phi_1, \phi_2) \cdot \frac{2|\phi_1||\phi_2|}{|\phi_1| + |\phi_2|} = \max \left[0, \frac{2\phi_1\phi_2}{|\phi_1| + |\phi_2|} \right], \\ L(\phi_1, \phi_2) &= S(\phi_1, \phi_2) \cdot \max [\min(2|\phi_1|, |\phi_2|), \min(|\phi_1|, 2|\phi_2|)] \end{aligned} \quad (4.17)$$

with

$$S(\phi_1, \phi_2) = \frac{1}{2} [\text{sign}(\phi_1) + \text{sign}(\phi_2)], \quad (4.18)$$

i.e., the Min-mod, the van Albada, or Roe's Superbee limiter could be used. For a discussion and analysis of limiters, reconstruction procedures, and monotonicity properties, the reader may refer to Appendix E.

It should be remarked that the dissipative fluxes of the the SLIP scheme effectively consists of a blend of differences of second and fourth order of the solution variables. From Eqs. (4.12), (4.13) and (4.14) it follows that the k -th component $d_{\xi,v,i+1/2}^k$ of the dissipative flux vector $\mathbf{d}_{\xi,v,i+1/2}$ at the interface $i + 1/2$ calculates as

$$\begin{aligned} d_{\xi,v,i+1/2}^k &= \frac{1}{2} (\Gamma\alpha')_{i+1/2} (1 - \mathcal{P}_{i+1/2}^k) \Delta q_{v,i+1/2}^k - \\ &\quad \frac{1}{4} (\Gamma\alpha')_{i+1/2} \mathcal{P}_{i+1/2}^k \left(\Delta q_{v,i-1/2}^k - 2\Delta q_{v,i+1/2}^k + \Delta q_{v,i+3/2}^k \right), \end{aligned} \quad (4.19)$$

$\forall k = 1, \dots, 5$ with $\mathcal{P}_{i+1/2}^k = P(\Delta q_{v,i-1/2}^k, \Delta q_{v,i+3/2}^k)$. Thus, it is evident that the dissipation vector $\mathbf{D}_\xi = \mathbf{d}_{\xi,v,i+1/2} - \mathbf{d}_{\xi,v,i-1/2}$ is constructed merely by the use of

second order differences of the solution variables in cases where the limiter is fully active ($P = 0$), while it is only constructed by fourth order differences in cases for which the limiter is fully shut off ($P = 1$) for each variable. A major difference between the SLIP and the JST scheme, is that in the former an individual limiter for each solution variable is applied, whereas in the JST scheme the switching between the dissipation terms based on second and fourth order differences is only determined by a pressure sensor and is carried out in the same fashion for all flow equations.

4.5 Characteristic upwind scheme of Roe

The scalar SLIP scheme can according to Jameson [129] resolve shock fronts over just a few grid nodes. While the scheme is perfectly suited for the discretization of single equations for transported scalars, for a system of transport equations like the Euler equations, the performance of the scheme can be improved by carrying out a characteristic decomposition and applying the SLIP reconstruction and limiting procedure individually for each transport equation. As shown in Appendix F, if a first order upwind scheme, which is based on a characteristic decomposition of the solution variables, is applied to the preconditioned Euler-equations the dissipative fluxes are given by

$$\mathbf{d}_{\xi,v,i+1/2} = \frac{1}{2} \Gamma_{v,i+1/2} |A_{\Gamma,\xi}^V|_{i+1/2} (\mathbf{Q}_{v,i+1} - \mathbf{Q}_{v,i}) \quad (4.20)$$

with the absolute Jacobian $|A_{\Gamma,\xi}|$ determined as

$$|A_{\Gamma,\xi}| = L_{\xi,v}^{-1} |\Lambda_{\xi}^V| L_{\xi,v}, \quad A_{\Gamma,\xi} = \Gamma_v^{-1} \frac{\partial \hat{\mathbf{E}}}{\partial \hat{\mathbf{Q}}}. \quad (4.21)$$

$L_{\xi,v}$ represents thereby the matrix of left eigenvectors of the Jacobian matrix $A_{\Gamma,\xi}$ for the fluxes in ξ -direction. The matrix $|\Lambda_{\xi}^V|$ is defined as the diagonal matrix of the absolute values of the volume weighted eigenvalues $\lambda_{\xi,i}^V; i = 1, \dots, 5$ of the Jacobian $A_{\Gamma,\xi}$, i.e., $|\Lambda_{\xi}^V| = \text{Diag.}(|\lambda_{\xi,1}^V|, \dots, |\lambda_{\xi,5}^V|)$. It should be noted that the volume weighted eigenvalues (cf. Eq. (F.38)) and not the eigenvalues based merely on contravariant velocities need to be taken in order to account for the area of the interface of the dual cell at $i + 1/2$.

A comparison of Eq. (4.20) with Eq. (4.9), shows that the dissipation term of the first order characteristic upwind scheme only differs from the scalar SLIP scheme in the sense that the absolute Jacobian matrix $|A_{\Gamma,\xi}|$ is used for scaling the dissipative terms instead of the eigenvalue based norm α' .

To attain a second order scheme, the states $\mathbf{Q}_{v,i}$ and $\mathbf{Q}_{v,i+1}$ in Eq. (4.20) for the dissipative flux vector may be replaced with the extrapolated states $\mathbf{Q}_{v,i+1/2,L}$ and $\mathbf{Q}_{v,i+1/2,R}$ on the respective left and the right side of the interface at $i + 1/2$. To determine these states, the SLIP reconstruction and limiting procedure as described in Eqs. (4.12) and (4.13) can be used.

4.5.1 Roe-averaging

Whether a first or a second order scheme is used, to be able to capture a shock front as accurately as possible, the absolute Jacobian should be calculated from the Roe-averaged states. If the Jacobian $A = \frac{\partial \mathbf{E}}{\partial \mathbf{Q}}$ at an interface $i + 1/2$ is based on the Roe-averaged [229] state vector $\bar{\mathbf{Q}}_{v,i+1/2}^{\text{Roe}} = f(\mathbf{Q}_{v,i+1/2,R}, \mathbf{Q}_{v,i+1/2,L})$, the following relation holds

$$\mathbf{E}(\mathbf{Q}_{v,i+1/2,R}) - \mathbf{E}(\mathbf{Q}_{v,i+1/2,L}) = A(\bar{\mathbf{Q}}_{v,i+1/2}^{\text{Roe}}) \cdot (\mathbf{Q}_{v,i+1/2,R} - \mathbf{Q}_{v,i+1/2,L}). \quad (4.22)$$

If Roe-averages are used, the Hugoniot jump conditions are fulfilled [118] and as shown in Appendix F a full upwind discretization results. As furthermore shown theoretically by Jameson [130], if a characteristic upwind scheme is used where the absolute Jacobian is based on Roe averaged states, shock fronts can be resolved over three nodes (where only one node is contained in the interior of the shock front).

4.5.2 Method adopted in the current work

In the current work, the absolute Jacobian $|A|_{i+1/2}$ is calculated from the Roe-average of the left $\mathbf{Q}_{v,i+1/2,L}$ and right $\mathbf{Q}_{v,i+1/2,R}$ states in the case of ideal gas flow. For incompressible fluids the reference state is calculated by simple arithmetic averaging of the left and right states. The dissipation operator for the ξ -direction can be written as

$$\mathbf{D}_{\xi,i,j,k} = \delta_{\xi}^{-} \left[(\Gamma_v |\bar{A}_{\xi}^V|) |_{\bar{\mathbf{Q}}_{v,RL}} \cdot \delta_{\xi}^{+} \mathbf{Q}_{v,RL} \right]_{i+1/2,j,k} \quad (4.23)$$

with the difference $\delta^{+} \mathbf{Q}_{v,i+1/2,RL} = \mathbf{Q}_{v,i+1/2,R} - \mathbf{Q}_{v,i+1/2,L}$ and $\bar{\mathbf{Q}}_{v,i+1/2,RL}$ as an average (Roe or arithmetic) between the left and right states. The dissipation for the η - and ζ -direction is determined analogously.

The characteristic upwind scheme was implemented in the flow solver ITSM3D. There the user can choose between the second order SLIP-reconstruction due to Jameson and a third order κ -extrapolation scheme [118] in conjunction with a van Albada type of limiter. In the latter case, the procedure used in the work of Raif [221] is followed, in which each of the components of the state variable vector $\mathbf{Q}_v = (q_v^1, \dots, q_v^5)^T$ at the interface $i + 1/2$ is determined by

$$\begin{aligned} q_{v,i+1/2,L}^k &= q_{v,i}^k + \left[\frac{s}{4} (f^+ \Delta^+ + f^- \Delta^-) \right]_{k,i}, \\ q_{v,i+1/2,R}^k &= q_{v,i+1}^k - \left[\frac{s}{4} (f^- \Delta^+ + f^+ \Delta^-) \right]_{k,i+1} \end{aligned} \quad (4.24)$$

with

$$\begin{aligned} f_{k,i}^- &= 1 - \kappa s_{k,i}, & f_{k,i}^+ &= 1 + \kappa s_{k,i}, & \kappa &= \frac{1}{3}, \\ \Delta_{k,i}^+ &= q_{v,i+1}^k - q_{v,i}^k, & \Delta_{k,i}^- &= q_{v,i}^k - q_{v,i-1}^k, \end{aligned}$$

where the van Albada limiter s at node i is defined as

$$s_{k,i} = \max \left[0, \frac{2\Delta_{k,i}^- \Delta_{k,i}^+ + \epsilon_l}{(\Delta_{k,i}^+)^2 + (\Delta_{k,i}^-)^2 + \epsilon_l} \right]. \quad (4.25)$$

It should be noted that the limiter given in the last equation is a modified version of the original limiter proposed by van Albada et al. [280]. As seen in Fig. E.1 where the limiter function is plotted in a $\Psi - r$ diagram (as "van Albada 2"), the modified limiter is not as the original limiter contained in Sweby's second order TVD region. However, since $\Psi(1) = 1$, the limiter is still leading to a third order accuracy of the resulting κ -scheme in smooth regions of the flow. Kermani et al. [139, 140] recommend the use of the modified form, albeit they refrain scaling the value of κ with the limiter function s .

Whether the SLIP reconstruction procedure or the κ -scheme with the modified van Albada limiter is used, the absolute Jacobian is calculated without applying anisotropically scaled eigenvalues ($\Theta_\xi = 1$). However, to increase the robustness of the scheme and to avoid the presence of unphysical expansion shocks in the numerical solution, the eigenvalues are limited according to Eq. (4.6) but with the value of the parameters V_l, V_n now both lowered to the range $V_l, V_n \in [0.02, 0.1]$.

4.6 Dissipation scheme based on the Advection Upstream Splitting Method (AUSM+)

With the characteristic upwind dissipation scheme presented in the last section one can resolve stationary shocks with one single interior point [130] and resolve boundary layers well. However, the performance of the upwind characteristic splitting scheme can be attained by a less complex scheme that is not based on a characteristic decomposition of the flow field. The use of so-called low diffusion schemes such as the AUSM type of schemes developed by Liou and Steffen [169] have gained popularity and has been implemented in both academic and commercial codes for a wide range of flow problems [88, 167, 172, 198].

As with other upwind methods, the interface flux formulas for low-diffusion flux-splitting schemes can be divided into a central flux plus a dissipation term. Liou and Steffen [169] show how this can be done for the original AUSM-scheme. By using a central discretization as a basis Radespiel and Kroll [220] present a modified version of that scheme. Some of the drawbacks of the AUSM-scheme have been eliminated by the work of Liou [165], where he presents a revised scheme called AUSM+ and also makes suggestions how to implement this scheme into a central differencing code. In a later publication Edwards and Liou [78] explain how this scheme can be extended for the use in conjunction with time-derivate preconditioning.

In the current work the suggestions of Liou were followed and his scheme has been implemented in the central differencing Navier-Stokes code ITSM3D. As will be seen from results from various test cases, the performance of the scheme is very encouraging.

In the following sections, the implementation of the AUSM+ scheme in a central differencing framework is described. Beginning with the original formulation for the sake of completeness, the fluxes of this upwind biased scheme

are then divided into a central plus a diffusive part. While Liou [165] showed that an approximation of his scheme is equivalent to the CUSP-scheme of Jameson [128], in this work it is shown in a more in-depth analysis that the dissipation terms of the AUSM+-scheme can be splitted up in an anti-diffusive and a diffusive part. Issues regarding preconditioning will be addressed before the explanation of how to control the anti-diffusive part for increasing the robustness is given and the implementation details of the scheme are presented.

4.6.1 The AUSM+ scheme

In order to formulate the original AUSM+ splitting of Liou [166] the preconditioned Euler equations

$$\Gamma_v \frac{\partial \hat{\mathbf{Q}}_v}{\partial t} + \frac{\partial \hat{\mathbf{E}}_c}{\partial \xi} + \frac{\partial \hat{\mathbf{F}}_c}{\partial \eta} + \frac{\partial \hat{\mathbf{G}}_c}{\partial \zeta} = 0 \quad (4.26)$$

with

$$\begin{aligned} \hat{\mathbf{Q}}_v &= \check{V}_{i,j,k} \mathbf{Q}_v, & \hat{\mathbf{E}}_c &= S_{\xi,x} \mathbf{E}_c + S_{\xi,\phi} \mathbf{F}_c + S_{\xi,r} \mathbf{G}_c, \\ \hat{\mathbf{F}}_c &= S_{\eta,x} \mathbf{E}_c + S_{\eta,\phi} \mathbf{F}_c + S_{\eta,r} \mathbf{G}_c, & \hat{\mathbf{G}}_c &= S_{\zeta,x} \mathbf{E}_c + S_{\zeta,\phi} \mathbf{F}_c + S_{\zeta,r} \mathbf{G}_c \end{aligned} \quad (4.27)$$

for a curvilinear coordinate system for which the source terms have been neglected (cf. Anker et al. [6]) are used as a basis. The quantities S_ξ , S_η , S_ζ denote the cell surface vectors of the dual mesh in the ξ -, η - and ζ -direction, respectively, and $\check{V}_{i,j,k}$ represents the corresponding cell volume. The dual mesh is defined by connecting the cell centers of the original mesh. In the following, only the splitting of the flux vector $\hat{\mathbf{E}}_c$ for the i -direction at the interface $i + 1/2, j, k$ will be considered, the splitting of the fluxes at the other faces is treated analogously. The subscript " $i + 1/2$ " (or simply " $1/2$ ") refers in the following to this specific interface.

In the AUSM type of schemes, the inviscid flux is split up into a convective flux and a pressure term

$$\hat{\mathbf{E}}_{i+1/2} = \dot{m}_{i+1/2} \Phi_{i+1/2} + \mathbf{P}_{i+1/2} \quad (4.28)$$

with the state vector Φ defined as $\Phi = [1, \hat{v}_\xi, \hat{v}_\eta, \hat{v}_\zeta, h_0]^T$ with \hat{v}_ξ , \hat{v}_η , and \hat{v}_ζ representing the contravariant velocity components in the absolute system in ξ -, η - and ζ -direction of the grid, respectively. If relative systems are considered, the absolute contravariant velocity vector $\hat{\mathbf{v}} = [\hat{v}_\xi, \hat{v}_\eta, \hat{v}_\zeta]$ has to be replaced with the relative contravariant velocity vector $\hat{\mathbf{w}} = [\hat{w}_\xi, \hat{w}_\eta, \hat{w}_\zeta]$.

For the i -direction the state vector $\Phi_{i+1/2}$ at the interface $S_{i+1/2}$ between node i and $i + 1$ of the grid is taken as

$$\Phi_{i+1/2} = \begin{cases} \Phi_i, & m_{i+1/2} \geq 0, \\ \Phi_{i+1}, & m_{i+1/2} < 0. \end{cases} \quad (4.29)$$

The interface mass flux $\dot{m}_{i+1/2}$ is given by

$$\dot{m}_{i+1/2} = a_{i+1/2}^S m_{i+1/2} \varrho_{i+1/2} \quad (4.30)$$

where $a_{i+1/2}^S$ denotes the surface weighted speed of sound, which calculates as

$$a_{i+1/2}^S = a_{i+1/2} \cdot \|\mathbf{S}_\xi\|_{i+1/2} \quad (4.31)$$

with $\|\mathbf{S}_\xi\|_{i+1/2}$ representing the projection of the interface of the dual mesh between the nodes i and $i + 1$ in the ξ -direction. The interface Mach number $m_{i+1/2}$ is defined as

$$m_{i+1/2} = \mathcal{M}^+(M_{1/2,i}) + \mathcal{M}^-(M_{1/2,i+1}) \quad (4.32)$$

and the interface density reads as

$$\varrho_{i+1/2} = \begin{cases} \varrho_i, & m_{i+1/2} \geq 0, \\ \varrho_{i+1}, & m_{i+1/2} < 0. \end{cases} \quad (4.33)$$

The pressure flux vector $\mathbf{P}_{\xi,i+1/2}$ is determined by the following equation

$$\mathbf{P}_{\xi,i+1/2} = [0, p_{i+1/2} S_{\xi,i+1/2,x}, p_{i+1/2} S_{\xi,i+1/2,\phi}, p_{i+1/2} S_{\xi,i+1/2,r}, 0]^T \quad (4.34)$$

with the interface pressure defined as

$$p_{i+1/2} = \mathcal{P}^+(p_i)p_i + \mathcal{P}^-(p_{i+1})p_{i+1}. \quad (4.35)$$

Before explaining how the Mach numbers M_i, M_{i+1} and the splitting functions \mathcal{M} and \mathcal{P} are defined it should be noted that the resulting flux in Eq. (4.28) also can be written in the following form

$$\begin{aligned} \hat{\mathbf{E}}_{i+1/2} &= a_{i+1/2}^S (\varrho_i \Phi_i m_{i+1/2}^+ + \varrho_{i+1} \Phi_{i+1} m_{i+1/2}^-) + \mathbf{P}_{i+1/2}, \\ &= a_{i+1/2}^S (\Psi_i m_{i+1/2}^+ + \Psi_{i+1} m_{i+1/2}^-) + \mathbf{P}_{i+1/2}, \end{aligned} \quad (4.36)$$

with the state vector Ψ defined as $\Psi = [\varrho, \varrho \hat{v}_\xi, \varrho \hat{v}_\eta, \varrho \hat{v}_\zeta, \varrho h_0]^T$ and the positive and negative interface Mach numbers $m_{i+1/2}^\pm$ given as

$$m_{i+1/2}^\pm = \frac{1}{2}(m_{i+1/2} \pm |m_{i+1/2}|). \quad (4.37)$$

The Mach numbers $M_{1/2,i}, M_{1/2,i+1}$ for determination of the interface Mach number $m_{i+1/2}$ according to Eq. (4.32) are defined as

$$M_{1/2,i} = \frac{\hat{v}_{\xi,1/2,i}}{a_{i+1/2}}, \quad \hat{v}_{\xi,1/2,i} = \frac{\mathbf{v}_i \cdot \mathbf{S}_{\xi,i+1/2}}{\|\mathbf{S}_{\xi,i+1/2}\|}, \quad (4.38)$$

and

$$M_{1/2,i+1} = \frac{\hat{v}_{\xi,1/2,i+1}}{a_{i+1/2}}, \quad \hat{v}_{\xi,1/2,i+1} = \frac{\mathbf{v}_{i+1} \cdot \mathbf{S}_{\xi,i+1/2}}{\|\mathbf{S}_{\xi,i+1/2}\|}, \quad (4.39)$$

respectively, with $\mathbf{v} = [v_x, v_\phi, v_r]$ representing the velocity vector in the cylindrical $x - \phi - r$ coordinate system. The quantity $\mathbf{S}_{\xi,i+1/2} = [S_{\xi,x}, S_{\xi,\phi}, S_{\xi,r}]_{i+1/2}$ represents the surface vector of the cell interface at $i + 1/2$; its components represent the projections in the x, ϕ , and r directions, respectively.

The Mach number \mathcal{M}^\pm and pressure splitting functions \mathcal{P}^\pm are calculated as

$$\mathcal{M}^\pm = \begin{cases} \mathcal{M}_{(1)}^\pm, & |M| \geq 1, \\ \mathcal{M}_{(4)}^\pm, & |M| < 1, \end{cases} \quad (4.40)$$

with

$$\mathcal{M}_{(1)}^\pm = \frac{1}{2}(M \pm |M|), \quad \mathcal{M}_{(4)}^\pm = \pm \frac{1}{4}(M \pm 1)^2 \pm \beta(M^2 - 1)^2 \quad (4.41)$$

and

$$\mathcal{P}^\pm = \begin{cases} \frac{1}{2}[1 \pm \text{sign}(M)], & |M| \geq 1, \\ \frac{1}{4}(M \pm 1)^2(2 \mp M) \pm \alpha M(M^2 - 1)^2, & |M| \leq 1, \end{cases} \quad (4.42)$$

respectively. When monotonicity of the polynomials is required, the parameters have to be chosen within the ranges $\alpha \in [-3/4, 3/16]$ and $\beta \in [-1/16, 1/2]$ as discussed by Liou [165]. As will be clear from the expressions that will be derived for the diffusive fluxes, increasing the values of the parameters α and β gives a larger inherent diffusion of the AUSM discretization.

Liou [166] recommends setting the parameters α and β to

$$\alpha = 3/16, \quad \beta = 1/8. \quad (4.43)$$

For a discussion of the setting of the parameters and the properties of the splitting functions the reader may refer to the work of Liou [166].

According to Liou the interface speed of sound $a_{1/2}$ may be calculated as a simple average of the right and left states:

$$a_{i+1/2} = \frac{1}{2}(a_i + a_{i+1}). \quad (4.44)$$

In order to be able resolve a stationary shock exactly, Liou [166] shows that the speed of sound should be calculated as follows

$$a_{i+1/2} = \min(\tilde{a}_i, \tilde{a}_{i+1}), \quad \tilde{a} = a^{*2} / \max(a^*, |\hat{v}_\xi|), \quad (4.45)$$

where a^* denotes the critical speed of sound.

4.6.2 Formulation of the AUSM+ scheme for a cell-vertex scheme

There are several ways to implement the AUSM+ scheme in a finite volume code. When a cell-centered scheme is used, the implementation of the original upwind formulation given by Eqs. (4.28) to (4.45) is straightforward. Alternatively, if a cell vertex scheme is used for discretization of the inviscid fluxes, then the original formulation of Liou [165] can also be applied directly if a dual mesh with control volumes $\check{V}_{i,j,k}$ is constructed. As a further option, the AUSM+ interface fluxes can as be split up into a central and a diffusive contribution. This is the approach that was used in the current work; the central part of the fluxes is calculated as described in Section 2.2.1, i. e., the fluxes are

evaluated at each individual of the four faces of each side of the control volume $V_{i,j,k}$ (cf. Fig. 2.1). Opposed to this, the diffusive fluxes are calculated using the dual mesh using a cell-centered approach; the diffusive fluxes are calculated from the reconstructed states located on the center of each face of the control volumes $\check{V}_{i,j,k}$ of the dual mesh. This corresponds to the way the central and the diffusive fluxes of the JST scheme are implemented in ITSM3D [190].

The use of the dual-volume for the calculation of both the central and the diffusive terms would have the advantage that an exact cancellation between central and dissipation terms and full upwinding is obtained for supersonic flows. The approach used here is however favorable when the flow and the flow phenomena are not aligned with the grid. The separate calculation of the diffusive and central terms has furthermore the advantage that a hybrid Runge-Kutta scheme can be used, in which the former terms are not recalculated in every stage.

In the AUSM+ scheme the convective interface flux given by Eqs. (4.28) or (4.36) can be split into central and diffusive terms according to

$$\hat{\mathbf{E}}_{i+1/2} = \hat{\mathbf{E}}_{c,i+1/2}^{\text{CD}} + \hat{\mathbf{P}}_{i+1/2}^{\text{CD}} - \hat{\mathbf{d}}_{c,i+1/2} - \hat{\mathbf{d}}_{p,i+1/2}, \quad (4.46)$$

where the central terms are defined as

$$\begin{aligned} \hat{\mathbf{E}}_{c,i+1/2}^{\text{CD}} &= \frac{1}{2} a_{i+1/2}^S (M_i \Psi_i + M_{i+1} \Psi_{i+1}), \\ \hat{\mathbf{P}}_{i+1/2}^{\text{CD}} &= p_{1/2}^{\text{CD}} \cdot \mathbf{T}, \quad \mathbf{T} = [0, S_{\xi,x}, S_{\xi,\phi}, S_{\xi,r}, 0]^T, \quad p_{1/2}^{\text{CD}} = \frac{1}{2} (p_i + p_{i+1}). \end{aligned} \quad (4.47)$$

It should be noted that the vector $\hat{\mathbf{E}}_{c,i+1/2}^{\text{CD}}$ represents only a fully central term if the interface speed of sound $a_{i+1/2}$ is determined in a central fashion according to Eq. (4.44). With this definition of the central fluxes and the consistency property $\mathcal{P}^+(M) + \mathcal{P}^-(M) = 1$ it follows that the diffusion terms related to the discretization of the pressure term becomes

$$\begin{aligned} \hat{\mathbf{d}}_{p,1/2} &= \left[\frac{1}{2} (p_i + p_{i+1}) - \mathcal{P}^+(M_i) p_i - \mathcal{P}^-(M_{i+1}) p_{i+1} \right] \mathbf{T} \\ &= \left[\Delta \mathcal{P}(M_{i+1}) p_{i+1} - \Delta \mathcal{P}(M_i) p_i \right] \cdot \mathbf{T} \end{aligned} \quad (4.48)$$

with the function $\Delta \mathcal{P}(M) = \mathcal{P}^+ - \mathcal{P}^-$ defined as

$$\Delta \mathcal{P} = \begin{cases} \text{sign}(M), & |M| \geq 1, \\ \frac{1}{2} M [3 - M^2 + 4\alpha(M^2 - 1)^2], & |M| \leq 1, \end{cases} \quad (4.49)$$

which is in agreement with the result of Liou [166].

If the resulting interface Mach number $m_{1/2}$ is positive-semidefinite, then $m_{1/2}^-$ is vanishing and the diffusive part of the convective terms is obtained as

$$\begin{aligned} \hat{\mathbf{d}}_{c,1/2} &= \frac{1}{2} a_{i+1/2}^S [M_i \Psi_i + M_{i+1} \Psi_{i+1}] - a_{i+1/2}^S m_{i+1/2}^+ \Psi_i \\ &= a_{i+1/2}^S \left\{ \left[\left(\frac{1}{2} M_i - \mathcal{M}_i^+ \right) \Psi_i + \left(\frac{1}{2} M_{i+1} - \mathcal{M}_{i+1}^- \right) \Psi_{i+1} \right] + \mathcal{M}_{i+1}^- (\Psi_{i+1} - \Psi_i) \right\} \\ &= a_{i+1/2}^S \left\{ \frac{1}{2} [|\Delta \mathcal{M}(M_{i+1})| \Psi_{i+1} - |\Delta \mathcal{M}(M_i)| \Psi_i] + \mathcal{M}_{i+1}^- (\Psi_{i+1} - \Psi_i) \right\}, \end{aligned} \quad (4.50)$$

with $\mathcal{M}_i^+ = \mathcal{M}^+(M_i)$, $\mathcal{M}_{i+1}^- = \mathcal{M}^-(M_{i+1})$. To obtain the last expression, the consistency property $\mathcal{M}^+(M) + \mathcal{M}^-(M) = M$ was exploited. The Mach number function $|\Delta\mathcal{M}|$ is defined as

$$|\Delta\mathcal{M}| := \mathcal{M}^+ - \mathcal{M}^- = \begin{cases} |M|, & |M| \geq 1, \\ \frac{1}{2}(M^2 + 1) + 2\beta(M^2 - 1)^2, & |M| \leq 1. \end{cases} \quad (4.51)$$

Similarly, for negative semi-definite interface Mach numbers $m_{1/2}$ the convective dissipation becomes

$$\begin{aligned} \hat{\mathbf{d}}_{c,1/2} &= \frac{1}{2}a_{i+1/2}^S [M_i\Psi_i + M_{i+1}\Psi_{i+1}] - a_{i+1/2}^S m_{i+1/2}^- \Psi_{i+1} \\ &= a_{i+1/2}^S \left\{ \left[\left(\frac{1}{2}M_i - \mathcal{M}_i^+ \right) \Psi_i + \left(\frac{1}{2}M_{i+1} - \mathcal{M}_{i+1}^- \right) \Psi_{i+1} \right] - \mathcal{M}_i^+ (\Psi_{i+1} - \Psi_i) \right\} \\ &= \frac{1}{2}a_{i+1/2}^S \left\{ [\Delta\mathcal{M}(M_{i+1})\Psi_{i+1} - \Delta\mathcal{M}(M_i)\Psi_i] - \mathcal{M}_i^+ (\Psi_{i+1} - \Psi_i) \right\}. \end{aligned} \quad (4.52)$$

Since the function \mathcal{M}^+ is positive semi-definite and the function \mathcal{M}^- is negative semi-definite for all Mach numbers, the last term in both Eq. (4.50) and Eq. (4.52), represent an antidiffusive contribution. As will be shown later in this chapter, it will be useful to divide the convective dissipation vector $\hat{\mathbf{d}}_{c,1/2}$ into an essentially diffusive $\hat{\mathbf{d}}_{c,\text{edi},1/2}$ and an anti-diffusive part $\hat{\mathbf{d}}_{c,\text{atd},1/2}$:

$$\hat{\mathbf{d}}_{c,1/2} = \hat{\mathbf{d}}_{c,\text{edi},1/2} + \hat{\mathbf{d}}_{c,\text{atd},1/2}, \quad (4.53)$$

with the essentially diffusive part defined as

$$\hat{\mathbf{d}}_{c,\text{edi},1/2} = \frac{1}{2}a_{i+1/2}^S [\Delta\mathcal{M}(M_{i+1})\Psi_{i+1} - \Delta\mathcal{M}(M_i)\Psi_i] \quad (4.54)$$

and the antidiffusive contribution $\hat{\mathbf{d}}_{c,\text{atd},1/2}$ given by

$$\hat{\mathbf{d}}_{c,\text{atd},1/2} = \begin{cases} +a_{i+1/2}^S \mathcal{M}_{i+1}^- (\Psi_{i+1} - \Psi_i), & \forall m_{1/2} \geq 0, \\ -a_{i+1/2}^S \mathcal{M}_i^+ (\Psi_{i+1} - \Psi_i), & \forall m_{1/2} \leq 0. \end{cases} \quad (4.55)$$

For a vanishing interface Mach number $m_{1/2}$, the Mach numbers M_i and M_{i+1} must be equal in magnitude but opposite in sign. This follows from the symmetry property $-\mathcal{M}^-(-M) = \mathcal{M}^+(M)$ of the Mach number functions \mathcal{M}^\pm . In this case, both expressions of the anti-diffusive dissipation term in Eq. (4.55) are equal. It should however also be noted that in the special case that the Mach number M_i and M_{i+1} are equal in magnitude but are opposite in sign, the anti-diffusive dissipation fully cancels the dissipation term defined in Eq. (4.54); however in this case also the central part $\hat{\mathbf{E}}_c^{\text{CD}}$ of the convective fluxes vanishes.

In order to analyze the convective dissipation term, the Mach number variation over the interface is neglected, i.e., the validity of $M_{1/2} := M_i \approx M_{i+1}$ is assumed. With this supposition, the following relation

$$\hat{\mathbf{d}}_{c,1/2} = -\frac{1}{2}a_{1/2}^S |\Delta\mathcal{M}(M_{1/2})| \Delta\Psi_i + a_{1/2}^S |\mathcal{N}| (M_{1/2}) \Delta\Psi_i, \quad \Delta\Psi_i = \Psi_{i+1} - \Psi_i \quad (4.56)$$

with

$$|\mathcal{N}| = \frac{1}{4}(1 - M_m)^2 + \beta(M_m^2 - 1)^2, \quad M_m = \min(|M|, 1) \quad (4.57)$$

holds for both positive and negative Mach numbers $M_{1/2}$.

The first part of the dissipation term corresponds to the convective part of the dissipation of the CUSP scheme introduced by Jameson [129] if the constant a_0 in his scheme is set equal to $a_0 = 2\beta + 1/2$ and his modifications [130] for resolving stationary shocks sharply and capturing contact discontinuities are not taken into account. The second anti-diffusive part of the dissipation vanishes for $|M_{1/2}| \geq 1$.

A simple addition of both dissipation terms in Eq. (4.56) results in the following expression for the convective dissipation

$$\hat{\mathbf{d}}_{c,1/2} = -\frac{1}{2}a_{1/2}^S |M_{1/2}| \Delta \Psi_i. \quad (4.58)$$

Since the convective dissipation term for the original AUSM+ scheme vanishes for $M_{1/2} = 0$, measures must be taken in order to stabilize the scheme near stagnation points and walls. This point will be addressed in a later section.

4.6.3 Preconditioned AUSM+-scheme

In order for the AUSM+ dissipation to scale correctly at low Mach numbers preconditioning must be used. As shown by Edwards and Liou [78] attention must thereby be paid to how the dissipative contributions of the fluxes scale with the speed of sound. Furthermore, pressure-velocity coupling at low speed flows must be ensured. In this section their work is reviewed and it is explained which modifications were adopted in the preconditioned AUSM+ scheme that was implemented in the flow solver ITSM3D.

To attain a correct scaling of the flux terms in the low Mach number limit, the physical Mach numbers M_i and M_{i+1} used in the flux splitting must be substituted with the effective numerical Mach number M'_i and M'_{i+1} of the preconditioned Navier-Stokes equations, respectively. These numerical Mach numbers are given by

$$M'_i = \frac{\hat{v}_{\xi,i}}{a'_{i+1/2}}, \quad M'_{i+1} = \frac{\hat{v}_{\xi,i+1}}{a'_{i+1/2}}, \quad (4.59)$$

where a' represents the numerical speed of sound and \hat{v}_{ξ} the contravariant velocity component in the ξ -direction of the grid. The numerical speed of sound $a'_{1/2}$ at the interface $i + 1/2$ is defined to be

$$a'_{1/2} = \frac{1}{2}(a'_i + a'_{i+1}), \quad a' = \frac{\sqrt{\mathbf{v} \cdot \mathbf{S}_{\xi} \left(1 - \frac{d}{d'}\right)^2 + 4 \frac{\rho h_T}{d'} \|\mathbf{S}_{\xi}\|^2}}{\left(1 + \frac{d}{d'}\right) \|\mathbf{S}_{\xi}\|}. \quad (4.60)$$

For $M \rightarrow 1$ preconditioning is successively turned off and $d' \rightarrow d$ so that the numerical speed of sound a' for $|M| \geq 1$ equals the physical speed of sound a . It is important to be aware that regardless of how a' may be calculated, the product of a' and M' must give the physical velocity component \hat{v}_{ξ} in ξ -direction for consistency reasons.

The introduction of a numerical speed a' and an accordingly defined Mach number M' is not sufficient for using the AUSM+ scheme for the simulation of low Mach number flow. This will be shown in the following by carrying out an analysis of the dissipative terms according to Edwards and Liou [78]. Based on this analysis, appropriate measures to enforce the pressure-velocity coupling will be derived.

To analyse the numerical dissipation resulting from the discretization of the pressure with the numerical speed of sound a' and the scaled Mach number M' , the effective interface pressure given in Eq. (4.35) is in accordance with Edwards and Liou [78] for subsonic flows written out as

$$p_{i+1/2} = \underbrace{\frac{1}{2}(p_i + p_{i+1})}_{p^{CD}} - \underbrace{\frac{1}{2}\sigma_p(M'_i + M'_{i+1})(p_{i+1} - p_i)}_{d_{p,1}} - \underbrace{\frac{1}{2}\sigma_p(p_i + p_{i+1})(M'_{i+1} - M'_i)}_{d_{p,2}} + \mathcal{O}(\delta p \cdot |\Delta \mathcal{P}|) \quad (4.61)$$

with the factor

$$\sigma_p = 3 + 4\alpha + \mathcal{O}(M'^2). \quad (4.62)$$

As long as $\alpha > -3/4$ the second order terms in the last expression can be neglected for low Mach numbers. To be able to analyze their scaling with respect to the Mach number level, the dissipative terms are normalized with the reference quantities $u^\dagger, \varrho^\dagger, p^\dagger$. This yields the following expression for the first dissipation term:

$$d_{p,1}^* = \frac{1}{2}\sigma_p(M'_i + M'_{i+1})(p_{i+1}^* - p_i^*) = \sigma_p \bar{M}' \cdot \delta p^*. \quad (4.63)$$

For low Mach number, steady state flow it should be noted that the spatial pressure difference δp^* represents a difference of the second order pressure. These kind of pressure differences are connected to the kinetic, incompressible part of the velocity field. For steady state problems, these differences can neither be linked to global pressure variations (zeroth order pressure) nor to temporal pressure fluctuations related to the propagation of acoustic waves (first order pressure). The reader may refer to Chapter D.1 or to the work of Müller [194] for a discussion on the role of the zeroth, first and second order pressure. As elaborated in Appendix A it should also be noted that the use of time-derivative preconditioning also ensures that the temporal pressure variations scale in the same order as the advection terms for low Mach number flow. Thus, the pressure differences δp^* appearing in Eq. (4.63) are for low Mach number flow proportional to the variation of the kinetic energy of the flow field, i.e., $\delta p^* \sim \delta(\varrho^* v^{*2})$. In this case the dissipation term $d_{p,1}^*$ obviously scales correctly in the order of the convective scales:

$$d_{p,1}^* = \sigma_p \bar{M}' \cdot \delta p^* \sim \bar{M}' \cdot \delta p^* \sim \bar{M}' \cdot \delta(\varrho^* v^{*2}) = \mathcal{O}(1). \quad (4.64)$$

The term $d_{p,2}$ in Eq. (4.61) can for ideal gas flow be written as

$$d_{p,2}^* = \frac{1}{2}\sigma_p(p_i^* + p_{i+1}^*)(M'_{i+1} - M'_i) \sim \sigma_p \bar{\varrho}^* \bar{a}^{*2} \delta M' = \sigma_p \bar{\varrho}^* / \bar{M}^2 \cdot \delta M'. \quad (4.65)$$

Since $\delta M'$ scales in the order of unity, the dissipation term $d_{p,2}^*$ scales inversely proportional to the square of the Mach number, i.e., $d_{p,2}^* = \mathcal{O}(\bar{M}^{-2})$.

In order to be able to treat each of the parts $d_{p,1}$ and $d_{p,2}$ of the pressure diffusion separately and so alleviate the wrong scaling of the second part of the pressure dissipation term, the following Mach numbers

$$\begin{aligned}\check{M}'_i &= \frac{1}{2} [(1 + \bar{M}_r^2)M'_i + (1 - \bar{M}_r^2)M'_{i+1}], \\ \check{M}'_{i+1} &= \frac{1}{2} [(1 - \bar{M}_r^2)M'_i + (1 + \bar{M}_r^2)M'_{i+1}]\end{aligned}\quad (4.66)$$

as suggested by Edwards and Liou [78] should be used for the flux splitting, where \bar{M}_r represents a reference Mach number. Generally, the reference Mach number has to be calculated locally as the ratio of the pseudoacoustic velocity a' to the physical sonic speed a :

$$\bar{M}_r = \bar{a}'/\bar{a}. \quad (4.67)$$

The use of a Mach number defined by Eq. (4.66) and (4.67) for the flux splitting makes both parts of the pressure dissipation terms scale correctly for low Mach number, ideal gas flow:

$$\begin{aligned}d_{p,1}^* &= \frac{1}{2}\sigma_p(\check{M}'_i + \check{M}'_{i+1})(p_{i+1}^* - p_i^*) = \frac{1}{2}\sigma_p(M'_i + M'_{i+1})(p_{i+1}^* - p_i^*) \\ &\sim \bar{M}' \cdot \delta p^* \sim \bar{M}' \cdot \delta(\bar{\rho}^* u^{*2}) = \mathcal{O}(1), \\ d_{p,2}^* &= \frac{1}{2}\sigma_p(p_i^* + p_{i+1}^*)(\check{M}'_{i+1} - \check{M}'_i) = \frac{1}{2}\sigma_p(p_i^* + p_{i+1}^*)(M'_{i+1} - M'_i) \cdot \bar{M}_r^2 \\ &\sim \bar{p}^* \bar{M}_r^2 \cdot \delta M' \sim \bar{\rho}^* \bar{a}^{*2} \bar{M}_r^2 \cdot \delta M' \sim \bar{\rho}^* \bar{M}_r^2 / \bar{M}^2 \cdot \delta M' = \mathcal{O}(1).\end{aligned}\quad (4.68)$$

For an incompressible fluid or compressible flow in the low Mach number limit the reference Mach number goes to zero, hence the left and right Mach numbers \check{M}'_i and \check{M}'_{i+1} become identical. Thus, in this case the expression in Eq. (4.58) for the convective dissipation is exact, since the assumption of a vanishing Mach number variation over the interfaces is fulfilled. This means that the convective dissipation terms completely vanish as the velocity magnitude approaches zero, which is a desirable property for resolving contact discontinuities or boundary layers in special. However, this property is responsible for raising the possibility of odd-even decoupling with vanishing flow speed. To alleviate this problem Edwards and Liou [78] suggest adding one element of the pressure diffusion used in the AUSMDV scheme to enhance the pressure-velocity coupling at low speeds. In this case the pressure diffusion term $\dot{m}_{D,i+1/2}$ defined as

$$\dot{m}_{D,i+1/2} = -a_{i+1/2}^S |\Delta \mathcal{D}(M_i, M_{i+1})| \frac{p_{i+1} - p_i}{p_i/\varrho_i + p_{i+1}/\varrho_{i+1}} \quad (4.69)$$

with

$$|\Delta \mathcal{D}(M_i, M_{i+1})| = \mathcal{D}^+ - \mathcal{D}^-, \quad \mathcal{D}^+ = M_{(4)}^+ - M_{(1)}^+, \quad \mathcal{D}^- = M_{(4)}^- - M_{(1)}^- \quad (4.70)$$

and $\beta = 1/8$ is added to the interface mass flux defined in Eq. (4.30), so that the resulting interface mass flux reads as

$$\dot{m}_{i+1/2} = a_{i+1/2}^S (\Psi_i m_{i+1/2}^+ + \Psi_{i+1} m_{i+1/2}^-) + \dot{m}_{D,i+1/2}. \quad (4.71)$$

The function $|\Delta\mathcal{D}|$ for $\beta = 1/8$ becomes

$$|\Delta\mathcal{D}| = 3/4 - \frac{1}{2}(|M_{m,i}| + |M_{m,i+1}|) + \frac{1}{8}(M_{m,i}^4 + M_{m,i+1}^4), \quad M_m = \min(1, M). \quad (4.72)$$

The function $|\Delta\mathcal{D}|$ attains its maximum value of $3/4$ for vanishing Mach numbers M_i, M_{i+1} and reduces to zero for supersonic flows.

In the low Mach number limit the normalized pressure diffusion term scales as

$$\dot{m}_{D,i+1/2}^* = -\frac{3}{4}a_{i+1/2}^{*S} \frac{p_{i+1}^* - p_i^*}{p_i^*/\varrho_i^* + p_{i+1}^*/\varrho_{i+1}^*} \sim \frac{1}{\bar{a}^*} \delta p^* \sim \frac{1}{\bar{a}^*} \delta(\varrho^* u^{*2}) = \bar{M} \delta(\varrho^* u^{*2}), \quad (4.73)$$

which means that this term will not provide any effect for low Mach numbers if not scaled differently.

When preconditioning is used, the interface speed of sound $a_{i+1/2}$ is replaced with the numerical speed of sound $a'_{i+1/2}$, which for low Mach number flow scales in the order of the convective velocity v . Thus, when preconditioning is used for the simulation of low Mach number flow, the pressure diffusion term scales as $\dot{m}_{D,i+1/2}^* \sim \frac{v^*}{\bar{a}^{*2}} \delta(\varrho^* u^{*2}) = \bar{M}^2 \delta(\varrho^* u^{*2})$. To achieve a correct scaling, the pressure diffusion term has to be scaled with $1/M_r^2$ with M_r defined according to Eq. (4.67). To also ensure that the pressure diffusion terms are shut off rapidly enough with an increasing Mach number level, Edwards and Liou suggests scaling the pressure term with the factor $d_M = (1 - M_r^2)/M_r^2$. With this scaling the pressure diffusion term reads as follows

$$\dot{m}_{D,i+1/2} = -a'_{i+1/2}{}^S \frac{1 - M_{r,i+1/2}^2}{M_{r,i+1/2}^2} \cdot |\Delta\mathcal{D}(M'_i, M'_{i+1})| \cdot \frac{p_{i+1} - p_i}{p_i/\varrho_i + p_{i+1}/\varrho_{i+1}}. \quad (4.74)$$

For low Mach number flow the term $\dot{m}_{D,i+1/2}$ scales in dimensional form in the order of the variations of the mass flux ($\mathcal{O}[\delta(\varrho v)]$); in dimensionless form this term scales in the order of unity, which is correct.

In the case of incompressible flow the scaling term $(1 - M_r^2)/M_r^2$ is not used since there is no relation between the terms p/ρ in Eq. (4.69) and the sonic speed, i.e., these terms must not be compensated for anymore in order to obtain a correct scaling of the diffusion terms. Since an incompressible flow field is not affected by the magnitude of the pressure but only by spatial or temporal variations in the pressure, the pressure difference term in Eq. (4.69) should be normalized with the local value for the dynamic pressure $p_i^{\text{dyn}} = (\varrho v^2)_i$. Thus, for incompressible flow, the pressure diffusion term is calculated as follows

$$\dot{m}_{D,i+1/2} = -\frac{a'_{i+1/2}}{V_{i+1/2}^2} \cdot |\Delta\mathcal{D}(M'_i, M'_{i+1})| \cdot \|\mathbf{S}_\xi\| \cdot (p_{i+1} - p_i). \quad (4.75)$$

For incompressible flows, the Mach number M' based on the numerical speed of sound a' is constant as long as the reference velocity V_r used for scaling the preconditioning parameter ϱ'_p is based on the local velocity scale, i.e.,

$a' = \sqrt{5v^2}$ and $M' = 1/\sqrt{5}$. In this case the Mach number function $|\Delta\mathcal{D}|$ can be approximated to $|\Delta\mathcal{D}| \approx 0.31$. With $a'_{i+1/2}$ scaling in the order of the magnitude of convective velocity v , the pressure diffusion term, which is defined in Eq. (4.75) for constant density flow, scales in the order of the mass flux variations in the flow field, which is appropriate.

4.6.4 Robustness issues

With the original formulation of the anti-diffusive part of the convective dissipation as given in Eq. (4.55), the net dissipation vanishes completely in the low Mach number limit. From a theoretical viewpoint this is ideal but is detrimental to the robustness of the scheme. In order to ensure stability of a given solution scheme for practical problems, some dissipation should always be added to the central terms. This is accomplished by a proper scaling of the anti-diffusive term $\hat{\mathbf{d}}_{c,\text{atd},1/2}$.

To obtain the best compromise between robustness and low-diffusivity of the solution scheme on stretched grids, the applied part $\hat{\mathbf{d}}_{c,\text{atd},1/2,\xi}^{\text{apl}}$ of the anti-diffusive dissipation for the ξ -direction of the mesh is determined as

$$\hat{\mathbf{d}}_{c,\text{atd},1/2,\xi}^{\text{apl}} = \tilde{\omega}_{\text{AUSM},\xi} \cdot \hat{\mathbf{d}}_{c,\text{atd},1/2,\xi} \quad (4.76)$$

with the scaling parameter $\tilde{\omega}_{\text{AUSM}}$ defined as

$$\tilde{\omega}_{\text{AUSM},\xi} = 1 - \omega_{\text{AUSM}} \cdot \gamma_{1/2,\xi}. \quad (4.77)$$

The term ω_{AUSM} is a user defined parameter ($\omega_{\text{AUSM}} \in [0, 1]$) and the second quantity $\gamma_{1/2,\xi}$ is given by

$$\gamma_{1/2,\xi} = \min \left[1, \max \left(\frac{\sigma_\eta}{\sigma_\xi}, \frac{\sigma_\zeta}{\sigma_\xi} \right) \right] \quad (4.78)$$

as a function of the spectral radii σ_ξ , σ_η and σ_ζ of the inviscid flux Jacobians in ξ -, η - and ζ -direction, respectively. The scaling of the anti-diffusive terms in the η - and ζ -direction is given analogously. This approach is similar to that one used by Radespiel and Kroll [216] for the regular AUSM-scheme with the difference that in the current work the anti-diffusive term is controlled while they limit the Mach number used as argument for the dissipation function. If the parameter ω_{AUSM} is set to zero, the original AUSM+ dissipation is recovered. For finite values of this parameter, the amount of anti-diffusion added can be controlled, which improves the damping behaviour of the solution scheme but does not degrade the ability of the original dissipation scheme for resolving boundary layers accurately.

With this scaling, the anti-diffusive terms are primarily contributing to the dissipation at the largest faces of the cells. In viscous flow simulations, the grid is usually clustered in the wall normal direction. If the ξ -direction of the grid corresponds to this direction, the cell face area $\|\mathbf{S}_\xi\|$ will typically be larger than the cell face areas $\|\mathbf{S}_\eta\|$ and $\|\mathbf{S}_\zeta\|$. Since the variations of the

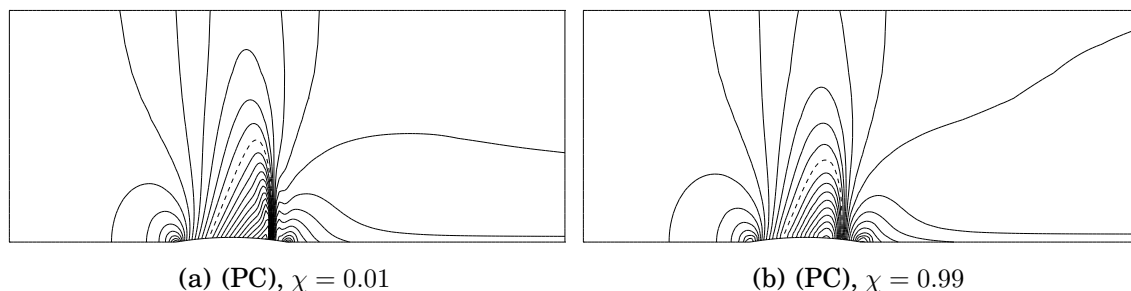


Figure 4.1: Calculated Mach number contours ($\Delta M = 0.025$) of the transonic Ni-Bump test case ($M_{is} = 0.85$) using the preconditioned JST-scheme with the original [131] and the modified pressure switch [268]

velocities within a cell are negligible, the corresponding spectral radius σ_ξ will consequently be larger than σ_η and σ_ζ . Thus, anti-diffusive terms will be reduced in grid directions parallel to the wall but will be retained in the wall-normal direction so that the original non-smearing behaviour of the AUSM scheme is preserved.

4.7 Computational results

4.7.1 Ni-Bump test case

To demonstrate the effect of the improved pressure switch of Swanson and Turkel, which is described in Chapter 4.1, the inviscid flow in the Ni-Bump test case [226] was simulated for an isentropic Mach number of $M_{is,a} = 0.85$. A description of the grid and the boundary conditions used, can be found in Chapter 3.4.1, where the test case was used to assess the preconditioning scheme.

In Fig. 4.1 the calculated Mach number contours are shown for two different values of the parameter χ of the pressure switch defined in Eq. (4.1). It should be noted that when the parameter χ of the modified pressure switch is set to unity the solution scheme should obtain TVD-properties [268]. The new pressure switch reverts to the original one for a value $\chi = 0$. From Fig. 4.1a it is apparent that a value of $\chi = 0$ for the pressure switch leads to overshoots of the pressure around the shock. With a full activation of the modified form of the pressure switch ($\chi = 0.99$), the wiggles in the vicinity of the shock are prevented as can be seen from Fig. 4.1b. Obviously, the modified pressure switch is a suitable means to ensure monotone pressure distributions in transonic, inviscid flow simulations with the JST scheme.

4.7.2 Flat plate laminar boundary layer

As a test case for assessing the ability of the different dissipation schemes to resolve viscous flows, a laminar boundary layer developing over a flat blade at

zero incidence was chosen. In the investigated set-up of the case the computational domain is rectangular with the inflow and outflow boundary located directly at the leading edge and the trailing edge of the flat plate, respectively. Figure 4.2 provides an overview over the geometry modeled and the boundary conditions applied. The grids used consist of $49 \times 3 \times 73$ and $97 \times 3 \times 145$ grid points in x -, ϕ - and r -direction, respectively. The mesh points in the stream-wise direction and in the direction normal to the wall were clustered with a stretching factor of 1.015% in order to provide an adequate resolution of the boundary layer and of the flow near the leading edge.

The results of the simulations in which the fluid was modeled as incompressible and those in which the fluid was modeled as an ideal gas were nearly identical. For the sake of brevity, only the latter ones are presented in the following. The ratio of the total inlet pressure $p_{0,e}$ to the static outlet pressure p_a was chosen to give a low isentropic outlet Mach number ($M_{is,a} = 0.136$). Thus, the flow field can be considered as incompressible, which makes a comparison of the computed variables with the theoretical Blasius solution meaningful.

In Figs. 4.3 and 4.4 the simulated dimensionless tangential velocity $u^* = u/U_\infty$ is shown as a function of the normalized wall distance $\eta = y\sqrt{\text{Re}_x}/x$ gained with the different dissipation schemes on the fine grid. The velocity distributions are evaluated at the end of the plate; the numerical solution obtained with the current grid is self-similar from the middle of the plate and onwards in the downstream direction. Plots of the solutions obtained with the AUSM type dissipation and Roe's Characteristic Upwind Dissipation scheme are given in Fig. 4.3a. The free parameters of these schemes were defined such that these schemes yield low-diffusive solutions; the actual values of the parameters are listed in Table 4.1. Evidently, these schemes are able to reproduce the Blasius solution quite well.

In order to distinguish more clearly between different dissipation schemes with regard to their resolution capability, simulations were also run on the coarser grid. The corresponding results are displayed in Figs. 4.5 to 4.8.

Obviously, the AUSM dissipation and Roe's Characteristic Upwind Dissipation scheme exhibit the best performance of all dissipation models considered in the current work, when the parameters of these schemes are set such that corresponding dissipation terms almost vanish as the Mach number approaches zero. In contrast to the results produced by the dissipation schemes based on fourth order differences (JST and JSTMatd), the AUSM dissipation scheme and the Characteristic Upwind Dissipation scheme do not result in an overshoot of the normalized tangential velocities. However, even though the Matrix Dissipation Scheme fails to provide a non-monotone solution, it clearly outperforms the scalar JST-scheme.

From Fig. 4.6 it is seen that the preconditioned JST-scheme obviously exhibits a less diffusive behaviour than the non-preconditioned one, even though a higher value for $k^{(4)}$ was used in the preconditioned solution scheme.

In Figs. 4.8a and 4.8b the solutions obtained with the scalar JST scheme for the extreme values $\chi = 0.01$ and $\chi = 0.99$ (TVD) of the pressure switch

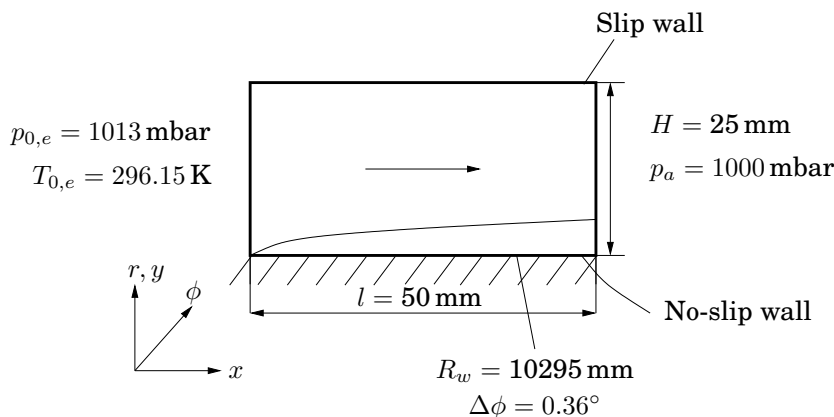


Figure 4.2: Geometry and boundary conditions of the flat plate laminar boundary layer test case

Scheme	Parameters	Limiter
JSTLoD(NonPC)	$k^{(4)} = 0.015$	-
JST(NonPC)	$k^{(4)} = 0.03$	-
JSTLoD	$k^{(4)} = 0.03 / k^{(4)} = 0.015$ (TVD)	-
JST	$k^{(4)} = 0.05$	-
JSTMatdLoD	$k^{(4)} = 0.015, V_l = 0.3, V_n = 0.4$	-
JSTMatd	$k^{(4)} = 0.05, V_l = 0.3, V_n = 0.4$	-
JSTMatdHiD	$k^{(4)} = 0.05, V_l = 0.5, V_n = 0.5$	-
CharUpwDissLoD	$V_l = 0.02, V_n = 0.02$	v. Albada
CharUpwDiss	$V_l = 0.1, V_n = 0.1$	v. Albada
AUSM	$\omega_{\text{AUSM}} = 0.5, \alpha = 3/16, \beta = 1/8$	v. Albada
AUSMLoD	$\omega_{\text{AUSM}} = 0.1, \alpha = 3/16, \beta = -1/16$	v. Albada

Table 4.1: Values of the parameters used in the dissipation schemes

parameter are depicted. The pressure switch has only a small effect on the solution since the pressure gradient normal to the wall is negligible. This shows that a switch based on the pressure alone is not suitable for all kinds of flows.

4.7.3 Supersonic flow through a row of wedges

To validate the preconditioned solution scheme for supersonic flow and to assess the shock resolution capability of the different dissipation schemes, the supersonic flow through a row of wedges was simulated.

The geometry and the boundary conditions of the test case are given in Fig. 4.9. As indicated, air flow enters the configuration with a Mach number of $M_e = 2$. With the assumption that the flow is inviscid, it can be shown by using basic aerodynamical arguments, that an oblique shock starts at the tip of each wedge, hits the lower wall of the neighbouring wedge and is reflected back to the wedge from which it originated. Under the given boundary conditions the

reflected shock hits the corner of the wedge and gets canceled there.

The computational grid is shown in Fig. 4.10 and it consists of $169 \times 3 \times 33$ grid points. With the prescription of an inlet Mach number of $M_e = 2$ the simulated shock impinged on the wall behind the corner, which led to additional reflections of the shock in the channel between the wedges. To compensate for numerical dissipation and to ensure that the shock actually hits the corner and gets annihilated there, the inlet Mach number used in the simulations was lowered to $M_e = 1.985$.

In Fig. 4.11 the simulated static pressure contours obtained by using the JST scheme ($\chi = 0.01$) with and without preconditioning are plotted for a radial height of $r = 1060$ mm in dependence of the axial position. The difference between the results is marginal. Thus, it is once more shown that preconditioning does not negatively affect the shock capturing properties of the JST-scheme.

A comparison of the solutions obtained with the JST-scheme and the JST-based matrix dissipation for the extreme values $\chi = 0.01$ and $\chi = 0.99$ (TVD) of the pressure switch parameter is given in Fig. 4.12. Obviously, the solutions obtained with the scalar JST-scheme and with the JST-switched Matrix Dissipation scheme are monotone when the pressure switch parameter is set to $\chi = 0.99$. The use of the original pressure switch ($\chi = 0.01$) leads to a less diffusive behaviour and larger gradients in the solution, but results in unphysical oscillations. It should be noted, that the robustness of the solution scheme improves with an increasing value of this parameter; when the matrix dissipation in this test case was used with $\chi = 0.01$ the other parameters V_l , V_n and $k^{(4)}$ had to be increased in order to obtain a stable integration. Nevertheless, independent of the setting of the pressure switch parameter χ , the matrix dissipation scheme clearly leads to a better resolution of shocks than the scalar scheme does.

In Fig. 4.13 the results obtained with the Characteristic Upwind Dissipation scheme of Roe, the AUSM dissipation scheme and the matrix dissipation scheme are compared. Of the schemes compared, the JST-switched matrix dissipation leads to the largest gradients, but at the cost that oscillations are produced in the solution. The Roe as well as the AUSM dissipation scheme lead to a nearly monotone solution; both schemes are less diffusive than the matrix-dissipation scheme when the parameter of the pressure switch is set to $\chi = 0.99$.

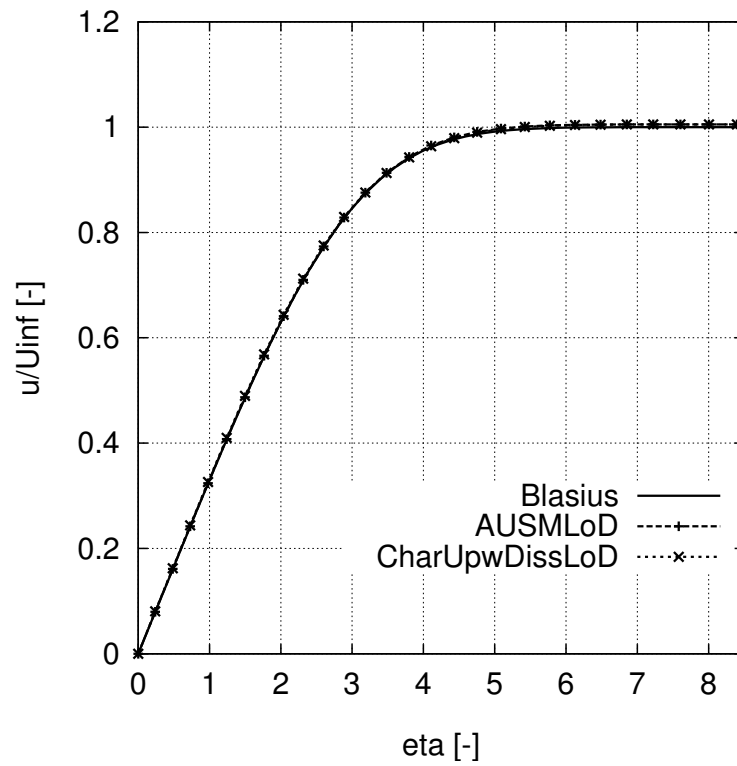
For this test case, the AUSM dissipation model led to the best compromise between robustness, shock resolution ability and monotonicity of the solution scheme. For a comparison of the most and the least diffusive scheme that did not lead to unphysical oscillations in the vicinity of the shock, the static pressure field obtained with the AUSM+ dissipation scheme and the solution gained with the scalar JST-scheme (TVD) are plotted in Fig. 4.14.

4.7.4 Low-speed turbine

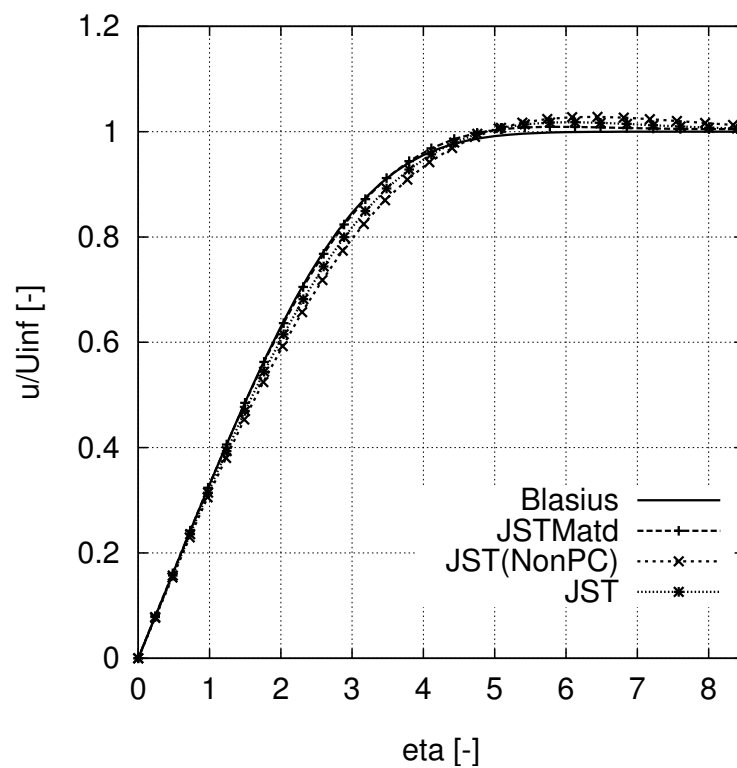
To further assess the performance of the dissipation schemes, the low-speed multistage turbomachinery test case already presented in Chapter 3.4.4 was simulated using the various dissipation schemes presented above.

In Figs. 4.15a and 4.15b the results for the JST Matrix Dissipation scheme, Roe's Characteristic Upwind Dissipation scheme, and the AUSM+ dissipation are compared. These schemes have been used in conjunction with time-derivative preconditioning where the fluid was modelled as an ideal gas. The capability of these schemes to resolve the flow features are better than that of the preconditioned scalar JST scheme; for the results obtained with the latter scheme with and without the use of preconditioning, the reader may refer to Chapter 3.4.4.

In this case, the ability to resolve secondary flow effects appears to be similar for the JST-switched matrix dissipation ($\chi = 0.99$), the AUSM dissipation, and the Characteristic Upwind Dissipation scheme. However, as can be seen from Fig. 4.16, the Characteristic Upwind Dissipation scheme and the AUSM dissipation scheme, which both are applying limiters, do not generate overshoots of the solution variables in the vicinity of the boundary layers like the JST-type of schemes do. Thus, it can also for this test case be concluded that the upwind-biased dissipation schemes are superior to the ad hoc JST dissipation techniques.

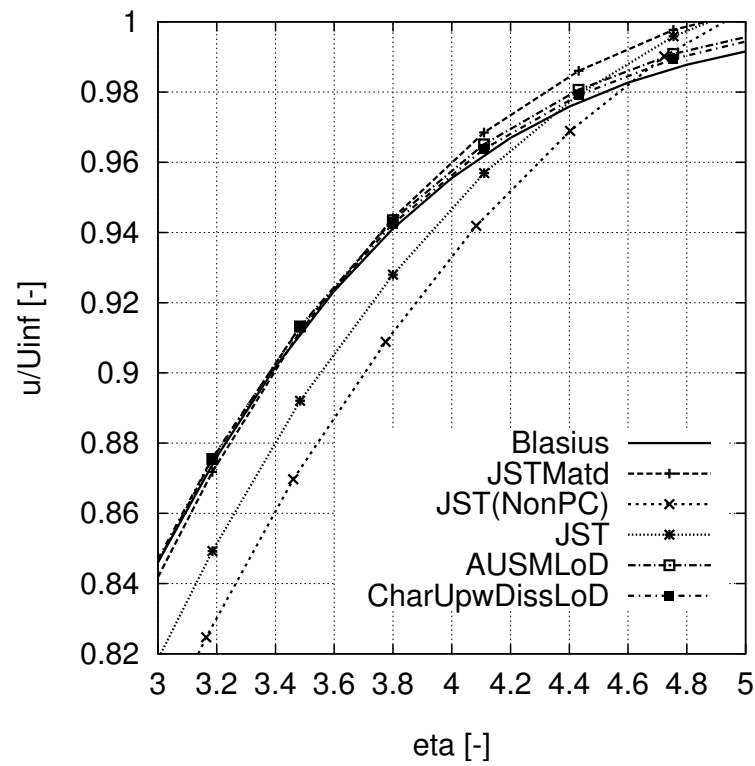


(a)



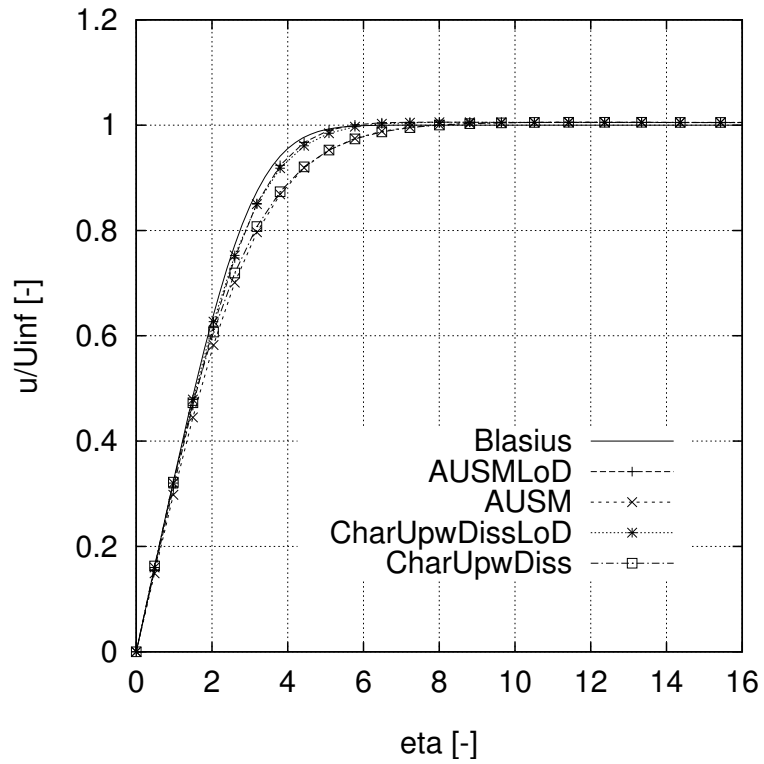
(b)

Figure 4.3: Laminar flow over a flat plate: Simulated normalized tangential velocity $u^* = u/U_{\infty}$ over the normalized wall distance $\eta = y\sqrt{\text{Re}_x}/x$ in dependence of the dissipation scheme on the fine grid with $97 \times 3 \times 145$ nodes

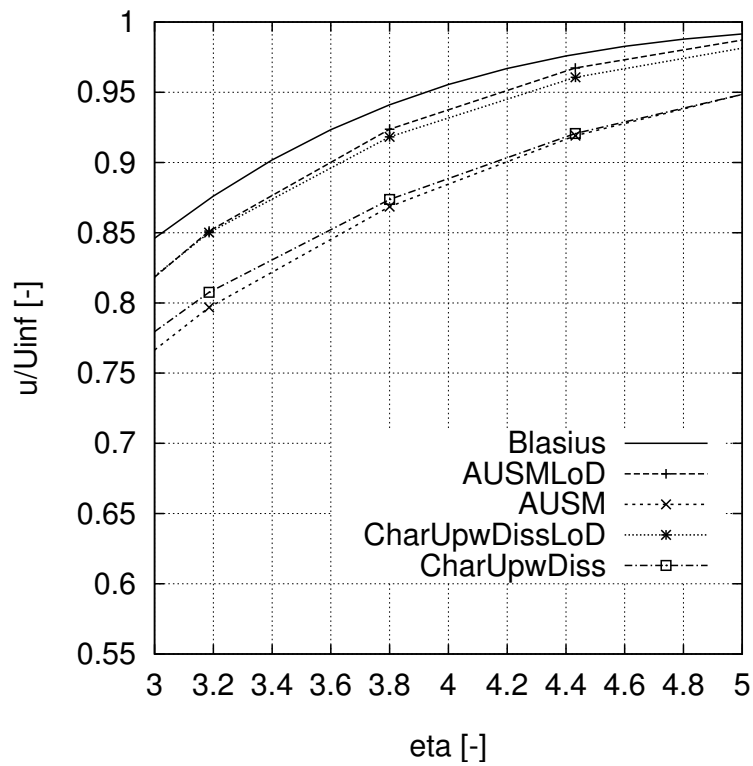


(a) Close-up

Figure 4.4: Laminar flow over a flat plate: Simulated normalized tangential velocity $u^* = u/U_\infty$ over the normalized wall distance $\eta = y\sqrt{\text{Re}_x}/x$ in dependence of the dissipation scheme on the fine grid with $97 \times 3 \times 145$ nodes

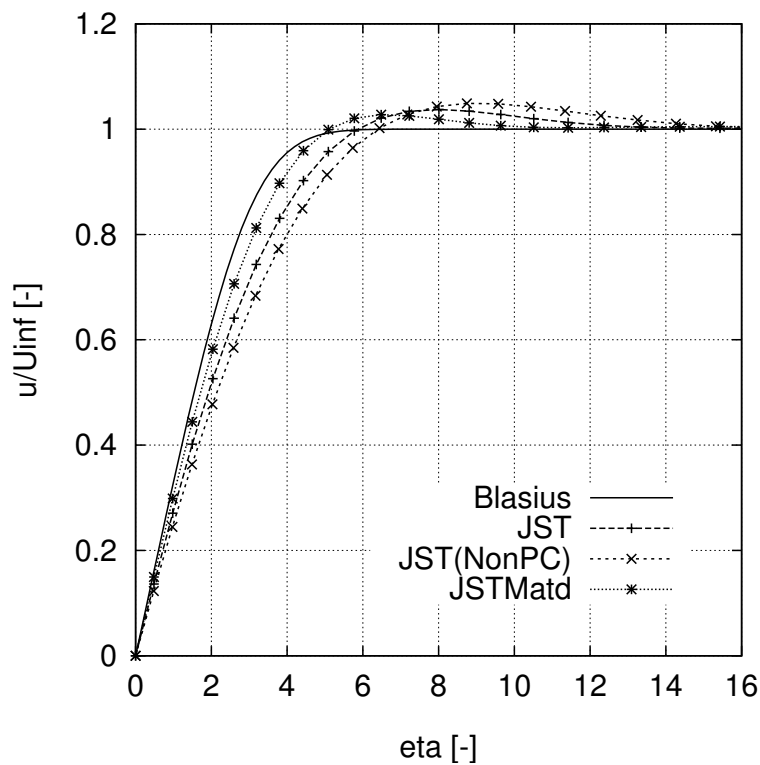


(a)

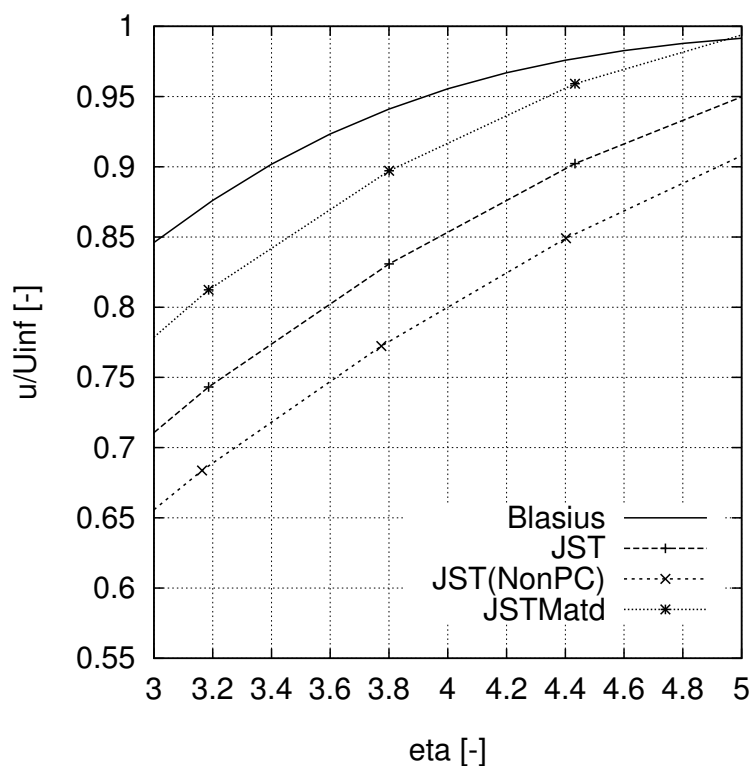


(b) Close-up

Figure 4.5: Laminar flow over a flat plate: Simulated normalized tangential velocity $u^* = u/U_\infty$ over the normalized wall distance $\eta = y\sqrt{\text{Re}_x}/x$ in dependence of the dissipation scheme on the coarse grid with $49 \times 3 \times 73$ nodes

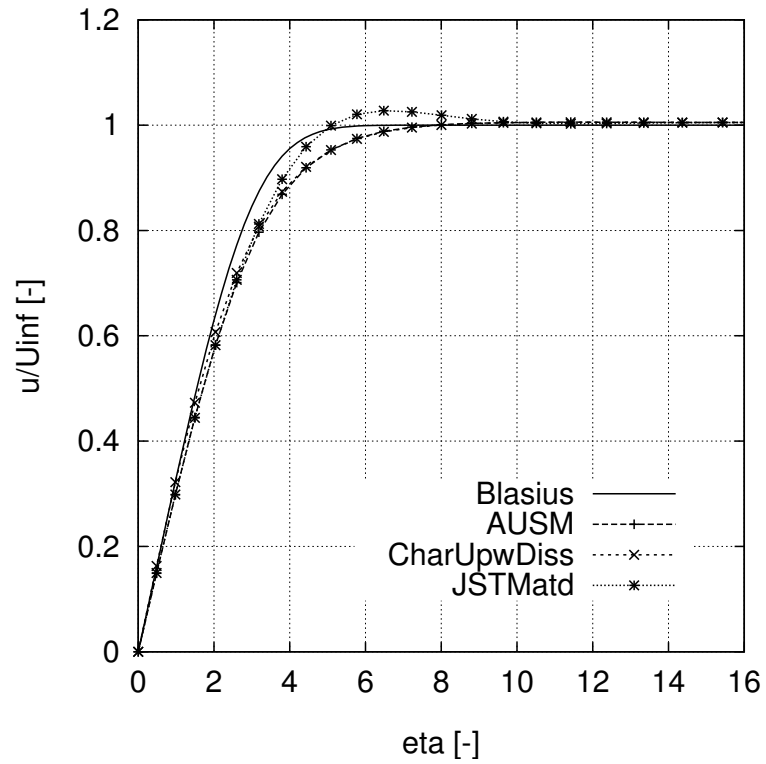


(a)

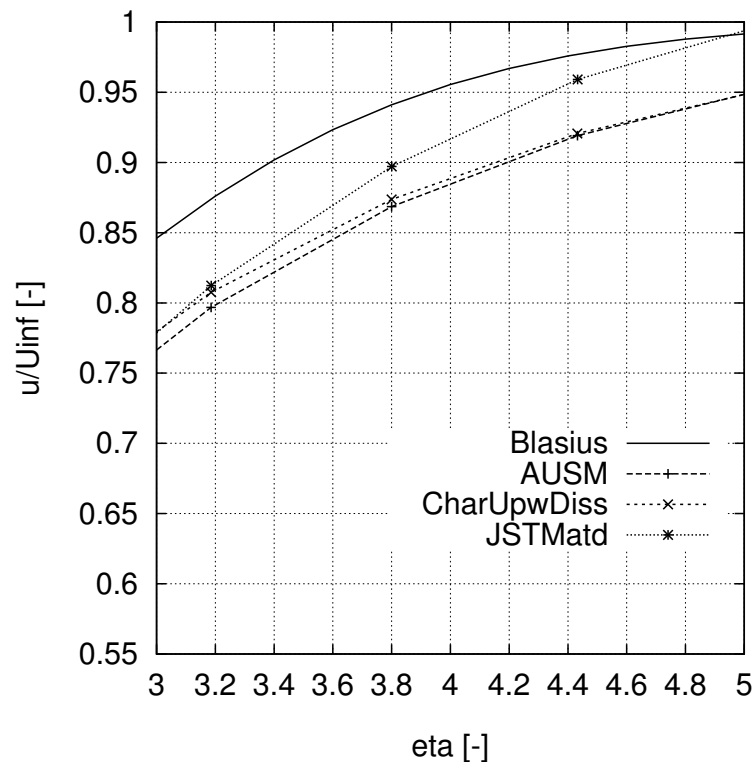


(b) Close-up

Figure 4.6: Laminar flow over a flat plate: Simulated normalized tangential velocity $u^* = u/U_{\infty}$ over the normalized wall distance $\eta = y\sqrt{\text{Re}_x}/x$ in dependence of the dissipation scheme on the coarse grid with $49 \times 3 \times 73$ nodes

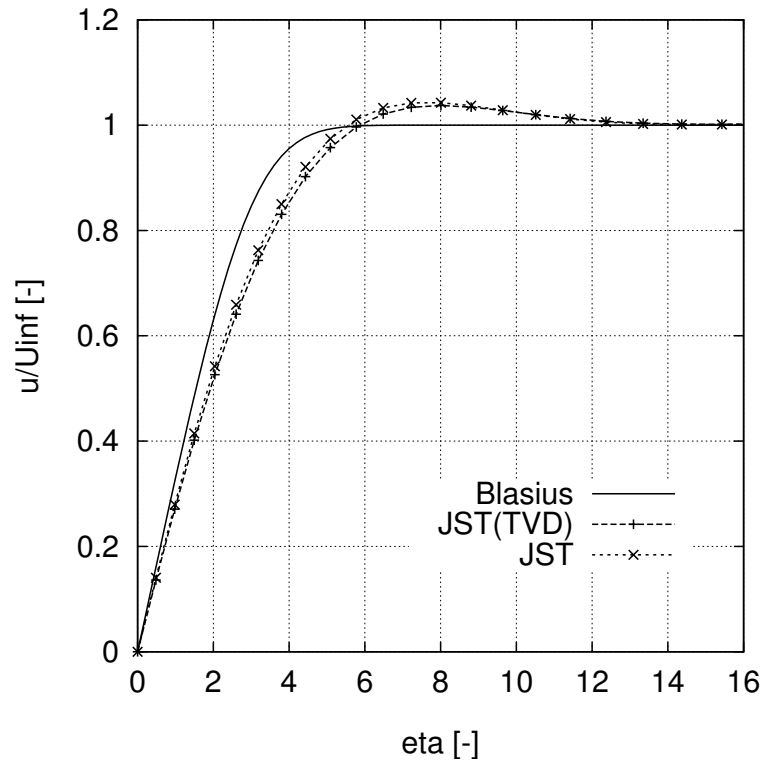


(a)

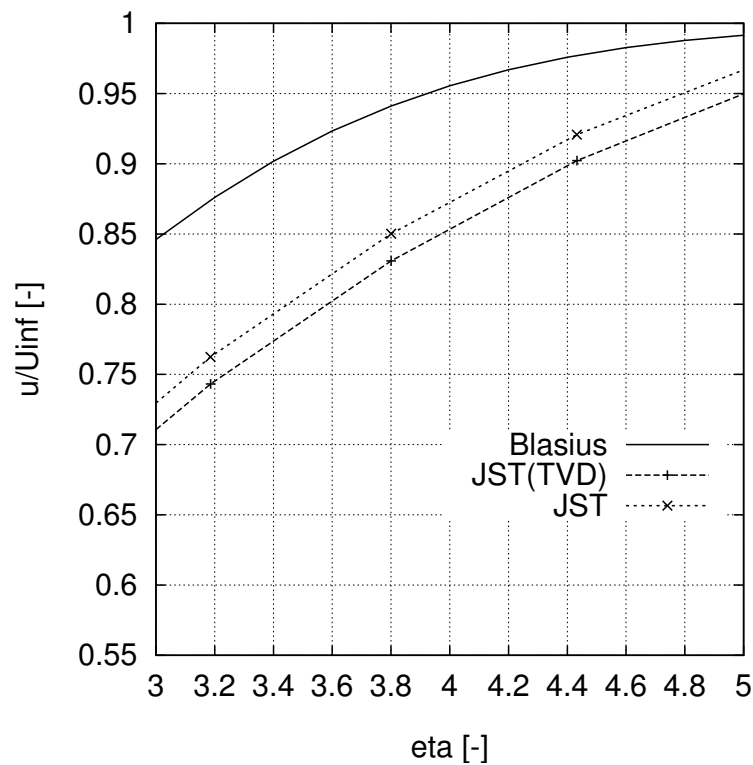


(b) Close-up

Figure 4.7: Laminar flow over a flat plate: Simulated normalized tangential velocity $u^* = u/U_\infty$ over the normalized wall distance $\eta = y\sqrt{\text{Re}_x}/x$ in dependence of the dissipation scheme on the coarse grid with $49 \times 3 \times 73$ nodes



(a)



(b) Close-up

Figure 4.8: Laminar flow over a flat plate: Simulated normalized tangential velocity $u^* = u/U_{\infty}$ over the normalized wall distance $\eta = y\sqrt{\text{Re}_x}/x$ in dependence of the dissipation scheme on the coarse grid with $49 \times 3 \times 73$ nodes

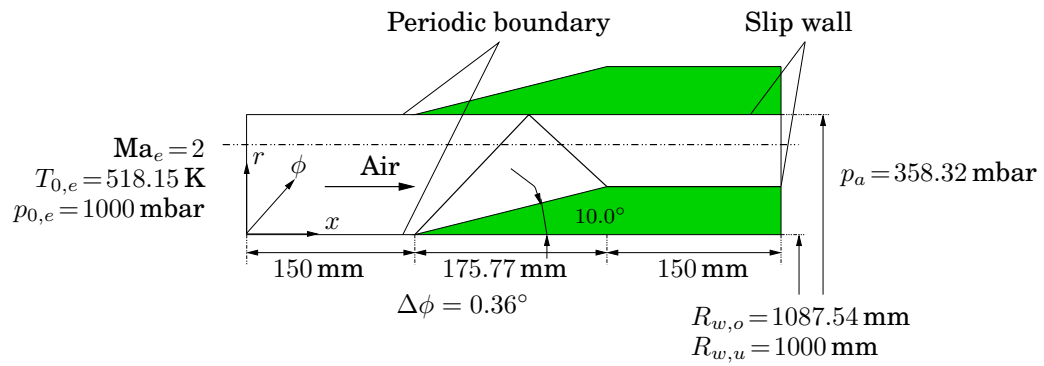


Figure 4.9: Geometry and boundary conditions of the test case where the supersonic flow through a row of wedges is simulated

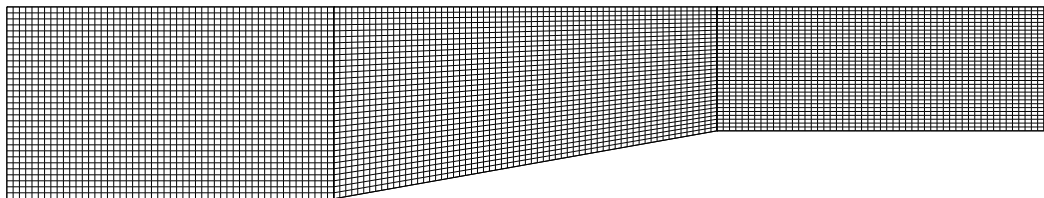
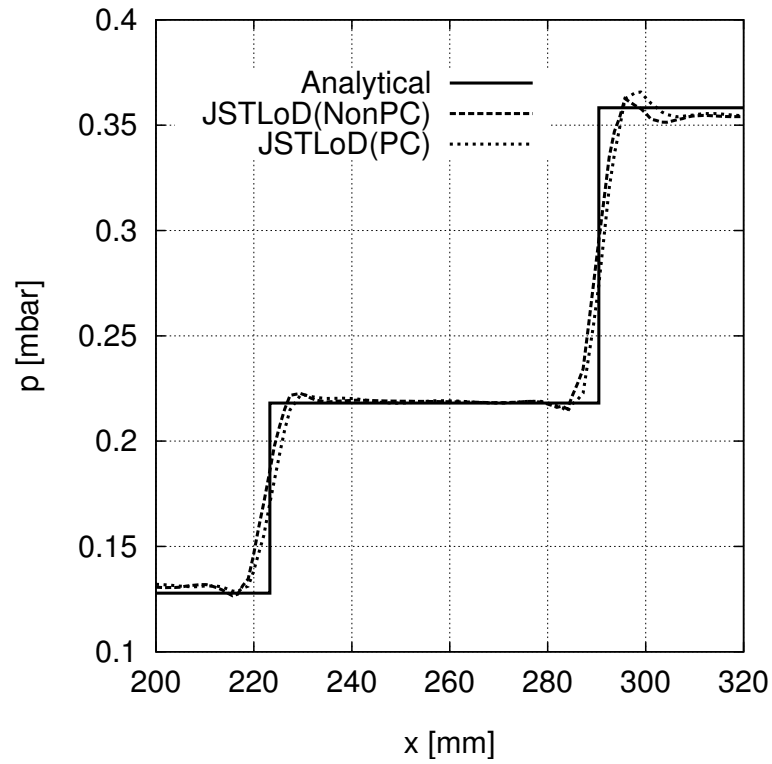
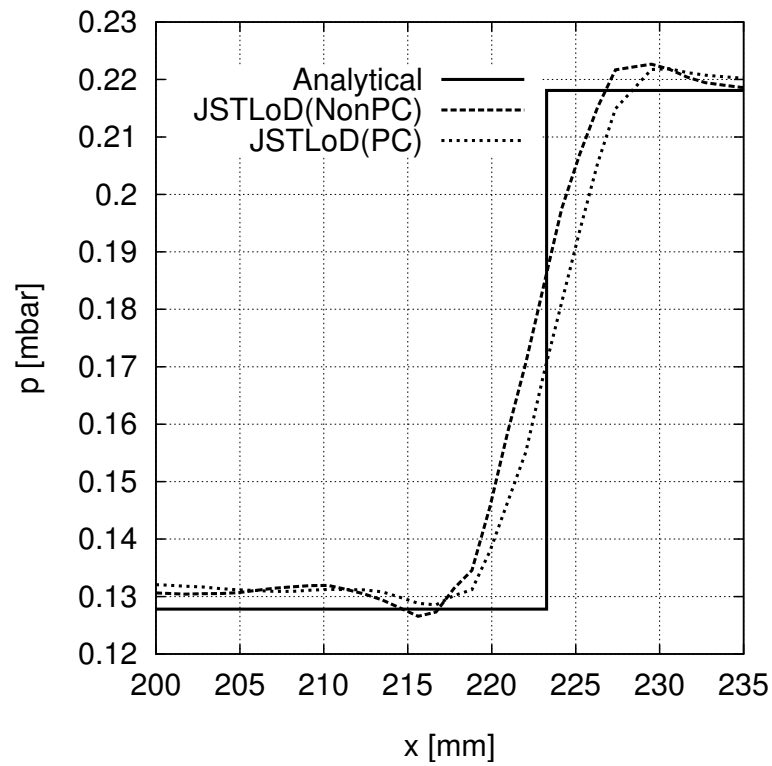


Figure 4.10: Computational grid for the simulation of the supersonic flow through a row of wedges

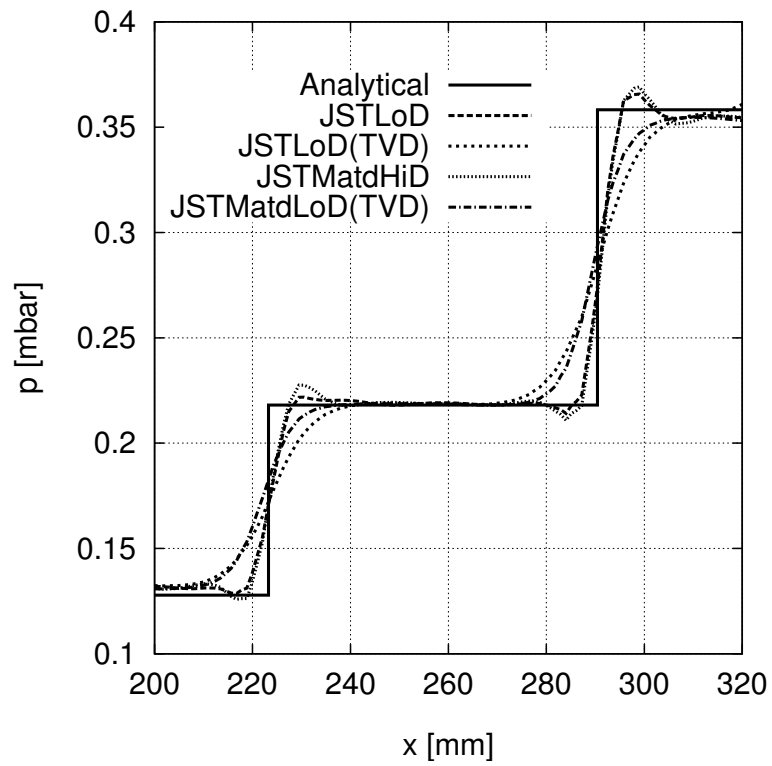


(a)

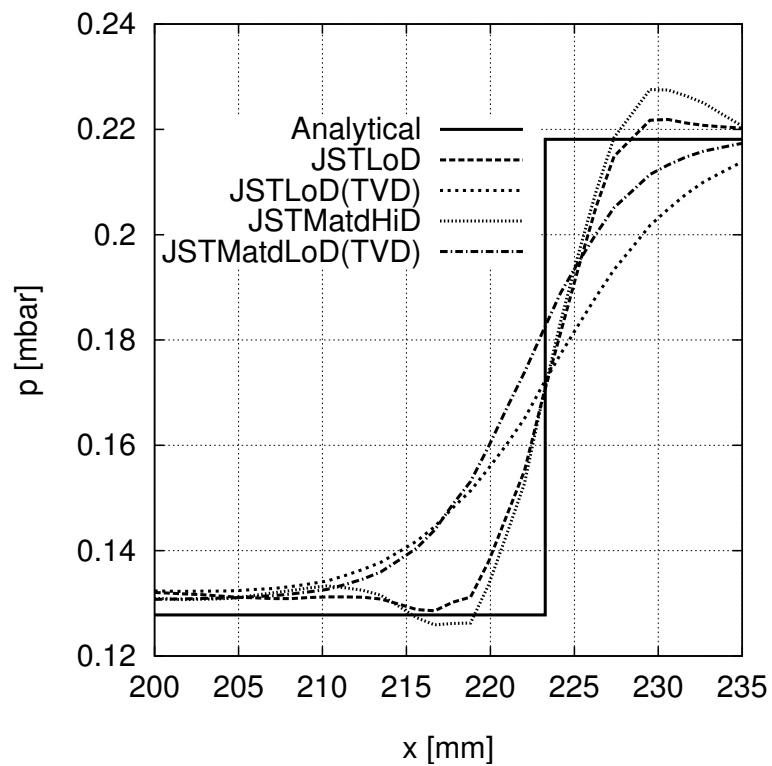


(b) Close-up

Figure 4.11: Supersonic flow through a row of wedges: Simulated static pressure at $r = 1060$ mm in dependence of the dissipation scheme

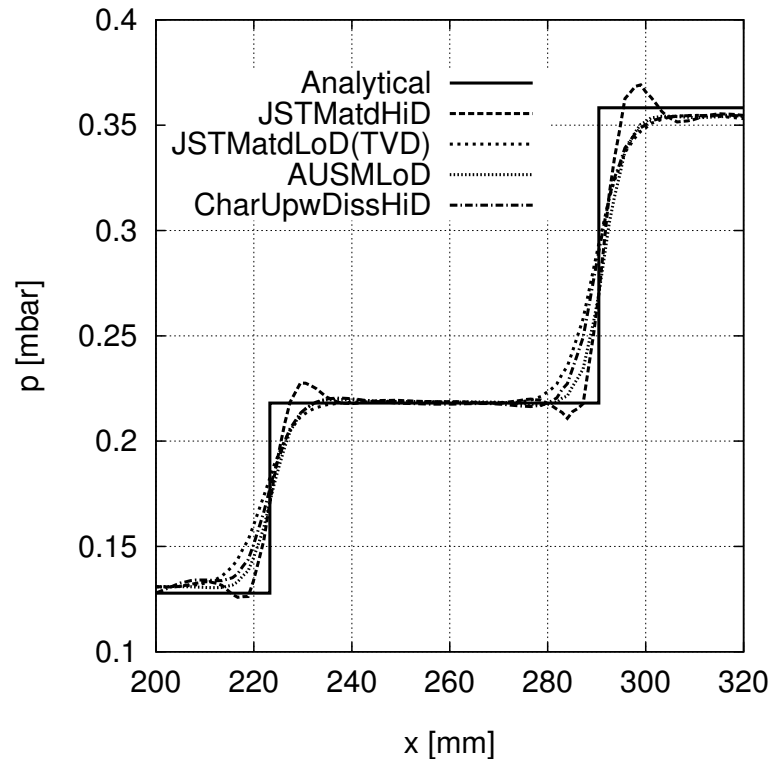


(a)

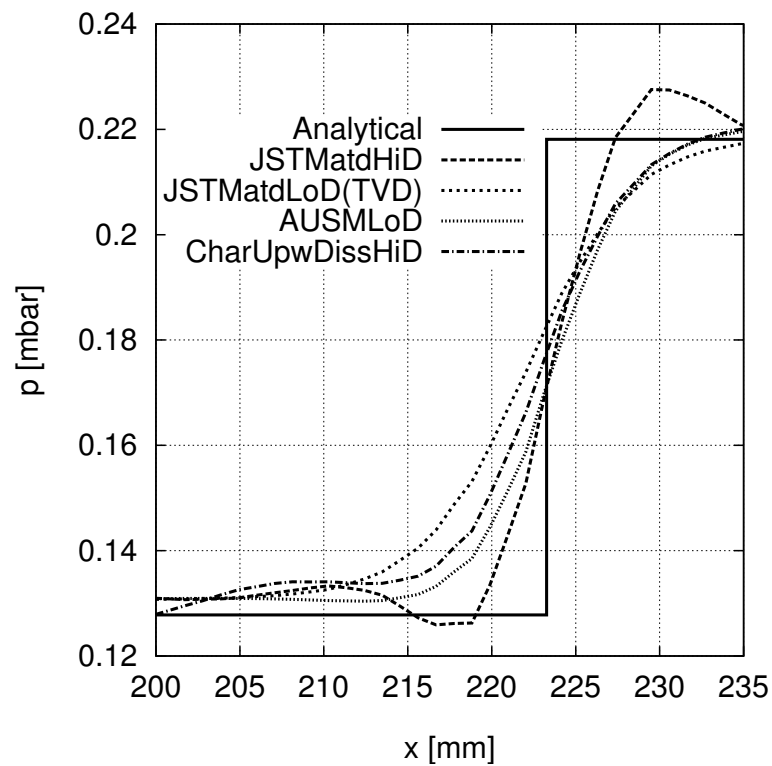


(b) Close-up

Figure 4.12: Supersonic flow through a row of wedges: Simulated static pressure at $r = 1060$ mm in dependence of the dissipation scheme



(a)



(b) Close-up

Figure 4.13: Supersonic flow through a row of wedges: Simulated static pressure at $r = 1060$ mm in dependence of the dissipation scheme

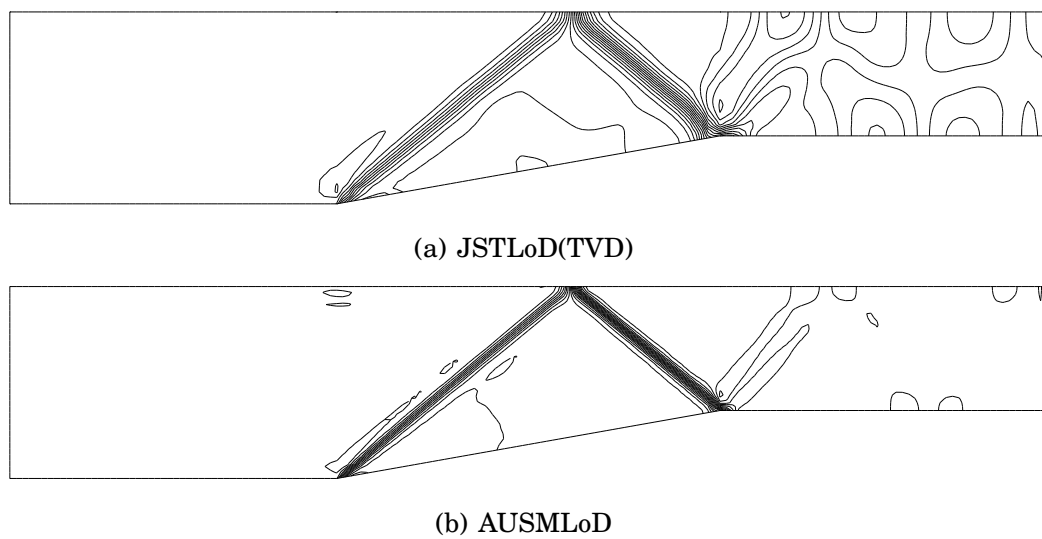
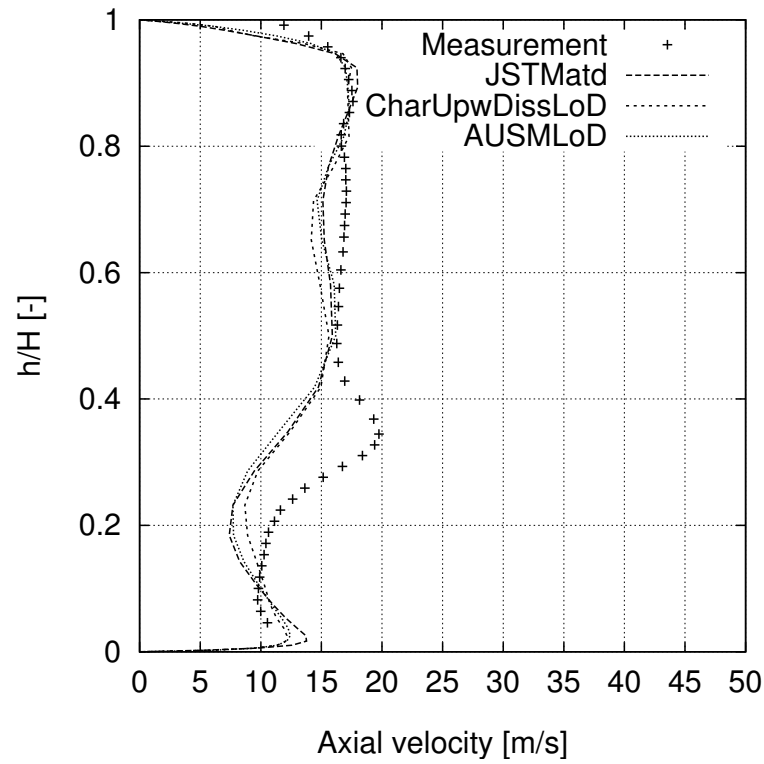
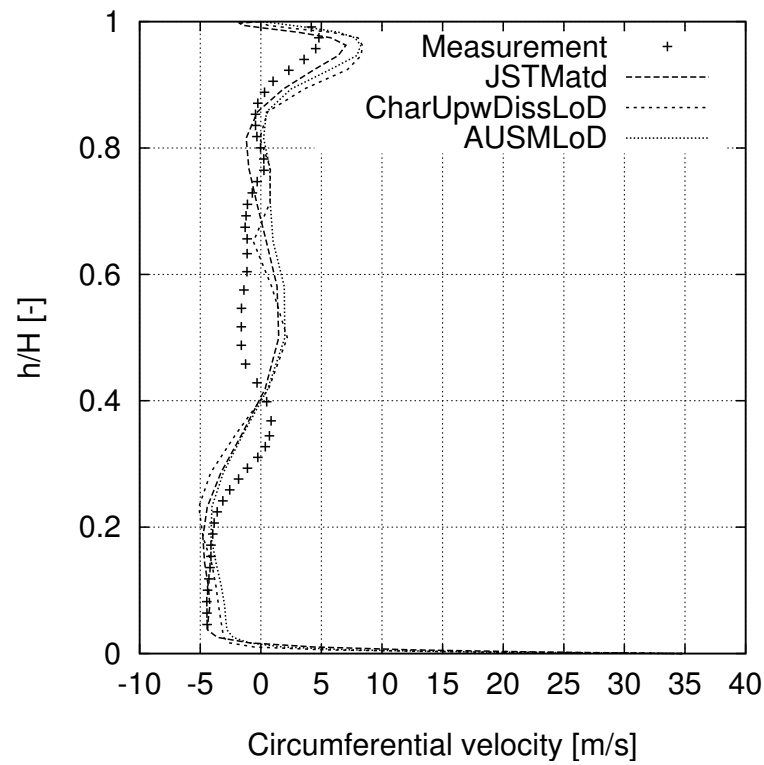


Figure 4.14: Static pressure contours ($\Delta p = 0.01$ mbar) of the simulated supersonic flow field through a row of wedges in dependence of the dissipation scheme



(a)



(b)

Figure 4.15: Circumferentially averaged velocities over the relative channel height h/H in the measurement plane M2 (30 mm behind rotor) of the low-speed turbine

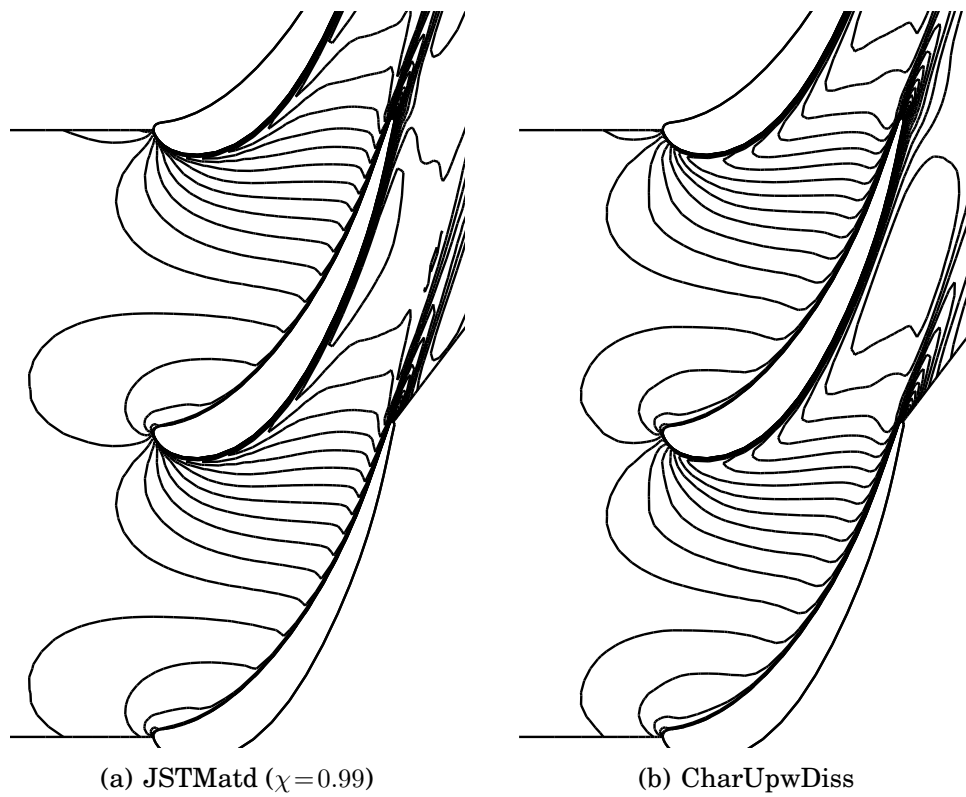


Figure 4.16: Mach number contours of the simulated flow in the first stator of the low-speed turbine in dependence of the discretization scheme

Chapter 5

Development of a non-reflecting boundary condition treatment

In the numerical simulation of turbomachinery it is often necessary to impose inlet and outlet boundaries near the blades where the flow is far from being uniform. The correct distribution of the values at the boundaries, however, is in general unknown and the boundary conditions can only be specified as averaged values. In order to achieve a solution that does not contain unphysical reflections at the boundaries and is practically independent of the size of the computational domain, it is important to be able to apply a non-reflecting boundary condition (NRBC) treatment.

The quasi-three-dimensional boundary condition treatment developed by Saxer and Giles [242, 243] is state-of-the-art for steady-state simulations of turbomachinery flow. These boundary conditions were developed for the unscaled Navier-Stokes equations for ideal gas flow. In order to be able to use this kind of boundary condition treatment with a solution scheme for the simulation of both incompressible and compressible flows with arbitrary Mach numbers, the boundary condition treatment of Saxer and Giles is extended to preconditioned system and general equations of state.

5.1 The quasi-three-dimensional approach of Giles and Saxer for a NRBC treatment

In the original boundary condition treatment devised by Giles and Saxer the solution at the boundary is decomposed into Fourier modes, where the zeroth mode corresponds to the average solution. This average mode is treated according to standard one-dimensional characteristic theory and enables the user to specify the circumferential averages of certain flow field parameters at the boundary. The remaining harmonics of the solution at the boundary are altered to satisfy a condition derived by Giles [98] based on the linearized, two-dimensional Euler equations, which ensures that any variation corresponding to incoming (or reflected) waves are eliminated. Using the quasi-three-dimensional approach of Saxer [242], the grid layers in the radial di-

rection are treated independently; the required Fourier decomposition of the state variables at the boundary is consequently limited to the circumferential direction. This method is motivated by the fact, that in axial turbomachinery the flow field variations are usually larger in the pitch-wise than in the radial direction.

5.2 The Giles-condition for a non-reflecting boundary for preconditioned systems

In order to arrive at the Giles-condition for a non-reflecting boundary for preconditioned systems, the Navier-Stokes equations (3.4) are linearized about the average state $\bar{\mathbf{Q}}_v$. Neglecting the diffusive fluxes and the source terms, the following equations are obtained

$$\Gamma_v \frac{\partial \tilde{\mathbf{Q}}_v}{\partial t} + A \frac{\partial \tilde{\mathbf{Q}}_v}{\partial x} + B \frac{\partial \tilde{\mathbf{Q}}_v}{\partial y} + C \frac{\partial \tilde{\mathbf{Q}}_v}{\partial z} = \mathbf{0} \quad (5.1)$$

for the perturbed state variable $\tilde{\mathbf{Q}}_v = \mathbf{Q}_v - \bar{\mathbf{Q}}_v$ with the matrices A, B, C given by $A = \frac{\partial \mathbf{E}_c}{\partial \mathbf{Q}_v} |_{\bar{\mathbf{Q}}_v}$, $B = \frac{\partial \mathbf{F}_c}{\partial \mathbf{Q}_v} |_{\bar{\mathbf{Q}}_v}$, $C = \frac{\partial \mathbf{G}_c}{\partial \mathbf{Q}_v} |_{\bar{\mathbf{Q}}_v}$. To simplify the analysis, Cartesian coordinates are now used; substituting (w_x, w_ϕ, w_r) with (u, v, w) the convective terms in Eq. (2.1) can otherwise be kept unchanged.

In order to be able to separate waves into incoming and outgoing ones, the perturbed state variable is decomposed into Fourier modes

$$\tilde{\mathbf{Q}}_v(x, y, z, t) = \sum_{\ell=-\infty}^{\infty} \hat{\mathbf{q}}_{v,\ell}^R e^{i(-\omega_\ell t + k_\ell x + l_\ell y + m_\ell z)}. \quad (5.2)$$

Applying one particular mode $\hat{\mathbf{q}}_{v,\ell}^R e^{i(-\omega_\ell t + k_\ell x + l_\ell y + m_\ell z)}$ to the linearized Euler equations leads to the following relation

$$\mathbf{0} = (-\omega_l \Gamma_v + k_l A + l_l B + m_l C) \hat{\mathbf{q}}_{v,\ell}^R = (k_l I \underbrace{-\omega_l A^{-1} \Gamma_v + l_l A^{-1} B + m_l A^{-1} C}_{A_p}) \hat{\mathbf{q}}_{v,\ell}^R. \quad (5.3)$$

Due to the linearity of the Equations (5.1), this relation holds for any mode; for the sake of brevity the index ℓ is dropped in the following analysis. Non-trivial solutions $\hat{\mathbf{q}}_v^R$ of Eq. (5.3) exist when the dispersion relation

$$|A_p + kI| = 0 \quad (5.4)$$

is satisfied; this equation relates the wave numbers k, l, m to the frequency ω over a homogeneous fifth-order polynomial expression. As can be seen from Eq. (5.3), $\hat{\mathbf{q}}_v^R$ is a right eigenvector of the matrix A_p with eigenvalue $-k$. It should be noted, that to discern between modes going in axial positive and axial negative directions, it is not the eigenvectors in dependence of the frequency ω that are of interest but the eigenvectors in dependence of the axial wave number k .

To formulate a condition for a non-reflecting axial boundary, the perturbed state vector $\tilde{\mathbf{Q}}_v$ for a particular mode is decomposed into the sum of its eigenfunctions

$$\tilde{\mathbf{Q}}_v = \left(\sum_{n=1}^5 a_n \hat{\mathbf{q}}_{v,n}^R e^{ik_n x} \right) e^{i(l y + m z - \omega t)}, \quad (5.5)$$

where k_i , $i = 1, \dots, 5$ represent the roots of the dispersion relation (5.4). Reflections at the boundary can now be prevented by specifying $a_i = 0$ for each i in Eq. (5.5) corresponding to an incoming wave. An equivalent condition for a non-reflecting boundary is

$$(\hat{\mathbf{p}}_{v,i}^L)^T \cdot \tilde{\mathbf{Q}}_v = 0 \quad (5.6)$$

for vectors $\hat{\mathbf{p}}_{v,i}^L(k_i)$ that belong to incoming waves and have the property of being orthogonal to the right eigenvectors $\hat{\mathbf{q}}_{v,j}^R(k_j)$, i.e.,

$$(\hat{\mathbf{p}}_{v,i}^L)^T(\omega, k_i, l, m) \cdot \hat{\mathbf{q}}_{v,j}^R(\omega, k_j, l, m) = 0, \quad \forall i \neq j. \quad (5.7)$$

It should be noted that since the relation in Eq. (5.6) is formulated for a particular wave-mode, it represents a condition in the frequency domain. The vectors $\hat{\mathbf{p}}_{v,i}^L$ with the desired orthogonality property are found as left eigenvectors of the matrix A_p , i.e.,

$$\mathbf{0} = (\hat{\mathbf{p}}_{v,i}^L)^T(-\omega A^{-1} \Gamma_v + k_i I + l A^{-1} B + m A^{-1} C), \quad i = 1, 2, \dots, 5. \quad (5.8)$$

5.3 Quasi-three-dimensional steady-state NRBC treatment for preconditioned systems

In the last section the Giles-condition for a non-reflecting boundary was reviewed for the general three-dimensional, unsteady case and the necessary left eigenvectors were defined for the case of preconditioning. Assuming that the variations in the span-wise directions are small compared to the variations in the circumferential directions, the necessary Fourier transform for implementing the Giles-condition given by Eq. (5.6) can be limited to the circumferential direction by setting the radial wave number m to zero. In this way, radial flow variations are only considered in the average modes.

Since steady flows are considered, only a treatment that yields a non-reflecting boundary in the limit of a converged solution for which the temporal modes vanish is of interest, i.e., a boundary condition treatment for $\omega \rightarrow 0$ is sought. In this case, at a boundary $x = x_0$ the wave representation of the perturbed state variable according to Eq. (5.2) can be simplified to

$$\tilde{\mathbf{Q}}_v(x_0, z) = \bar{\mathbf{q}}(x_0, z) + \sum_{n=-\infty, n \neq 0}^{\infty} \hat{\mathbf{q}}_{v,n}(x_0, z) \cdot e^{i y l n}. \quad (5.9)$$

$\bar{\mathbf{q}}(x, z)$ corresponds to the zeroth Fourier mode and represents the pitch-wise solution average at the boundary specified using the one-dimensional characteristic boundary theory for preconditioned systems given in the next section.

At every span-wise location the Giles-condition given by Eq. (5.6) is applied for every Fourier mode $n \neq 0$. In the limit of $l/\omega \rightarrow \infty$ and $m = 0$ the left special eigenvectors defined in Eq. (5.8) are, after a considerable amount of algebra, calculated to be

$$L_{v,s,\text{comp}} = \begin{bmatrix} \hat{\mathbf{P}}_1^T \\ \dots \\ \hat{\mathbf{P}}_5^T \end{bmatrix}_{\text{comp}} = \begin{bmatrix} -\frac{1-\varrho h_p}{\varrho h_T} & 0 & 0 & 0 & 1 \\ -\frac{1}{\varrho} & -u & -v & 0 & 0 \\ 0 & 0 & 0 & 1 & 0 \\ -\beta & \varrho v a & -\varrho u a & 0 & 0 \\ \beta & \varrho v a & -\varrho u a & 0 & 0 \end{bmatrix} \quad (5.10)$$

for compressible fluids ($\varrho_p \neq 0$) with the general thermal $\varrho = \varrho(p, T)$ and caloric $h = h(p, T)$ equation of state. For incompressible fluids with $\varrho = \text{const.}$ as the thermal equation of state, the set of left special eigenvectors becomes

$$L_{v,s,\text{incomp}} = \begin{bmatrix} \hat{\mathbf{P}}_1^T \\ \dots \\ \hat{\mathbf{P}}_5^T \end{bmatrix}_{\text{incomp}} = \begin{bmatrix} -\frac{1-\varrho h_p}{\varrho h_T} & 0 & 0 & 0 & 1 \\ -\frac{1}{\varrho} & -u & -v & 0 & 0 \\ 0 & 0 & 0 & 1 & 0 \\ \gamma & -\varrho v & \varrho u & 0 & 0 \\ -\gamma & -\varrho v & \varrho u & 0 & 0 \end{bmatrix}. \quad (5.11)$$

The parameters β and γ in Eqs. (5.10) and (5.11) are given by

$$\begin{aligned} \gamma &= \hat{i} \cdot \text{sign}(l), \\ \beta &= \begin{cases} \hat{i} \cdot \text{sign}(l) \sqrt{a^2 - (u^2 + v^2)}, & u^2 + v^2 \leq a^2, \\ -\text{sign}(v) \sqrt{(u^2 + v^2) - a^2}, & u^2 + v^2 \geq a^2. \end{cases} \end{aligned} \quad (5.12)$$

For a detailed derivation of the eigenvectors, the reader may refer to a separate report of Anker et al. [19]. The first left special eigenvector for the compressible case presented here differs from the result obtained by Saxer [242] since a different set of primitive variables and a general and not an ideal equation of state are used. However, the four last eigenvectors correspond to the eigenvectors derived by Saxer, which can be explained by the fact that preconditioning does not affect the steady state. The matrix of left special eigenvectors $L_{s,\text{comp}}$ for the primitive variable vectors $\mathbf{Q}_p = [\varrho, u, v, w, p]^T$ (which Saxer uses) and compressible flow can in fact be calculated from

$$L_{s,\text{comp}} = L_{v,s,\text{comp}} \begin{bmatrix} \partial \mathbf{Q}_v \\ \partial \mathbf{Q}_p \end{bmatrix}. \quad (5.13)$$

Because the physical speed of sound is infinite in incompressible fluids, it is obvious that the eigenvectors $[\hat{\mathbf{p}}_1, \dots, \hat{\mathbf{p}}_5]_{\text{comp}}^T$ that are formulated in dependence of the speed of sound cannot be used for the incompressible case. The eigenvectors $[\hat{\mathbf{p}}_1, \dots, \hat{\mathbf{p}}_5]_{\text{incomp}}^T$ were derived taking the property $\varrho = \text{const.}$ into account.

5.4 Boundary condition treatment based on one-dimensional characteristic theory

In the quasi-three-dimensional boundary condition treatment approach of Giles and Saxer, the circumferential averages of flow variables at the boundary are imposed by means of one-dimensional characteristic theory. In the following subsections standard one-dimensional boundary condition treatment is extended to preconditioned systems and general equations of state.

5.4.1 One-dimensional characteristic theory as a means to impose compatible boundary conditions

When a time-stepping scheme is used for the simulation of fluid flow, the unsteady Navier-Stokes equations are solved. Whether or not time-derivative preconditioning is used, the governing equations are hyperbolic-parabolic in time and the propagation speeds of the different physical modes will consequently be of importance. As one immediately sees from a physical point of reasoning, for the boundary condition treatment it is essential whether pressure perturbations can propagate upstream or not.

The idea of using characteristic theory for imposing boundary conditions is to decompose the solution at a boundary in contributions of waves entering and leaving the computational domain. While the outgoing waves can not be manipulated, the ingoing modes can be acted upon in order to impose certain values at the boundaries. As the characteristic variables represent decoupled state variables, the application of a characteristic boundary condition treatment ensures that the individual corrections of the solution variables at the boundary do not interfere with each other and that the corrections are compatible with the propagation of the waves in the interior of the computational domain.

A boundary condition treatment based on one-dimensional boundary condition treatment assumes that it is sufficient to only consider the propagation of waves perpendicular to the boundary under consideration; it is assumed that the flow is homogeneous in the directions transverse to the normal of the boundary, that the flow is convection dominated and that the influence of the diffusive terms on the wave propagation can be neglected.

For the sake of simplicity, it will in the following be assumed that the inlet boundary is positioned at $x = x_0 = \text{const.}$ and the outlet boundary located further downstream at $x = x_1 = \text{const.}$. In this way, the fluxes in the y - and z -direction do not need to be accounted for so that the one-dimensional, preconditioned Euler equations, which have been linearized about the averaged state \bar{Q}_v ,

$$\frac{\partial \tilde{Q}_v}{\partial t} + \underbrace{\Gamma_v^{-1} A}_{A^*} \frac{\partial \tilde{Q}_v}{\partial x} = 0 \quad (5.14)$$

with the flux Jacobian A defined as $A = \frac{\partial \mathbf{E}}{\partial \mathbf{Q}_v} |_{\bar{Q}_v}$, are sufficient for a proper

description of the transport of information near the boundaries.

By multiplying the last equation with the matrix L of the left eigenvectors of the system matrix $A^* = \Gamma_v^{-1}A$, one obtains the decoupled system of equations

$$L \frac{\partial \tilde{\mathbf{Q}}_v}{\partial t} + \underbrace{L A^* L^{-1}}_{\Lambda_\Gamma} L \frac{\partial \tilde{\mathbf{Q}}_v}{\partial x} = \mathbf{0}. \quad (5.15)$$

As shown in Anker et al. [19] the matrix L reads as

$$L = \begin{bmatrix} \mathbf{1}_1^T \\ \vdots \\ \mathbf{1}_5^T \end{bmatrix} = \begin{bmatrix} -\frac{1-\varrho h_p}{\varrho h_T} & 0 & 0 & 0 & 1 \\ 0 & 0 & 1 & 0 & 0 \\ 0 & 0 & 0 & 1 & 0 \\ 1 & \varrho(u_0'' + a'') & 0 & 0 & 0 \\ 1 & \varrho(u_0'' - a'') & 0 & 0 & 0 \end{bmatrix} \quad (5.16)$$

and its inverse L^{-1} , which equals the matrix of the right eigenvector R , becomes

$$L^{-1} = R = [\mathbf{r}_1, \dots, \mathbf{r}_5] = \begin{bmatrix} 0 & 0 & 0 & \frac{a'' - u_0''}{2a''} & \frac{a'' + u_0''}{2a''} \\ 0 & 0 & 0 & \frac{1}{2\varrho a''} & -\frac{1}{2\varrho a''} \\ 0 & 1 & 0 & 0 & 0 \\ 0 & 0 & 1 & 0 & 0 \\ 1 & 0 & 0 & \frac{1-\varrho h_p}{\varrho h_T} \frac{a'' - u_0''}{2a''} & \frac{1-\varrho h_p}{\varrho h_T} \frac{a'' + u_0''}{2a''} \end{bmatrix}. \quad (5.17)$$

The auxiliary quantities a'' , u'' and u_0'' are defined as

$$u'' = \frac{1}{2}u\left(1 + \frac{d}{d'}\right), \quad u_0'' = \frac{1}{2}u\left(1 - \frac{d}{d'}\right), \quad a'' = \sqrt{u_0''^2 + a'^2}. \quad (5.18)$$

The terms d , d' and pseudo-acoustic velocity a' are defined by Eqs. (3.7) and (3.10). It should be noted that these quantities reduce to

$$a'' = a, \quad u'' = u, \quad u_0'' = 0 \quad (5.19)$$

in the case that preconditioning is switched off.

With the definition of the vector of the characteristic variables ϕ as $\phi = L\mathbf{Q}_v$, the relation (5.15) can be transformed to the following system of transport equations

$$\frac{\partial \tilde{\phi}}{\partial t} + \Lambda_\Gamma \frac{\partial \tilde{\phi}}{\partial x} = \mathbf{0}. \quad (5.20)$$

Since Λ_Γ is a diagonal matrix,

$$\Lambda_\Gamma = \text{Diag}(\lambda'_1, \dots, \lambda'_5), \quad \text{with} \quad \lambda'_{1,2,3} = u'', \quad \lambda'_{4,5} = u'' \pm a'', \quad (5.21)$$

the perturbed characteristic variables $\tilde{\phi} = L\tilde{\mathbf{Q}}_v$ represent decoupled quantities; from Eq. (5.20) it is evident that each characteristic variable $\tilde{\phi}_i$ is transported at its own characteristic speed λ'_i ($i = 1, \dots, 5$).

It should be noted, that in the preconditioning method used, the scaling of the flow equations is shut off for supersonic speed. Furthermore, the preconditioning matrix Γ_v is defined in such a way that the signs of the eigenvalues of the system matrix A^* are not altered. Consequently, for a flow along the positive x -direction ($u > 0$), the signs of the first four eigenvalues are always positive, whereas the fifth eigenvalue is dependent on whether or not the flow is axially supersonic or not:

$$\text{sign}(\lambda'_{1,2,3,4}) > 0, \quad \text{sign}(\lambda'_5) = \text{sign}(u - a). \quad (5.22)$$

Only those characteristic variables that are entering the domain at a boundary can and should be prescribed; the value of the outgoing characteristic variables are determined by the evolution of the flow field in the interior of the computational domain and can not be manipulated. Thus, at a subsonic inlet boundary, the first four characteristic quantities ($\tilde{\phi}_i$, $i = 1, \dots, 4$) need to be prescribed whereas the value of the fifth characteristic quantity $\tilde{\phi}_5$ is determined by extrapolation. Vice versa at a subsonic outflow boundary, only the fifth characteristic quantity $\tilde{\phi}_5$ is associated with a boundary condition, the others are a mere consequence of the flow field upstream.

At a supersonic inflow boundary, the value of all characteristics follow from the specification of the state variables at the boundary. This obviates the need for a distinction between in- and outgoing wave modes and makes the implementation of a suitable boundary condition treatment easy. A proper numerical treatment of a supersonic outflow is even simpler; since all characteristic variables are determined by the dynamics of the interior of the flow field, the states that are predicted at the boundary by the flow solver can be taken over without any correction.

In the following the boundary condition treatment for each of the four aforementioned cases is discussed.

5.4.2 Axially subsonic inlet

The average changes in the four incoming characteristics are calculated from the requirement that the average flow field match the total temperature $T_{0,bc}(r)$, the total pressure $p_{0,bc}(r)$, the relative flow angle $\beta_{bc}(r)$ in the n - ϕ -plane and the pitch angle $\gamma_{bc}(r)$ in the n - t -plane specified by the user. Accordingly, in the following u, v, w represent the velocity component in the normal, circumferential and tangential direction of the boundary, respectively. An equivalent specification of the average inlet conditions is to drive the following boundary residuals to zero:

$$\begin{aligned} R_1 &:= \bar{\rho} \bar{T} (\bar{s} - s_{bc}(r)), & R_2 &:= \bar{\rho} \bar{a}'' (\bar{v} - \bar{u} \beta_{bc}^*(r)), \\ R_3 &:= \bar{\rho} \bar{a}'' (\bar{w} - \bar{u} \gamma_{bc}^*(r)), & R_4 &:= \bar{\rho} (\bar{h}_0 - h_{0,bc}(r)) \end{aligned} \quad (5.23)$$

with $\beta_{bc}^* = \tan \beta_{bc}$, $\gamma_{bc}^* = \tan \gamma_{bc}$ and the entropy and total enthalpy given by $s_{bc} = s(p_{0,bc}, T_{0,bc})$ and $h_{0,bc} = h(p_{0,bc}, T_{0,bc})$, respectively. A bar “-” denotes a circumferential average of the respective quantity. In coherence with the original boundary condition treatment devised by Giles, the boundary residuals

are defined in dependence of the total enthalpy and the entropy to ensure a uniform distribution of these quantities; as noted by Giles [97] if the boundary residuals are directly specified in dependence of the total pressure and the total temperature, a linear numerical treatment may introduce second order effects that will cause variations in the total enthalpy and the entropy at the boundary. The residuals have been scaled with $\bar{\rho}T$, $\bar{\rho}\bar{a}''$, and $\bar{\rho}$, respectively, in order to obtain simpler expressions in the boundary condition treatment. These reference quantities are assumed to be constant within a time-step.

For the definition of the first boundary residual Giles employs the entropy related function s^* with $s^* := \ln(p) - \gamma \ln \rho$, which for ideal gases corresponds to $s^* = \frac{s}{c_v}$. Since specifying $s^* := \text{const.}$ does not enforce $s = \text{const.}$ for general equations of state for which the isochoric heat capacity c_v may be temperature and pressure dependent, the entropy function is used directly. This choice is also more convenient, as the specific isochoric heat capacity can neither be calculated directly from the thermal $\rho = \rho(p, T)$ and caloric $h = h(p, T)$ equation of state nor from the entropy function $s = s(p, T)$.

The nonlinear equations (5.23) are linearized about the circumferentially averaged solution $\bar{\mathbf{Q}}_v^{(n)}$ of the last time-step n

$$\mathbf{R}^{(n+1)} = \mathbf{R}^{(n)} + \underbrace{\frac{\partial(R_1, R_2, R_3, R_4)}{\partial(\phi_1, \phi_2, \phi_3, \phi_4)}}_J \bigg|_{\bar{\mathbf{Q}}_v^{(n)}} \cdot \begin{bmatrix} \delta\bar{\phi}_1 \\ \delta\bar{\phi}_2 \\ \delta\bar{\phi}_3 \\ \delta\bar{\phi}_4 \end{bmatrix}^{(n)} := 0. \quad (5.24)$$

The Jacobian J is calculated as

$$J = \frac{\partial(R_1, R_2, R_3, R_4)}{\partial(p, u, v, w, T)} \underbrace{\frac{\partial(p, u, v, w, T)}{\partial(\phi_1, \phi_2, \phi_3, \phi_4)}}_{(\mathbf{r}_1, \mathbf{r}_2, \mathbf{r}_3, \mathbf{r}_4)}, \quad (5.25)$$

where $\mathbf{r}_i; i = 1, \dots, 4$ represent the first four right of the eigenvectors given in Eq. (5.17). When solving these linearized equations one obtains the necessary variations of the average incoming characteristic variables $\delta\bar{\phi}_i^{(n)} = \bar{\phi}_i^{(n+1)} - \bar{\phi}_i^{(n)}$; $i = 1, \dots, 4$ for driving the boundary residuals with increasing time-step to zero:

$$\begin{bmatrix} \delta\bar{\phi}_1 \\ \delta\bar{\phi}_2 \\ \delta\bar{\phi}_3 \\ \delta\bar{\phi}_4 \end{bmatrix}^{(n)} = -J^{-1} \big|_{\bar{\mathbf{Q}}_v^{(n)}} \cdot \begin{bmatrix} R_1 \\ R_2 \\ R_3 \\ R_4 \end{bmatrix}^{(n)}. \quad (5.26)$$

By exploiting the identity

$$\frac{1 - \rho h_p}{\rho h_T} + \frac{s_p}{s_T} \equiv 0, \quad (5.27)$$

which holds for general equations of state, the inverse of the Jacobian becomes

$$J^{-1} = \begin{bmatrix} \frac{1}{\rho h_T} & 0 & 0 & 0 \\ -\frac{\beta_{bc}^*}{\rho a'' M''} & \frac{M'' - M_y'' \beta_{bc}^*}{\rho a'' M''} & -\frac{M_z'' \beta_{bc}^*}{\rho a'' M''} & \frac{\beta_{bc}^*}{\rho a'' M''} \\ -\frac{\gamma_{bc}^*}{\rho a'' M''} & -\frac{M_y'' \gamma_{bc}^*}{\rho a'' M''} & \frac{M_z'' - M_y'' \gamma_{bc}^*}{\rho a'' M''} & \frac{\gamma_{bc}^*}{\rho a'' M''} \\ -\frac{2}{M''} & -\frac{2M_y''}{M''} & -\frac{2M_z''}{M''} & \frac{2}{M''} \end{bmatrix} \quad (5.28)$$

with the Mach numbers M'' , M_y'' , M_z'' and the abbreviations Ξ , given by

$$\begin{aligned} M'' &= \frac{\Xi}{a''}, & M_y'' &= \frac{v}{a''}, & M_z'' &= \frac{w}{a''}, \\ \Xi &= a'' + u'' + v\beta_{bc}^* + w\gamma_{bc}^*. \end{aligned} \quad (5.29)$$

In the work of Anker et al. [19] details of the derivation of the inverse Jacobian J^{-1} and the proof of the validity of the thermodynamic identity in Eq. (5.27) are given.

The determinant D of the Jacobian J is given by

$$D = \frac{1}{2} \rho^3 a'' c_p \Xi. \quad (5.30)$$

Since D is greater than zero for physical thermal state variables ($p, T > 0 \Rightarrow \rho, c_p, a'', u'' > 0$) and inflow conditions $u > 0$, the regularity of the Jacobian J for physically meaningful applications is guaranteed.

The average variation of the outgoing fifth characteristic variable $\delta \bar{\phi}_5$ is given by

$$\begin{aligned} \delta \bar{\phi}_5^{(n)} &= \mathbf{I}_5^T |_{\bar{\mathbf{Q}}^{(n)}} \cdot (\delta \bar{\mathbf{Q}}_v)_{\text{cal}}^{(n)} \\ &= \delta \bar{p}_{\text{cal}}^{(n)} - [\bar{\rho}(a'' - \bar{u}_0'')]^{(n)} \cdot \delta \bar{u}_{\text{cal}}^{(n)} \end{aligned} \quad (5.31)$$

where the subscript "cal" denotes changes predicted by the flow solver, i.e., $\delta \bar{p}_{\text{cal}}^{(n)} = \bar{p}_{\text{cal}}^{(n+1)} - \bar{p}^{(n)}$ where $\bar{p}_{\text{cal}}^{(n+1)}$ represents the predicted static pressure at the actual time step $n + 1$ before the boundary values are post-corrected. The left eigenvectors for calculating the characteristic variables are given in Eq. (5.16) above.

When the boundary treatment is simply based on the average one-dimensional characteristic variables, the solution variables $\mathbf{Q}_{v,j}$ at every point $j = 1, \dots, N + 1$ of the current circumferential grid line are post-corrected according to

$$\mathbf{Q}_{v,j}^{(n+1)} = \bar{\mathbf{Q}}_v^{(n)} + R |_{\bar{\mathbf{Q}}_v^{(n)}} \delta \bar{\phi}^{(n)} \quad (5.32)$$

with $\delta \bar{\phi} = [\delta \bar{\phi}_1, \delta \bar{\phi}_2, \delta \bar{\phi}_3, \delta \bar{\phi}_4, \delta \bar{\phi}_5]^T$ where R represents the matrix of right eigenvectors given in Eq. (5.17).

5.4.3 Axially subsonic outlet

At an axially subsonic boundary four characteristics are leaving and one characteristic is entering the computational domain. The implementation of the boundary conditions at outflow is easier than at inflow, because only one

boundary condition has to be imposed. As outlet boundary condition for axially subsonic flow, the user has to specify the radial variation of the static pressure $p_{bc}(r)$. Using the residual $R_5 = \bar{p}(r) - p_{bc}(r)$ and linearizing from the current time level yields

$$R_5^{(n+1)} = R_5^{(n)} + \left. \frac{\partial R_5}{\partial \phi_5} \right|_{\bar{\mathbf{Q}}_v^{(n)}} \delta \bar{\phi}_5^{(n)} := 0. \quad (5.33)$$

Calculating the scalar Jacobian $\frac{\partial R_5}{\partial \phi_5}$ and solving the equation for the average change in the fifth characteristic variable leads to

$$\delta \bar{\phi}_5^{(n)} = - \left. \frac{2a''}{a'' + u_0''} \right|_{\bar{\mathbf{Q}}_v^{(n)}} \cdot R_5^{(n)}. \quad (5.34)$$

The variations of the four first characteristics are calculated according to

$$\begin{bmatrix} \delta \bar{\phi}_1 \\ \delta \bar{\phi}_2 \\ \delta \bar{\phi}_3 \\ \delta \bar{\phi}_4 \end{bmatrix}^{(n)} = \begin{bmatrix} \mathbf{I}_1^T \\ \mathbf{I}_2^T \\ \mathbf{I}_3^T \\ \mathbf{I}_4^T \end{bmatrix}_{\bar{\mathbf{Q}}_v^{(n)}} \cdot \delta \bar{\mathbf{Q}}_{v,\text{cal}}^{(n)} = \begin{bmatrix} -\frac{1-\rho h_p}{\rho h_T} & 0 & 0 & 0 & 1 \\ 0 & 0 & 1 & 0 & 0 \\ 0 & 0 & 0 & 1 & 0 \\ 1 & \rho(u_0'' + a'') & 0 & 0 & 0 \end{bmatrix}_{\bar{\mathbf{Q}}_v^{(n)}} \cdot \begin{bmatrix} \delta \bar{p} \\ \delta \bar{u} \\ \delta \bar{v} \\ \delta \bar{w} \\ \delta \bar{T} \end{bmatrix}_{\text{cal}}^{(n)}. \quad (5.35)$$

If a boundary condition treatment based on one-dimensional characteristic theory is applied, the characteristic changes determined in the last two equations are transformed back into corrections of the solution variables at the boundary according to Eq. (5.32).

5.4.4 Axially supersonic inlet

In the case that the flow is axially supersonic at the inlet, all characteristics are incoming so that five boundary conditions have to be given. In addition to the boundary conditions for the axially subsonic case, the user has to specify the radial distribution of the axial Mach number $M_{x,\text{bc}}(r)$. Since the flow field at the boundary is independent of the downstream flow field, the correct boundary values can be calculated once and for all from the boundary conditions specified by the user. When general equations of state are used, a Newton-Raphson procedure must be applied in order to find the correct values of the primitive, viscous variables from the set of nonlinear algebraic equations

$$\begin{aligned} h_0(p_{0,\text{bc}}, T_{0,\text{bc}}) &= h(p_{0,\text{bc}}, T_{0,\text{bc}}) = h(p, T) + \frac{1}{2}(u^2 + v^2 + w^2 - (\Omega r)^2), \\ s(p_{0,\text{bc}}, T_{0,\text{bc}}) &= s(p, T), \quad \tan \beta_{bc} = \frac{v}{u}, \quad \tan \gamma_{bc} = \frac{w}{u}, \quad \mathbf{M}_{x,\text{bc}} = \frac{u}{a(p, T)}. \end{aligned} \quad (5.36)$$

A concrete description of an algorithm to determine the boundary conditions for general equation of state can be found in the work of Anker et al. [19]. For ideal gases, the vector of primitive, viscous state variables can be determined analytically from the boundary conditions:

$$\begin{aligned} \mathbf{M} &= \sqrt{1 + \tan^2 \beta_{bc} + \tan^2 \gamma_{bc}} \cdot \mathbf{M}_{x,\text{bc}}, \quad T = \frac{T_{0,\text{bc}}}{1 + \frac{\gamma-1}{2} \mathbf{M}^2}, \\ p &= p_{0,\text{bc}} \cdot \left(1 + \frac{\gamma-1}{2} \mathbf{M}^2\right)^{-\frac{\gamma}{\gamma-1}}, \quad u = a \cdot \mathbf{M}_{x,\text{bc}} = \sqrt{\gamma R T} \cdot \mathbf{M}_{x,\text{bc}}, \\ v &= u \tan \beta_{bc}, \quad w = u \tan \gamma_{bc}. \end{aligned} \quad (5.37)$$

For the practical use of this boundary condition treatment in a numerical simulation, it should be noted that the flow field must be initialized to be supersonic in the vicinity of the boundary. If upstream running pressure waves can reach the boundary, this boundary condition treatment will not be compatible with the dynamics of the flow field in the computational domain.

5.4.5 Axially supersonic outlet

When the flow is axially supersonic at the outlet boundary, all characteristics are outgoing, so that no boundary condition can be imposed. For practical simulations it is recommended to apply a subsonic outlet boundary for the case that the simulated flow field during the simulation should be subsonic. In the case that the flow is supersonic, the presence of a subsonic outlet boundary will not affect the interior of the flow field.

5.5 Implementation of the Q3D non-reflecting boundary condition treatment

Except in the case that the flow is supersonic in the flow direction normal to the boundary (which here for simplicity is assumed to be the axial direction), the Giles-condition must be applied in addition to a one-dimensional characteristic theory to obtain a non-reflecting boundary condition treatment. At an axially supersonic inflow boundary, all characteristic variables are incoming, which obviates the need for a non-reflecting boundary condition treatment; if a proper discretization scheme is used, all wave modes are exclusively transported downstream and reflections can not be produced. By the same token, at an axially supersonic outflow boundary, where all characteristics are leaving the domain, the non-reflectivity of the boundary condition treatment is not an issue.

If a quasi-three-dimensional non-reflecting boundary condition treatment is applied, then the variations in the characteristic variables $\delta\phi_j^{(n)} = \phi_j^{(n+1)} - \phi_j^{(n)}$ at each grid point j at a boundary are divided into the circumferential average $\delta\bar{\phi}^{(n)} := \bar{\phi}^{(n+1)} - \bar{\phi}^{(n)}$ over one pitch and a local change $\delta\phi_j'^{(n)}$ according to

$$\delta\phi_j^{(n)}(r) = \delta\bar{\phi}^{(n)}(r) + \delta\phi_j'^{(n)}, \quad j = 1, 2, \dots, N, \quad (5.38)$$

where N denotes the number of grid points in the circumferential direction when only accounting for the periodic point once.

It should be noted that the reference state used $\bar{Q}_v^{(n)}$ for the calculation of the perturbed state variable \tilde{Q}_v and the perturbed characteristic variable vector ϕ in the post-correction procedure of the boundary values between time-step n and $n + 1$ is the same. It is thus not of any importance whether the variations in the aforementioned quantities are determined using the respective absolute or the perturbed quantities; for the total variation of the charac-

teristic variables the following relation holds:

$$\delta\phi_j^{(n)} := \phi_j^{(n+1)} - \phi_j^{(n)} = \tilde{\phi}_j^{(n+1)} - \tilde{\phi}_j^{(n)} = \delta\tilde{\phi}_j^{(n)}; \quad j = 1, 2, \dots, N. \quad (5.39)$$

As suggested by Giles [98], to ensure that the boundary condition treatment does not cause instabilities in the solution process, the correction in the incoming characteristic variables should be relaxed, i.e., the overall variations of the incoming characteristic variables

$$\delta\phi_j^{(n)}(r) = \sigma(\delta\bar{\phi}^{(n)}(r) + \delta\phi_j'^{(n)}(r)) \quad (5.40)$$

are attenuated with a relaxation factor σ . Numerical investigations of Giles [98] suggest that a suitable choice of the relaxation factor is given by

$$\sigma = 1/N. \quad (5.41)$$

In the following subsections the implementation of the non-reflecting corrections at the boundaries will be described in dependence of the prevailing flow conditions at the boundaries.

5.5.1 Subsonic inflow boundary

At a subsonic inflow boundary, the changes in the average incoming characteristic variables are determined using one-dimensional characteristic theory as described in Section 5.4.2.

In order to obtain a non-reflecting inlet boundary, the Giles-condition

$$[\hat{\mathbf{p}}_1, \hat{\mathbf{p}}_2, \hat{\mathbf{p}}_3, \hat{\mathbf{p}}_4]^T \cdot \hat{\mathbf{q}}_k = 0 \quad (5.42)$$

has to be satisfied for each Fourier mode $\hat{\mathbf{q}}_k$ ($k \neq 0$) of the perturbed viscous, primitive variables $\tilde{\mathbf{Q}}_v = \mathbf{Q}_v - \bar{\mathbf{Q}}_v$. By using the relation $L^{-1}\hat{\phi}_k = \hat{\mathbf{q}}_k$, this boundary condition can be expressed in terms of the spatial Fourier modes of the characteristic variables. For compressible flows it is given by

$$\begin{bmatrix} 1 & 0 & 0 & 0 & 0 \\ 0 & -v & 0 & -\frac{a''+u-u_0''}{2\rho a''} & -\frac{a''-u+u_0''}{2\rho a''} \\ 0 & 0 & 1 & 0 & 0 \\ 0 & -\rho u a & 0 & -\frac{\beta(a''-u_0'')-va}{2a''} & -\frac{\beta(a''+u_0'')+va}{2a''} \end{bmatrix} \cdot \hat{\phi}_k = 0. \quad (5.43)$$

For incompressible fluids the corresponding condition is determined analogously; for a detailed description, the reader may refer to the work of Anker et al. [19]. In the following only the compressible case is discussed for the sake of brevity. The condition given in the last equation is satisfied trivially when all Fourier components (except the average Fourier mode) of the characteristic variables are zero, i.e., $\hat{\phi}_k=0, \forall k \neq 0$. This shows that one-dimensional characteristic theory alone can be applied to uniform flow fields, such as the far-field of external aerodynamic applications. However, in the general case

inhomogeneous flow fields are encountered which implies that the condition stated in Eq. (5.43) needs to be fulfilled non-trivially.

Since the outgoing characteristics do not depend on the boundary conditions but are only given by the interior flow field, they are not manipulable. Thus, the general way to satisfy the condition given in Eq. (5.43) is to define the incoming characteristics as functions of the outgoing ones:

$$\begin{bmatrix} \hat{\phi}_{1,k} \\ \hat{\phi}_{2,k} \\ \hat{\phi}_{3,k} \\ \hat{\phi}_{4,k} \end{bmatrix}^{(n)} := \begin{bmatrix} 0 \\ -\frac{\beta u + va}{\varrho[a(u^2+v^2)+(a''-u_0'')(ua-v\beta)]} \\ 0 \\ \frac{a(u^2+v^2)-(a''+u_0'')(ua-v\beta)}{a(u^2+v^2)+(a''-u_0'')(ua-v\beta)} \end{bmatrix} \cdot \hat{\phi}_{5,k}^{(n)} \cdot \bar{\mathbf{Q}}_v^{(n)} \quad (5.44)$$

Since the last condition is formulated in the frequency domain, the local outgoing characteristics have to be calculated as

$$\begin{aligned} \phi'_{5,j}{}^{(n)} &= \mathbf{I}_5^T \Big|_{\bar{\mathbf{Q}}_v^{(n)}} \cdot \tilde{\mathbf{Q}}_v^{(n)} \\ &= (p_j - \bar{p})^{(n)} + \bar{\varrho}^{(n)} (\bar{u}_0'' - \bar{a}'')^{(n)} \cdot (u_j - \bar{u})^{(n)} \end{aligned} \quad (5.45)$$

for $j = 1, 2, \dots, N$. Afterwards a discrete Fourier transformation according to

$$\hat{\phi}_{5,k}^{(n)} = \frac{1}{N} \sum_{j=0}^{N-1} \phi'_{5,j}{}^{(n)} \cdot e^{2\pi i j k / N}, \quad k = 0, 1, \dots, N-1 \quad (5.46)$$

by assuming periodicity ($\phi'_{5,1} = \phi'_{5,N+1}$) has to be carried out. The set of equidistantly distributed characteristic variables $\phi'_{5,j}{}^*$; $j = 0, \dots, N$ is obtained from the characteristic variables on the computational grid $\phi'_{5,j}$; $j = 1, \dots, N+1$ by using spline-interpolation where the endpoints of both sets match, i.e., $\phi'_{5,0} = \phi'_{5,1}$ and $\phi'_{5,N} = \phi'_{5,N+1} = \phi'_{5,1}$.

The Fourier coefficients of the second characteristic variable are calculated from the Fourier coefficients of the fifth characteristic according to Eq. (5.44):

$$\hat{\phi}_{2,ks}^{(n)} = - \underbrace{\frac{\beta u + va}{\varrho[a(u^2+v^2)+(a''-u_0'')(ua-v\beta)]}}_{c_{52}} \Big|_{\bar{\mathbf{Q}}_v^{(n)}} \cdot \hat{\phi}_{5,k}^{(n)} = c_{52} \cdot \hat{\phi}_{5,k}^{(n)} \quad (5.47)$$

$\forall k = 0, 1, \dots, N-1$. The correct steady state distribution of the second characteristic variables $\phi'_{2,j_s}{}^*$ is obtained from the Fourier coefficients $\hat{\phi}_{2,ks}$ by means of an inverse discrete Fourier transform:

$$\phi'_{2,j_s}{}^{(n)} = \sum_{k=0}^{N-1} \hat{\phi}_{2,ks}^{(n)} \cdot e^{-2\pi i j k / N}, \quad j = 0, 1, \dots, N-1. \quad (5.48)$$

Since the Fourier coefficients $\hat{\phi}_{5,k}$ originate from a real function, they possess a conjugate even symmetry with respect to $k=0$. Due to the definition of β in Eq. (5.12), where the wave number l corresponds to the Fourier-index k

used here, the factor c_{52} has the same property. The inverse discrete Fourier transform (5.48) for determining the correct steady state distribution of the second characteristics can, as shown in Anker et al. [19], then be simplified to

$$\phi'_{2,j_s} = \begin{cases} 2 \operatorname{Real} \left[\sum_{k=1}^{N/2-1} \hat{\phi}_{2,ks} \cdot e^{-2\pi i j k / N} \right] + \hat{\phi}_{2,N/2s}, & \text{for even } N, \\ 2 \operatorname{Real} \left[\sum_{k=1}^{(N-1)/2} \hat{\phi}_{2,ks} \cdot e^{-2\pi i j k / N} \right], & \text{for odd } N. \end{cases} \quad (5.49)$$

In Eq. (5.49) it was taken into account that the Fourier coefficient $\hat{\phi}_{2,0s}$ equals zero, since the characteristic variables are defined as perturbations from the average state of the last time step n .

The distribution of the correct steady state second characteristic variables on the computational grid ϕ'_{2,j_s} are gained from ϕ'_{2,j_s} , again using a cubic interpolation-spline. When the flow is supersonic, but axially subsonic, the factor c_{52} is real-valued and independent of the circumferential wave number, which is why the Giles-condition can be applied in the time domain and the discrete Fourier transformations can be omitted.

For each node j along the boundary, the local correction of the second characteristic variable $\delta\phi'_{2,j}$ is determined as the difference between the correct steady state value ϕ'_{2,j_s} and the current value $\phi'_{2,j}$:

$$\begin{aligned} \delta\phi'_{2,j} &= (\phi'_{2,j_s} - \phi'_{2,j})^{(n)} = \phi'_{2,j_s} - \mathbf{I}_2^T |_{\tilde{\mathbf{Q}}_v^{(n)}} \cdot \tilde{\mathbf{Q}}_v^{(n)} \\ &= \phi'_{2,j_s} - (v_j - \bar{v})^{(n)}. \end{aligned} \quad (5.50)$$

Since the harmonics of the correct third steady state characteristics are zero, the correction of the third characteristic variable is simply

$$\delta\phi'_{3,j} = -\phi'_{3,j} = -\mathbf{I}_3^T |_{\tilde{\mathbf{Q}}_v^{(n)}} \cdot \tilde{\mathbf{Q}}_v^{(n)} = -(w_j - \bar{w})^{(n)}. \quad (5.51)$$

As noted by Giles [98], an implementation of the other two of the four conditions in Eq. (5.44) would result in a flow field which to first-order would have uniform entropy and stagnation enthalpy at each radius. However, the neglected second order effects would introduce variations in entropy and stagnation enthalpy. To avoid this, the steady state corrections of the local first and fourth characteristic variables are obtained from the conditions that the local entropy s_j and the local stagnation enthalpy h_{0j} should match their average values, which is equivalent to drive the residuals

$$R_{1,j} = \bar{\rho} \bar{T} (s_j - \bar{s}), \quad R_{4,j} = \bar{\rho} (h_{0j} - \bar{h}_0) \quad (5.52)$$

to zero. The use of the residuals defined by Eq. (5.52) together with a one-step Newton-Raphson procedure results in the following local corrections of the first and fourth characteristic variables:

$$\begin{aligned} \delta\phi'_{1,j} &= -\frac{1}{\rho h_T} \Big|_{\tilde{\mathbf{Q}}_v^{(n)}} \cdot R_{1,j}^{(n)}, \\ \delta\phi'_{4,j} &= -\frac{2a''}{a'' + u - u_0''} \Big|_{\tilde{\mathbf{Q}}_v^{(n)}} \cdot [-R_{1,j} + (\bar{\rho} \bar{v}) \cdot \delta\phi'_{2,j} + (\bar{\rho} \bar{w}) \cdot \delta\phi'_{3,j} + R_{4,j}]^{(n)}. \end{aligned} \quad (5.53)$$

Now that the local variations of the incoming characteristic variables have been determined, they are added to the average changes according to

$$\delta\phi_{i,j} = \sigma(\delta\phi'_{i,j} + \delta\bar{\phi}_i); \quad i = 1, \dots, 4 \quad (5.54)$$

where the relaxation factor σ is chosen to be $1/N$. The total variation of the fifth characteristic variable $\delta\phi_{5,j}^{(n)}$ is calculated as

$$\begin{aligned} \delta\phi_{5,j}^{(n)} &= \mathbf{1}_5^T \Big|_{\bar{\mathbf{Q}}_v^{(n)}} (\mathbf{Q}_{v,j}^{(n+1)} - \mathbf{Q}_{v,j}^{(n)}) \\ &= p_{j,\text{cal}}^{(n+1)} - p_j^{(n)} + \bar{\varrho}(\bar{u}_0'' - \bar{a}'')^{(n)} (u_{j,\text{cal}}^{(n+1)} - u_j^{(n)}). \end{aligned} \quad (5.55)$$

Finally, the total characteristic changes $\delta\phi = [\delta\phi_1, \dots, \delta\phi_5]^T$ are transformed back into changes of the viscous, primitive variables and the state vector is updated according to

$$\mathbf{Q}_{v,j}^{(n+1)} = \mathbf{Q}_{v,j}^{(n)} + R \Big|_{\bar{\mathbf{Q}}_v^{(n)}} \cdot \delta\phi_j^{(n)}. \quad (5.56)$$

with the Matrix R of the right eigenvectors given in Eq. (5.16) above.

5.5.2 Subsonic outlet boundary

The Giles-condition for a non-reflecting spatial distribution of the perturbed primitive, viscous variables at the outlet boundary reads as

$$[\beta, \varrho va, -\varrho ua, 0, 0]_{\bar{\mathbf{Q}}_v^{(n)}} \cdot \hat{\mathbf{q}}_k = 0, \quad (5.57)$$

which in terms of the characteristic variables can be expressed as

$$\left[0, -\varrho ua, 0, \frac{\beta(a'' - u_0'') + va}{2a''}, \frac{\beta(a'' + u_0'') - va}{2a''} \right]_{\bar{\mathbf{Q}}_v^{(n)}} \cdot \hat{\phi}_k = 0 \quad (5.58)$$

for all Fourier modes $k \neq 0$. The Fourier modes of the ingoing fifth characteristic variable are defined as functions of the Fourier modes of the outgoing second and fourth characteristics according to

$$\hat{\phi}_{5,ks}^{(n)} := \frac{2\varrho uaa''}{\beta(a'' + u_0'') - va} \Big|_{\bar{\mathbf{Q}}_v^{(n)}} \cdot \hat{\phi}_{2,k}^{(n)} - \frac{\beta(a'' - u_0'') + va}{\beta(a'' + u_0'') - va} \Big|_{\bar{\mathbf{Q}}_v^{(n)}} \cdot \hat{\phi}_{4,k}^{(n)}, \quad (5.59)$$

for $k = 0, 1, \dots, N - 1$, where N again denotes the number of grid points in circumferential direction when accounting for the periodic nodes only once. The Fourier modes $\hat{\phi}_{2,k}^{(n)}$ and $\hat{\phi}_{4,k}^{(n)}$ are computed by first calculating $\phi'_{2,j}$ and $\phi'_{4,j}$ from the following relations:

$$\begin{aligned} \phi'_{2,j}^{(n)} &= \mathbf{I}_2^T \Big|_{\bar{\mathbf{Q}}_v^{(n)}} \cdot (\mathbf{Q}_{v,j} - \bar{\mathbf{Q}}_v)^{(n)} = (v_j - \bar{v})^{(n)}, \\ \phi'_{4,j}^{(n)} &= \mathbf{I}_4^T \Big|_{\bar{\mathbf{Q}}_v^{(n)}} \cdot (\mathbf{Q}_{v,j} - \bar{\mathbf{Q}}_v)^{(n)} \\ &= (p_j - \bar{p})^{(n)} + \bar{\varrho}^{(n)}(\bar{u}_0'' + \bar{a}'')^{(n)} \cdot (u_j - \bar{u})^{(n)}, \end{aligned} \quad (5.60)$$

$\forall j = 1, 2, \dots, N$. Then these quantities are transferred onto an equidistant grid and a discrete Fourier transformations of the spatially equidistantly distributed characteristic variables $\phi'_{2,j}^{*(n)}$ and $\phi'_{4,j}^{*(n)}$ are performed; for example the Fourier coefficients of the second characteristic variables $\phi'_{2,j}^{*(n)}$ are calculated as

$$\hat{\phi}_{2,k}^{(n)} = \frac{1}{N} \sum_{j=0}^{N-1} \phi'_{2,j}^{*(n)} \cdot e^{2\pi i j k / N}, \quad k = 0, 1, \dots, N-1. \quad (5.61)$$

Using the simplification due to conjugate even symmetry of the Fourier coefficients $\hat{\phi}_{5,ks}$ with respect to $k = 0$ allows the non-reflecting steady state values $\phi'_{5,j}^{*}$ for the incoming fifth characteristic variables to be written as

$$\phi'_{5,j}^{*(n)} = \begin{cases} 2 \operatorname{Real} \left[\sum_{k=1}^{(N/2)-1} \hat{\phi}_{5,ks}^{(n)} \cdot e^{-2\pi i j k / N} \right] + \hat{\phi}_{5,N/2s}, & \text{for even } N, \\ 2 \operatorname{Real} \left[\sum_{k=1}^{(N-1)/2} \hat{\phi}_{5,ks}^{(n)} \cdot e^{-2\pi i j k / N} \right], & \text{for odd } N, \end{cases} \quad (5.62)$$

$\forall j = 1, 2, \dots, N$. With $\phi'_{5,j}^{(n)}$ calculated as

$$\phi'_{5,j}^{(n)} = \mathbf{I}_5^T |_{\bar{\mathbf{Q}}_v^{(n)}} \tilde{\mathbf{Q}}_{v,j}^{(n)} = p_j^{(n)} - \bar{p}^{(n)} + \bar{\rho}^{(n)} (\bar{u}_0'' - \bar{a}'')^{(n)} (u_j^{(n)} - \bar{u}^{(n)}) \quad (5.63)$$

and the average variation of the fifth characteristic variable $\delta \bar{\phi}_5^{(n)}$ given by Eq. (5.34) one obtains the total variation as

$$\delta \phi_{5,j}^{(n)} = \sigma (\delta \bar{\phi}_5^{(n)} + \phi'_{5,j}^{(n)} - \phi_{5,j}^{(n)}). \quad (5.64)$$

The total variations of the first four characteristic variables are determined directly by

$$\begin{bmatrix} \delta \phi_1 \\ \delta \phi_2 \\ \delta \phi_3 \\ \delta \phi_4 \end{bmatrix}_j^{(n)} = \begin{bmatrix} \mathbf{1}_1^T \\ \mathbf{1}_2^T \\ \mathbf{1}_3^T \\ \mathbf{1}_4^T \end{bmatrix}_{\bar{\mathbf{Q}}_v^{(n)}} \cdot \begin{bmatrix} \delta p_j \\ \delta u_j \\ \delta v_j \\ \delta w_j \\ \delta T_j \end{bmatrix}_{j,\text{cal}}^{(n)} = \begin{bmatrix} -\frac{1-\varrho h_p}{\varrho h_T} & 0 & 0 & 0 & 1 \\ 0 & 0 & 1 & 0 & 0 \\ 0 & 0 & 0 & 1 & 0 \\ 1 & \varrho(u_0'' + a'') & 0 & 0 & 0 \end{bmatrix}_{\bar{\mathbf{Q}}_v^{(n)}} \cdot \begin{bmatrix} \delta p_j \\ \delta u_j \\ \delta v_j \\ \delta w_j \\ \delta T_j \end{bmatrix}_{\text{cal}}^{(n)}. \quad (5.65)$$

Finally, the total characteristic changes are transformed back into changes of the viscous, primitive variables and the state vector is updated according to Eq. (5.56).

5.5.3 Axially subsonic inlet or outlet boundaries in an overall supersonic flow

In the case that the flow is supersonic ($M > 1$) but that the axial flow velocity is subsonic ($M_x < 1$), then the boundary condition treatment described in the last sections only changes slightly. Under this condition the pressure waves

are still able to propagate upstream in the axial direction, which is why the in- and outgoing waves in the boundary condition treatment must be discriminated. However, in this case, the Giles-condition (5.6) simplifies due to the fact that the coefficient β , which is defined in Eq. (5.12), is only real-valued and not dependent of the wave number l anymore. Thus, for supersonic flows, a Giles-condition can be implemented directly without the need for applying Fourier-transforms of the boundary values.

5.5.4 Axially supersonic inlet and outlet boundaries

Since all wave modes at an axially supersonic inflow boundary are exclusively transported downstream, the boundary condition treatment can be implemented independently of the flow field located downstream. Thus, the boundary condition treatment described in Section 5.4.4 is sufficient to achieve a non-reflecting boundary.

At a supersonic outflow boundary all wave modes are leaving the domain, which makes it impossible to impose any boundary values. Consequently, any kind of boundary condition treatment in this case is inapplicable.

5.5.5 Adjacent solid walls

In calculations of viscous flow, the boundary points that lie in one of the flow boundary planes as well as on a solid wall require a special treatment, since the non-reflecting boundary treatment in combination with the preconditioning is singular at no-slip walls. The singularity of the walls becomes evident when the limit of coefficient c_{52} defined in Eq. (5.47) is taken for $v = 0$ and $u \rightarrow 0$.

In the current work, the grid points of the inlet- or outlet boundaries which simultaneously are located on a wall boundary are treated by first imposing the no-slip condition by setting all components of the velocity vector to zero. At the inlet boundary the static pressure and the temperature are set to the user specified total values. At the outlet boundaries the pressure is set to the corresponding user defined value, whereas the wall temperature is given by the specified thermal boundary condition.

5.6 Non-reflecting mixing-planes for the preconditioned Navier-Stokes equations

In steady multistage calculations of turbomachinery, mixing planes are used for coupling different frames of reference and transferring circumferentially averaged data from one row to another. The mixing planes developed in the frame of this work apply one-dimensional characteristic theory to enforce the condition that mass, impulse and energy are conserved across the interface. Reflections at these boundaries are prevented applying the Giles-condition given in Eq. (5.6). Since a mixing plane in principle represents an inlet

boundary coupled with an upstream outlet boundary, the extension of the non-reflecting inlet and outlet boundaries to non-reflecting mixing planes is straightforward. For this reason, in the following only a brief description of the mixing-planes developed for the simulation of turbomachinery flows using the preconditioned Navier-Stokes equations will be given.

5.6.1 Coupling condition

The developed mixing planes couple the flow in the rotor and stator rows by imposing that the circumferentially averaged, viscous, primitive state vectors \bar{Q}_v on each side $i \in \{1, 2\}$ of a given interface take on identical values in an absolute frame of reference for all radial position r , i.e.,

$$\bar{Q}_v(r)|_{1,\text{abs}} = \bar{Q}_v(r)|_{2,\text{abs}} , \quad \forall r. \quad (5.66)$$

To ensure that mass, momentum and energy fluxes are conserved, the latter condition (5.66) is applied on the flux averaged quantities at the circumferential lines where the mass flow does not vanish, as suggested by Saxer [242]. At the walls, simple area averaged flow quantities are used for coupling the stator and the rotor rows.

It should be noted that the use of circumferentially averaged quantities will lead to artificially increased values of the entropy in the downstream blade row as studied by Fritsch and Giles [89]. The use of mass-averaged stagnation flow quantities for coupling would lead to lower mixing losses; for a principal discussion of suitable averaging techniques in internal flows, the reader may refer to the work of Greitzer et al. [103]. Michelassi et al. [193] have compared various matching criteria and do not observe any noticeable difference between the use of stagnation and regular flow variables. Since deterministic stresses [2] would anyhow need to be modelled to achieve a mixing model that is as realistic as possible, in the current work the approach of Saxer was adopted for the sake of simplicity.

5.6.2 Numerical implementation

For the imposition of the coupling condition (5.66) it is necessary to distinguish between incoming and outgoing wave modes. For this reason a boundary condition treatment analogous to the procedure for inlet and outlet boundaries based on characteristic theory is used; in fact, the mixing planes can be regarded as inlet boundaries that are linked via the aforementioned coupling condition to an outflow boundary located upstream.

In a similar fashion as the treatment of the inlet and outlet boundaries, the overall variations of outgoing characteristic variables $\delta\phi_{5,j,\text{ex}}$ are accounted for in their entirety whereas the corresponding variations of the incoming variables are relaxed. The complete variations in the incoming characteristic variables $\delta\phi_{i,j,\text{in}}$, $i = 1, \dots, 4$ and $\delta\phi_{5,j,\text{in}}$ that are used in the boundary condition treatment of the downstream and the upstream side of each mixing plane,

respectively, are determined as

$$\delta\phi_{i,j,\text{in}} = \sigma_1\delta\bar{\phi}_{i,\text{in}} + \sigma_2\delta\phi'_{i,j,\text{in}}; \quad \forall i = 1, \dots, 5; \quad j = 1, \dots, N \quad (5.67)$$

with the relaxation factors $\sigma_1 = 0.3$ and $\sigma_2 = \max(0.02, 1/N)$. The quantities $\delta\bar{\phi}_{i,\text{in}}, i = 1, \dots, 5$ are calculated as the necessary change of the average incoming characteristic variables required to meet the coupling condition (5.66). For a derivation of the latter quantities and for a detailed description of the theory of the developed mixing planes treatment for preconditioned system, the reader may refer to the report of Anker et al. [19]. As in the case of an inlet or outlet boundary, the local variations in the incoming characteristic quantities $\delta\phi'_{i,j,\text{in}}, i = 1, \dots, 5$ are calculated applying the Giles-condition (5.6) for a non-reflecting distribution of the flow variables at the boundary.

5.7 Verification of the non-reflectivity of the developed NRBC treatment

An ideal boundary condition treatment for the steady-state simulation of turbomachinery flow should prevent unphysical reflections at the in- and outlet boundaries as well as at the mixing planes. To verify that a boundary condition treatment is non-reflecting, a single-blade simulation may be carried out on a short and a long domain. If a non-reflecting boundary condition treatment is used, pressure perturbations will only be generated by the turbomachinery blade. For this reason, the solution obtained on a small computational domain, should not differ from the solution obtained on a larger domain, if the circumferentially averaged solution of the large domain has been used as boundary condition for the smaller domain. To assess NRBC for unsteady flow simulations, it needs to be proven that the boundary condition treatment does not influence vortices, temperature streaks (or alternatively entropy variations), and pressure waves that are superimposed on free stream flow, when they are passing through the boundaries that are meant to be non-reflecting; cf. for instance the work of Yoo and Im [314] for a description of an appropriate set of test cases. For steady-state simulations such a verification procedure is not necessary as it only needs to be shown that the boundary condition treatment is non-reflecting in the limit of a converged solution; for this reason the aforementioned procedure of assessing the independence of the flow solution on the size of the domain is already a sufficient means to test the non-reflectivity of the boundary condition treatment for steady-state simulations.

In order to demonstrate that the developed NRBC treatment leads to solutions that are independent of the size of the computational domain, the viscous flow field in the linear VKI-1 cascade [253] was simulated at isentropic, outlet Mach numbers of $M_{\text{is},a} = 1.21, 0.81$ and 0.1 , respectively. The meshes used contain $154 \times 53 \times 3$ and $113 \times 53 \times 3$ nodes, respectively, and were constructed such that the nodes of the smallest grid coincide with the nodes of the

largest mesh. By proceeding in this way, grid dependence and interpolation errors can be avoided [247].

In Figs. 5.1 and 5.2 computational results are shown for the cases of an isentropic Mach number of $M_{is,a} = 0.81$ and $M_{is,a} = 1.21$, respectively. The results were obtained with the preconditioned (PC) solution scheme described in Chapter 3 and the NRBC treatment, that was developed for the preconditioned Navier-Stokes equations (NRPCBC) and described in the preceding sections. The solid lines represent isobars of the solution, that were obtained on the smallest domain, whereas the dotted lines represent the corresponding pressure contours of solution calculated on the largest domain. In order to have a reference and to show the consequences, which a reflecting boundary treatment may have, solutions obtained by Seybold [247] using the non-preconditioned solution scheme (NonPC) and boundary treatments based either solely on one-dimensional characteristic theory (1DpBC) or on the original quasi-three-dimensional non-reflecting theory (NRBC) due to Giles and Saxer [98, 242] for the unscaled Navier-Stokes equations are depicted for comparison.

For the case of an isentropic outlet Mach number of $M_{is} = 1.21$ it can be observed in Fig. 5.1 that the developed boundary treatment for the preconditioned Navier-Stokes equations leads to a solution that is dependent on the domain size of the solution in the vicinity of the outflow boundary. However, by comparing this solution with the corresponding solution obtained with the unscaled Navier-Stokes equations and the original, non-reflecting boundary condition treatment (NRBC-NonPC), this non-ideal behaviour is not specific for the developed boundary treatment. It is well known, that a boundary treatment based on the work of Giles is not capable of fully preventing reflections when shocks are crossing the boundary. This is due to the nonlinear nature of shock formation and second order effects not considered in the linear theory of Giles [63, 209, 247].

By comparing the solutions that were obtained with a non-reflecting boundary condition treatment (NRBC-NonPC or NRPCBC-PC) with the solutions gained by a treatment where one-dimensional characteristic theory is applied pointwise (1DpBC-NonPC) for the Mach numbers of $M_{is} = 1.21$ and $M_{is} = 0.81$, it becomes evident that the use of a non-reflecting boundary treatment only leads to relatively small deviations in the flow field when the size of the computational domain is changed. When a boundary treatment based merely on one-dimensional characteristic theory is applied, the solution obtained on a small and a large domain differ significantly.

In Figs. 5.3 and 5.4 computational results are shown, where a pressure ratio was prescribed, which for ideal gases corresponds to an isentropic outlet Mach number of $M_{is} = 0.10$. The results depicted in Fig. 5.3 were obtained by simulations, where the fluid was modelled as an ideal gas, whereas the results shown in Fig. 5.4 were obtained by simulations where the fluid was modeled as incompressible ($\rho = \text{const.}$). The boundary treatment that is simply based on one-dimensional characteristic theory for preconditioned systems (1DpPCBC) clearly leads to reflections for compressible and for incompress-

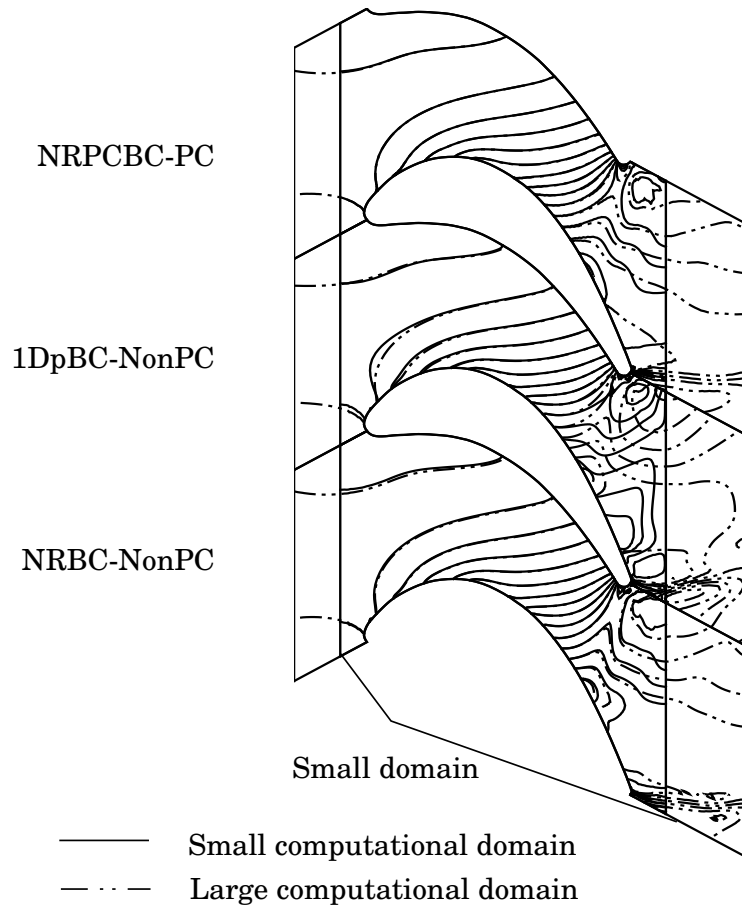


Figure 5.1: Pressure contours of the simulated flow field ($M_{is} = 1.21$) in the VKI-1 cascade in dependence of the boundary treatment and the size of the computational domain

ible fluids, whereas the solutions obtained with the developed non-reflecting boundary treatment on a small and large computational domain agree so well, that it is difficult to observe any difference between them.

It is thus verified that the developed boundary conditions are non-reflecting for incompressible fluids and subsonic, ideal gas flow.

5.8 Comparison of the developed and the original NRBC treatment

The preconditioning method described in Chapter 3 was first used with the original boundary conditions of Giles and Saxer, which is based on the characteristics of the unscaled Navier-Stokes equations. However this often led to instabilities in the vicinity of the inlet boundaries, outlet boundaries, and the mixing planes. In order to demonstrate the effectiveness of the novel bound-

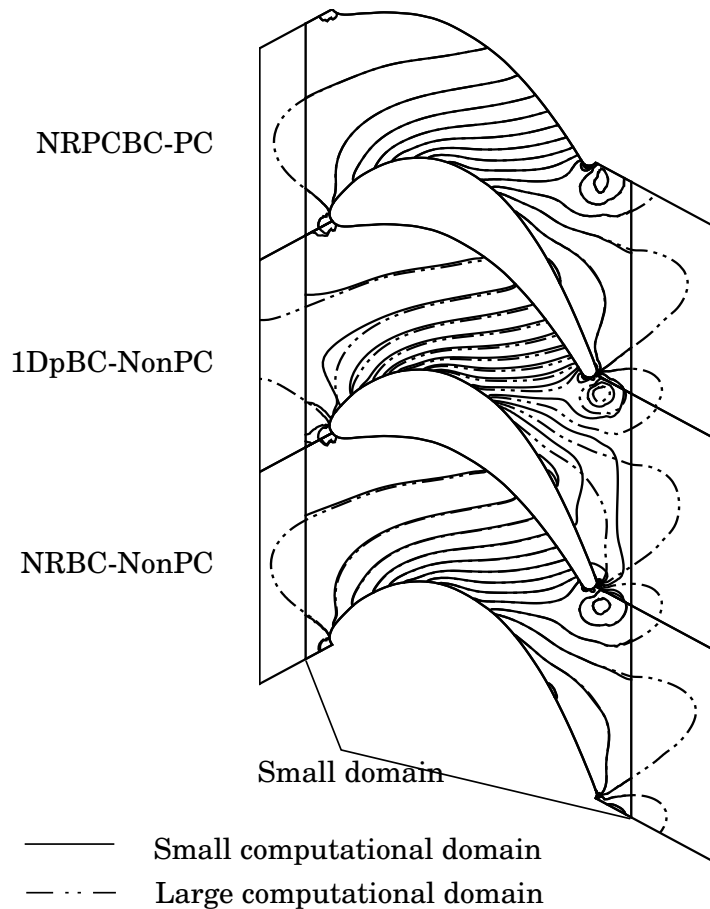


Figure 5.2: Pressure contours of the simulated flow field ($M_{is} = 0.81$) in the VKI-1 cascade in dependence of the boundary treatment and the size of the computational domain

ary treatment at low Mach numbers, the flow through the second stator row of the Bochum low speed turbine [6, 42] was simulated using the preconditioned scheme (PC) with the original quasi-three-dimensional, non-reflecting boundary treatment (NRBC) and with the consistent boundary treatment (NRPCBC) presented earlier in this chapter. The latter boundary conditions were also used without applying the non-reflecting correction, thereby basing this boundary treatment (1DmPCBC) on the averaged characteristics only.

As boundary conditions for the isolated vane an inlet total pressure of 1013 mbar and an outlet static pressure of 1000 mbar were specified. The difference of 13 mbar corresponds approximately to the actual pressure difference over the second stator.

The calculations were carried out on a grid consisting of $49 \times 25 \times 33$ grid points. The flow solver was run using the scalar JST-scheme with a CFL number of $CFL = 2.0$ and the coefficient $k^{(4)}$ of the fourth order dissipation set to $k^{(4)} = 0.05$. The coefficient of the pressure sensor of the preconditioning scheme ϵ_{pgr} was set to unity. The computations with a boundary condition

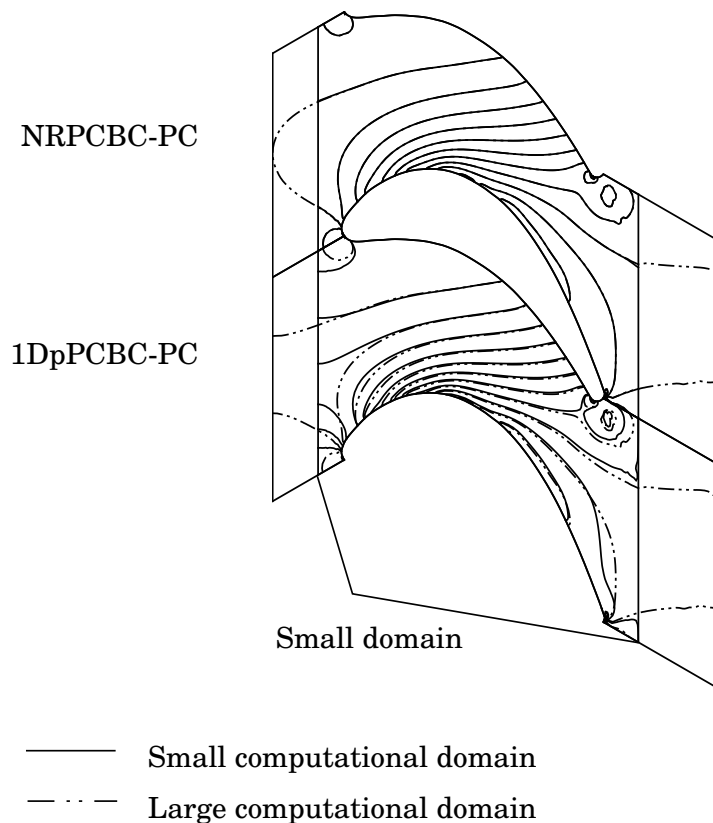


Figure 5.3: Pressure contours of the simulated flow field in the VKI-1 cascade for the isentropic outlet Mach number of $M_{is} = 0.10$ in dependence of the boundary treatment and the size of the computational domain. The fluid was modelled as an ideal gas

treatment based merely on the one-dimensional characteristics of the preconditioned scheme diverged on the finest grid level. In order to increase the robustness of the scheme the parameter ϵ_{pgr} was raised to $\epsilon_{pgr} = 10$. With this setting, divergence could be avoided, but the residual stagnated after a drop by 2.5 orders. In Fig. 5.5a the calculated flow field is depicted. It reveals an occurrence of unphysical reflections at the inlet and outlet boundaries.

The original boundary condition treatment of Giles and Saxer did not lead to a divergence of the flow computations, but with the preconditioning parameter set to $\epsilon_{pgr} = 1$ the residuals did not drop at all. First after increasing the parameter ϵ_{pgr} to $\epsilon_{pgr} = 10$ a residual drop by 1.5 orders was attained. From the computed flow field in Fig. 5.5b the reason for the poor convergence can be seen: The lines of constant pressure are wiggling at the boundary, revealing a poor boundary treatment. The deficiency in the boundary treatment is dependent on the Mach number. By lowering the outlet pressure to 700 mbar and thereby increasing the isentropic Mach number M_{is} to a value of $M_{is} = 0.6$, the solution converged and the original boundary condition seemed to be non-reflecting for this case, cf. Fig. 5.5c.

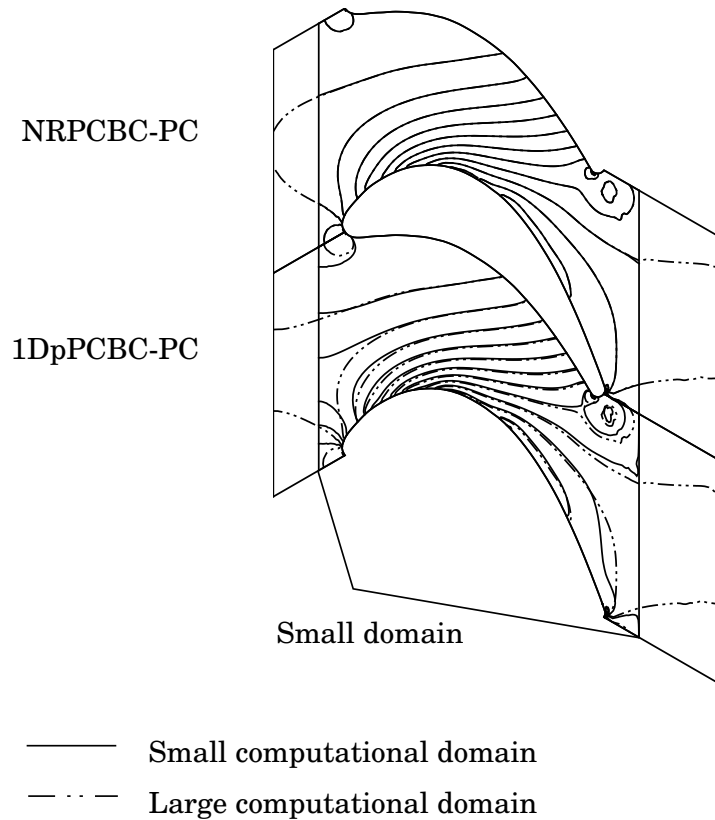
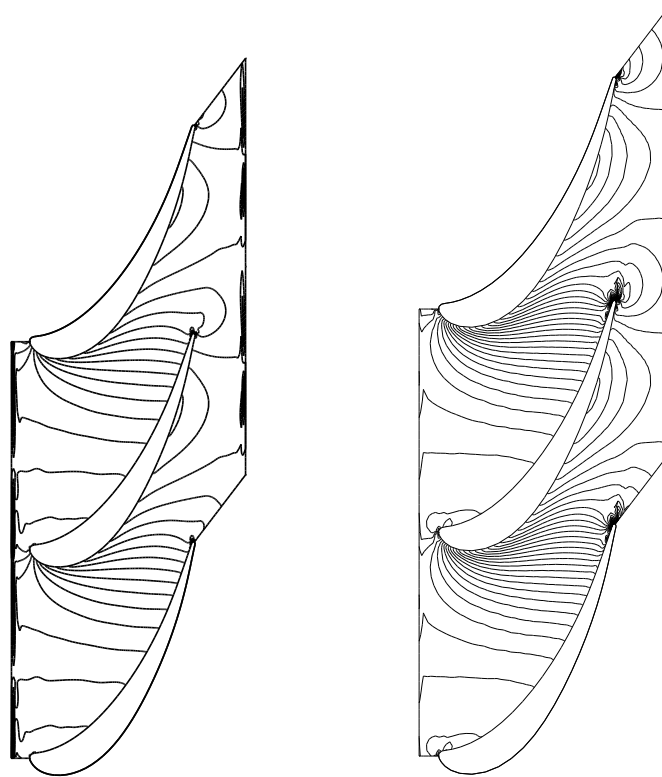


Figure 5.4: Pressure contours of the simulated flow field in the VKI-1 cascade for the isentropic outlet Mach number of $M_{is} = 0.10$ in dependence of the boundary treatment and the size of the computational domain. The fluid was modelled as an incompressible fluid ($\rho = \text{const.}$)

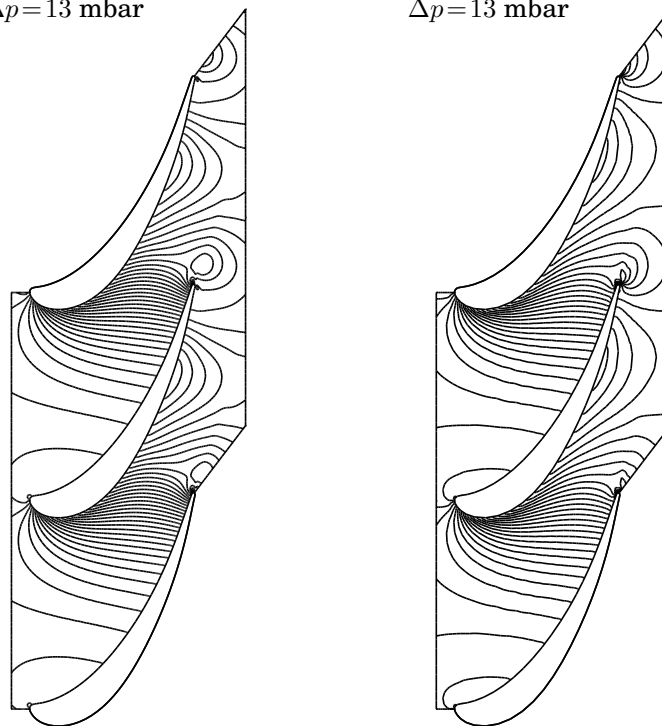
When using the novel non-reflecting boundary conditions for preconditioned systems (NRPCBC) the residuals converge well and a physical flow field is obtained. In Fig. 5.5d the isolines of the calculated static pressure are depicted.

The problems encountered when a reflective or a non-consistent boundary treatment is used, are worsened when the Mach number decreases. Furthermore, since setting ϵ_{pgr} to a value greater than unity is nothing other than reducing the preconditioning, the presented results show that the new boundary conditions are indispensable, when low Mach number flow is to be computed with time-derivative preconditioning methods.



(a) 1DmPCBC-PC,
 $\Delta p = 13$ mbar

(b) NRBC-PC,
 $\Delta p = 13$ mbar



(c) NRBC-PC,
 $\Delta p = 313$ mbar

(d) NRPCBC-PC,
 $\Delta p = 13$ mbar

Figure 5.5: Lines of constant pressure of the computed flow fields using different boundary condition treatments

Chapter 6

Analysis of leakage flow effects in axial turbomachinery

The solution scheme developed in the current work is in this chapter applied to study the interaction of the leakage and main flow in a $1\frac{1}{2}$ stage low-speed axial turbine with a shroud on the rotor row. The use of a preconditioned solution scheme with non-reflecting boundary conditions is important for obtaining reliable results as the Mach number level is low ($M = 0.05 - 0.15$) and there are three blade rows. The test turbine is situated at the Chair of Steam and Gas Turbines (DGT) of the Ruhr-University Bochum and the aerodynamics of this turbine was subject to investigation in several projects on leakage flow effects („Deckbandströmungsgeinfluss I-III“) funded by Forschungsvereinigung Verbrennungskraftmaschinen (FVV) in which the present author was involved in the numerical investigations [6, 7, 9, 10, 13, 14, 19, 92, 202, 207, 208, 310]. The analysis presented in the following originates from the aforementioned projects and contributes to the understanding of the interaction of leakage flow and main flow in axial turbomachinery.

6.1 Description of the shrouded, low-speed axial turbine and available experimental data

The turbine considered in the current work is a $1\frac{1}{2}$ stage axial low-speed air turbine comprising of inlet guide vane, rotor and stator blade rows. It is operated in a test rig at the Ruhr-University of Bochum. The turbine consists of two identical stator blade rows and a rotor with a labyrinth seal on the shroud in between them; see Fig. 6.1 for a three-dimensional plot of the turbine geometry. The prismatic profile of the turbine blades was taken from the tip-section of an industrial gas turbine rotor-blade.

The air through the turbine passes a filter and is straightened and aligned before it enters the measurement plane M0 ahead of the first stator. It is drawn through the turbine by a centrifugal blower located downstream of last measurement plane A1. In order to examine the effect of the influence

of the seal clearance height and to keep a constant cavity depth, the casing surface and not the wall separating the adjacent cavities was cut back in the experiments (Fig. 6.2).

Figure 6.3 shows also a meridional view of the turbine and its measurement planes. The axial distance between two adjacent blade rows corresponds to 59.2% of the axial chords, which is considerably larger than in normal practice, to allow space for measurement instrumentation. The test rig is operated at peak efficiency condition (design condition) with a rotor speed of $n = 500$ rpm. Additional operational data are listed in Table 6.1.

The flow fields in the planes M1, M2 and M3 were measured with a pneumatic 5-hole probe at defined inlet and outlet conditions in M0 and A1 for two different clearance heights, $s_{cl} = 1$ mm ($s_{cl}/D = 0.07\%$) and $s_{cl} = 3$ mm, respectively. In these planes time-accurate measurements were also carried out for the largest clearance height using special triple-hot-wire probes. A detailed description of the test rig and the extensive steady-state experimental data available can be found in the report of Pfost et al. [207].

Number of rotor blades	N_{rot}	36	Reynolds number	Re	$4 \cdot 10^5$
Number of stator blades	N_{st}	37	Stagger angle	β_{Bi}	37.5°
Chord length	s	163 mm	Rotational speed	\dot{n}	500 rpm
Axial chord length	s_x	101.2 mm	Rotor velocity (midspan)	$v_{\phi,rot}$	39 m/s
Blade height	H	170 mm	Flow coefficient	$\phi = v_x/v_{\phi,rot}$	0.35
Aspect ratio	H/s	1.043	Stage loading coefficient	$\psi = 2\Delta h_s/v_{\phi,rot}^2$	2.4
Mean diameter	D	1490 mm	Reaction	r	0.46
Hub/tip radius ratio	D_i/D_o	0.795			
Clearance height	s_{cl}	1 mm/3 mm			

Table 6.1: Test rig specifications [6]. Geometrical and operational data

6.2 Modeling of the shrouded turbine

6.2.1 Grids, geometrical modelling and boundary conditions

The $1\frac{1}{2}$ stage axial turbine with a generic labyrinth seal on the rotor was discretized using a block-structured grid. In Fig. 6.4 the block topology and the positions of the mixing planes are shown. Each of the individual blocks is an H-type grid with hexahedral cells. Except for the mixing planes, the block-interfaces are conformal, i.e., the grid points at the intersection of adjoint blocks overlap. Fig. 6.5 shows some views of the grid used for the simulation of the turbine for a clearance height of $s_{cl} = 3$ mm.

The numerical grids used for the discretization of the $1\frac{1}{2}$ stage turbine consist of 700 000 grid points in total. These grids were obtained from fine

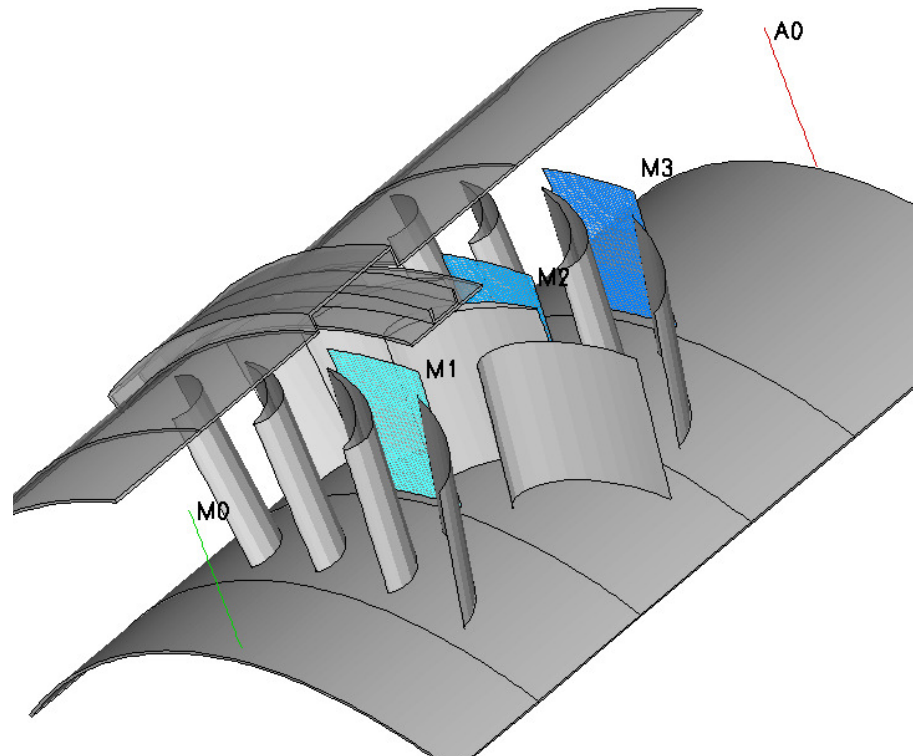


Figure 6.1: 3D-plot of the turbine geometry and indication of the measurement planes

meshes with 5.4 million grid points that were used in a grid independence study by deleting every other grid line. The clearance height of the stator seals is 0.1 mm. Since the experimental data has shown the stator hub leakage flows to be negligible, the stator seals were not modeled.

At the inlet plane (M0) the measured radial distribution of total pressure and temperature and axial flow direction is specified. For the outlet boundary in A1 the measured radial distribution of the static pressure is prescribed. Solid surfaces are assumed to be isothermal, and the no-slip condition is applied. Periodicity in the pitch-wise direction is ensured using phantom cells that keep copies of the periodic values such that the points on these boundaries can be treated like interior points.

In the current work the labyrinth geometry is completely discretized. In the work of Anker et al. [14] a numerical model for labyrinth seals was developed, with which a discretization of the labyrinth seal can be avoided. The results of this study are summarized in Appendix H. Even though good results were obtained in the aforementioned study, a simplified modelling is not suitable when the computational results are to be used for studying phenomenological effects.

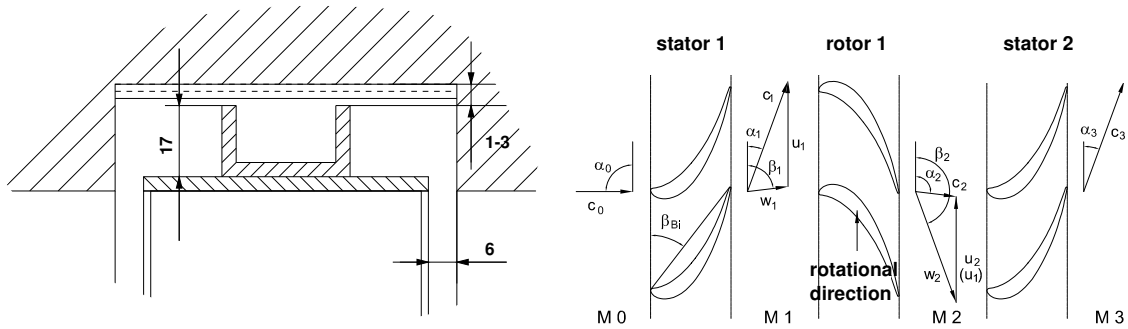


Figure 6.2: Turbine and labyrinth seal geometry, and the definition of flow angles

6.2.2 Numerical modeling

The equations solved are the three-dimensional Favre-averaged Navier-Stokes equations. They are formulated in a cylindrical coordinate system that rotates at a constant angular velocity. The fluid was modelled as a perfect gas and a modified algebraic Baldwin-Lomax model is used to describe the effect of turbulence.

Due to the presence of low Mach numbers flow in the turbine, the preconditioned solution scheme described in Chapter 3 was used. In order to prevent spurious reflections at the inlet and outlet boundaries and at the mixing planes the developed non-reflecting boundary treatment described in Chapter 5 is used. For the purpose of obtaining a good resolution of the flow field and simultaneously avoiding overshoots of the solution variables near the boundary layers, the Roe scheme, which was extended for the use in conjunction with Merkle's time derivative preconditioning method (Chapter 4), was employed in combination with a third order variable extrapolation and the van Albada limiter.

The interactions of the main flow, the leakage and the cavity flow due to the presence of the upstream and downstream stators are in the present turbine configuration relatively small due to the large axial gaps between the blade rows. As demonstrated in the work of Anker et al. [13] and as shown in a summarized fashion in Appendix I, it is sufficient to conduct steady state simulations in order to capture the time-average of the impact of the leakage flow on the main flow. For this reason, the analysis of the interaction between leakage and main flow focuses on results obtained from steady state simulations.

6.3 Validation of the computational results

To verify that the solver ITSM3D captures the important effects when leakage flow interacts with the main flow, the calculated circumferentially averaged

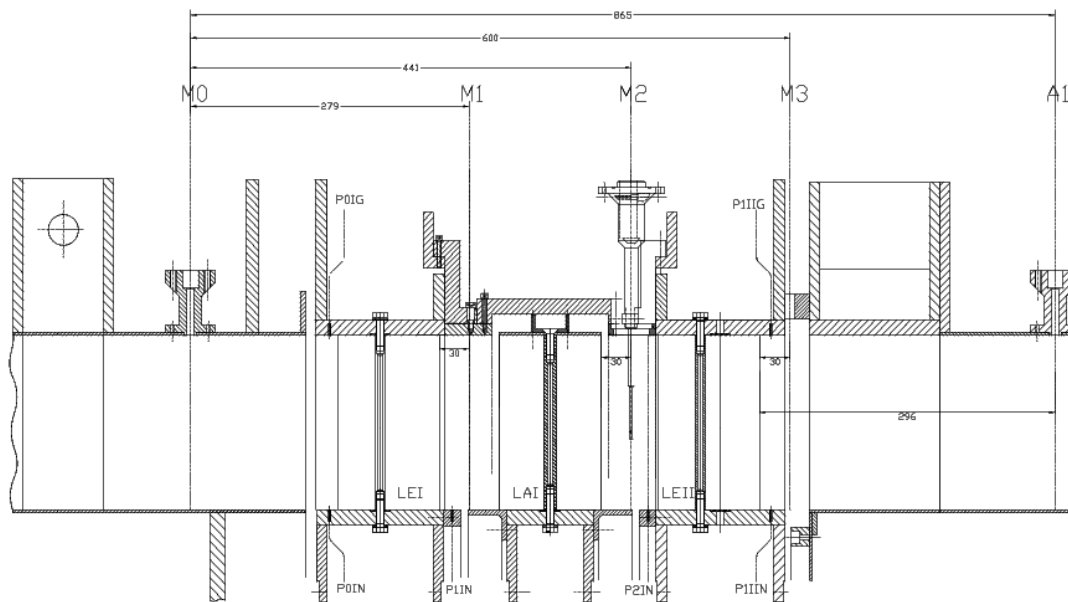


Figure 6.3: Location of the measurement planes

velocities at the measurement planes M2 and M3 are compared to the data obtained experimentally in the Bochum test facility for a clearance height of $s_{cl} = 3 \text{ mm}$, see Figs. 6.6 and 6.7. With the exception of the computational results denoted as "fine" (obtained on the fine grids with 5.6 Mio. grid points), the results used in this study were computed on meshes with 700 000 grid points. The results confirm that the solutions used in this study can be regarded as grid independent.

As with all other plots in this chapter, the velocities presented are normalized with the circumferential velocity $v_{\phi, \text{rot}}$ ($v_{\phi, \text{rot}} = 39 \text{ m/s}$) of the rotor at midspan and denoted with an asterisk "*". The measurement planes M2 and M3 are positioned at a distance of 30 mm behind the trailing edge of the rotor and the second stator, respectively. Since the flow field in M1 (30 mm behind the trailing edge of the first stator) is nearly invariant of the clearance height (cf. [6]), those results are omitted for brevity.

The measured circumferentially averaged axial velocity in M2 depicted in Fig. 6.6a reveals that there is a reduced throughput in the hub region of the rotor. The slightly reduced axial velocities near the hub are due to the hub-side passage vortex which causes an overturning of the main flow. Figure 6.6b shows the occurrence of large circumferential velocities in the casing region incurred by the injection of leakage flow with large components of swirl.

The measured and predicted circumferentially averaged axial and circumferential velocities in M3 are depicted in Fig. 6.7. Obviously, the flow solver overpredicts the under- and overturning of the flow caused by the upper secondary channel vortex (near the casing) and this may be due to a weakness of the Baldwin-Lomax turbulence model.

The computational results for a clearance height of $s_{cl} = 1 \text{ mm}$ are in similar

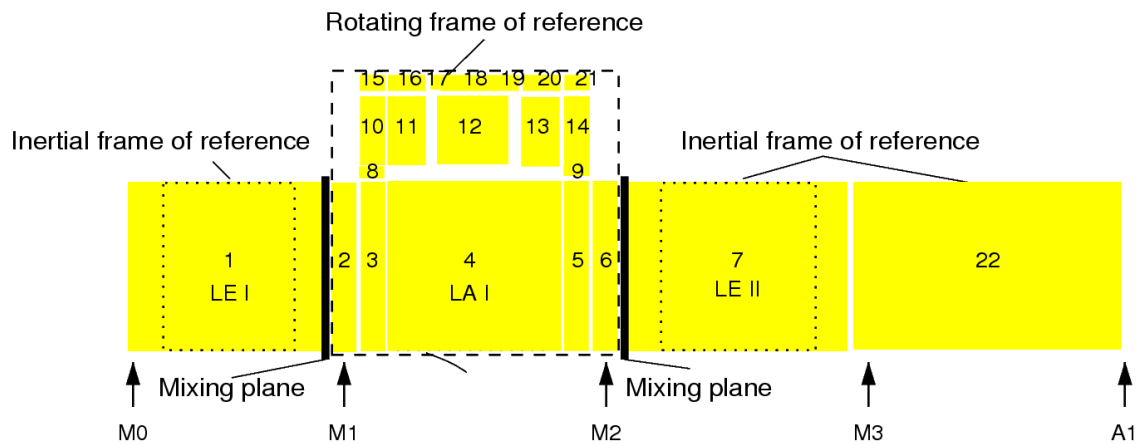


Figure 6.4: Block topology and the position of the mixing planes

good agreement with the measurement data and this justifies the use of the numerical results for discussing different aspects of the interaction of leakage flow with the main flow in the turbine considered. Additionally, it should be noted that the present results were compared with results computed with CFX-5 in the work of Söğüt [256]. The good agreement between the simulations of two different flow solvers furthermore confirms the validity of the results used in the following study.

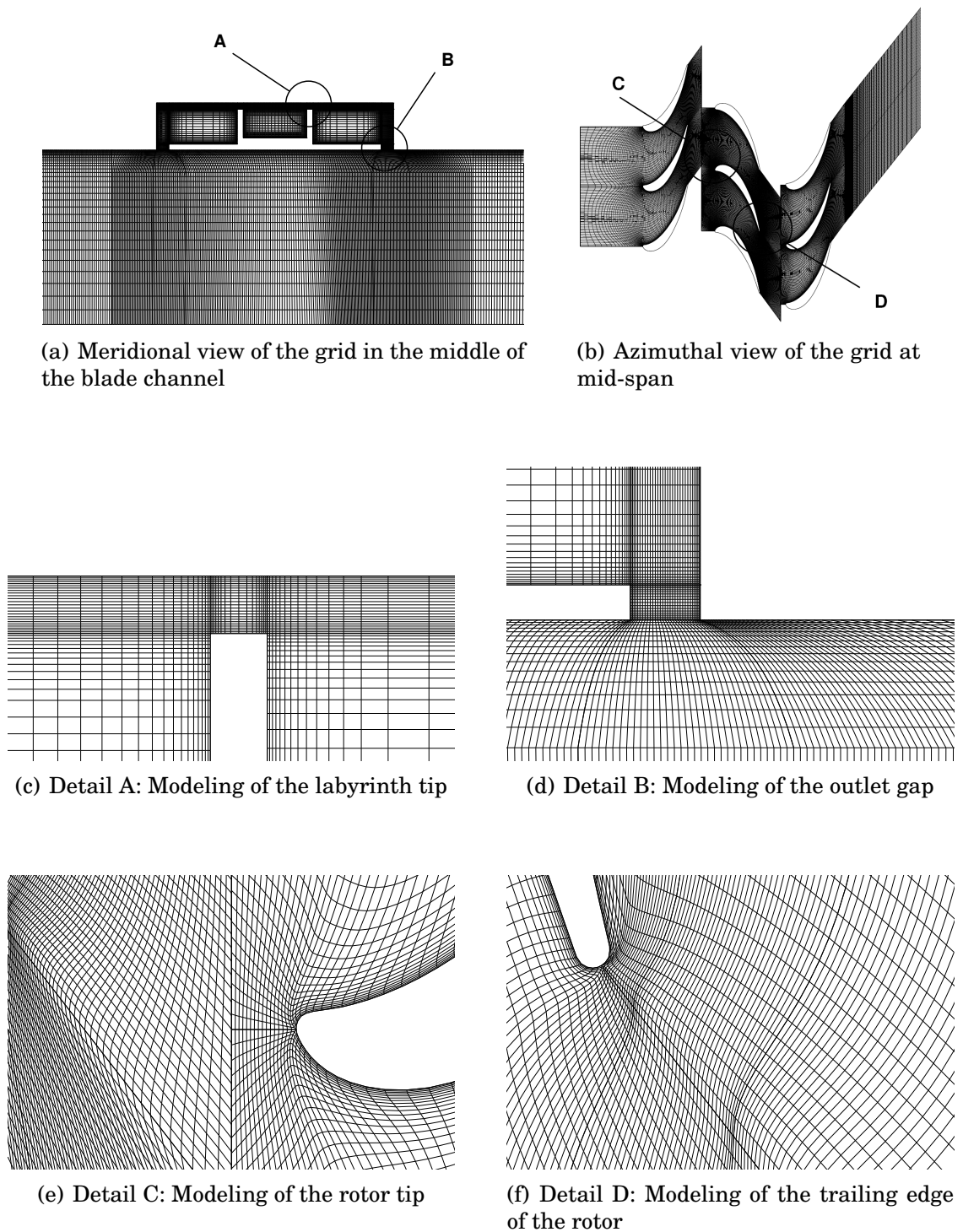
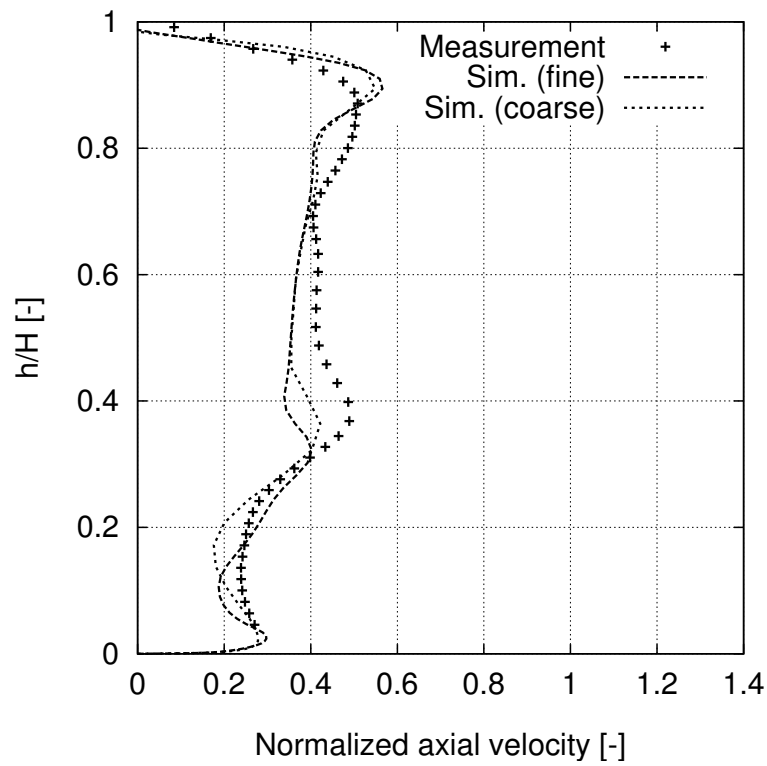
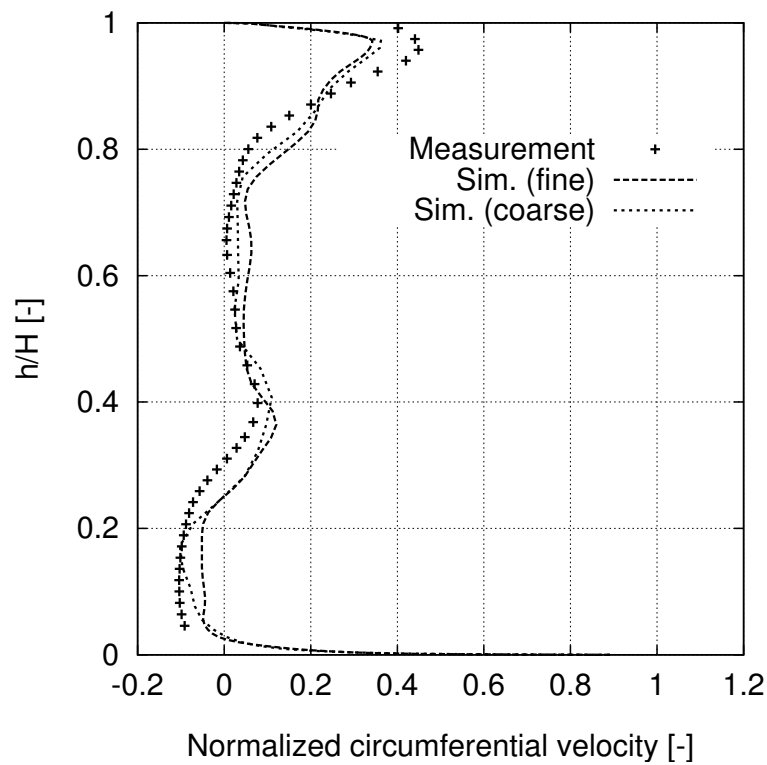


Figure 6.5: Computational grid (reduced) for a clearance height of $s_{cl} = 3 \text{ mm}$

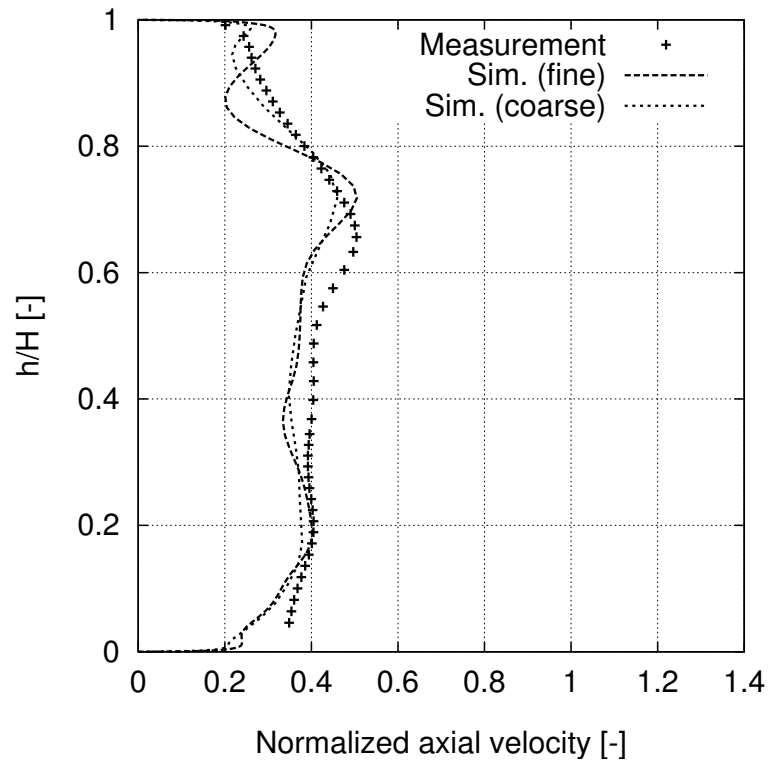


(a)

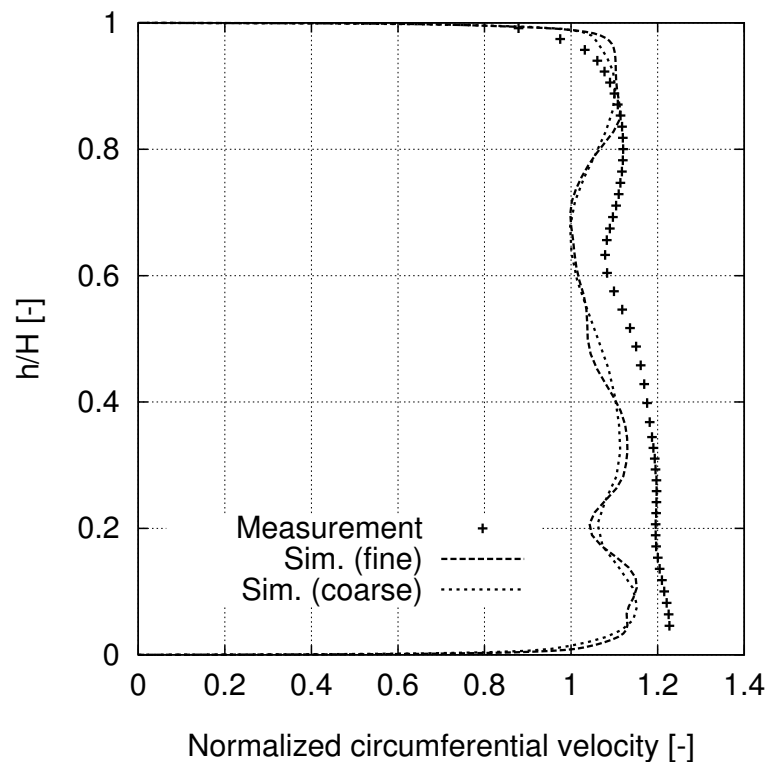


(b)

Figure 6.6: Measured and simulated circumferentially averaged normalized axial v_x^* and circumferential v_ϕ^* velocity components in M2 at a clearance height of $s_{cl} = 3$ mm



(a)



(b)

Figure 6.7: Measured and simulated circumferentially averaged normalized axial v_x^* and circumferential v_ϕ^* velocity components in M3 at a clearance height of $s_{cl} = 3$ mm

6.4 Relative importance of the geometrical parameters of the labyrinth seal

The influence of the various geometrical parameters of the labyrinth seal were investigated in the work of Anker et al. [14]. A short summary of the main results of that study can be found in Appendix G. One finding presented in the aforementioned publication was that the leakage flow effects are primarily dependent on the labyrinth seal leakage height s_{cl} . For this reason the labyrinth seal leakage height is the only geometrical parameter that is changed in the following study of the interaction between the leakage and the main flow.

6.5 Analysis of the interaction between leakage, main and secondary flow

In this section the computational results for four different configurations of the sealing arrangement of the rotor row are analysed, compared and discussed. The first two simulations for a tip clearance gap of $s_{cl} = 1$ mm and $s_{cl} = 3$ mm identify the effect of the leakage flow on the main flow and have already been addressed above. The second two identify the interaction of the cavity flow with the main flow. Both of these have no leakage flow (tip clearance gap of $s_{cl} = 0$ mm), whereby in one case a smooth rotor casing with no cavity is considered and in the second case the cavity at inlet and exit of the rotor shroud seal is included in the numerical model.

6.5.1 The impact of the leakage flow on the main flow

For the largest clearance height ($s_{cl} = 3$ mm) the leakage flow over the rotor shroud experiences nearly no net deflection. This is visible from Fig. 6.8 in which the streamlines of the flow passing through the labyrinth seal of the rotor row are visualized in the rotating frame of reference. When this leakage flow re-enters the main flow it leads to an increase of tangential momentum near the casing. This becomes evident from Fig. 6.9, where the difference between the simulated circumferential velocities for a clearance height of $s_{cl} = 3$ mm and $s_{cl} = 0$ mm are plotted in the measurement plane M2.

The ingress of leakage flow with a high component of swirl after the rotor leads to high suction side incidence (negative incidence) in the tip-region of the following stator row. This can be seen from Fig. 6.10 in which the streamlines of the flow around the second stator are visualized. The leakage flow through the seal experiences the same pressure drop over the rotor as the main flow but as no work is extracted this leads to increased velocities in the re-injected flow near the casing (Fig. 6.11).

The leakage flow re-enters the main flow from the downstream cavity preferentially on the suction side of the blade (Fig. 6.12). Due to the slower moving fluid in the wake, the leakage jet penetrates more deeply there than in

the mid-channel. For a clearance height of $s_{cl} = 3$ mm the leakage flow leads also to a reverse flow on the casing between the reentering leakage jet and the suction side of the rotor blade [12, 14]. The flow blockage that arises reduces the flow velocity on the suction side of the rotor flow near the tip (Fig. 6.13).

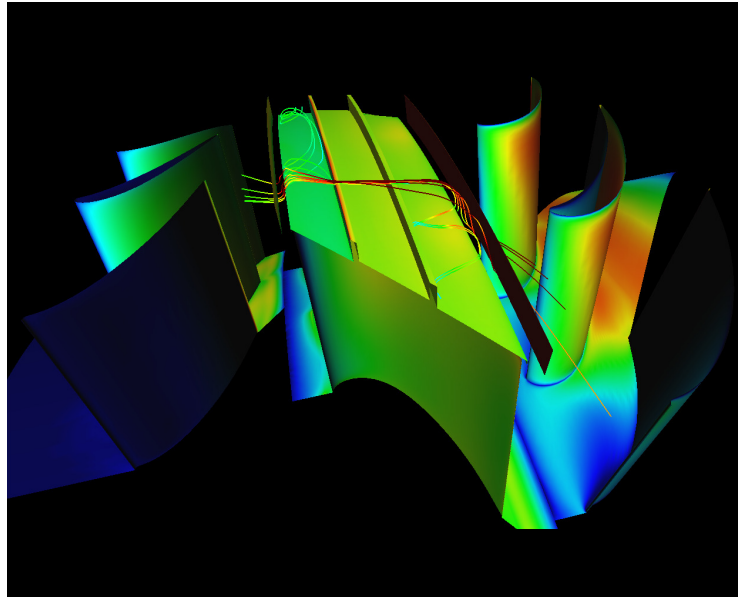


Figure 6.8: Undeflected streamlines in the labyrinth seal

6.5.2 Interaction between the potential field of the rotor and the cavity flow

In Fig. 6.14 the calculated radial velocities in the inlet and outlet planes of the labyrinth seal are plotted for the simulations with different clearance heights of the labyrinth seal. The location of the labyrinth inlet and outlet planes is sketched in Fig. 6.15. The largest positive radial velocity components (extraction from main flow) are found in the pressure region of the blades and the largest negative components (re-injection of leakage flow) are found in the vicinity of the suction side. For the smallest clearance heights of $s_{cl} = 0$ mm and $s_{cl} = 1$ mm the leakage flow re-enters the main flow at the labyrinth inlet plane, whereas for all clearance heights reverse flow situations occur at the outlet cavity.

The circumferential variation of the radial velocity components at the inlet and outlet planes of the cavities are caused by the potential field of the rotor. In the available time-accurate numerical results on this test case [8], this inhomogeneous distribution is the steady part of the rotor flow field in the rotating frame of reference. The time-accurate simulations show that unsteady perturbations are superimposed on this distribution by the wake of the upstream vane and the potential fields of both stator rows, but that these effects are small due to the large axial distance between the stator and rotor

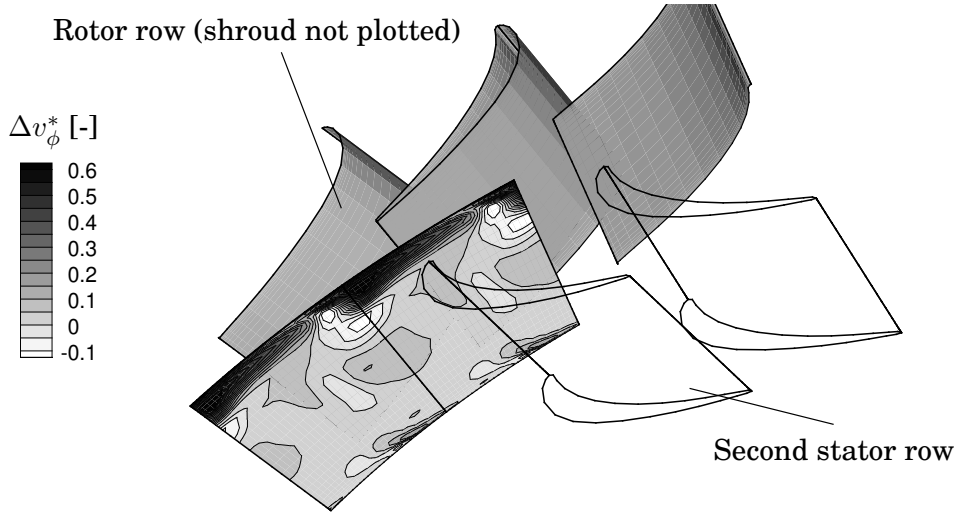


Figure 6.9: Difference Δv_ϕ^* between the simulated normalized circumferential velocities in M2 (30 mm downstream of the rotor) for a clearance height of $s_{cl} = 3$ mm and $s_{cl} = 0$ mm

rows. For a detailed discussion of the effect of the potential effects of the stator and the rotor row on the leakage flow, the reader is referred to the work of Anker et al. [8, 14].

6.5.3 Consequences of the leakage flow extraction on the secondary flow field of the rotor

The extraction of leakage flow has a negligible effect on the flow field in the first stator. In the rotor row the extraction of leakage flow leads to a removal of the slowly moving fluid on the shroud wall, such that there is a reduction of the boundary layer thickness at the casing wall of the rotor. This affects the development of the upper secondary channel vortex, as can be seen from Fig. 6.16 where the helicity H of the relative velocity vector field $w_i = w_i(x, y, z)$ defined as

$$H = w_i \cdot \omega_i, \quad \omega_i = \epsilon_{ijk} \frac{\partial w_k}{\partial x_j} \quad (6.1)$$

is plotted at an axial plane in the middle of the rotor as a function of the clearance height. Since the norm of the vorticity $\|\omega_i\|$ is a measure of the strength of the secondary flow, the helicity represents the rate of transport of secondary flow. Helicity has the advantage over vorticity that it identifies secondary flows more clearly than vorticity. Unlike the vorticity which is induced by the no-slip walls and has its maximum there, the helicity vanishes at the walls since the vorticity and velocity vector fields are orthogonal to each other in sheared layers.

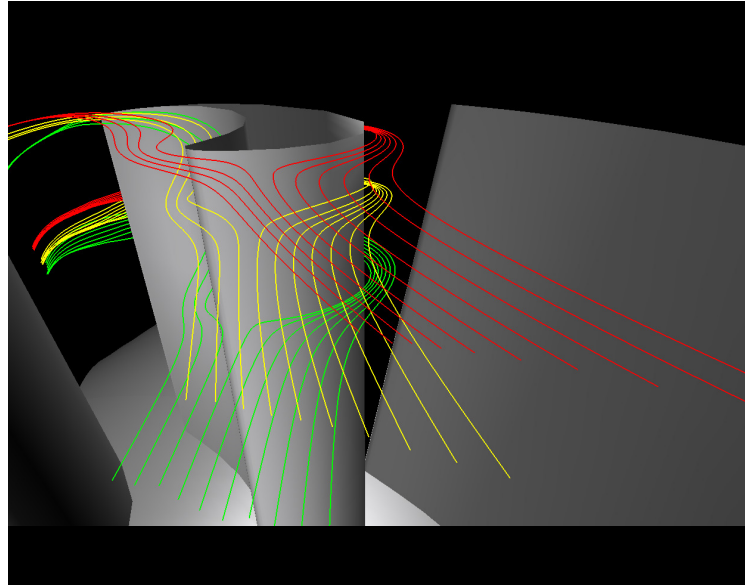


Figure 6.10: Calculated streamlines, showing a suction-sided incidence of the second stator caused by leakage flow

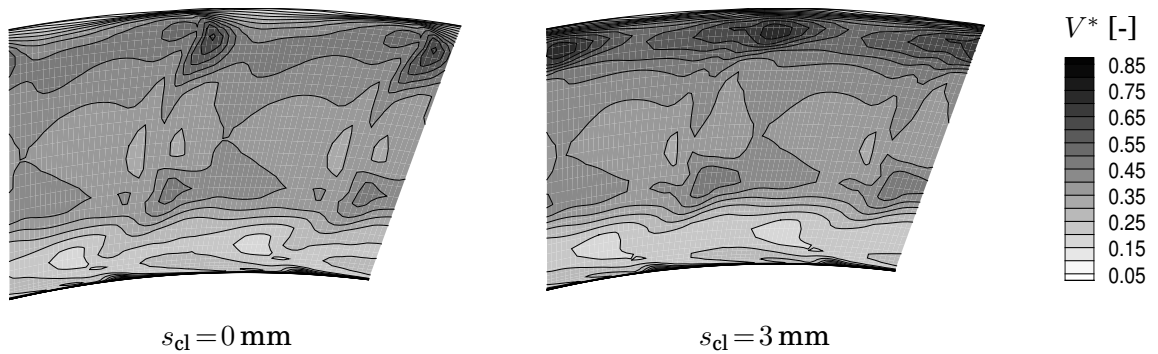


Figure 6.11: Magnitude V^* of the normalized absolute velocities in the measurement plane M2 (30 mm behind the rotor)

An increase in the shroud clearance height reduces the strength of the upper channel vortex such that the relative secondary kinetic energy decreases from the measurement plane M1 up to the axial midplane MP in the rotor, as can be seen from Table 6.2. The secondary kinetic energy coefficient is thereby defined as

$$\zeta_{\text{sec,MP-M1}}^{\circ} = \frac{E_{\text{sec,MP}}^{\circ} - E_{\text{sec,M1}}^{\circ}}{E_{\text{MP}}^{\circ} - E_{\text{M1}}^{\circ}} \quad (6.2)$$

where E° and E_{sec}° denote the kinetic energy of the main and secondary flow of the rotor, respectively. The secondary flow vectors were calculated as described in the report of Anker et al. [6]. The secondary kinetic energy coefficients have been used to identify changes in performance as they appear to be more reliable than predicted losses [114]. This method determines the strength of the secondary velocities at a point in the flow from the difference

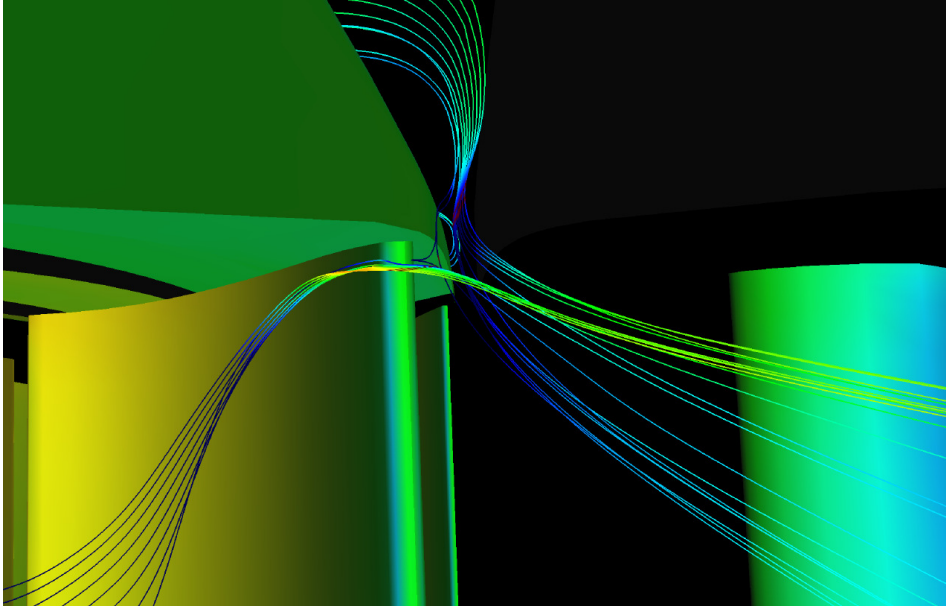


Figure 6.12: The leakage flow re-entering the main flow behind the rotor

Clearance height	$\zeta_{\text{sec,MP-M1}}^{\circ}$ [%]	$\zeta_{\text{sec,M2-M1}}^{\circ}$ [%]	$\zeta_{\text{M3-M2}}$ [%]
3 mm	-0.53	4.94	4.99
1 mm	-0.16	2.44	2.65
0 mm (w/o cavity)	0.83	1.65	2.84
0 mm (with cavity)	1.34	1.76	2.40

Table 6.2: Secondary kinetic energy coefficients for the rotor and the second stator row

between the local velocity vector and the main flow vector. The direction of the main flow is defined by the circumferential average of the pitch angle and by the spanwise average of the yaw angle for this point.

It should be noted that for the clearance heights of $s_{\text{cl}} = 1$ mm and $s_{\text{cl}} = 3$ mm the secondary kinetic energy coefficients $\zeta_{\text{sec,MP-M1}}^{\circ}$ have negative values, which implies that the extraction of leakage flow leads to a homogenization of the secondary flow field. Paradoxically, the secondary flow losses in the rotor tend to decrease with increasing tip gap as the leakage flow removes more of the endwall boundary layer.

6.5.4 Consequences of the leakage flow re-injection on the secondary flow field of the rotor

The re-injection of leakage flow strongly influences the secondary flow field in the casing region downstream of the rotor. This can be seen from Fig. 6.17a and 6.17b where the helicity in M2 is plotted for a clearance height of $s_{\text{cl}} = 0$ mm (with cavities) and $s_{\text{cl}} = 3$ mm, respectively. A positive helicity corresponds to a clockwise rotation of the flow seen from the perspective of a particle moving with the flow. Consequently, the white region near the cas-

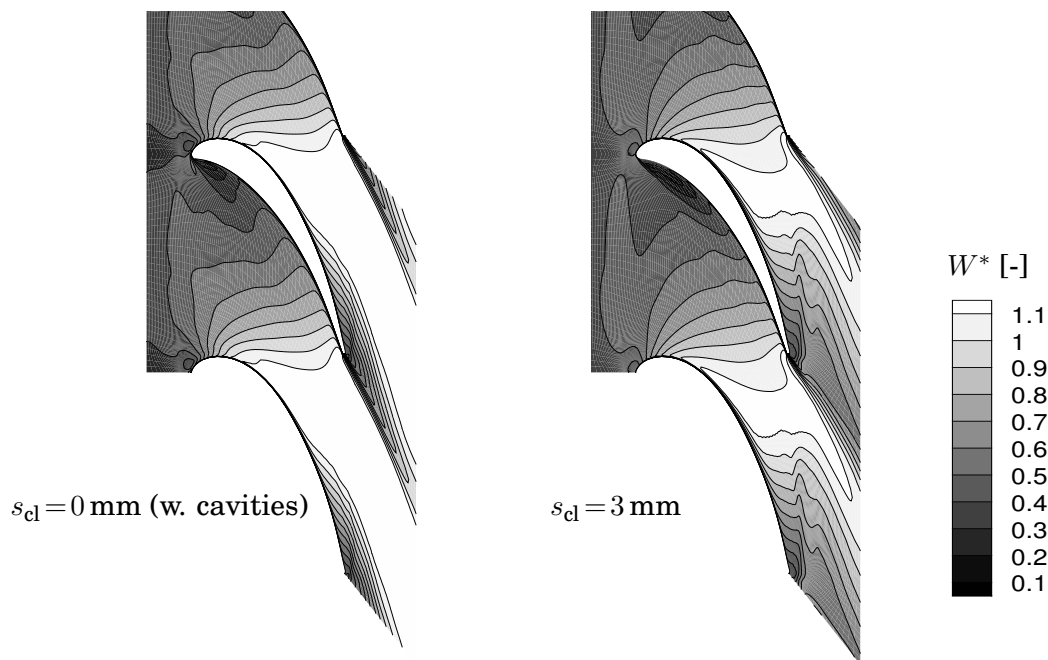


Figure 6.13: Magnitude W^* of the normalized velocities in the rotor system near the casing ($h/H=0.95$)

ing represents the upper secondary flow vortex. In Fig. 6.18a the simulated helicity for $s_{cl} = 0$ mm (with cavities) is subtracted from the simulated helicity for a clearance height of $s_{cl} = 3$ mm. Obviously, the circumferentially non-uniform leakage flow strengthens the upper channel vortex and leads to a more pronounced neighbouring trailing edge vortex. This effect leads to increased secondary kinetic energy coefficients in plane M2 (cf. Table 6.2). Thus, the re-injection considerably outweighs the benefits of the extraction of leakage flow discussed above, such that leakage flow leads to a net increase in the secondary losses over the rotor.

6.5.5 The impact of the presence of cavities on the formation of the secondary flow field

The changes in the rotor secondary flow field are not only caused by the leakage flow but also by the mere presence of cavities. When cavities are present, and the clearance height is of moderate size, the flow leaves the main flow on the pressure side and re-enters on the suction side of the rotor at both the inlet and the outlet cavity. This strengthens the secondary channel vortex in this region leading to an increased kinetic energy of the secondary flow field in the rotor. A comparison of the computed helicity in the axial midplane MP in the rotor for a vanishing clearance height with and without cavities (Figs. 6.16a and 6.16b) shows that the first cavity of the labyrinth seal is responsible for a strengthening of the upper channel vortex and for an increase in the secondary kinetic energy coefficient (cf. Table 6.2).

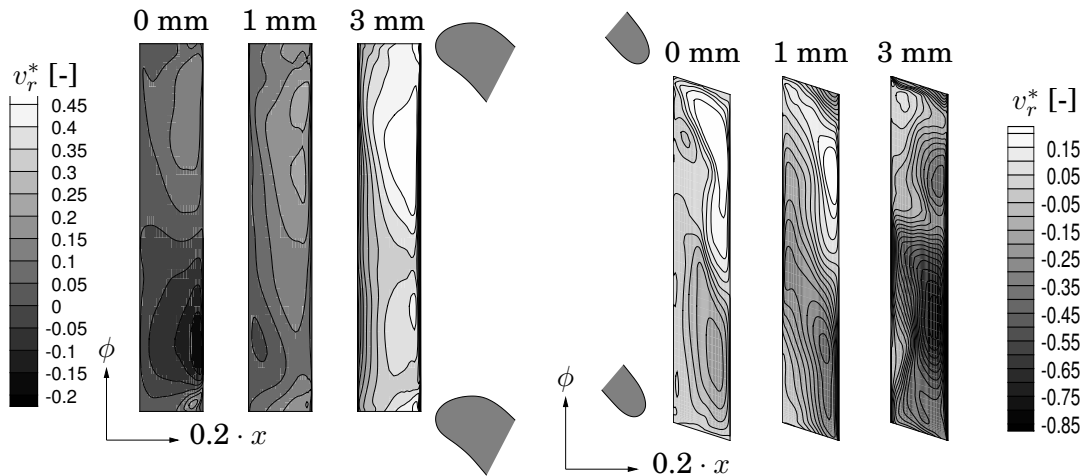


Figure 6.14: Normalized radial velocities v_r^* . Labyrinth inlet plane (left), labyrinth outlet plane (right)

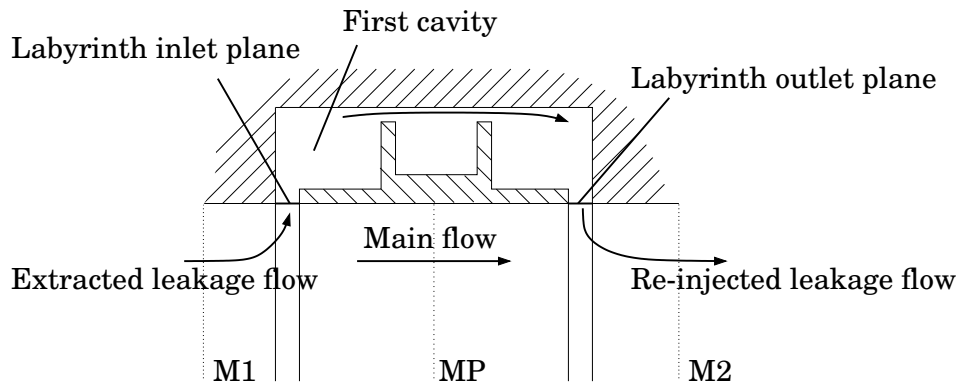


Figure 6.15: Location of the axial midplane MP in the rotor and the inlet- and outlet planes of the labyrinth seal

The presence of cavities does not lead to such a pronounced effect in the secondary flow field behind the rotor. As can be seen from Fig. 6.18b, where the difference in the simulated helicity for zero clearance height with and without cavities is plotted in M2, the presence of cavities reinforces the upper channel vortex. However, this effect only leads to a marginal change of the secondary kinetic energy coefficient. (It should be noted, that the helicity differences are plotted over a smaller range in Fig. 6.18b than in Fig. 6.18a.)

6.5.6 Impact of the Leakage Flow on the Secondary Flow Field in the Second Stator Row

The formation of secondary flow in the second stator is strongly influenced by the leakage flow. The helicity of the simulated flow fields in M3 (30 mm behind the second stator) for a clearance height of $s_{cl} = 3$ mm and $s_{cl} = 0$ mm is depicted in Fig. 6.19. A negative value for the helicity corresponds to a counterclock-

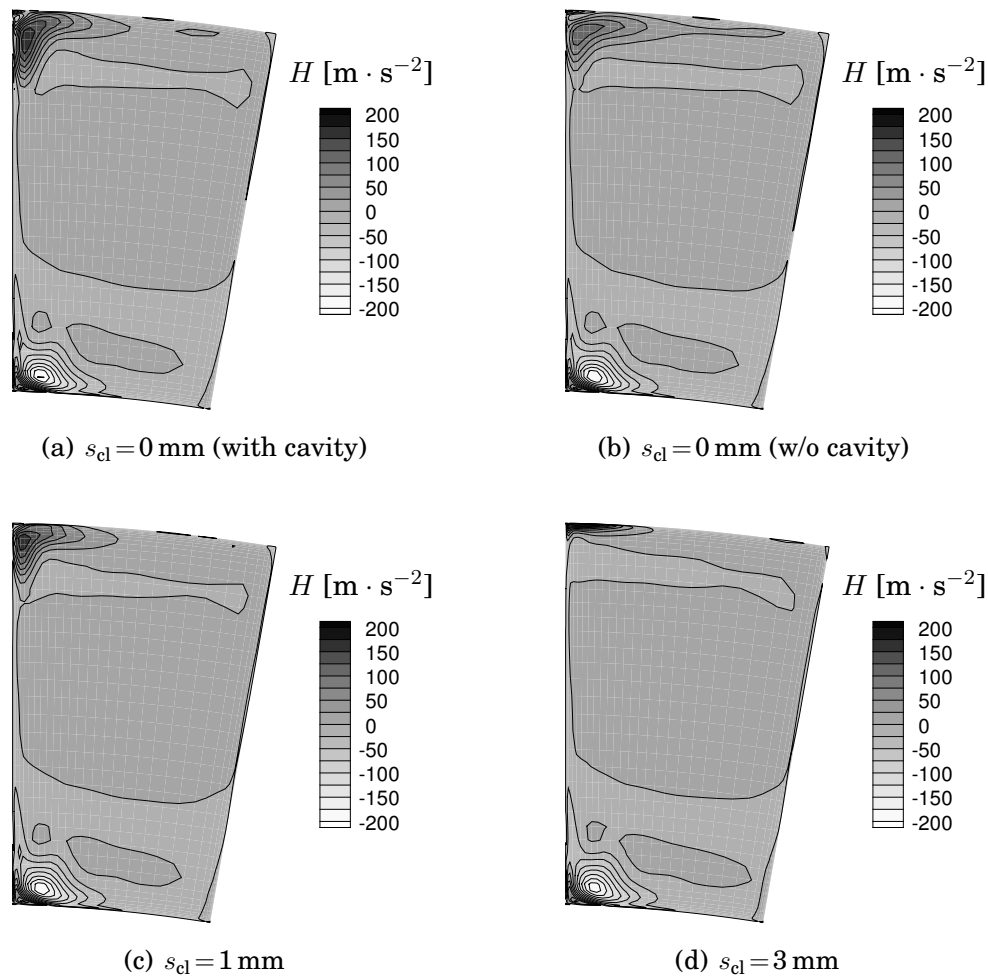


Figure 6.16: Helicity H in an axial plane in the middle of the rotor

wise rotation of the flow seen from the perspective of a particle moving with the flow. Thus, the upper channel secondary vortex can be identified by dark regions in the casing region. Apparently, the leakage flow gives rise to a magnification of the upper channel vortex, which also leads to an increased secondary kinetic energy coefficient, cf. Table 6.2. There are two reasons for this. Firstly, the leakage flow has a high swirl and causes a suction side incidence on the upper part of the second stator row. This generates a positive radial pressure gradient on the suction side and a negative radial pressure gradient on the pressure side, and this strengthens the driving mechanisms responsible for the development of the channel vortex. Secondly, the re-injection of leakage flow into the main flow behind the rotor leads to a recirculation zone which causes a thickening of the boundary layer ahead of the second stator. This thickening of the inlet boundary layer of the second blade row also augments the upper channel secondary vortex with an increase in the clearance height.

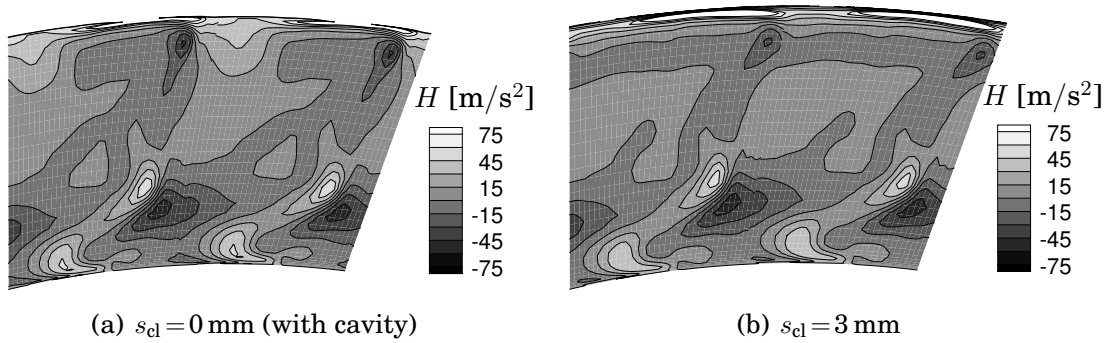


Figure 6.17: Helicity H in M2 (30 mm behind the rotor)

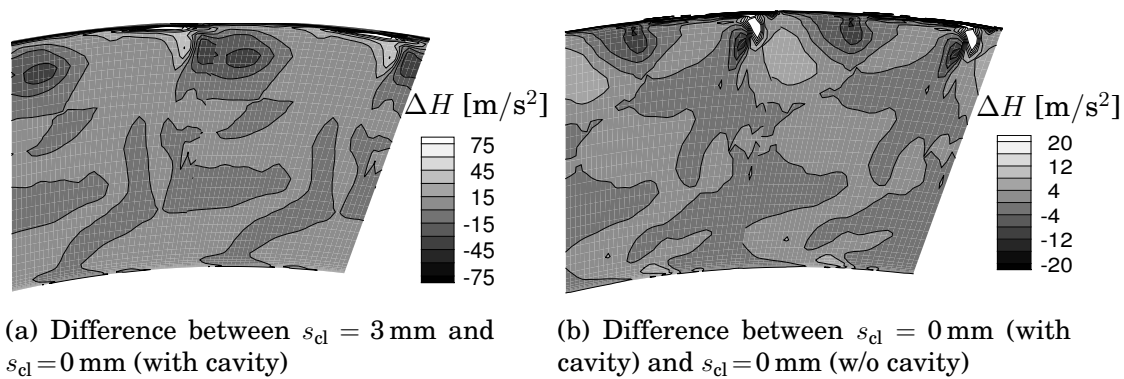


Figure 6.18: Helicity differences ΔH in M2 (30 mm behind the rotor)

6.6 Discussion of the results and consequences for the design of shrouded axial turbines

From the results presented above, several possible design improvements in shrouded axial turbines can be identified. Firstly, the leakage flow from the exit cavity should not be forced to enter radially into the main flow but should have more inclination in the axial direction to avoid the effects of flow blockage. Secondly, to avoid the negative effects incurred by the excess swirl in the leakage flow upon reentry in the main flow, it could prove advantageous to install deflectors on the casing immediately after the outlet of the labyrinth seal. Alternatively, for large clearance heights one might install turning devices directly on the shroud to lower the swirl of the leakage flow and simultaneously to extract work. In either case, the inlet of the labyrinth seal should be designed such that primarily near-wall fluid with a low level of swirl and exergy is extracted from the main flow. Furthermore, since not only the leakage flow but also the mere presence of cavities induces losses, the shape of the inlet and outlet cavities of the labyrinth seals must be considered with care in the design.

If the injection of leakage flow with a high level of swirl can not be avoided,

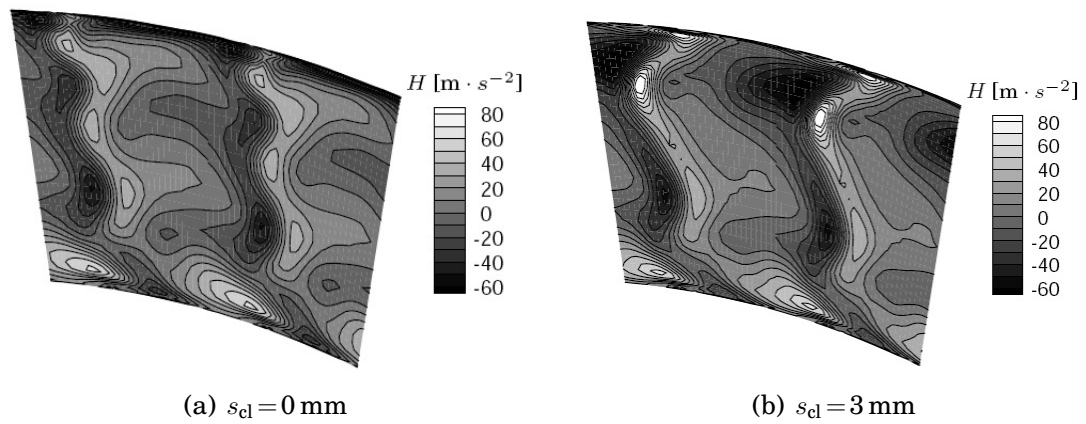


Figure 6.19: Helicity H in M3 (30 mm behind the second stator)

it would be important to twist the tip-section of the blade row following the labyrinth seal. In this case suction side incidence on the following blade row and subsequent increase in the aerodynamic losses could be avoided.

Chapter 7

Summary and conclusions

In this thesis a numerical scheme for the solution of the Navier-Stokes equations for the simulation of flows in turbomachinery at arbitrary Mach numbers is presented. The developed numerical methods are implemented in a density based solution scheme, which was originally concipated for the simulation of transonic flows in rotating machines. To ensure that the solution scheme is efficient and accurate at all Mach number levels, a time-derivative preconditioning method is incorporated in the solution scheme. In the present work the finite volume discretization and the applied time-stepping scheme are described, details of the preconditioning method are given, and general issues related to the simulation of low Mach number flows are addressed.

To ensure a sharp resolution of the flow features both for low-speed as well as for transonic flows, several low dissipation schemes are developed for the robust use in the context of time-derivative preconditioning methods. In the current work, both the scalar and the matrix dissipation scheme due to Jameson, Schmidt and Turkel (JST) are adapted for the use in conjunction with preconditioning methods. As demonstrated in the current work, while the improved pressure switch due to Swanson and Turkel suppresses overshoots of the solution near shocks, these schemes fail to produce monotone solutions for boundary layers regardless which form of the pressure switch is used.

For this reason, also Roe's characteristic upwind dissipation and Liou's AUSM+ scheme are formulated for the use in conjunction with the time-derivative preconditioning scheme of Merkle. Applying a variable extrapolation and limiters, these schemes yield monotone and bounded solutions both over shocks and boundary layers. In the current work it is in particular shown how the AUSM+ upwind scheme can be applied to a cell-vertex scheme. By splitting up the convective fluxes in a central, a diffusive, and an anti-diffusive part, an approach is developed for the implementation of this scheme in a central-differencing code. To enhance the robustness of the AUSM+ scheme, a method to control the anti-diffusive part of the dissipative fluxes is devised. Common for all of the dissipation schemes implemented in the current work, is that they have been formulated for fluids with arbitrary equations of state.

In order to avoid unphysical reflections at the inlet, outlet, and mixing planes in turbomachinery simulations, a non-reflecting boundary condition

treatment should be used. In the current work the quasi-three-dimensional non-reflecting boundary condition treatment devised by Giles and Saxer was extended to preconditioned systems and general equations of state; as demonstrated in the current work, since preconditioning changes the dynamics of the governing equations, a boundary condition treatment based on the characteristics of the unscaled Navier-Stokes equations can not be used. The theory of a new boundary treatment is derived and the main aspects of the implementation are presented.

To demonstrate the accuracy and efficiency of the developed preconditioned solution scheme several test cases are presented. Varying the isentropic Mach number in the Ni-Bump test case from 0.013 to 0.85 shows that with the use of time-derivative preconditioning Mach number independent convergence rates can be obtained. While preconditioning does not impair the shock capturing property of the original solution scheme, the accuracy of density based solution methods is preserved at low Mach numbers only when preconditioning is used.

In order to assess the ability of the presented dissipation schemes of resolving viscous flows, results from the simulation of a laminar boundary layer developing over a flat plate are discussed. It is shown that the AUSM dissipation and the Roe's characteristic upwind dissipation model lead to a better resolution than the dissipation schemes based on fourth order differences (the scalar and the matrix JST dissipation schemes); furthermore the former schemes do not result in overshoots in the solution variables. However, even though the matrix dissipation scheme fails to provide a monotone solution, it clearly represents an improvement of the scalar JST-scheme.

In a third test case the simulation of the supersonic flow through a row of wedges is considered. It is shown that the scalar JST-scheme with the original pressure switch resolves shocks very well but leads to oscillations in the solution variables in the vicinity of the shock. As a remedy, a modified pressure switch which gives the scheme TVD-properties may be used, but then the increased diffusivity of the scheme reduces the crispness of the shock-front. While the use of matrix dissipation lowers the numerical diffusion and enhances the shock resolution, it is the AUSM dissipation scheme that leads to the best compromise between shock resolution ability and monotonicity of the solution scheme.

In a further test case the turbulent flow in a 1.5 stage low-speed test rig was computed. Without the use of preconditioning unphysical wiggles in the pressure field are observed. On a coarse grid the original scheme completely fails to reproduce the secondary flow effects measured, whereas the preconditioned solver captures the tendencies of the secondary flow effects and produces smooth solutions in all regions of the flow.

To validate the novel non-reflecting boundary condition treatment developed in the present work, two test cases are presented. In the first test case the viscous flow through a linear cascade with VKI-1 turbine blades are simulated at different Mach numbers. By varying the size of the computational domain it is verified that the developed boundary conditions are non-reflecting

for incompressible fluids and subsonic, ideal gas flows.

Furthermore, the flow through an isolated vane using different boundary conditions in conjunction with the preconditioned scheme is simulated. The original boundary condition treatment due to Giles and Saxer for the unscaled Navier-Stokes equations can be used in the case of an isentropic outlet Mach number of $M_{is} = 0.6$. However, the use of these unmodified boundary conditions leads to instabilities and an unphysical pressure distribution in the vicinity of the boundaries at low Mach numbers. Obviously, the original boundary treatment can only be used at compressible flow conditions, where the preconditioned equations revert to the physical ones. The benefit of the novel boundary conditions presented in this work is given by the fact, that they are the only ones that lead to stable integration and non-reflecting boundaries over a broad Mach number range.

The developed solution scheme is used to investigate the impact of rotor labyrinth seal leakage flow on the main flow and on the loss generation mechanisms in an axial turbine. After a validation of the computational results with available measurement data, a parameter study is carried out to study the influence of the geometrical parameters on the leakage flow effects. Of all parameters investigated, the labyrinth seal leakage gap has the most important effect.

A variation of the latter parameter between a vanishing and a realistic clearance height allows a systematic investigation of the impact of the leakage flow on main and secondary flow. The computational results show that the ingress of leakage flow downstream of the shrouded rotor not only leads to excess swirl but also to an increased kinetic energy in the upper part of the casing region. Furthermore, the circumferentially non-uniform re-injection of the leakage flow leads to a blockage of the main flow on the suction side of the rotor near the tip.

The influence of extraction and re-injection of the leakage flow on the secondary flow field in the rotor and downstream stator is studied. The egress of leakage flow reduces the boundary layer thickness on the casing wall of the rotor which weakens the upper secondary channel vortex in the rotor channel. However, the non-uniform re-injection of leakage flow strengthens this vortex and leads to an overall increase of the losses in the rotor. The high swirl of the leakage flow causes a suction side incidence onto the following stator row and thus gives rise to radial pressure gradients. The re-injection of leakage flow also leads to a recirculation zone after the rotor, which results in a thickening of the boundary layer ahead of the second stator. Both effects are responsible for the amplification of the upper secondary channel vortex in the subsequent stator.

The effect of the inlet and exit cavities on the rotor flow field is also studied. It is shown that, when cavities are present and the clearance height is of moderate size, the flow leaves the main flow on the pressure side and re-enters on the suction side of the rotor both at the inlet and the exit cavity. This effect is also responsible for a strengthening of the secondary channel vortex in the rotor.

Several possible design improvements are identified from the analysed flow effects. The leakage flow from the exit cavity should not be forced to enter radially into the main flow but should have more inclination in the axial direction to avoid the effects of flow blockage. The excess swirl of the reentering leakage flow could either be reduced via baffles mounted on the casing wall after the outlet of the labyrinth seal or by applying winglets or turning devices in the labyrinth seal. If the flow velocity of the re-entering leakage flow can not be adjusted by constructive means to avoid excess swirl, the blade of the following stator row should be twisted in the casing region to avoid suction side incidence and a subsequent increase in the aerodynamic losses. Since the present results show that not only the leakage flow but also the mere presence of cavities induce aerodynamic losses, the geometry of the inlet and outlet cavities must be considered with care in the design and optimization process of sealing arrangements for axial turbines.

Appendix A

Derivation of time-derivative preconditioning methods by the use of perturbation analysis

Time-derivative preconditioning methods can be designed as methods that cluster the eigenvalues of the flow equations under consideration. With the motivation of alleviating the disparity of the eigenvalues, these techniques were introduced for the simulation of inviscid, low Mach number flows. It is sufficient to analyse and modify the eigenvalue distribution to avoid stiffness of the flow equations and so attain an efficient computation of inviscid flows, but not for systems of transport equations like the Navier-Stokes equations that with the presence of both diffusive and convective terms describe flows governed by multiple physical processes. A more general method of achieving a good conditioning of the flow equations is to scale the various physical terms such that all are of the same order even under limiting conditions. In the following a perturbation analysis similar to that of Merkle and Venkateswaran [186, 189] will be used to derive a preconditioning technique that leads to well-conditioned flow equations in the limit of low Mach and/or Reynolds numbers.

A.1 Derivation of a preconditioning method for inviscid, low Mach number flows

In this section perturbation analysis applied on the Euler equations will be used to demonstrate that the Merkle preconditioning technique for inviscid, low speed flows can be derived by the criterion that all terms in the flow equations are of the same order in the limit of low Mach number flows. The following derivation will show an alternative way of determining the preconditioning parameter ϱ'_p in Merkle's preconditioning scheme.

The one-dimensional Navier-Stokes equations

$$\frac{\partial \mathbf{Q}}{\partial t} + \frac{\partial \mathbf{E}}{\partial x} = \mathbf{0} \quad (\text{A.1})$$

with

$$\mathbf{Q} = [\varrho, \varrho u, \varrho e_0]^T, \quad \frac{\partial \mathbf{E}}{\partial x} = [\varrho u, \varrho u^2 + p, \varrho u h_0]^T \quad (\text{A.2})$$

serve as a basis for the following analysis. By using the chain rule, the unsteady term can be rewritten as $\frac{\partial \mathbf{Q}}{\partial t} = \frac{\partial \mathbf{Q}}{\partial \mathbf{Q}_v} \frac{\partial \mathbf{Q}_v}{\partial t}$ with

$$\mathbf{Q}_v = [p, u, T]^T \quad (\text{A.3})$$

and the last equations can be transformed to

$$\begin{aligned} \varrho_p \frac{\partial p}{\partial t} + \varrho_T \frac{\partial T}{\partial t} + \frac{\partial(\varrho u)}{\partial x} &= 0, \\ \varrho \frac{\partial u}{\partial t} + \varrho u \frac{\partial u}{\partial x} + \frac{\partial p}{\partial x} &= 0, \\ -(1 - \varrho h_p) \frac{\partial p}{\partial t} + \varrho h_T \frac{\partial T}{\partial t} + \varrho u \frac{\partial h}{\partial x} - u \frac{\partial p}{\partial x} &= 0. \end{aligned} \quad (\text{A.4})$$

A normalization with the reference scales

$$L^\dagger, u^\dagger, p^\dagger, \rho^\dagger, T^\dagger \quad (\text{A.5})$$

leads to the following system [5]:

$$\begin{aligned} \varrho_p^* \frac{\partial p^*}{\partial t^*} + \varrho_T^* \frac{\partial T^*}{\partial t^*} + \frac{\partial(\varrho^* u^*)}{\partial x^*} &= 0, \\ \varrho^* \frac{\partial u^*}{\partial t^*} + \varrho^* u^* \frac{\partial u^*}{\partial x^*} + \left(\frac{p^\dagger}{\varrho^\dagger u^{\dagger 2}} \right) \frac{\partial p^*}{\partial x^*} &= 0, \\ -(1 - \varrho^* h_p^*) \frac{\partial p^*}{\partial t^*} + \varrho^* h_T^* \frac{\partial T^*}{\partial t^*} + \varrho^* u^* \frac{\partial h^*}{\partial x^*} - u^* \frac{\partial p^*}{\partial x^*} &= 0 \end{aligned} \quad (\text{A.6})$$

where the asterix "*" denotes that a flow variable has been normalized, i.e., a state variable ϕ^* is defined as $\phi^* = \phi/\phi^\dagger$, where ϕ^\dagger is a reference state. To avoid the presence of the dimensionless characteristic numbers $p^\dagger/(\varrho^\dagger h^\dagger)$ and $L^\dagger/(t^\dagger u^\dagger)$ in the flow equations, the enthalpy scale h^\dagger and the time scale t^\dagger were respectively related to the other dimensionless quantities according to

$$h^\dagger = p^\dagger/\rho^\dagger, \quad t^\dagger = L^\dagger/u^\dagger. \quad (\text{A.7})$$

If the reference pressure p^\dagger is set to the thermodynamic pressure, then the characteristic number $p^\dagger/(\varrho^\dagger h^\dagger)$ is in the order of unity for ideal gases. The reference time scale t^\dagger could also have been defined using the speed of sound a^\dagger as reference velocity. The use of the convective velocity u^\dagger as reference speed is however more convenient than the use of the speed of sound as the former term appears explicitly in the flow equations and consequently leads to the simplest algebra. Also for incompressible flows, the application of the convective velocity as reference velocity is a natural choice. For a rigorous analysis of low Mach number flow, a multi-scale analysis should be carried out in which both an acoustic reference time scale τ^\dagger based on the sonic speed

and a convective time scale t^\dagger are used. However, as shown by Müller [194], if the temporal resolution of acoustic effects is not of interest, a multiple-scale analysis, in which both convective and acoustic velocity and time scales are accounted for, leads to the same conclusions as a single scale analysis in the study of the asymptotical behaviour of the Navier-Stokes equations at low Mach numbers. In the work of Müller [194] it is shown that the acoustically filtered asymptotic flow equations derived by a multiple-scale analysis coincide with the asymptotic flow equations derived by a single-scale analysis.

With the aforementioned choice of reference scales, only the ratio of the dynamic pressure to the static pressure,

$$\epsilon = \varrho^\dagger u^{\dagger 2} / p^\dagger, \quad (\text{A.8})$$

appears in the flow equations. At low Mach numbers the reference velocity u^\dagger approaches zero so that this ratio ϵ , which is scaling the pressure gradient in the momentum equations, becomes small. For an ideal gas the ratio ϵ is proportional to the square of the Mach number, i.e., $\epsilon = \gamma M^2$. In the following the limiting form of the equations as this term goes to zero is studied.

Since the term ϵ only appears before the pressure gradient in the momentum equations, it is natural to expand the pressure in a power series of this parameter

$$p = p_{(0)} + \epsilon p_{(2)} + \dots \quad (\text{A.9})$$

It would also have been possible to expand the pressure in dependence of the Mach number and then also having a first order pressure $p_{(1)}$ in the series expansion:

$$p = p_{(0)} + M p_{(1)} + M^2 p_{(2)} + \dots \quad (\text{A.10})$$

As can be shown by a more thorough analysis [5, 194], the first order pressure drops out of the flow equations and does not need to be considered, unless time-accurate, acoustic effects are of importance. In a single-scale analysis all the variables should ideally be perturbed; however as shown by Müller [194] this does not change the result of the current perturbation analysis. When applying the pressure expansion in Eq. (A.9) in the following equations, it must be assumed that the Mach numbers are at least one order less than unity ($M \ll 1$) to ensure a separation of the zeroth, first and second order pressure.

Using the expansion given in Eq. (A.9) the normalized momentum equation

$$\varrho \frac{\partial u^*}{\partial t^*} + \varrho^* u^* \frac{\partial u^*}{\partial x^*} + \frac{1}{\epsilon} \frac{\partial (p_{(0)}^* + \epsilon p_{(2)}^* + \dots)}{\partial x^*} = 0 \quad (\text{A.11})$$

is obtained. Since the term $\frac{1}{\epsilon} \frac{\partial p_{(0)}^*}{\partial x^*}$ cannot be matched by any other term in the equation, it follows

$$\frac{\partial p_{(0)}^*}{\partial x^*} = 0, \quad (\text{A.12})$$

i.e., the zeroth order pressure is independent of the spatial coordinate and can only vary temporally by being subject to a global change. This implies that the

zeroth order pressure does not directly have an impact on the velocity field; it only has an indirect impact on the flow field by a change in the thermodynamic states like the density. By assuming steady boundary conditions, vanishing temporal variations of the zeroth order pressure follows. For this reason only the second order pressure $p_{(2)}^*$ and not the zeroth order pressure $p_{(0)}^*$ appears in the following flow equations.

After separating out the zeroth order pressure, the momentum equation can be written as

$$\varrho^* \frac{\partial u^*}{\partial t^*} + \varrho^* u^* \frac{\partial u^*}{\partial x^*} + \frac{\partial p_{(2)}^*}{\partial x^*} = 0. \quad (\text{A.13})$$

Since this equation only has a temporal term containing the velocity, it can only be used in a time marching scheme to update the velocity but not the second order pressure. With the expansion of the pressure in Eq. (A.9) and by accounting for relation (A.12), the energy equation can be written as

$$-(1 - \varrho^* h_p^*) \epsilon \frac{\partial p_{(2)}^*}{\partial t^*} + \varrho^* h_T^* \frac{\partial T^*}{\partial t^*} + \varrho^* u^* \frac{\partial h^*}{\partial x^*} - \epsilon u^* \frac{\partial p_{(2)}^*}{\partial x^*} = 0. \quad (\text{A.14})$$

It should be noted that all the terms in the last equation involving the pressure are of second order while the other terms are of zeroth order in the Mach number. From this it follows that the energy equation is not an adequate means to update the second order pressure $p_{(2)}$ unless one scales the quantity h_p^* . The last equation furthermore show that even the energy equation for inviscid, ideal gas flows can be represented by the following transport equation for the pressure p

$$\frac{\partial p}{\partial t} + u \frac{\partial p}{\partial x} + \gamma p \frac{\partial u}{\partial x} = 0, \quad (\text{A.15})$$

the energy equation is better suited to update the temperature than the pressure in the case of low Mach number flow. It should be noted that for incompressible flows, the term $1 - \varrho h_p$ is zero, from which it follows that the energy field for constant density flow is independent of the temporal variations of the second order pressure.

Having separated out the zeroth order pressure term, the continuity equation reads as follows

$$\varrho_p^* \epsilon \frac{\partial p_{(2)}^*}{\partial t^*} + \varrho_T^* \frac{\partial T^*}{\partial t^*} + \frac{\partial(\varrho^* u^*)}{\partial x^*} = 0. \quad (\text{A.16})$$

In the last equation all terms are of zeroth order in ϵ except the temporal derivative of the pressure which is of first order and consequently will vanish for low values of ϵ . Hence this equation is not suitable for updating the pressure at low Mach numbers. To ensure that the time derivative of the pressure is of the same order as the convective term irrespective of the Mach number level of the flow, the physical property ϱ_p^* should be replaced with an artificial quantity $\varrho_p'^*$ defined as

$$\varrho_p'^* = \frac{k_p}{\epsilon} = \frac{k_p p^\dagger}{\varrho^\dagger u^{\dagger 2}} \quad (\text{A.17})$$

with the constant k_p in the order of unity. In dimensional form the last equation reads as

$$\varrho'_p = k_p/u^\dagger{}^2. \quad (\text{A.18})$$

By replacing the property ϱ_p with the quantity ϱ'_p , the following system of flow equations results

$$\begin{aligned} k_p \frac{\partial p_{(2)}^*}{\partial t^*} + \varrho_T^* \frac{\partial T^*}{\partial t^*} + \frac{\partial(\varrho^* u^*)}{\partial x^*} &= 0, \\ \varrho^* \frac{\partial u^*}{\partial t^*} + \varrho^* u^* \frac{\partial u^*}{\partial x^*} + \frac{\partial p_{(2)}^*}{\partial x^*} &= 0, \\ \varrho^* h_T^* \frac{\partial T^*}{\partial t^*} + \varrho^* u^* \frac{\partial h^*}{\partial x^*} &= 0 \end{aligned} \quad (\text{A.19})$$

for ideal gases in the limit of a vanishing Mach number. As all terms are in the order of unity, the convective and the temporal terms are in balance and the system is well-conditioned for time marching schemes. The property ϱ_T may be changed to avoid the appearance of temporal derivatives of the temperature in the continuity equation; with the aforementioned modification of the parameter ϱ_p , the other properties h_T and $(1 - \varrho h_p)$ need not to be scaled [5, 289] to achieve a good conditioning of the flow equations for inviscid flow in the low Mach number limit.

A.2 Derivation of a preconditioning method for low Mach number, viscous flows

In this section perturbation analysis applied on the Navier-Stokes equations will be used to show that the Merkle preconditioning technique for viscous, low speed flows can be derived by the criterion that all terms in the flow equations are of the same order in the limit of low Mach and low Reynolds number flows. The derivation will show an alternative way of determining proper values for the preconditioning parameters ϱ'_p , ϱ'_T , h'_T , and h'_p in Merkle's time-derivative preconditioning scheme.

The Navier-Stokes equations

$$\begin{aligned} \varrho_p \frac{\partial p}{\partial t} + \varrho_T \frac{\partial T}{\partial t} + \frac{\partial(\varrho u)}{\partial x} &= 0, \\ \varrho \frac{\partial u}{\partial t} + \varrho u \frac{\partial u}{\partial x} + \frac{\partial p}{\partial x} &= \frac{4}{3} \frac{\partial}{\partial x} \left(\mu \frac{\partial u}{\partial x} \right), \\ -(1 - \varrho h_p) \frac{\partial p}{\partial t} + \varrho h_T \frac{\partial T}{\partial t} + \varrho u \frac{\partial h}{\partial x} &= u \frac{\partial p}{\partial x} + \frac{\partial}{\partial x} \left(k_\lambda \frac{\partial T}{\partial x} \right) + \mu \frac{4}{3} \left(\frac{\partial u}{\partial x} \right)^2 \end{aligned} \quad (\text{A.20})$$

are used as a starting point of the following analysis. By normalizing the flow quantities with the following reference scales

$$L^\dagger, u^\dagger, p^\dagger, \rho^\dagger, T^\dagger, h^\dagger, t^\dagger, \mu^\dagger, k_\lambda^\dagger, \quad (\text{A.21})$$

and by expanding the pressure according to Eq. (A.9), the Navier-Stokes equation reads as

$$\begin{aligned}
& \left(\frac{L^\dagger}{t^\dagger u^\dagger} \right) \left(\epsilon \varrho_p^* \frac{\partial p_{(2)}^*}{\partial t^*} + \varrho_T^* \frac{\partial T^*}{\partial t^*} \right) + \frac{\partial(\varrho^* u^*)}{\partial x^*} = 0, \\
& \left(\frac{\text{Re} L^\dagger}{t^\dagger u^\dagger} \right) \varrho^* \frac{\partial u^*}{\partial t^*} + \text{Re} \varrho^* u^* \frac{\partial u^*}{\partial x^*} + \epsilon \text{Re} \frac{p^\dagger}{\varrho^\dagger u^{\dagger 2}} \frac{\partial p_{(2)}^*}{\partial x^*} = \frac{4}{3} \frac{\partial}{\partial x^*} \left(\mu^* \frac{\partial u^*}{\partial x^*} \right), \\
& \left(\frac{\text{Pe} L^\dagger}{t^\dagger u^\dagger} \right) \left[\varrho^* h_T^* \frac{\partial T^*}{\partial t^*} - d_p \epsilon \frac{\partial p_{(2)}^*}{\partial t^*} \right] + \text{Pe} \varrho^* u^* \frac{\partial h^*}{\partial x^*} = \epsilon u^* \text{Pe} \frac{\partial p_{(2)}^*}{\partial x^*} + \frac{\partial}{\partial x^*} \left(k_\lambda^* \frac{\partial T^*}{\partial x^*} \right) + \\
& \qquad \qquad \qquad \text{Pr} \frac{u^{\dagger 2}}{h^\dagger} \mu^* \left(\frac{\partial u^*}{\partial x^*} \right)^2
\end{aligned} \tag{A.22}$$

with the abbreviation d_p given by $d_p = 1 - \varrho h_p$ and the Reynolds, Prandtl, and Peclet numbers defined as

$$\text{Re} = \frac{\varrho^\dagger u^\dagger L^\dagger}{\mu^\dagger}, \quad \text{Pr} = \frac{\mu^\dagger h^\dagger}{k_\lambda^\dagger T^\dagger}, \quad \text{Pe} = \text{Re Pr} = \frac{\varrho^\dagger u^\dagger L^\dagger h^\dagger}{k_\lambda^\dagger T^\dagger}. \tag{A.23}$$

Here it is assumed that the Mach number level is low. It then follows that the gradient of the zeroth order pressure vanishes, just as in the perturbation analysis for the inviscid flow equations in the previous section. By assuming steady boundary conditions, it follows that the temporal variations of the zeroth order pressure vanish. For this reason, only the second order pressure $p_{(2)}^*$ and not the zeroth order pressure $p_{(0)}^*$ appears in the flow equations (A.22).

The reference time scale t^\dagger is determined by the condition that the coefficient of the time-derivative term in the momentum equations should be in the order of unity to balance the viscous term. This leads to the following expression

$$t^\dagger = \frac{\text{Re} L^\dagger}{u^\dagger} = \frac{L^{\dagger 2}}{\nu^\dagger}. \tag{A.24}$$

To ensure that the pressure gradient term in the momentum equations balances the viscous forces, the term $\epsilon \text{Re} p^\dagger / (\varrho^\dagger u^{\dagger 2})$ must be in the order of unity. From this condition it follows that the perturbation parameter ϵ has to satisfy

$$\epsilon = \frac{\varrho^\dagger u^{\dagger 2}}{p^\dagger} \frac{1}{\text{Re}^\dagger}, \tag{A.25}$$

which for ideal gases leads to the requirement $\epsilon = \gamma M^{\dagger 2} / \text{Re}^\dagger$.

With the aforementioned definitions of the time scale and the perturbation

parameter ϵ , the normalized Navier-Stokes equations read as follows

$$\begin{aligned}
\varrho_p^* \frac{\varrho^\dagger u^{\dagger 2}}{p^\dagger \mathbf{Re}^{\dagger 2}} \frac{\partial p_{(2)}^*}{\partial t^*} + \frac{\varrho_T^*}{\mathbf{Re}} \frac{\partial T^*}{\partial t^*} + \frac{\partial(\varrho^* u^*)}{\partial x^*} &= 0, \\
\varrho^* \frac{\partial u^*}{\partial t^*} + \mathbf{Re} \varrho^* u^* \frac{\partial u^*}{\partial x^*} + \frac{\partial p_{(2)}^*}{\partial x^*} &= \frac{\partial}{\partial x^*} \left(\mu^* \frac{\partial u^*}{\partial x^*} \right), \\
\mathbf{Pr} \left[\varrho^* h_T^* \frac{\partial T^*}{\partial t^*} - d_p \frac{\varrho^\dagger u^{\dagger 2}}{p^\dagger} \frac{1}{\mathbf{Re}} \frac{\partial p_{(2)}^*}{\partial t^*} \right] + & \\
\mathbf{Pe} \varrho^* u^* \frac{\partial h^*}{\partial x^*} - \mathbf{Pr} u^* \frac{\varrho^\dagger u^{\dagger 2}}{p^\dagger} \frac{\partial p_{(2)}^*}{\partial x^*} &= \frac{\partial}{\partial x^*} \left(k_\lambda^* \frac{\partial T^*}{\partial x^*} \right) + \\
&\mathbf{Pr} \frac{u^{\dagger 2}}{h^\dagger} \mu^* \left(\frac{\partial u^*}{\partial x^*} \right)^2.
\end{aligned} \tag{A.26}$$

To make sure that the temporal pressure term in the continuity equation scales correctly for low Mach number viscous flows, the physical quantity ϱ_p^* needs to be replaced by the artificial quantity $\varrho_p'^*$ defined as

$$\varrho_p'^* = k_v \frac{\mathbf{Re}^2 p^\dagger}{\varrho^\dagger u^{\dagger 2}} \tag{A.27}$$

where k_v is a constant in the order of one. Written in dimensional form the last definition reads as follows

$$\varrho_p' = k_v \frac{\mathbf{Re}^2}{u^2}. \tag{A.28}$$

For ideal gases the last relation can also be written as

$$\varrho_p' = k_v \frac{\mathbf{Re}^2}{\gamma \mathbf{M}^2} \varrho_p. \tag{A.29}$$

To avoid that the temporal derivative of the temperature dominates the continuity equation, the coefficient ϱ_T^*/\mathbf{Re} should not exceed unity. In terms of dimensional quantities, this is given when

$$\varrho_T \leq \varrho^\dagger \mathbf{Re} / T^\dagger. \tag{A.30}$$

This is achieved by replacing the physical property ϱ_T with the scaled property ϱ_T' that fulfills the last condition. As already mentioned in previous sections, the scaled property ϱ_T' should ideally be proportional to the physical property ϱ_T , such that the energy equation remains decoupled from the continuity equation in the case of incompressible flows. With ϱ_T' defined as $\varrho_T' = \delta_{\text{pc}} \varrho_T$, $\delta_{\text{pc}} \in [0, 1]$ according to Eq. (3.13), the condition (A.30) is fulfilled when the parameter δ_{pc} is limited by

$$\delta_{\text{pc}} \leq \frac{\varrho^\dagger \mathbf{Re}}{\varrho_T T^\dagger}. \tag{A.31}$$

An analysis of the energy equation shows that there are circumstances, where the physical properties h_T and $d_p = 1 - \rho h_p$ need to be changed in order to ensure that the various physical terms are of the same order. Before discussing this, it should be noted that if the reference enthalpy is related to the thermodynamic pressure according to $h^\dagger = p^\dagger/\rho^\dagger$ then the term $u^{\dagger 2}/h^\dagger$ scales with the square of the Mach number for the case of ideal gas flow. Hence, for low Mach and moderate Prandtl numbers (i.e., $\text{Pr} M^2 \ll 1$) the viscous dissipation term $\text{Pr} \frac{u^{\dagger 2}}{h^\dagger} \mu^* \left(\frac{\partial u^*}{\partial x^*}\right)^2$ can be neglected. In the case of low Mach, moderate Prandtl number, ideal gas flow, the pressure gradient term $\text{Pr} u^* \frac{\rho^\dagger u^{\dagger 2}}{p^\dagger} \frac{\partial p^*(2)}{\partial x^*}$ can be neglected as well. To ensure a good conditioning of the flow equations, the temporal temperature derivative in the energy equation should scale in the same order as the diffusive terms. The only diffusive term of significance for low Mach number flow is the heat conduction term. From this it follows that the factor $\text{Pr} \rho^* h_T^*$ of the temporal temperature derivative should scale in the order of unity. Thus, for the simulation of flow with Prandtl numbers far from unity, the normalized isobaric heat capacity h_T^* may be replaced with a scaled quantity $h_T'^*$ defined as $h_T'^* = 1/\rho^* \text{Pr}$. In terms of dimensional quantities this reads as

$$h_T' = \frac{p^\dagger}{T^\dagger} \frac{1}{\rho \text{Pr}}. \quad (\text{A.32})$$

For viscous, ideal gas, low Mach number flow, where the local value for the density is close to the reference density, the scaled quantity h_T' may be introduced as $h_T' = R/\text{Pr}$. Alternatively, one might, as suggested by Merkle, set the scaled quantity h_T' to $h_T' = h_T/\text{Pr}$.

The term in the energy equation containing the temporal pressure derivative, $d_p \frac{\rho^\dagger u^{\dagger 2}}{p^\dagger} \frac{\text{Pr}}{\text{Re}} \frac{\partial p^*(2)}{\partial t^*}$, scales in the order of $\mathcal{O}(\text{Pr} M^2/\text{Re})$ for ideal gas flow. To avoid that this term dominates the energy equation for situations where the Reynolds number is significantly lower than the square of the Mach number ($\text{Re} \ll M^2$) and the Prandtl number is in the order of unity, the coefficient $d_p = 1 - \rho h_p$ needs to be replaced with an artificial coefficient h_p' such that the term $h_p' \frac{\rho^\dagger u^{\dagger 2}}{p^\dagger} \frac{\text{Pr}}{\text{Re}}$ stays in the order of unity. From this condition it follows that the coefficient h_p' must be bounded by

$$h_p' \leq \frac{p^\dagger}{\rho^\dagger u^{\dagger 2}} \frac{\text{Re}}{\text{Pr}}, \quad (\text{A.33})$$

which for ideal gas flow translates into the following condition $h_p' \leq \frac{1}{\gamma M_p^2} \frac{\text{Re}}{\text{Pr}}$. In flows encountered in engineering systems the Reynolds number is usually many orders larger than the Mach number. For this reason the last condition is practically always met and the scaling of the temporal pressure derivative in the energy equation is not much of an issue.

A.3 Summary of the implications for the preconditioning parameters

The conditions derived in the previous sections to ensure a proper balance between the various physical terms in the flow equations in the limit of low Mach and Reynolds numbers are summarized in Table A.1.

The main preconditioning parameter ϱ'_p in the limit of low Mach number, inviscid flow should be determined as

$$\varrho'_p = k_p/u^\dagger{}^2. \quad (\text{A.34})$$

Using eigenvalue analysis the following condition for the preconditioning parameter ϱ'_p was derived (Eq. 3.12):

$$\varrho'_p = \frac{1}{V_r^2} - \frac{1 - \varrho h_p}{\varrho h_T} \varrho'_T.$$

This relation gives the same result as Eq. (A.34) when the reference speed V_r is set to the reference scale u^\dagger for the convective velocity and the parameter ϱ'_T is set to zero.

For low Mach number viscous flow, it follows from Eq. (A.28) that the reference speed V_r used to determine ϱ'_p should be oriented after the diffusion velocity, i.e., V_r is to be determined as $V_r = k_v \nu / L^\dagger$.

The preconditioning parameter ϱ'_T should vanish for constant density flow to avoid the presence of temporal derivatives of the temperature in the continuity equation. This can be achieved by setting this parameter proportional to its physical counterpart. For low Reynolds number flow, the parameter ϱ'_T should be constrained by the condition given in Eq. (A.30).

In the case of inviscid flow, the parameters h'_T and h'_p are not subject to any restriction to attain a good conditioning of the flow equations. To achieve simple expressions for the eigenvalues it is favorable to set both parameters to their physical counterparts, i.e., $h'_T = h_T$ and $h'_p := d_p = 1 - \varrho h_p$. The former choice ensures that three of the eigenvalues of the linearized Euler equations corresponds to the convective velocity. For low Reynolds number flows both parameters h'_T and h'_p are subject to restrictions if a good conditioning is to be achieved. In the case of viscosity dominated flow, the parameter h'_p should be bounded by the constraint given in Eq. (A.33) to avoid that temporal pressure variations dominate the evolution of the energy field. For low Reynolds number flows where the Prandtl number is far from unity (e.g., flow of engine oil) the parameter h'_T should, according to Eq. (A.32), be scaled inversely proportional to the Prandtl number.

Preconditioning parameter	ϱ'_p	ϱ'_T	h'_p	h'_T
Inviscid, low Mach no. flow	k_p/u^\dagger^2	$k_T \varrho_T$, (i,iv)	Rem. (ii)	No cond., Rem. (iii)
Viscous, low Mach no. flow	$k_v \mathbf{Re}^2 / u^\dagger^2$	$\varrho'_T \leq \varrho^\dagger \mathbf{Re} / T^\dagger$	$h'_p \leq \frac{p^\dagger}{\varrho^\dagger u^\dagger^2} \frac{\mathbf{Pr}}{\mathbf{Re}}$	$p^\dagger / (\varrho T^\dagger \mathbf{Pr})$

Table A.1: Summary of conditions imposed on the preconditioning parameters in the low Mach number and low Reynolds number limit. Remarks and explanations: i) ϱ'_T should vanish for incompressible flows - for this reason this parameter should be formulated proportional to its physical counterpart; ii) the choice $h'_p := d_p = 1 - \varrho h_p$ is favorable as this gives simpler expressions for the eigenvalues; iii) the choice $h'_T := h_T$ gives also simpler eigenvalues and ensures that the speed of the entropy wave is not altered; iv) for compressible flow the parameter k_T should not exceed unity to ensure regularity of the preconditioning matrix for subsonic reference speeds.

Appendix B

Dispersion analysis of the unscaled and the preconditioned Navier-Stokes equations

In viscous flow various physical phenomena interplay; whether the transport processes are governed by advection, acoustic waves and/or viscous diffusion is dependent on the Mach and Reynolds number levels. With the purpose of analysing the role of the various physical processes and to determine the wave speeds under different limiting conditions, a dispersion analysis similar to that one of Buelow [46] is carried out in this chapter. In contrast to the analysis conducted by Buelow, the dispersion analysis here is carried out for two different values of the preconditioning parameter ϱ'_T , which steers the amount of coupling between the energy and the continuity equation. In addition to ideal gas flow, the wave speeds of the preconditioned Navier-Stokes equations are analysed for the case that the fluid is incompressible.

B.1 Governing equations and dispersion analysis employed for determining wave speeds

To analyse the wave speeds of the unscaled and preconditioned Navier-Stokes equations, a dispersion analysis is carried out using the one-dimensional Navier-Stokes equations

$$\frac{\partial \mathbf{Q}}{\partial t} + \frac{\partial \mathbf{E}_c}{\partial x} = \frac{\partial \mathbf{E}_v}{\partial x} \quad (\text{B.1})$$

with

$$\begin{aligned} \mathbf{Q} &= [\rho, \varrho u, \varrho e_0]^T, & \mathbf{E}_c &= [\rho u, \varrho u^2 + p, \varrho h_0]^T, \\ \mathbf{E}_v &= [0, \tau_{xx}, \tau_{xx}u - \dot{q}_x]^T, & \tau_{xx} &= 4/3\mu \frac{\partial u}{\partial x}, & \dot{q}_x &= -k_\lambda \frac{\partial T}{\partial x}. \end{aligned} \quad (\text{B.2})$$

Changing from the vector \mathbf{Q} of conservative variables to the vector $\mathbf{Q}_v = [p, u, T]^T$ of primitive, viscous variables and linearizing the equations about an arbitrary, but fixed averaged state $\bar{\mathbf{Q}}_v$ yields

$$\Gamma_e \frac{\partial \tilde{\mathbf{Q}}_v}{\partial t} + A \frac{\partial \tilde{\mathbf{Q}}_v}{\partial x} = \frac{\partial}{\partial x} R_{xx} \frac{\partial \tilde{\mathbf{Q}}_v}{\partial x} \quad (\text{B.3})$$

with

$$\Gamma_e = \left. \frac{\partial \mathbf{Q}}{\partial \mathbf{Q}_v} \right|_{\bar{\mathbf{Q}}_v}, \quad A_v = \left. \frac{\partial \mathbf{E}}{\partial \mathbf{Q}_v} \right|_{\bar{\mathbf{Q}}_v}, \quad R_{xx} = \begin{bmatrix} 0 & 0 & 0 \\ 0 & 4/3\mu & 0 \\ 0 & 4/3\mu u & k_\lambda \end{bmatrix}_{\bar{\mathbf{Q}}_v} \quad (\text{B.4})$$

and the linearized state vector $\tilde{\mathbf{Q}}_v$ defined as $\tilde{\mathbf{Q}}_v = \mathbf{Q}_v - \bar{\mathbf{Q}}_v$. To simplify the equations, a constant viscosity and a fixed thermal conductivity are assumed in the current analysis. When Merkle's preconditioning technique is applied, the physical Jacobian Γ_e is replaced with the preconditioning matrix

$$\Gamma_v = \begin{bmatrix} \varrho'_p & 0 & \varrho'_T \\ \varrho'_p u & \varrho & \varrho'_T u \\ \varrho'_p h_0 + \varrho h_p - 1 & \varrho u & \varrho'_T h_0 + \varrho h_T \end{bmatrix} \quad (\text{B.5})$$

for which the quantities ϱ_p and ϱ_T have been substituted with the artificial quantities ϱ'_p and ϱ'_T , so that the numerical speed of sound a' is in the same order as the maximum of the convective and diffusive velocity scales. In the first instance ideal gas flow will be assumed which is why the notion of Buelow will be used, in which the pseudo-acoustic velocity a' is related to the isentropic speed of sound a according to

$$a'^2 = \epsilon \cdot a^2. \quad (\text{B.6})$$

Hence, if ϵ is set to the square of the Mach number $M = u/a$, the numerical speed of sound a' reduces to the convective velocity u . With the last equation and Eqs. (3.10) and (3.12) the following relation for ϱ'_p is obtained:

$$\varrho'_p = \frac{1}{\epsilon a^2} - \frac{1 - \varrho h_p}{\varrho h_T} \varrho'_T. \quad (\text{B.7})$$

The parameter ϱ'_T is determined according to Eq. (3.13), i.e., $\varrho'_T = \delta_{\text{pc}} \varrho_T$ where δ_{pc} is a constant parameter in the range $\delta_{\text{pc}} = [0, 1]$. It should be noted that if both parameters ϵ and δ_{pc} are set to unity, then the preconditioning matrix Γ_v reverts to the Jacobian matrix $\left. \frac{\partial \mathbf{Q}}{\partial \mathbf{Q}_v} \right|_{\bar{\mathbf{Q}}_v}$.

A dispersion analysis consists of analysing for which values of the wave-number k and angular frequency ω waves exist in the form

$$\tilde{\mathbf{Q}}_v(x, t) = \hat{\mathbf{Q}}_v(x, t) e^{i(kx - \omega t)} \quad (\text{B.8})$$

as a solution of the preconditioned Navier-Stokes equations. By substituting this expression in Eq. (B.3) it follows that non-trivial solutions exist for

$$|-\hat{\omega} I + \hat{i} k A_{\Gamma, v} + k^2 R_{\Gamma, xx}| = 0 \quad (\text{B.9})$$

with $A_{\Gamma, v} = \Gamma_v^{-1} A_v$ and $R_{\Gamma, xx} = \Gamma_v^{-1} R_{xx}$. The problem of finding solutions of the dispersion relation in Eq. (B.9) can be recast as finding the roots ω/k of the polynomial given by

$$|A_{\Gamma, v, xx} - (\omega/k) \cdot I| = 0, \quad (\text{B.10})$$

with the matrix $A_{\Gamma, v, xx}$ given by

$$A_{\Gamma, v, xx} = A_{\Gamma, v} - \hat{i} \frac{u}{\nu \text{Re}_k} \cdot R_{xx, \Gamma} \quad (\text{B.11})$$

and the wave number based Reynolds number Re_k defined as

$$\text{Re}_k = \frac{u}{\nu k}. \quad (\text{B.12})$$

The roots $(\omega/k)_j$, $j = 1, \dots, 3$ of the dispersion relation (B.9) correspond to the phase velocity (i.e., the propagation velocity) [304] of the different wave modes $\hat{\mathbf{Q}}_{v,j}(x, t)e^{\hat{i}(k_j x - \omega_j t)}$ governed by the Navier-Stokes equations (B.3).

B.1.1 Dispersion analysis for ideal gas flow

For an ideal gas the preconditioned inviscid flux Jacobian $A_{\Gamma,v} = \Gamma_v^{-1} \hat{A}$ reads as

$$A_{\Gamma,v} = \Gamma_v^{-1} \hat{A} = \begin{bmatrix} u\epsilon[\gamma - (\gamma - 1)\delta_{\text{pc}}] & \varrho\epsilon c^2 & -\frac{\epsilon(1-\delta_{\text{pc}})\varrho u c^2}{T} \\ \frac{1}{\varrho} & u & 0 \\ \frac{u[\epsilon(\gamma - (\gamma - 1)\delta_{\text{pc}}) - 1]}{\varrho c_p} & \epsilon(\gamma - 1)T & u[1 - \gamma_{\text{pc}}] \end{bmatrix} \quad (\text{B.13})$$

with the abbreviation $\gamma_{\text{pc}} = \epsilon(1 - \delta_{\text{pc}})(\gamma - 1)$ while the preconditioned viscous flux Jacobian $R_{\Gamma,xx} = \Gamma_v^{-1} R_{xx}$ becomes

$$R_{xx,\Gamma} = \Gamma_v^{-1} R_{xx} = \begin{bmatrix} 0 & 0 & 0 \\ 0 & 4/3\nu & 0 \\ 0 & 0 & \nu/\text{Pr} \end{bmatrix} \quad (\text{B.14})$$

with the Prandtl number defined as $\text{Pr} = c_p \mu / k_\lambda$. To simplify the expressions, the Prandtl number is set to 3/4 in the following analyses.

The roots of the dispersion relation can be calculated as

$$\begin{aligned} (\omega/k)_1 &= u\left(1 - \hat{i}\frac{4}{3}\frac{1}{\text{Re}_k}\right), \\ (\omega/k)_{2,3} &= \frac{u}{2} \left[(1 + \epsilon) - \hat{i}\frac{4}{3}\frac{1}{\text{Re}_k} \right] \pm u \sqrt{\epsilon\frac{1}{M^2} + \left(\hat{i}\frac{2}{3}\frac{1}{\text{Re}_k} + \frac{\epsilon-1}{2} \right)^2 + \hat{i}\frac{4}{3}\frac{1}{\text{Re}_k}\gamma_{\text{pc}}}. \end{aligned} \quad (\text{B.15})$$

In subsequent sections these roots will be analysed for different limits of the Mach and Reynolds numbers.

B.1.2 Dispersion analysis for incompressible flow

For the unscaled, linearized Navier-Stokes equations for incompressible flows for which the temporal derivative of the density vanishes ($\frac{\partial \varrho}{\partial t} = 0$), it is immediately seen that waves of the form $\tilde{\mathbf{Q}} = \hat{\mathbf{Q}}e^{\hat{i}(kx - \omega t)}$ with finite transport velocities do not exist. For the constant density case, the flow equations exhibit only then a hyperbolic character when the artificial compressibility method or a preconditioning approach is used where temporal derivatives of the pressure and the temperature are added to the continuity equation.

In the case of a convection dominated incompressible fluid flow, the prescriptions for the preconditioning parameters ϱ'_p and ϱ'_T given by Eqs. (3.12) and (3.13) reduce to

$$\varrho'_p = \frac{1}{V_r^2}, \quad \varrho'_T = 0 \quad (\text{B.16})$$

and the reference velocity V_r might be set to the convection velocity u , i.e., $V_r = u$. With the other preconditioning parameters ϱ'_T , h'_T and h'_p set to their physical counterparts, i.e.,

$$\varrho'_T = \varrho_T = 0, \quad h'_T = h_T, \quad h'_p = 1 - \varrho h_p = 0 \quad (\text{B.17})$$

the matrices $A_{\Gamma,v}$ and $R_{xx,\Gamma}$ become

$$A_{\Gamma,v} = \Gamma_v^{-1} \hat{A} = \begin{bmatrix} 0 & \varrho u^2 & 0 \\ \frac{1}{\varrho} & u & 0 \\ 0 & 0 & u \end{bmatrix}, \quad R_{xx,\Gamma} = \Gamma_v^{-1} R_{xx} = \begin{bmatrix} 0 & 0 & 0 \\ 0 & \frac{4}{3}\nu & 0 \\ 0 & 0 & \nu/\text{Pr} \end{bmatrix}. \quad (\text{B.18})$$

As for the ideal gas flow case, the Prandtl number is set to $3/4$ to simplify the following analyses. With the preconditioned flux Jacobians in Eq. (B.18), the solution of the dispersion relation (B.10) becomes

$$\begin{aligned} (\omega/k)_1 &= u \left(1 - \frac{4}{3} \hat{i} \frac{1}{\text{Re}_k} \right), \\ (\omega/k)_{2,3} &= \frac{1}{2} u \left(1 - \frac{4}{3} \hat{i} \frac{1}{\text{Re}_k} \right) \pm \frac{1}{2} u \sqrt{\left(1 - \frac{4}{3} \hat{i} \frac{1}{\text{Re}_k} \right)^2 + 4}. \end{aligned} \quad (\text{B.19})$$

For viscosity dominated flow, the preconditioning parameter ϱ'_p may be determined as

$$\varrho'_p = \frac{\text{Re}_k^{n_e}}{u^2} \quad (\text{B.20})$$

with the exponent n_e either set to 1 or 2. The preconditioned flux Jacobian matrix $A_{\Gamma,v}$ in this case becomes

$$A_{\Gamma,v} = \begin{bmatrix} 0 & \frac{\varrho u^2}{\text{Re}_k^{n_e}} & 0 \\ \frac{1}{\varrho} & u & 0 \\ 0 & 0 & u \end{bmatrix}, \quad (\text{B.21})$$

if the other preconditioning parameters have not been scaled, i.e., they have been set according to Eq. (B.17). Whether the preconditioning parameter ϱ'_p is specified according to Eq. (B.16) or (B.20), the flux Jacobian $R_{\Gamma,xx} = \Gamma_v^{-1} R_{xx}$ given in Eq. (B.18) remains the same. In the case of viscous preconditioning, for which the parameter ϱ'_p has been set according to Eq. (B.20), the roots of the dispersion relation (B.9) become

$$\begin{aligned} (\omega/k)_1 &= u \left(1 - \frac{4}{3} \hat{i} \frac{1}{\text{Re}_k} \right), \\ (\omega/k)_{2,3} &= \frac{1}{2} u \left(1 - \frac{4}{3} \hat{i} \frac{1}{\text{Re}_k} \right) \pm \frac{1}{2} u \sqrt{\left(1 - \frac{4}{3} \hat{i} \frac{1}{\text{Re}_k} \right)^2 + \frac{4}{\text{Re}_k^{n_e}}}. \end{aligned} \quad (\text{B.22})$$

Further below, the roots of the dispersion relation for inviscid and viscous preconditioning will be examined in the low and high Reynolds number limit.

B.2 Wave speeds of the preconditioned Navier-Stokes equations for ideal gas flow

In the following, the wave speeds of the Navier-Stokes equations for ideal gas flow will be determined using dispersion analysis. The effect of using low Mach or low Reynolds number time-derivative preconditioning will be studied by calculating the distribution of the wave speeds for various limiting flow conditions.

B.2.1 Wave speeds when time-derivative preconditioning is not applied

In this subsection, the wave speeds of the unscaled Navier-Stokes equations will be analysed. Thus, the roots of Eq. (B.15) will be investigated for $\epsilon = 1$ and $\delta_{pc} = 1$ for which the preconditioning matrix Γ_v given in Eq. (B.5) reverts to the physical Jacobian $\Gamma_e = \frac{\partial \mathbf{Q}}{\partial \mathbf{Q}_v}$.

In the limit of high Reynolds numbers, the roots of the dispersion relation simplify to

$$(\omega/k)_1 = u, \quad (\omega/k)_{2,3} = u \pm a. \quad (\text{B.23})$$

These roots represent the speed of the particle wave (i.e., the convection of entropy) and the speed of the two acoustic waves. The physical condition number σ becomes $\sigma = 1 + \frac{1}{\text{M}}$. Obviously, the condition number goes beyond all bounds as the Mach number tends to zero, which demonstrates the stiffness of the inviscid flow equations as the Mach number goes to zero.

For viscosity dominated flows where the Reynolds number is low, different cases appear depending on the ratio between the Mach and the Reynolds number. The ratio Re_k/M can be regarded as an acoustic Reynolds number $\text{Re}_{a,k}$ based on the speed of sound, i. e.,

$$\text{Re}_{a,k} = \text{Re}_k/\text{M} = a/(\nu k). \quad (\text{B.24})$$

For viscous dominated flow ($\text{Re}_k \ll 1$) having a high acoustic Reynolds number ($\text{Re}_k/\text{M} \gg 1$) the roots of the dispersion relation become

$$(\omega/k)_1 = -i \frac{4}{3} \frac{u}{\text{Re}_k}, \quad (\omega/k)_{2,3} = u \pm a. \quad (\text{B.25})$$

This result is based on the assumption that the ratio Re_k/M^2 is at least one order larger than unity. This ratio determines the ratio between the pressure forces and viscous stresses in the momentum equations as well as the ratio between the viscous dissipation and the pressure work term in the energy equation [182].

The roots in Eq. (B.25) show that the pressure waves are not effectively attenuated by the presence of viscosity and that only the entropy wave is subject to viscous damping in the case of large acoustic Reynolds numbers ($\text{Re}_{a,k} \gg 1$). The physical condition number σ in this case becomes $\sigma = \frac{3}{4}(1 +$

Limits	ω_1/k	ω_2/k	ω_3/k	σ
$\text{Re} \gg 1$	u	$u + a$	$u - a$	$1 + \frac{1}{M}$
$\text{Re} \ll 1, \text{Re}/M \gg 1,$ $\text{Re}/M^2 \gg 1$	$-\hat{i}\frac{4}{3}\frac{u}{\text{Re}_k}$	$u + a$	$u - a$	$\frac{3}{4}(1 + \frac{1}{M})\text{Re}_k$
$\text{Re} \ll 1, \text{Re}/M \ll 1$	$-\hat{i}\frac{4}{3}\frac{u}{\text{Re}_k}$	$u \quad [\gamma \cdot u]$	$-\hat{i}\frac{4}{3}\frac{u}{\text{Re}_k}$	$\frac{4}{3}\frac{1}{\text{Re}_k} \quad [\frac{4}{3}\frac{1}{\gamma\text{Re}_k}]$

Table B.1: The roots of the dispersion relation and the condition number of the unscaled Navier-Stokes equations for ideal gas flow ($\epsilon = 1, \delta_{\text{pc}} = 1$). The values listed in brackets are the transport velocities for $\delta_{\text{pc}} = 0$ if they differ from those for $\delta_{\text{pc}} = 1$.

$\frac{1}{M})\text{Re}_k = \frac{3}{4}(\text{Re}_k + \text{Re}_{a,k})$, which shows that there is a significant disparity in the wave speeds for large acoustic Reynolds numbers.

For viscous dominated flow ($\text{Re}_k \ll 1$) and low acoustic Reynolds numbers ($\text{Re}_{a,k} \ll 1$) the wave speeds are determined as

$$(\omega/k)_{1,3} = -\hat{i}\frac{4}{3}\frac{u}{\text{Re}_k}, \quad (\omega/k)_2 = u. \quad (\text{B.26})$$

Thus, in this case two wave modes are subject to viscous damping, while the third mode represents an undamped particle velocity. The condition number σ for this situation becomes $\sigma = \frac{4}{3}\frac{1}{\text{Re}_k}$. This shows that not only in the limit of low Mach numbers but also in the limit of low Reynolds numbers, a disparity of the wave speeds of the unscaled Navier-Stokes equations occurs.

Table B.1 summarizes the roots of the dispersion relation (B.10) for the unscaled Navier-Stokes equations under various limiting conditions. In the table the wave speeds are also listed for the case that the parameter δ_{pc} is set to zero instead of unity. As can be seen from the table, the parameter δ_{pc} has no impact other than for the low acoustic Reynolds number case. In that case, the parameter leads only to an insignificant change in the condition number.

B.2.2 Wave speeds when low Mach number time-derivative preconditioning is applied

In this section the roots of the dispersion relation (B.10) are determined and analysed for various limiting conditions for the case that low Mach number time-derivative preconditioning is used. To determine the wave speeds in this case, the dispersion relation (B.10) is evaluated with the parameter ϵ set to $\epsilon = M^2$. In the first instance, the roots will be determined for the parameter δ_{pc} set to unity. With this choice of the parameters ϵ and δ_{pc} , the preconditioning parameters ϱ'_p and ϱ'_T become

$$\varrho'_p = \frac{1}{V_r^2} - \frac{1 - \varrho h_p}{\varrho h_T} \varrho'_T, \quad V_r = \sqrt{\epsilon}a = u, \quad \varrho'_T = \varrho_T. \quad (\text{B.27})$$

In the limit of high Reynolds ($\text{Re}_k \rightarrow \infty$) and low Mach numbers ($M \ll 1$), the roots of the dispersion relation for the aforementioned choices of the

parameters ϵ and δ_{pc} become

$$\omega_1/k = u, \quad \omega_{2,3}/k = \frac{1}{2}(1 \pm \sqrt{5})u. \quad (\text{B.28})$$

The condition number in this case is $\sigma = |(1 + \sqrt{5})/(1 - \sqrt{5})| \approx 2.62$, which shows that good conditioning is attained for this choice of preconditioning parameters in the limit of low Mach number flow.

In the limit of low Reynolds number flow ($\text{Re}_k \ll 1$), the use of low Mach number preconditioning exacerbates the disparity of the wave speeds. To show this, the roots of the dispersion relation (B.10) are calculated in the limit of low Reynolds numbers ($\text{Re}_k \ll 1$) for both high and low values of the acoustic Reynolds number $\text{Re}_{a,k} = \text{Re}_k/M$. In the former case, under the additional assumption that the ratio Re_k/M^2 is also large ($\text{Re}_k/M^2 \gg 1$), the roots of the dispersion relation (B.10) are

$$(\omega/k)_1 = -i\frac{4}{3}\frac{u}{\text{Re}_k}, \quad (\omega/k)_2 = -i\frac{3}{4}\text{Re}_k u, \quad (\omega/k)_3 = -i\frac{4}{3}\frac{u}{\text{Re}_k}, \quad (\text{B.29})$$

which leads to a condition number of $\sigma = \frac{16}{9}\frac{1}{\text{Re}_k^2}$. For low acoustic Reynolds numbers ($\text{Re}_{a,k} \ll 1$) the roots are determined as

$$(\omega/k)_1 = -i\frac{4}{3}\frac{u}{\text{Re}_k}, \quad (\omega/k)_2 = uM^2, \quad (\omega/k)_3 = -i\frac{4}{3}\frac{u}{\text{Re}_k}, \quad (\text{B.30})$$

which leads to a condition number of $\sigma = \frac{4}{3}\frac{1}{\text{Re}_k M^2}$.

In the limit of low Reynolds numbers, it can be concluded that the use of low Mach number preconditioning does not lead to an equilibration of the wave speeds.

Table B.2 summarizes the roots of the dispersion relation in the case that low Mach preconditioning is used ($\epsilon = M^2$). In the table the wave speeds for the case that the parameter δ_{pc} was set to zero instead of unity are also given. As for the unscaled flow equations, a change of this parameter has only a minor impact; the wave speeds are only altered insignificantly for the low acoustic Reynolds number case.

B.2.3 Wave speeds when low Reynolds number time-derivative preconditioning is applied

As suggested by Buelow [46] for low particle and high acoustic Reynolds numbers ($\text{Re}_k \ll 1$, $\text{Re}_{a,k} = \text{Re}_k/M \gg 1$) the value for the preconditioning parameter ϵ must be defined such that the numerical speed of sound a' is oriented after the viscous diffusion velocity. This is achieved by scaling the numerical speed of sound inversely proportional to the reciprocal value of the acoustic Reynolds number. With the parameter ϵ set to

$$\epsilon = M^2/\text{Re}_k^2 \quad (\text{B.31})$$

Limits	ω_1/k	ω_2/k	ω_3/k	σ
$\text{Re} \gg 1$	u	$\frac{1}{2}u(1 + \sqrt{5})$	$\frac{1}{2}u(1 - \sqrt{5})$	2.62
$\text{Re} \ll 1, \text{Re}/M \gg 1,$ $\text{Re}/M^2 \gg 1$	$-\hat{i}\frac{4}{3}\frac{u}{\text{Re}_k}$	$-\hat{i}\frac{3}{4}\text{Re}_k u$	$-\hat{i}\frac{4}{3}\frac{u}{\text{Re}_k}$	$\frac{16}{9}\frac{1}{\text{Re}_k^2}$
$\text{Re} \ll 1, \text{Re}/M \ll 1$	$-\hat{i}\frac{4}{3}\frac{u}{\text{Re}_k}$	uM^2 [$\gamma u M^2$]	$-\hat{i}\frac{4}{3}\frac{u}{\text{Re}_k}$	$\frac{4}{3}\frac{1}{\text{Re}_k M^2}$ [$\frac{4}{3}\frac{1}{\gamma \text{Re}_k M^2}$]

Table B.2: The roots of the dispersion relation and the condition number of the preconditioned Navier-Stokes equations for ideal gas flow ($\epsilon = M^2$ and $\delta_{\text{pc}} = 1$). The values listed in brackets are the transport velocities for $\delta_{\text{pc}} = 0$ if they differ from those for $\delta_{\text{pc}} = 1$.

the magnitude of the numerical speed of sound a' follows from Eq. (B.6)

$$a'^2 = \epsilon a^2 = (\nu k)^2. \quad (\text{B.32})$$

In the following, wave speeds for this particular choice of the parameter ϵ and with the parameter δ_{pc} set to unity will be analyzed for various limiting conditions.

In the limit of high Reynolds numbers ($\text{Re}_k \rightarrow \infty$) and bounded values for the Mach number, the roots of the dispersion become

$$(\omega/k)_1 = u, \quad (\omega/k)_{2,3} = \frac{1}{2}(1 \pm 1)u. \quad (\text{B.33})$$

This leads to a condition number σ that goes beyond all limits, which shows that the preconditioning choice according to Eq. (B.31) is not suited for high Reynolds number flow.

In the limit of low Reynolds numbers ($\text{Re}_k \ll 1$) and large acoustic Reynolds numbers ($\text{Re}_{a,k} = \text{Re}_k/M \gg 1$) the roots of the dispersion relation (B.10) become

$$(\omega/k)_1 = -\hat{i}\frac{4}{3}\frac{u}{\text{Re}_k}, \quad (\omega/k)_{2,3} = \frac{u}{6\text{Re}_k}(-4\hat{i} \pm 2\sqrt{5}). \quad (\text{B.34})$$

To arrive at these expressions, it was again necessary to assume that the ratio Re_k/M^2 is large ($\text{Re}_k/M^2 \gg 1$). For the case of high acoustic Reynolds numbers, setting the preconditioning parameter according to Eq. (B.31) is favorable, as this leads to a condition number of $\sigma = 4/3$.

For low acoustic Reynolds numbers ($\text{Re}_{a,k}/M \ll 1$) however, the preconditioning parameter does not prevent Mach or Reynolds number stiffness, since the roots in this case are given by

$$(\omega/k)_1 = -\hat{i}\frac{4}{3}\frac{u}{\text{Re}_k}, \quad (\omega/k)_2 = u\frac{M^2}{\text{Re}_k^2}, \quad (\omega/k)_3 = -\hat{i}\frac{4}{3}\frac{u}{\text{Re}_k}, \quad (\text{B.35})$$

which leads to a spectral radius σ of $\sigma = \frac{3}{4}\frac{M^2}{\text{Re}_k}$.

Table B.3 summarizes the roots of the dispersion relation (B.10) when the preconditioning parameter ϵ is set according to Eq. (B.31). As can be seen

Limits	ω_1/k	ω_2/k	ω_3/k	σ
$\text{Re} \gg 1$	u	0	u	∞
$\text{Re} \ll 1, \text{Re}/\text{M} \gg 1,$ $\text{Re}/\text{M}^2 \gg 1$	$-\hat{i}\frac{4}{3}\frac{u}{\text{Re}_k}$	$\frac{u}{6\text{Re}_k}(-4\hat{i} + 2\sqrt{5})$	$\frac{u}{6\text{Re}_k}(-4\hat{i} - 2\sqrt{5})$	$\frac{4}{3}$
$\text{Re}_k \ll 1, \text{Re}_k/\text{M} \ll 1$	$-\hat{i}\frac{4}{3}\frac{u}{\text{Re}_k}$	$u\frac{\text{M}^2}{\text{Re}_k^2}$ $[\gamma u\frac{\text{M}^2}{\text{Re}_k^2}]$	$-\hat{i}\frac{4}{3}\frac{u}{\text{Re}_k}$	$\frac{3}{4}\frac{\text{M}^2}{\text{Re}_k}$ $[\frac{3}{4}\gamma\frac{\text{M}^2}{\text{Re}_k}]$

Table B.3: The roots of the dispersion relation and the condition number of the preconditioned Navier-Stokes equations for ideal gas flow and the preconditioning parameters ϵ and δ_{pc} set to $\epsilon = \text{M}^2/\text{Re}_k^2$ and $\delta_{\text{pc}} = 1$, respectively. The values listed in brackets are the wave speeds for $\delta_{\text{pc}} = 0$ if they differ from those for $\delta_{\text{pc}} = 1$.

from the table, if the preconditioning parameter δ_{pc} is set to zero instead of unity, this changes the spectral radius for the case of low acoustic Reynolds numbers but only by an insignificant factor γ .

For low particle and low acoustic Reynolds numbers ($\text{Re}_k \ll 1, \text{Re}_{a,k} = \text{Re}_k/\text{M} \ll 1$) Buelow [46] suggests setting the preconditioning parameter ϵ to

$$\epsilon = 1/\text{Re}_k. \quad (\text{B.36})$$

The roots of the dispersion equation (B.10) for this choice of the preconditioning parameter are given in Table B.4 for various limiting conditions. While a preconditioning parameter according to Eq. (B.36) does not relieve stiffness in the low Mach number limit for inviscid flow ($\text{M} \ll 1, \text{Re}_k \rightarrow \infty$) or eliminate Reynolds number stiffness at low particle but high acoustic Reynolds numbers ($\text{Re}_k \ll 1, \text{Re}_k/\text{M} \gg 1$), it leads to a favorable condition number of $\sigma = 4/3$ in the limit of low particle and acoustic Reynolds numbers ($\text{Re}_k \ll 1, \text{Re}_k/\text{M} \ll 1$).

If the preconditioning parameter δ_{pc} is changed from unity to zero, the condition numbers change only in the case of low particle and acoustic Reynolds numbers. The change in the condition number in that case is not important; however, in the case that the parameter δ_{pc} is set to zero, the second root

$$(\omega/k)_2 = \frac{u}{2\text{Re}_k}(2.42 + \hat{i}0.33) \quad (\text{B.37})$$

contains a positive imaginary part, which corresponds to a growing mode. Thus, if the choice for the parameter ϵ according to Eq. (B.36) should be used, the parameter δ_{pc} should be set to unity.

B.3 Wave speeds of the preconditioned Navier-Stokes equations for incompressible flow

In the following the wave speeds of the preconditioned Navier-Stokes equations for incompressible flow will be determined using dispersion analysis.

Limits	ω_1/k	ω_2/k	ω_3/k	σ
$\text{Re} \gg 1$	u	0	u	∞
$\text{Re} \ll 1, \text{Re}/M \gg 1,$ $\text{Re}/M^2 \gg 1$	$-\hat{i}\frac{4}{3}\frac{u}{\text{Re}_k}$	$\frac{u}{\sqrt{\text{Re}_k M}}\hat{i}$	$-\frac{u}{\sqrt{\text{Re}_k M}}\hat{i}$	$\frac{3}{4}\frac{\sqrt{\text{Re}_k}}{M}$
$\text{Re} \ll 1, \text{Re}/M \ll 1$	$-\hat{i}\frac{4}{3}\frac{u}{\text{Re}_k}$	$\frac{u}{\text{Re}_k}$ [$-\frac{u}{2\text{Re}_k}(2.42+\hat{i}0.33)$]	$-\hat{i}\frac{4}{3}\frac{u}{\text{Re}_k}$ [$-\frac{u}{2\text{Re}_k}(0.42+\hat{i}3.0)$]	$\frac{4}{3}$ [1.23]

Table B.4: The roots of the dispersion relation and the condition number of the preconditioned Navier-Stokes equations for the preconditioning parameters set to $\epsilon = \frac{1}{\text{Re}_k}$ and $\delta_{\text{pc}} = 1$. The values listed in brackets are the transport velocities for $\delta_{\text{pc}} = 0$ if they differ from those for $\delta_{\text{pc}} = 1$.

The effect of using time-derivative preconditioning for inviscid or viscous flows will be studied by calculating the wave speeds for various limiting flow conditions.

B.3.1 Wave speeds when time-derivative preconditioning for inviscid flows is applied

With the preconditioning parameter set to

$$\varrho'_p = \frac{1}{V_r^2} \quad \text{with} \quad V_r = u \quad (\text{B.38})$$

and the other parameters ϱ'_T , h'_T and h'_p set their respective physical counterparts, the roots of the dispersion relation (B.10) of the Navier-Stokes equations (B.3) under the assumption of constant density flow ($\varrho = \text{const.}$) reduce to

$$(\omega/k)_1 = u, \quad (\omega/k)_{2,3} = \frac{1}{2}(1 \pm \sqrt{5})u. \quad (\text{B.39})$$

This leads to a condition number of $\sigma = \left| \frac{1+\sqrt{5}}{1-\sqrt{5}} \right| \approx 2.62$, which shows that the wave speeds are properly clustered.

For low Reynolds number flow ($\text{Re}_k \ll 1$) the wave speeds become

$$\lambda_1 = -\frac{4}{3}\hat{i}\frac{u}{\text{Re}_k}, \quad \lambda_2 = -\frac{4}{3}\hat{i}\frac{u}{\text{Re}_k}, \quad \lambda_3 = -\frac{3}{4}\hat{i}u\text{Re}_k. \quad (\text{B.40})$$

This leads to a condition number of $\sigma = \frac{16}{9}\frac{1}{\text{Re}_k^2}$, which shows that the prescription in Eq. (B.38) for the preconditioning parameter ϱ'_p is not suited for low Reynolds number flow. Table B.5 summarizes the roots of the dispersion relation for $\varrho'_p = 1/u^2$ and incompressible flow under various limiting conditions.

B.3.2 Wave speeds when time-derivative preconditioning for viscous dominated flows is applied

In the following, the effect of choosing the preconditioning parameter ϱ'_p such that the numerical speed of sound a' is oriented after the diffusion velocity

Limits	ω_1/k	ω_2/k	ω_3/k	σ
$\text{Re} \gg 1$	u	$\frac{1}{2}u(1 + \sqrt{5})$	$\frac{1}{2}u(1 - \sqrt{5})$	2.62
$\text{Re} \ll 1$	$-\hat{i}\frac{4}{3}\frac{u}{\text{Re}_k}$	$-\hat{i}\frac{3}{4}\text{Re}_k u$	$-\hat{i}\frac{4}{3}\frac{u}{\text{Re}_k}$	$\frac{16}{9}\frac{1}{\text{Re}_k^2}$

Table B.5: The roots of the dispersion relation and the condition number of the preconditioned Navier-Stokes equations for incompressible flows with $\varrho'_p = 1/u^2$

Limits	ω_1/k	ω_2/k	ω_3/k	σ
$\text{Re} \gg 1$	u	$-\frac{u}{\text{Re}_k^2}$	u	Re_k^2
$\text{Re} \ll 1$	$-\hat{i}\frac{4}{3}\frac{u}{\text{Re}_k}$	$\frac{u}{6\text{Re}_k}(-4\hat{i} + 2\sqrt{5})$	$\frac{u}{6\text{Re}_k}(-4\hat{i} - 2\sqrt{5})$	$\frac{4}{3}$

Table B.6: The roots of the dispersion relation and the condition number σ of the preconditioned Navier-Stokes equations for incompressible flows and $\varrho'_p = \text{Re}_k^2/u^2$

$V_{\text{vis}} = \nu k$ will be examined. Thus, the wave speeds when the preconditioning parameter ϱ'_p is set to

$$\varrho'_p = \frac{\text{Re}_k^2}{u^2} = \frac{1}{V_{\text{vis}}^2} = (\nu k)^2 \quad (\text{B.41})$$

will be examined.

The roots (B.22) of the dispersion relation (B.10) of the Navier-Stokes equations (B.3) under the assumption of constant density flow ($\varrho = \text{const.}$) become

$$(\omega/k)_{1,3} = u, \quad (\omega/k)_2 = -\frac{u}{\text{Re}_k^2}, \quad (\text{B.42})$$

for large Reynolds numbers ($\text{Re}_k \gg 1$), which leads to a condition number of $\sigma = \text{Re}_k^2$. Thus, for high Reynolds numbers, the prescription in Eq. (B.41) for the preconditioning parameter ϱ'_p is not suitable.

In the limit of low Reynolds numbers ($\text{Re}_k \ll 1$), a dispersion analysis leads to the following values of the wave speeds

$$(\omega/k)_1 = -\frac{4}{3}\hat{i}\frac{1}{\text{Re}_k}, \quad (\omega/k)_{2,3} = \frac{u}{6\text{Re}_k}(-4\hat{i} \pm 2\sqrt{5}). \quad (\text{B.43})$$

The condition number σ in this case reads as $\sigma = \frac{4}{3}$, which shows that a prescription of the preconditioning parameter ϱ'_p according to Eq. (B.41) is suited for low Reynolds number flow. Table B.6 summarizes the roots of the dispersion relation for incompressible flows when the preconditioning parameter ϱ'_p is defined according to Eq. (B.41).

For the case of ideal gas flow the wave velocities were determined for the case that the preconditioning parameter ϵ was set to $\epsilon = 1/\text{Re}_k$. For incompressible flows, this choice corresponds to setting the preconditioning parameter ϱ'_p as

$$\varrho'_p = \text{Re}_k/u^2. \quad (\text{B.44})$$

Limits	ω_1/k	ω_2/k	ω_3/k	σ
$\text{Re}_k \gg 1$	u	$-\frac{u}{\text{Re}_k}$	u	Re_k
$\text{Re}_k \ll 1$	$-\hat{i}\frac{4}{3}\frac{u}{\text{Re}_k}$	$-\frac{3}{4}\hat{i}u$	$-\hat{i}\frac{4}{3}\frac{u}{\text{Re}_k}$	$\frac{16}{9}\frac{1}{\text{Re}_k}$

Table B.7: The roots of the dispersion relation and the condition number of the preconditioned Navier-Stokes equations for incompressible flows with $\varrho'_p = \frac{\text{Re}_k}{u^2}$

For this choice of the preconditioning parameter, the roots of the dispersion relation (B.10) reduce to

$$(\omega/k)_{1,3} = u, \quad (\omega/k)_2 = -\frac{u}{\text{Re}_k} \quad (\text{B.45})$$

for high Reynolds number flow ($\text{Re}_k \gg 1$), which leads to a condition number σ of $\sigma = \text{Re}_k$. For low Reynolds numbers ($\text{Re}_k \ll 1$) the wave speeds become

$$(\omega/k)_1 = -\frac{4}{3}\hat{i}\frac{u}{\text{Re}_k}, \quad (\omega/k)_2 = -\frac{3}{4}\hat{i}u, \quad (\omega/k)_3 = -\frac{4}{3}\hat{i}\frac{u}{\text{Re}_k} \quad (\text{B.46})$$

from which a condition number σ of $\sigma = \frac{16}{9}\frac{1}{\text{Re}_k}$ follows. Thus, both for high and low Reynolds numbers, the prescription according to Eq. (B.44) for the preconditioning parameter ϱ'_p does not lead to favorable condition numbers. Table B.7 summarizes the wave speeds of the preconditioned Navier-Stokes equations under various limiting conditions when the preconditioning parameter ϱ'_p is set according to Eq. (B.44).

B.4 Conclusions and implications of the results of the dispersion analysis

The dispersion analysis above shows that the use of low Mach preconditioning with

$$\epsilon = \epsilon_c, \quad \epsilon_c = M^2 \quad (\text{B.47})$$

or

$$\varrho'_p = \frac{1}{V_r^2} - \frac{1 - \varrho h_p}{\varrho h_T} \varrho'_T, \quad V_r = \sqrt{\epsilon} \cdot a = u \quad (\text{B.48})$$

with $\varrho'_T = \delta_{\text{pc}} \varrho_T$, $\delta_{\text{pc}} \in [0, 1]$, $h'_T = h_T$, and $h'_p = 1 - \varrho h_p$ leads to a good conditioning ($\sigma \approx 2.62$) of the linearized Navier-Stokes in the case of high Reynolds numbers, ideal gas flow. Analogously, by setting the parameters ϱ'_T , h'_T , h'_p to their respective physical counterparts and the preconditioning parameter ϱ'_p to

$$\varrho'_p = \frac{1}{V_r^2} \quad \text{with} \quad V_r = u \quad (\text{B.49})$$

a good conditioning ($\sigma \approx 2.62$) is also achieved for incompressible flows.

For low particle Reynolds numbers, viscous effects must be accounted for in the preconditioning formulation, since the use of time-derivative preconditioning otherwise may aggravate the low Reynolds number stiffness. For low particle ($\text{Re}_k \ll 1$) and high acoustic Reynolds numbers ($\text{Re}_{a,k} = \text{Re}_k/\text{M} \gg 1$) the following preconditioning strategy

$$\epsilon = \max(\epsilon_c, \epsilon_v), \quad \epsilon_v = \text{M}^2/\text{Re}_k^2 = (\nu k)^2/a^2 \quad (\text{B.50})$$

or equivalently

$$\varrho'_p = \frac{1}{V_r^2} - \frac{1 - \varrho h_p}{\varrho h_T} \varrho'_T, \quad V_r = \max(u, \nu k) \quad (\text{B.51})$$

with $\varrho'_T = \delta_{\text{pc}} \varrho_T$, $\delta_{\text{pc}} \in [0, 1]$ leads to a good conditioning ($\sigma = 4/3$) for ideal gas flow.

In cases with low particle ($\text{Re}_k \ll 1$) and low acoustic Reynolds numbers ($\text{Re}_{a,k} \ll 1$) the prescription for the preconditioning parameter ϱ'_p given in Eq. (B.51) is not suitable. A good conditioning ($\sigma = 4/3$) for low acoustic Reynolds numbers and ideal gas flow is attained using the following set of preconditioning parameter

$$\epsilon = \max(\epsilon_c, \epsilon_v), \quad \epsilon_v = 1/\text{Re}_k \quad (\text{B.52})$$

or analogously

$$\varrho'_p = \frac{1}{V_r^2} - \frac{1 - \varrho h_p}{\varrho h_T} \varrho'_T, \quad V_r = \max(u, a/\sqrt{\text{Re}_k}). \quad (\text{B.53})$$

For incompressible flows the Mach number is identically equal zero, so that only the case analogous to the high acoustic Reynolds number case for ideal gas flow can be considered. To accommodate for regions of low particle Reynolds numbers $\text{Re}_k = u/(\nu k) \ll 1$ in incompressible flows, the prescription (B.51) for the preconditioning parameter should be used. In the limit of low particle Reynolds numbers this yields a condition number of $\sigma = 4/3$, which is the same as for the case of ideal gas flow.

Whether the parameter δ_{pc} is set to unity or to zero for ideal gas flow this only changes the condition number in the limit of low Reynolds number flow. The value of δ_{pc} does not alter the condition number significantly, but it should be noted that a value of $\delta_{\text{pc}} = 0$ for the low particle and low acoustic Reynolds number case leads to growing modes. Thus, if the prescription (B.52) for the preconditioning parameters ϵ should be used or the preconditioning parameter ϱ'_p should be defined according to Eq. (B.53), it is recommended to set the parameter δ_{pc} to unity. For incompressible flows the parameter δ_{pc} has no effect since ϱ_T vanishes identically.

As discussed by Buelow [46], to obtain a preconditioning method that follows the prescription (B.52) for low particle and acoustic Reynolds and the prescription (B.51) for low particle and high acoustic Reynolds numbers, the following definition for ϵ_v could be applied

$$\epsilon_v = \frac{\text{M}^2(1 - \text{Re}_k)}{\text{Re}_k^2 + \text{M}^2\text{Re}_k(1 - \text{Re}_k)}. \quad (\text{B.54})$$

With this prescription, the parameter ϵ_v goes to M^2/Re_k^2 for high acoustic Reynolds numbers and to $1/\text{Re}_k$ for low values of the same.

It should however be noted, that the Reynolds number is wave number dependent. Thus, the desired behaviour of the preconditioning scheme under limiting conditions can only be ensured for a given wave number. As suggested by Choi and Merkle [60] the parameter ϵ_v may be selected such that the von Neumann Number of the solution scheme is controlled.

For most practical CFD simulations, the Reynolds number is much larger than the Mach number; – cases for which the Mach number is high and the Reynolds number simultaneously is low are seldom encountered, which is why it was decided not to account for the case of low particle and low acoustic Reynolds number flow in the current work.

For the case of low particle and high acoustic Reynolds number flow, the Reynolds number Re_k used in the definition of the preconditioning parameter ϵ_v is taken to be the cell Reynolds number. The Reynolds number is oriented after the wave number $k = 2\pi/\Delta x$ of the shortest waves, i.e., the Reynolds number is defined as

$$\text{Re}_k = \frac{u\Delta x}{\nu} \quad (\text{B.55})$$

with Δx as the local distance between two grid nodes. The reason for this choice is that the viscosity will predominantly act on the shortest wave lengths. Stability analysis of the discretized flow equations [46] also shows that the cell Reynolds number is a critical parameter in judging the influence of the diffusive terms in the discretized flow equations. With this choice, the preconditioning parameter ϵ reads for ideal gases as

$$\epsilon = \max(\epsilon_c, \epsilon_v), \quad \epsilon_c = M^2, \quad \epsilon_v = M^2/\text{Re}_k^2, \quad (\text{B.56})$$

which in terms of the preconditioning parameters ϱ'_p and ϱ'_T translates into

$$\varrho'_p = \frac{1}{V_r^2} - \frac{1 - \varrho h_p}{\varrho h_T} \varrho'_T, \quad V_r = \max(u, \nu/\Delta x), \quad \varrho'_T = \delta_{\text{pc}} \varrho_T \quad (\text{B.57})$$

with $\delta_{\text{pc}} \in [0, 1]$. The formulation in Eq. (B.57) applies both for incompressible fluid and for ideal gas flow.

Appendix C

Scaling of the artificial dissipation for inviscid and viscous, low Mach number flow

In order to avoid low frequency errors and to stabilize a numerical scheme for convection equations, dissipative terms must be introduced in the discretization. The dissipative terms may be introduced implicitly via the use of an upwind discretization or as artificial terms that are explicitly added to centrally discretized fluxes. Whichever type of scheme is used, it is essential for the accuracy and stability of the solution scheme that the dissipative terms remain in the same order as the physical, non-dispersive part of the convective fluxes.

In this chapter it will be shown that the artificial dissipation in the scheme of Jameson, Schmidt and Turkel (JST) [131] scales wrongly in the low Mach or low Reynolds number limit. If, however, a suitable preconditioning scheme is applied and properly accounted for in the construction of the artificial dissipation, a correct scaling of the dissipative terms can be ensured both in the limit of inviscid and viscous low Mach number flow.

The analysis carried out in this chapter is based on the perturbation methods introduced in Appendix A and on the theoretical work of Venkateswaran and Merkle [289].

C.1 Scaling of artificial dissipation of the JST-scheme for inviscid flows

In order to analyse how the artificial dissipation of JST-scheme scales in the low Mach number limit both with and without preconditioning, the linearized Euler equations

$$\frac{\partial \mathbf{Q}}{\partial t} + A \frac{\partial \mathbf{Q}}{\partial x} = \mathbf{D}, \quad A = \left. \frac{\partial \mathbf{E}}{\partial \mathbf{Q}} \right|_{\mathbf{Q}} \quad (\text{C.1})$$

are used. The vector

$$\mathbf{D} = \delta^+ \left[k^{(4)} \frac{\sigma}{\Delta x} (\delta^- \delta^+ \delta^- \mathbf{Q}) \right] \quad (\text{C.2})$$

represents thereby the artificial dissipation with $k^{(4)}$ as a scaling coefficient and $\sigma = |u| + a$ as the spectral radius. The operators δ^+ and δ^- represent the forward and backward difference operators; for an arbitrary state variable ϕ these operators are defined as

$$\delta^+ \phi_i = \phi_{i+1} - \phi_i, \quad \delta^- \phi_i = \phi_i - \phi_{i-1}, \quad (\text{C.3})$$

where the subscripts $i - 1$, i , and $i + 1$ denote the index of successive nodes.

Changing from the vector of conservative variables $\mathbf{Q} = [\rho, \rho u, \rho e_0]^T$ to the vector $\mathbf{Q}_v = [p, u, T]^T$ of viscous, primitive variables by applying the chain rule, the following formulation is obtained

$$\Gamma_e \frac{\partial \mathbf{Q}_v}{\partial t} + A_v \frac{\partial \mathbf{Q}_v}{\partial x} = \mathbf{D}, \quad (\text{C.4})$$

with the Jacobians Γ_e and A_v defined as

$$\Gamma_e = \left(\frac{\partial \mathbf{Q}}{\partial \mathbf{Q}_v} \right), \quad A_v = \left(\frac{\partial \mathbf{E}}{\partial \mathbf{Q}_v} \right), \quad (\text{C.5})$$

respectively. Assuming that the grid spacing, the Jacobian matrix Γ_e , and the spectral radius are locally constant, the artificial dissipation vector can be written as

$$\mathbf{D}_v = \frac{k^{(4)} \sigma}{\Delta x} \Gamma_e \delta^{(4)} \mathbf{Q}_v \quad (\text{C.6})$$

where $\delta^{(4)} = \delta^+ \delta^- \delta^+ \delta^-$ represents the fourth order central difference operator.

To analyse the size of the various terms, a non-dimensionalization of the inviscid flow equations is carried out in the same manner as for the preconditioned Euler equation in Appendix A.1 where the following reference scales

$$L^\dagger, u^\dagger, \rho^\dagger, T^\dagger, p^\dagger, t^\dagger = L^\dagger / u^\dagger, h^\dagger = p^\dagger / \rho^\dagger \quad (\text{C.7})$$

were used for normalization. With this kind of normalization the parameter ϵ with $\epsilon = \rho^\dagger u^{\dagger 2} / p^\dagger$ appears as the only dimensionless number in the flow equations. This quantity represents the ratio of the dynamic to the static pressure and for ideal gases is proportional to the square of Mach number, i.e., $\epsilon = \gamma \mathbf{M}^{\dagger 2}$. By expanding the pressure in a series of this parameter

$$p = p^{(0)} + \epsilon p^{(2)} + \mathcal{O}(\epsilon^2) \quad (\text{C.8})$$

and afterwards separating out the zeroth order pressure assuming low Mach numbers ($\mathbf{M} \ll 1$), one arrives at the following form of the non-dimensionalized linearized Euler equations

$$\Gamma_e^* \frac{\partial \mathbf{Q}_v^*}{\partial t^*} + A_v^* \frac{\partial \mathbf{Q}_v^*}{\partial x^*} = \mathbf{D}_v^* \quad (\text{C.9})$$

with

$$\Gamma_e^* = \begin{bmatrix} \rho_p^* \epsilon & 0 & \rho_T^* \\ 0 & \rho^* & 0 \\ -d_p^* \epsilon & 0 & \rho^* h_T^* \end{bmatrix}, \quad A_v^* = \begin{bmatrix} u^* \rho_p^* \epsilon & \rho & u^* \rho_T^* \\ 1 & \rho^* u^* & 0 \\ -d_p^* \epsilon u^* & 0 & \rho^* u^* h_T^* \end{bmatrix} \quad (\text{C.10})$$

and the artificial dissipation vector written as

$$\mathbf{D}_v = k^{(4)} \frac{\sigma^*}{\Delta x^*} \begin{bmatrix} \varrho_p^* \epsilon \delta^{(4)} p_{(2)}^* + \varrho_T^* \delta^{(4)} T^* \\ \varrho^* \delta^{(4)} u^* \\ -d_p^* \epsilon \delta^{(4)} p_{(2)}^* + \varrho^* h_T^* \delta^{(4)} T^* \end{bmatrix} \quad (\text{C.11})$$

with $d_p^* = 1 - \varrho^* h_p^*$. The asterix "*" as a superscript on a flow variable denotes that it has been normalized, i.e., a state variable ϕ^* is defined as $\phi^* = \phi/\phi^\dagger$. All terms in the temporal and spatial terms above scale in the order of unity in magnitude and zeroth order in the Mach number except those involving the parameter ϵ .

In the artificial dissipation terms the normalized spectral radius $\sigma^* = |u^*| + a^*$ can be written as $\frac{M+1}{M}$, which for low Mach number yields the following approximation $|u^*| + a^* \approx \frac{1}{M}$. With the parameter ϵ proportional to the square of the Mach number, the artificial dissipation vector scales as

$$\mathbf{D}_v = [D_{v,1}, D_{v,2}, D_{v,3}]^T = [\mathcal{O}(M), \mathcal{O}(1/M), \mathcal{O}(1/M)]^T. \quad (\text{C.12})$$

This result shows that if preconditioning is not used for the simulation of low Mach number flow, the artificial dissipation added to the continuity equation is too low while excess dissipation is added to the momentum and the energy equations.

The result in Eq. (C.12) is attained by neglecting the temperature difference term that is added to the continuity equation and the pressure difference term that is added to the energy equation. In the limit of a vanishing thermal expansion coefficient of the fluid, both of the neglected terms vanish identically. For low Mach number, ideal gas flow the pressure difference term added to the energy equation is two orders in magnitude smaller the temperature difference term. For ideal gas flow, the temperature difference term $D_{v,1,T}$ added to the continuity equation scales as $D_{v,1,T} = \mathcal{O}(1/M)$. However, for the stabilization of the continuity and momentum equation it is the pressure and velocity difference terms that are important since it is the differences in the total pressure that is the driving force for the kinetic motion of the flow when gravity is not accounted for. Anyhow, whether the temperature difference term is accounted for or not, the dissipation terms of the unpreconditioned JST scheme scale only correctly, i.e., in the same order as the convective terms, for sonic flow conditions.

Ideally, the dissipative fluxes should scale in the order of unity for all Mach number levels so that these terms match the convective terms. If inviscid preconditioning is used, the parameter ϱ_p^* is replaced by the scaled quantity $\varrho_p'^*$ defined as

$$\varrho_p'^* = \frac{p^\dagger}{\varrho^\dagger u^{\dagger 2}}, \quad (\text{C.13})$$

which implies that all terms in the matrices Γ_ϵ^* and A_v^* will scale in the same order, except the terms $-d_p^* \epsilon$ and $-d_p^* \epsilon u^*$, which can be omitted for low Mach numbers. Additionally, if the spectral radius σ , which is used as a scaling

parameter of the artificial dissipation, is set to the spectral radius of the preconditioned system, i.e., $\sigma^* = |u^*|$, all dissipation terms will scale in the order unity

$$\mathbf{D}_v = [\mathcal{O}(1), \mathcal{O}(1), \mathcal{O}(1)]^T, \quad (\text{C.14})$$

i.e., they scale correctly independently of the Mach number level. This result for the artificial dissipation of the preconditioned JST scheme is achieved irrespective of the value of the thermal expansion coefficient and regardless whether the temperature difference term $D_{v,1,T}$ is added to the continuity equation or not.

C.2 Scaling of artificial dissipation of the JST-scheme for viscous dominated flows

To investigate the scaling of artificial dissipation terms of the JST discretization scheme, the linearized Navier-Stokes equations (B.3) to which the artificial dissipation vector \mathbf{D}_v defined in Eq. (C.6) has been added

$$\Gamma_e \frac{\partial \mathbf{Q}_v}{\partial t} + A \frac{\partial \mathbf{Q}_v}{\partial x} = \frac{\partial}{\partial x} \left(R_{xx} \frac{\partial \mathbf{Q}_v}{\partial x} \right) + \mathbf{D}_v \quad (\text{C.15})$$

are normalized using the following reference quantities

$$L^\dagger, u^\dagger, p^\dagger, \rho^\dagger, T^\dagger, t^\dagger, \mu^\dagger, k_\lambda^\dagger, h^\dagger = p^\dagger / \rho^\dagger. \quad (\text{C.16})$$

This yields

$$\Gamma_e^* \frac{\partial \mathbf{Q}_v^*}{\partial t^*} + A_v^* \frac{\partial \mathbf{Q}_v^*}{\partial x^*} = \frac{\partial}{\partial x^*} \left(R_{xx}^* \frac{\partial \mathbf{Q}_v^*}{\partial x^*} \right) + \mathbf{D}_v^* \quad (\text{C.17})$$

with

$$\Gamma_e^* = \begin{bmatrix} \frac{\varrho_p^*}{\text{Re}} & 0 & \frac{1}{\text{Re}} \varrho_T^* \\ 0 & \varrho^* & 0 \\ -d_p^* \text{Pr} & 0 & \varrho^* h_T^* \text{Pr} \end{bmatrix}, \quad A_v^* = \begin{bmatrix} u^* \varrho_p^* & \varrho & u^* \varrho_T^* \\ \text{Re} \frac{p^\dagger}{\varrho u^{\dagger 2}} & \varrho^* u^* & 0 \\ -d_p^* u^* \text{Pe} & 0 & \varrho^* u^* h_T^* \text{Pe} \end{bmatrix}, \quad (\text{C.18})$$

$$R_{xx}^* = \begin{bmatrix} 0 & 0 & 0 \\ 0 & 4/3 \mu^* & 0 \\ 0 & 4/3 \mu^* u^* & \mu^* / \text{Pr} \end{bmatrix}, \quad \mathbf{D}_v^* = \frac{k^{(4)} \sigma^*}{\Delta x^*} \begin{bmatrix} (\varrho_p^* \delta^{(4)} p^* + \varrho_T^* \delta^{(4)} T) \frac{1}{\text{Re}} \\ \varrho^* \delta^{(4)} u^* \\ (\varrho^* h_T^* \delta^{(4)} T^* - d_p^* \delta^{(4)} p^*) \text{Pr} \end{bmatrix}.$$

The Reynolds, Prandtl and Peclet numbers are defined according to Eq. (A.23). To arrive at the normalized equations (C.17), the same procedure as applied in Chapter A.2 has been used, which means that the reference time scale t^\dagger is defined as

$$t^\dagger = \frac{\text{Re} L^\dagger}{u^\dagger} = \frac{L^{\dagger 2}}{\nu^\dagger}. \quad (\text{C.19})$$

This reference time scale has been chosen such that the temporal term balances the viscous forces in the momentum equations.

The coefficient $\text{Re} \frac{p^\dagger}{\varrho^\dagger u^\dagger{}^2}$ of the pressure gradient term in the momentum equation should scale in the same order as the other terms to ensure a balance between temporal, acoustic, advective and diffusive terms. This coefficient is used as perturbation variable

$$\epsilon = \frac{\varrho^\dagger u^\dagger{}^2}{p^\dagger} \frac{1}{\text{Re}}, \quad (\text{C.20})$$

to expand the pressure into the following series

$$p = p^{(0)} + \epsilon p^{(2)} + \mathcal{O}(\epsilon^2). \quad (\text{C.21})$$

Applying this pressure expansion, Eq. (C.17) can be written as

$$\Gamma_e^* \frac{\partial \tilde{\mathbf{Q}}_v^*}{\partial t^*} + A_v^* \frac{\partial \tilde{\mathbf{Q}}_v^*}{\partial x^*} = \frac{\partial}{\partial x^*} \left(R_{xx}^* \frac{\partial \tilde{\mathbf{Q}}_v^*}{\partial x^*} \right) + \mathbf{D}_v^* \quad (\text{C.22})$$

with the perturbed state vector $\tilde{\mathbf{Q}}^* = [p_{(2)}^*, u^*, T^*]$ and the matrices

$$\Gamma_e^* = \begin{bmatrix} \frac{\varrho_p^*}{\text{Re}} \epsilon & 0 & \frac{1}{\text{Re}} \varrho_T^* \\ 0 & \varrho^* & 0 \\ -(1 - \varrho^* h_p^*) \text{Pr} \epsilon & 0 & \varrho^* h_T^* \text{Pr} \end{bmatrix}, \quad A_v^* = \begin{bmatrix} u^* \varrho_p^* & \varrho^* & u^* \varrho_T^* \\ 1 & \varrho^* u^* & 0 \\ -d_p^* \epsilon u^* \text{Pe} & 0 & \varrho^* u^* h_T^* \text{Pe} \end{bmatrix},$$

$$R_{xx}^* = \begin{bmatrix} 0 & 0 & 0 \\ 0 & 4/3 \mu^* & 0 \\ 0 & 4/3 \mu^* u^* & \mu^* / \text{Pr} \end{bmatrix}, \quad \mathbf{D}_v^* = k^{(4)} \frac{\sigma^*}{\Delta x^*} \begin{bmatrix} \epsilon \varrho_p^* \frac{1}{\text{Re}} \delta^{(4)} p_{(2)}^* + \frac{\varrho_T^*}{\text{Re}} \delta^{(4)} T^* \\ \varrho^* \delta^{(4)} u^* \\ \varrho^* h_T^* \text{Pr} \delta^{(4)} T^* - \epsilon d_p^* \text{Pr} \delta^{(4)} p_{(2)}^* \end{bmatrix}. \quad (\text{C.23})$$

From the perturbation analysis carried out in Appendix A.2 for low Reynolds number flow, it was deduced that the spatial gradients of the zeroth order pressure vanishes when the quantity ϵ approaches zero. Assuming constant boundary conditions, the temporal derivatives of the zeroth order pressure also vanishes. For this reason only the second order pressure $p_{(2)}^*$ and not the zeroth order pressure $p_{(0)}^*$ appears in the last equations.

If the Prandtl number scales in the order of unity, then the leading term of the convective and the diffusive fluxes in the equations (C.22) above scales in order of unity for low Reynolds number flow. As will be shown in the following, if preconditioning is not used, the dissipative terms do not scale in the order of unity and will consequently not be in proper balance with the convective and diffusive fluxes.

With the perturbation variable ϵ for viscous, low Mach number flow defined by Eq. (C.20), which for an ideal gases can be expressed as $\epsilon = k_v \gamma M^2 / \text{Re}$, and with the normalized spectral radius $\sigma^* = |u^*| + a^*$, which can be approximated as $\sigma^* \approx \frac{1}{M}$ for low speed flows, the artificial dissipation vector scales as

$$\mathbf{D}_v = [D_{v,1}, D_{v,2}, D_{v,3}]^T = [\mathcal{O}(M/\text{Re}^2), \mathcal{O}(1/M), \mathcal{O}(1/M)]^T \quad (\text{C.24})$$

when preconditioning is not used. To arrive at this result, it was assumed that the Prandtl number is in the order of unity and that no dissipation based on temperature differences are added to the continuity equation. It was also assumed that the dissipation term, which is based on pressure differences and is added to the energy equation, can be neglected. For incompressible flows, the last two assumptions are fulfilled since both ϱ_T and d_p vanish identically; for ideal gas flow not. The neglected dissipation term $D_{v,1,T} = k^{(4)}\sigma/\Delta x \cdot \varrho_T^*/\text{Re} \cdot \delta^{(4)}T$ based on temperature differences and the neglected pressure dissipation term $D_{v,3,p} = -k^{(4)}\sigma/\Delta x \cdot \epsilon d_p^* \varrho_T^* \cdot \text{Pr} \delta^{(4)}p$ scale as

$$D_{v,1,T} = \mathcal{O}(1/\text{M} \cdot 1/\text{Re}), \quad D_{v,3,p} = \mathcal{O}(\text{M}/\text{Re}) \quad (\text{C.25})$$

for Prandtl numbers in the order of unity. Whether or not the last terms are accounted for, the scaling of the artificial dissipation will in any case be wrong unless both the Mach and the Reynolds number scale in the order of unity. If preconditioning is not used then the unsteady terms in Eq. (C.22) will neither scale in the order of unity. However, what matters for the accuracy of the converged solution is that the dissipation terms scale in the order of the leading flux term.

In the case that time-derivative preconditioning is used, the physical derivatives ϱ_p and ϱ_T appearing in the matrix Γ_e and in the dissipation vector \mathbf{D}_v are replaced with the scaled quantities ϱ'_p and ϱ'_T , respectively. Furthermore, the spectral radius σ^* is oriented after the spectral radius of the preconditioned system, i.e., $\sigma^* \approx |u^*|$. When preconditioning is used, the leading term of the convective and diffusive fluxes in each of the equations (C.22) still scales in the order of unity. If preconditioning for inviscid flow is used, the preconditioning parameter ϱ'_p is set to $\varrho'_p = k_{\text{inv}} p^\dagger / (\varrho^\dagger u^{\dagger 2})$, which for ideal gas flow can be written as $\varrho'_p = k_{\text{inv}} \gamma / \text{M}^{\dagger 2}$. In the case the inviscid preconditioning is used the artificial dissipation vector scales as

$$\mathbf{D}_v = [\mathcal{O}(1/\text{Re}^2), \mathcal{O}(1), \mathcal{O}(1)]^T, \quad (\text{C.26})$$

if the terms $D_{v,1,T}$ and $D_{v,3,p}$ are neglected and it is assumed that the Prandtl number scales in the order of unity. If the parameter ϱ'_T is set to its physical counterpart ϱ_T the term $D_{v,1,T}$ can, due to its scaling $D_{v,1,T} = \mathcal{O}(1/\text{Re})$, be neglected as the pressure diffusion term $D_{v,1,p}$ with $D_{v,1,p} = \mathcal{O}(1/\text{Re}^2)$ will dominate for low Reynolds number flow. The temperature dissipation term $D_{v,1,T}$ vanishes identically in the case that the preconditioning parameter ϱ'_T is set to zero. The second term $D_{v,3,p}$ can also be neglected as it scales in the order of the perturbation parameter ϵ , which in the present analysis is assumed to be small.

If, however, viscous preconditioning is used, then the parameter ϱ'_p is set according to Eq. (A.27), which for ideal gases yields

$$\varrho'_p = k_v \frac{\text{Re}^2 p^\dagger}{\varrho^\dagger u^{\dagger 2}} = k_v \frac{\text{Re}^2}{\gamma \text{M}^{\dagger 2}}. \quad (\text{C.27})$$

If in addition the preconditioning parameter ϱ_T^* is set to zero, all components of the artificial dissipation vector \mathbf{D}_v will scale in the same order as the convective and diffusive terms, i.e.,

$$\mathbf{D}_v = [\mathcal{O}(1), \mathcal{O}(1), \mathcal{O}(1)]. \quad (\text{C.28})$$

The pressure diffusion term $D_{v,3,p}$ can be neglected for low values of the perturbation variable ϵ ; the temperature diffusion term $D_{v,1,T}$ vanishes identically for $\varrho_T^* = 0$. This result is valid for all Mach and Reynolds numbers for which the perturbation parameter is at least one order less than unity, i.e., $\epsilon = \text{M}^2/\text{Re} \ll 1$.

If the preconditioning parameter ϱ_T^* is set to be proportional to its physical counterpart $\varrho_T^* = \delta_{\text{pc}} \varrho_T$, then also a dissipation term $D_{v,1,T}$ based on temperature differences is added to the continuity equation. This term then scales as

$$D_{v,1,T}^* = \mathcal{O}(\delta_{\text{pc}} \varrho_T^* T^* / \text{Re}). \quad (\text{C.29})$$

If this term is added to the continuity equation, its magnitude should not exceed unity. For the sake of avoiding that this term overwhelms the other terms in the continuity equation the restriction

$$\delta_{\text{pc}} \leq \text{Re} / (\varrho_T^* T^*) \quad (\text{C.30})$$

for the preconditioning parameter δ_{pc} follows. As discussed in Chapter A.2, this condition has anyway to be met by the preconditioning scheme to ensure that the temporal temperature derivative term added to the continuity equation is not dominating.

Appendix D

General issues in simulating low Mach number flow

As elaborated in Chapter 3 as well as in the previous appendices, a major challenge in simulating low Mach number flows consists in accommodating for the disparity of the advective and acoustic wave speeds. An additional matter of general importance that needs to be dealt with is that in the limit of vanishing Mach numbers the compressible Navier-Stokes equations do not necessarily converge to the corresponding transport equations for incompressible flows. Furthermore, several flow quantities, like the pressure and the temperature, are nearly constant for low Mach number flow. If no measures are taken when simulating low speed flows, the largest part of the mantissa is used on storing the constant part of the solution. This may lead to an insufficient numerical resolution of the variations in the solution variables, which in turn can cause significant round-off errors.

D.1 Singularity of the flow equations

To discuss the importance of a proper normalization of the pressure, so that the compressible flow equations coincide with the ones for incompressible flows in the limit of a vanishing Mach number, an analysis similar to that of Müller [194] is carried out in the following.

The starting point of the analysis are the Euler equations, which have been normalized with the reference quantities $p^\dagger, \rho^\dagger, u^\dagger, L^\dagger$, and $t^\dagger = L^\dagger/u^\dagger$. The momentum equations read as

$$\frac{\partial(\varrho^* c_i^*)}{\partial t^*} + \frac{\partial(\varrho^* c_i^* c_j^*)}{\partial x_j^*} + \frac{p^\dagger}{\varrho^\dagger u^{\dagger 2}} \frac{\partial p^*}{\partial x_i^*} = 0, \quad (\text{D.1})$$

where the asterisk * as a superscript denotes that the respective quantity has been normalized. The pressure gradient in the momentum equation for ideal gases can be expressed in the form

$$\frac{p^\dagger}{\varrho^\dagger u^{\dagger 2}} \frac{\partial p^*}{\partial x_i^*} = \frac{1}{\gamma M^{\dagger 2}} \frac{\partial p^*}{\partial x_i^*}. \quad (\text{D.2})$$

Thus, in the limit of vanishing Mach numbers, the momentum equations read as

$$\frac{\partial p^*}{\partial x_i^*} = 0_i. \quad (\text{D.3})$$

A multi-scale perturbation analysis [5, 194] of the compressible Navier-Stokes equations for low Mach number flows, in which the pressure p is expanded in a series

$$p = p_{(0)} + Mp_{(1)} + M^2p_{(2)} + \dots \quad (\text{D.4})$$

of the Mach number, reveals that the zeroth order pressure term $p_{(0)}$ represents the thermodynamic part of the pressure and only influences the global compression of the flow field and the average value of the thermodynamic state variables (like the density) but not the variation of the local flow properties. The first order pressure $p_{(1)}$, on the other hand, is linked to the acoustics waves and the local compression of the flow field, whereas the second order pressure $p_{(2)}$ is directly coupled to the advection of the flow and the incompressible part of flow dynamics. To avoid a decoupling of the pressure and the local velocity field, it must be ensured that the second order pressure term $p_{(2)}$ remains effective in the flow equations in the limit of vanishing Mach numbers.

To avoid a so-called pressure-velocity decoupling at low Mach numbers, Bijl [35] suggests to introduce a dimensionless pressure defined as

$$p^* = \frac{p - p_{(0)}}{\varrho^\dagger u_i^{\dagger 2}}, \quad (\text{D.5})$$

where $p_{(0)}$ represents the zeroth order pressure in the flow; for practical computations the zeroth order pressure $p_{(0)}$ can be taken as the inlet or outlet pressure of the domain. With this choice of normalization, the pressure p^* is in the order of unity and the normalized momentum equations can be written as

$$\frac{\partial(\varrho^* c_i^*)}{\partial t^*} + \frac{\partial(\varrho^* c_i^* c_j^*)}{\partial x_j^*} + \frac{\partial p^*}{\partial x_i^*} = 0. \quad (\text{D.6})$$

This means that the pressure gradient term is of the same order as the convective and the unsteady terms.

For the purpose of normalizing the pressure as well as the velocity components, it is appropriate to orient the reference velocity u^\dagger after the maximum norm of the velocity in the flow. This ensures that the normalized velocities scale in the order of unity for low Mach number flow. The density at the inlet may be used as reference density ϱ^\dagger for the normalization of the pressure in Eq. (D.5).

D.2 Avoidance of round-off errors at low Mach numbers

In low Mach number flows some flow quantities like the pressure are nearly constant. Thus, if no care is taken the major part of the mantissa will be

used for storing the constant part of the pressure and large round-off errors may arise. To quantify round-off errors and to demonstrate how the use of a perturbed pressure may alleviate the numerical accuracy issue, an analysis similar to that one of Müller [194] will be carried out in the following.

In order to estimate the round-off errors associated with the numerical calculation of a pressure difference $\Delta p^* = p_R^* - p_L^*$ between the right and the left state of a cell interface, we assume that the flow quantities have been normalized by the reference quantities given in Eq. (A.21) such that their magnitude is in the order of unity.

Due to finite precision the exact values for pressures p_L^* and p_R^* are truncated; their numerical representations \tilde{p}_L^* and \tilde{p}_R^* can be written as

$$\tilde{p}_i^* = (1 + \epsilon_{m,i})p_i^*, \quad i \in \{L, R\} \quad (\text{D.7})$$

where ϵ_m represents the machine accuracy, which in other words is the smallest machine number that added to unity gives a numerical sum different from unity [215]. The numerical representation of a pressure difference $\Delta \tilde{p}^*$ can be expressed in the following fashion

$$\Delta \tilde{p}^* = \tilde{p}_R^* - \tilde{p}_L^* = \Delta p^* \left(1 + \frac{p_R^*}{\Delta p^*} \epsilon_{m,R} - \frac{p_L^*}{\Delta p^*} \epsilon_{m,L} \right). \quad (\text{D.8})$$

The relative error of the pressure difference $\Delta \tilde{p}^*$ due to numerical round-off errors can be estimated as

$$\epsilon_{\text{rnd}} = \left| \frac{\Delta \tilde{p}^* - \Delta p^*}{\Delta p^*} \right| \leq \frac{p_L^* + p_R^*}{|\Delta p^*|} \epsilon_m \quad (\text{D.9})$$

with $\epsilon_m = \max(|\epsilon_{m,L}|, |\epsilon_{m,R}|)$. For convection dominated, steady state flow it follows from the Bernoulli equation that the variations in the normalized pressure scale in the order of $\mathcal{O}(M^2)$:

$$\delta p^* = \frac{\delta p}{p} = -\frac{\rho u^2}{p} \frac{\delta u}{u} = -\gamma M^2 \delta u^*. \quad (\text{D.10})$$

Assuming the presence of low Mach number flow and that the variations in the normalized velocity differences are in the order of unity, the round-off error associated with the calculation of pressure differences is of the order $\mathcal{O}(\epsilon_m M^{-2})$. With a 4 byte representation (single precision) of floating numbers the machine accuracy on common computers is approximately 10^{-7} . Already at a Mach number of $M = 10^{-3}$ the relative error becomes of the order of $\mathcal{O}(10^{-1})$ for steady state flows, which is clearly unacceptable.

Round-off errors can be avoided if the nearly constant part is subtracted from the pressure and this part is stored separately. Whether the pressure variable itself $p(x_i, t)$ or a perturbed pressure variable $p'(x_i, t)$ defined as

$$p'(x_i, t) = p(x_i, t) - p_0, \quad (\text{D.11})$$

is used, where p_0 represents the pressure on some point of the computational domain, does not matter in the calculation of gradients or differences:

$$\frac{\partial p'}{\partial x} = \frac{\partial p}{\partial x}, \quad \Delta p = \Delta p'. \quad (\text{D.12})$$

When thermodynamical quantities have to be calculated, which depend on the absolute pressure and the absolute temperature level, the perturbed thermodynamic state variables can only be utilized after adding the constant reference quantity to them. When perturbed thermodynamic state variables are used, the density is for ideal gas flows calculated from the following relation

$$\rho = \frac{p' + p_0}{R(T' + T_0)}. \quad (\text{D.13})$$

The relative round-off errors in the computation of the differences $\Delta p'$ of the perturbed pressure variable can be determined as

$$\epsilon_{\text{rnd}} = \left| \frac{\Delta \tilde{p}' - \Delta p}{\Delta p} \right| \leq \frac{|p'_L| + |p'_R|}{|\Delta p|} \epsilon_m. \quad (\text{D.14})$$

If the reference pressure p_0 is chosen as

$$\min(p_L, p_R) \leq p_0 \leq \max(p_L, p_R) \quad (\text{D.15})$$

then the round-off error is bounded by

$$\epsilon_{\text{rnd}} = \left| \frac{\Delta \tilde{p}' - \Delta p}{\Delta p} \right| \leq \epsilon_m. \quad (\text{D.16})$$

The relative error is independent of the Mach number and is bounded by the machine accuracy. The validity of the analysis above is not compromised when the static pressure variable is normalized by the dynamic pressure as developed in Section D.1.

D.3 Use of a perturbed temperature variable in the simulations of low Mach number flow

In the preceding sections it has been shown that it is important to use a pressure that is both perturbed and normalized to ensure that the Navier-Stokes equations for compressible flows coincide with the Navier-Stokes equations for incompressible flows in the limit of a vanishing Mach number. The use of a perturbed pressure has also the advantage that round-off errors can be avoided in numerical simulations.

In this section it will be shown that the temperature needs to be perturbed as well to ensure that the kinetic energy term is of comparable size as the static enthalpy when applying the energy equation.

If the total enthalpy h_0 for a caloric perfect gas is formulated as

$$h_0(T, u) = c_p T + \frac{1}{2} u^2, \quad (\text{D.17})$$

then the contribution of the kinetic energy term may become negligible in comparison to the inner energy. To make this apparent, the flow quantities are normalized with a reference velocity u^\dagger , which yields

$$h_0^*(T, u) = \frac{\gamma R T}{(\gamma - 1) u^{\dagger 2}} + \frac{1}{2} u^{*2} = \frac{1}{(\gamma - 1) \mathbf{M}^2} + \frac{1}{2} u^{*2}. \quad (\text{D.18})$$

Thus, the total enthalpy should be formulated as

$$h_0(T) - h_0(T_0) = c_p(T - T_0) + \frac{1}{2}u^2, \quad (\text{D.19})$$

which in normalized variables yields

$$\Delta h_0^* = c_p^*(T^* - T_0^*) + \frac{1}{2}u^{*2}. \quad (\text{D.20})$$

For adiabatic, inviscid flow, the temperature variations δT are directly related to the velocity variations δu via the relation $c_p \delta T \sim u \delta u$, from which it follows, that if a suitable reference temperature T_0 is chosen, the static enthalpy term will not dominate the kinetic energy term in magnitude. It should furthermore be noted that for adiabatic, inert, low Mach number ideal gas flow, the variation in temperature or in enthalpy can be low. Thus, also for the sake of generally avoiding round-off errors in the calculation of differences and gradients, not only a perturbed pressure variable but also a perturbed temperature or enthalpy variable should be used.

If the flow is non-adiabatic, or if the flow is viscous and the Peclet numbers are less than unity, additional measures must be applied to avoid singularity of the flow equations and round-off errors in the low Mach number limit. These issues will not be addressed here since in the current work only flows with marginal heat losses are considered. The interested reader may refer to the work of Müller [194] for details on how to accommodate for such flow conditions.

Appendix E

Flux limiters to ensure bounded and monotone solutions

For flow simulations it can be of large importance to have a numerical scheme that leads to bounded and monotone solutions. The property of being monotone means that the numerical scheme for the solution of linear transport equations does not increase the total variation of the solution and that the solution scheme does not introduce any new extremes in the state variables [113, 119]. It is important to avoid that the state variables that are naturally bounded (e.g., the density, which has to be positive) take on unphysical values at any stage in the solution process. Overshoots and undershoots in the solution may not only be a nuisance from a physical point of view, but may also trigger instability of the solution scheme.

Gudunov's order barrier theorem [101, 102, 302] states that a linear numerical scheme that leads to monotone solutions in general can at most be first-order accurate. In other words, there are no linear schemes of second or higher order which will be able to prevent the generation of oscillations in the solution in regions of large gradients. Since a first order scheme does not yield a sufficient accuracy for practical computational meshes, non-linear schemes have to be constructed, in order to simultaneously obtain a scheme that is monotone and is essentially of higher order [119]. Such non-linear schemes can be realized by the use of slope or flux limiters, which prevent oscillations by locally reducing the order of the scheme in the vicinity of local extrema in the solution.

E.1 Monotonicity conditions and limiters

To demonstrate the ideas of limiters, potential spatial discretizations of the scalar convection equation

$$\frac{\partial \phi}{\partial t} + c \frac{\partial \phi}{\partial x} = 0 \tag{E.1}$$

for the transport variable ϕ for a positive convection velocity c will be considered in the following. A discretization of this transport equation on a mesh

$\Pi : x = 0, \dots, i \cdot \Delta x, \dots; i \in \mathbb{N}; \Delta x > 0$ leads to the following difference equation

$$\frac{\partial \phi_i}{\partial t} + \frac{c}{\Delta x} (\phi_{i+1/2,L} - \phi_{i-1/2,L}) = 0. \quad (\text{E.2})$$

With the state variable $\phi_{i+1/2}$ at the interface taken as

$$\phi_{i+1/2,L} = \phi_i + \frac{1}{2} \Psi(r_i) (\phi_i - \phi_{i-1}) \quad (\text{E.3})$$

with r_i as the ratio of successive gradients at point i given as $r_i = (\phi_{i+1} - \phi_i) / (\phi_i - \phi_{i-1})$ various schemes can be defined in dependence on how the limiter function Ψ is defined. For $\Psi(r) = r$ a second order central scheme results, whereas $\Psi(r) = 1$ yields a second order upwind scheme [70]. Obviously, choosing $\Psi = 2r$ leads to a first order downwind and setting Ψ to $\Psi = 0$ to a first order upwind scheme.

The reconstruction procedure above applies for positive wave speeds $c > 0$; for negative wave speeds, the state at the interface $i+1/2$ can be reconstructed as

$$\phi_{i+1/2,R} = \phi_{i+1} - \frac{1}{2} \Psi(r'_{i+1}) (\phi_{i+2} - \phi_{i+1}), \quad (\text{E.4})$$

with $r'_{i+1} = (\phi_i - \phi_{i+1}) / (\phi_{i+1} - \phi_{i+2}) = 1/r_{i+1}$. Thus, the interface state $\phi_{i+1/2}$ is for $c < 0$ rather reconstructed from the right from the states in the nodes $i, i+1, i+2$ than from left from the states in the nodes $i-1, i, i+1$. To distinguish whether the states at the interface have been constructed from the left or the right the subscripts 'L' and 'R' are used. For $c < 0$ the convection equation reads as

$$\frac{\partial \phi_i}{\partial t} + \frac{c}{\Delta x} (\phi_{i+1/2,R} - \phi_{i-1/2,R}) = 0, \quad (\text{E.5})$$

which is the same form as the semi-discrete equations (E.2) with the difference that the interface states have been reconstructed from the right rather than from the left.

In order to formulate conditions for the limiter function, the explanations of Hirsch [119] will be followed and the difference equation (E.2) is rewritten in the following form

$$\frac{\partial \phi_i}{\partial t} + \frac{c}{\Delta x} \left[1 + \frac{1}{2} \Psi(r_i) - \frac{1}{2} \frac{\Psi(r_{i-1})}{r_{i-1}} \right] (\phi_i - \phi_{i-1}) = 0, \quad \forall c > 0. \quad (\text{E.6})$$

For negative wave speeds, the corresponding difference equation (E.5) can be rewritten accordingly

$$\frac{\partial \phi_i}{\partial t} + \frac{(-c)}{\Delta x} \left[1 - \frac{1}{2} r_{i+1} \Psi(1/r_{i+1}) + \frac{1}{2} \Psi(1/r_i) \right] (\phi_i - \phi_{i+1}) = 0, \quad \forall c < 0. \quad (\text{E.7})$$

To yield a monotone scheme, the term in the square brackets in both discretizations (E.6) and (E.7) must be positive. The reason for the positivity condition is that if the solution possesses a local maximum at node i ($\phi_i > \phi_{i\pm 1}$), the solution should decrease ($\frac{\partial \phi_i}{\partial t} < 0$), whereas the solution should increase

at node i if it has a local minimum there. The square bracket in Eq. (E.6) is positive when

$$\frac{\Psi(r_{i-1})}{r_{i-1}} - \Psi(r_i) \leq 2 \quad (\text{E.8})$$

and the square in the brackets in Eq. (E.7) is positive when

$$r_{i+1}\Psi(1/r_{i+1}) - \Psi(1/r_i) \leq 2. \quad (\text{E.9})$$

In the following conditions will be derived under which Eq. (E.8) and (E.9) are valid.

The limiter $\Psi(r)$ should preserve the sign of the gradient used for the reconstruction. In addition, it would be natural to reduce the scheme to a first order scheme, when there is an extremum of the solution at point i , i.e., when r_i is negative. Expressed mathematically, this leads to the following conditions on the limiter:

$$\Psi(r) \geq 0, \quad \forall r \geq 0; \quad \Psi(r) = 0, \quad \forall r < 0. \quad (\text{E.10})$$

To derive a further condition on the limiter function $\Psi(r)$, it should be noted that the state $\phi_{i+1/2,L}$ of the left side of the interface at $i + 1/2$ could as well be reconstructed via the following relation

$$\phi_{i+1/2,L} = \phi_i + \frac{1}{2}\Psi(1/r_i)(\phi_{i+1} - \phi_i) = \phi_i + \frac{1}{2}\Psi(1/r_i)r_i(\phi_i - \phi_{i-1}) \quad (\text{E.11})$$

instead of Eq. (E.3). Since the reconstructed states should be independent whether the limiter applies forward or backward ratios of successive slopes, the relation $\Psi(r) = r\Psi(1/r)$ must be fulfilled. With this property and the conditions given in Eq. (E.10), the following sufficient conditions for the fulfillment of Eq. (E.8) and (E.9) can be formulated:

$$\Psi(r) \leq 2 \quad \wedge \quad \Psi(r) \leq 2r. \quad (\text{E.12})$$

Summarizing these last two last conditions and the constraints formulated in Eq. (E.10), the solution of the scalar convection equation will be monotone with the discretization defined by either Eqs. (E.2) and (E.3) or Eqs. (E.4) and (E.5) if the following condition is satisfied:

$$0 \leq \Psi(r) \leq \min(2r, 2). \quad (\text{E.13})$$

In the case of a linear solution on an equidistant mesh the ratio r of successive gradients is unity. In this case, it would be desirable that the limiter function Ψ equal unity, so that the reconstruction given by Eq. (E.3) leads to a scheme of second order accuracy. To make sure that a limiter function $\Psi(r)$ fulfills this property, the following restriction

$$1 \geq \Psi(r) \geq r \quad \vee \quad r \geq \Psi(r) \geq 1 \quad (\text{E.14})$$

may be required from a limiter in addition to the condition given in Eq. (E.13). The last condition also follow from Sweby's suggestion [269] to formulate a limiter that represents a convex combination of the Lax-Wendroff and Beam-Warming scheme to avoid that a limiter be too compressive or be too diffusive. The resulting admissible region of a limiter is referred to in the literature as Sweby's second order TVD region [161, 302].

E.2 Limiter functions

Various limiter functions $\Psi(r)$ can be defined, that with the discretization (E.2), (E.3) leads to a second order TVD scheme. The limiter following the lower bound of Sweby's second order TVD region is the so-called Min-mod limiter

$$\Psi(r) = \max[0, \min(r, 1)]. \quad (\text{E.15})$$

The limiter is formulated in a different form in Eq. (4.17). It takes the minimum of the consecutive slopes for the reconstruction and leads to the most diffusive solutions of the limiter functions which fall in Sweby's second order TVD region. A limiter that is following the upper bound of the second order TVD region is the Superbee limiter of Roe:

$$\Psi(r) = \max[0, \min(2r, 1), \min(r, 2)]. \quad (\text{E.16})$$

For reconstruction, it takes the maximum of two consecutive slopes, as long as their ratio is less than 2. In the other case, it takes the minimum of both slopes. It is the least diffusive and the most compressive limiter that leads to a second order TVD scheme. In Fig. E.1 both the Min-mod and the Superbee limiter functions, as well as other classical limiters are shown. For a detailed discussion of the performance of various limiters the reader may refer to the book of Hirsch [119].

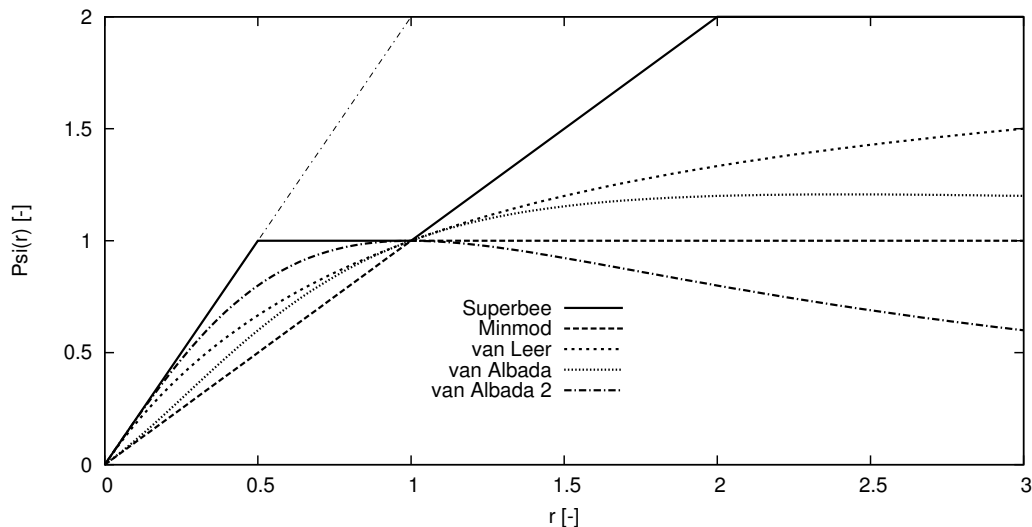


Figure E.1: Various limiter functions plotted in the Sweby-diagram. For $0 \leq \Psi(r) \leq \min(2r, 2)$ a limiter yields a monotone scheme if applied with the reconstruction procedure given in Eq. (E.3). For limiters lying between or on the Min-mod and the Superbee limiters, a second order TVD scheme results.

E.3 Discussion of Jameson's SLIP and USLIP schemes

The SLIP scheme of Jameson [129, 130] can not be analysed with the Sweby-diagram since the respective limiter as defined in Eq. (4.13) used for controlling the reconstruction (4.12) of the left and right states at an interface $i + 1/2$ is not using consecutive slopes. Furthermore, the method of reconstruction used in the SLIP scheme is different from that one described in either of the Eqs. (E.3) and (E.4). However, the conditions given in Eq. (4.16) on the limiter function $L(\phi_1, \phi_2)$ are sufficient to ensure that the resulting diffusive flux formulation in Eq. (4.9), which is based on the reconstruction given in Eq. (4.12), leads to a monotone scheme.

If Jameson's Upstream Symmetric Limited Positive (USLIP) scheme is used as discretization method, which is an upwind-biased form of the SLIP scheme, then the condition given in Eq. (E.13) on a limiter function $\Psi(r)$ can be applied. In the USLIP scheme, the states at an interface $i + 1/2$ are reconstructed as follows

$$\begin{aligned} q_{v,i+1/2,L}^k &= q_{v,i}^k + \frac{1}{2}L(\Delta q_{v,i-1/2}^k, \Delta q_{v,i+1/2}^k), \\ q_{v,i+1/2,R}^k &= q_{v,i+1}^k - \frac{1}{2}L(\Delta q_{v,i+1/2}^k, \Delta q_{v,i+3/2}^k). \end{aligned} \quad (\text{E.17})$$

This is the same reconstruction as the one given in Eqs. (E.3) and (E.4), wherefore the limiter function $L(\phi_1, \phi_2)$ of Jameson given in Eq. (4.13) for the use in the USLIP scheme can be analysed with the Sweby-diagram described above. The limiter function $L(\phi_1, \phi_2)$ of Jameson can be written as $L(\phi_1/\phi_2, 1) \cdot \phi_2 = L(r, 1) \cdot \phi_2 = L(1, r) \cdot \phi_1$. The limiter function $L(\phi_1, \phi_2)$ is constructed in such a manner that it for $\phi_1 \cdot \phi_2 < 0$ returns zero. For positive ratios r of successive gradients and for the parameter e_q set either to $e_q = 1$ or $e_q = 2$, the limiter can be rewritten as

$$\Psi(r)|_{e_q=1} = L(r, 1) = \frac{1}{2}(1+r) - \frac{1}{2}|1-r| \quad \text{and} \quad \Psi(r)|_{e_q=2} = L(r, 1) = \frac{2r}{r+1}, \quad (\text{E.18})$$

respectively. For a parameter e_q set to $e_q = 1$ the Jameson limiter corresponds to the Min-mod limiter, whereas it for $e_q = 2$ corresponds to the van Leer limiter. Thus, for $e_q = 1$ or $e_q = 2$, the limiter of Jameson given in Eq. (4.13) together with the USLIP reconstruction procedure described in Eq. (E.17) leads to a second order TVD scheme.

Appendix F

Roe's Characteristic Upwind Dissipation scheme for preconditioned systems

In this chapter Roe's characteristic upwind dissipation scheme is formulated for preconditioned systems and the necessary absolute Jacobians for the flux difference splitting are defined. Both a conservative and a non-conservative scheme will be formulated and the choice of the solution variable will be discussed. The principles of Roe-averaging will be explained and finally the necessary system-matrices, eigenvectors and resulting artificial dissipation terms are derived.

F.1 Conservative and non-conservative formulation

As a basis for the following analysis, the one-dimensional preconditioned Euler equations

$$\Gamma_v \frac{\partial \hat{\mathbf{Q}}_v}{\partial t} + \frac{\partial \hat{\mathbf{E}}_c}{\partial \xi} = \mathbf{0} \quad (\text{F.1})$$

for the ξ -direction are used. The vectors $\hat{\mathbf{Q}}_v$ and $\hat{\mathbf{E}}_c$ are defined in Eq. (4.27) and denote the vector of primitive viscous variables and the vector of fluxes in the ξ -direction, respectively.

A linearisation around an average state $\bar{\hat{\mathbf{Q}}}_v$ leads to the following equations

$$\frac{\partial \hat{\mathbf{Q}}_v}{\partial t} + \hat{A}_{\Gamma_v, \xi} \Big|_{\bar{\hat{\mathbf{Q}}}_v} \cdot \frac{\partial \hat{\mathbf{Q}}_v}{\partial \xi} = \mathbf{0}, \quad \hat{A}_{\Gamma_v, \xi} = \Gamma_v^{-1} \hat{A}_{\xi, v}, \quad \hat{A}_{\xi, v} = \frac{\partial \hat{\mathbf{E}}_c}{\partial \hat{\mathbf{Q}}_v} \quad (\text{F.2})$$

and a successive multiplication with the left eigenvector matrix $L_{\xi, v}$ of the flux Jacobian $\hat{A}_{\Gamma_v, \xi}$ yields the following system of decoupled equations

$$L_{\xi, v} \frac{\partial \hat{\mathbf{Q}}_v}{\partial t} + \underbrace{L_{\xi, v} \Gamma_v^{-1} \hat{A}_{\xi, v} L_{\xi, v}^{-1}}_{\Lambda_{\xi, v}} L_{\xi, v} \frac{\partial \hat{\mathbf{Q}}_v}{\partial \xi} = \mathbf{0}, \quad (\text{F.3})$$

where $\Lambda_{\xi,v} = L_{\xi,v} \Gamma_v^{-1} \hat{A}_{\xi,v} L_{\xi,v}^{-1} = \text{Diag.} (\lambda'_{1,v}, \dots, \lambda'_{5,v})$ is a diagonal matrix of the eigenvalues of the preconditioned flux Jacobian matrix. Defining the characteristic variable $\hat{\phi}$ as $\hat{\phi} = L_{\xi,v} \hat{\mathbf{Q}}_v$, the last equation can be transformed to the following system

$$\frac{\partial \hat{\phi}}{\partial t} + \Lambda_{\xi,v} \frac{\partial \hat{\phi}}{\partial \xi} = \mathbf{0} \quad (\text{F.4})$$

of decoupled characteristic variables.

Formulated as a semi-discrete first order upwind scheme the last equation yields

$$\frac{\partial \hat{\phi}}{\partial t} + \Lambda_{\xi,v} \frac{\hat{\phi}_{i+1} - \hat{\phi}_{i-1}}{2\Delta\xi} = |\Lambda_{\xi,v}| \frac{\hat{\phi}_{i+1} - 2\hat{\phi}_i + \hat{\phi}_{i-1}}{2\Delta\xi}, \quad (\text{F.5})$$

with the diagonal matrix $|\Lambda_{\xi,v}| = \text{Diag.} (|\lambda'_{\xi,v,1}|, \dots, |\lambda'_{\xi,v,5}|)$ of the absolute eigenvalues.

By multiplying the last equation from the left with the inverse of the matrix of the left eigenvectors, the following system of semi-discrete equations results

$$\frac{\partial \hat{\mathbf{Q}}_{v,i}}{\partial t} + A_{\Gamma_{v,\xi}} \frac{1}{2\Delta\xi} (\hat{\mathbf{Q}}_{v,i+1} - \hat{\mathbf{Q}}_{v,i-1}) = |A_{\Gamma_{v,\xi}}| \frac{1}{2\Delta\xi} (\hat{\mathbf{Q}}_{v,i+1} - 2\hat{\mathbf{Q}}_{v,i} + \hat{\mathbf{Q}}_{v,i-1}) \quad (\text{F.6})$$

with the absolute Jacobian $|A_{\Gamma_{v,\xi}}|$ given by $|A_{\Gamma_{v,\xi}}| = L_{\xi,v}^{-1} |\Lambda_{\xi,v}| L_{\xi,v}$. Treating the central and the dissipation terms nonlinearly yields the following formulation

$$\frac{\partial \hat{\mathbf{Q}}_{v,i}}{\partial t} + \Gamma_{v,i}^{-1} \frac{1}{2\Delta\xi} (\hat{\mathbf{E}}_{c,i+1} - \hat{\mathbf{E}}_{c,i-1}) = \mathbf{D}_{v,nc,i} \quad (\text{F.7})$$

with the dissipation term defined as

$$\mathbf{D}_{v,nc,i} = \frac{1}{2\Delta\xi} \left[(|A_{\Gamma_{v,\xi}}|_{i+1/2}) (\hat{\mathbf{Q}}_{v,i+1} - \hat{\mathbf{Q}}_{v,i}) - (|A_{\Gamma_{v,\xi}}|_{i-1/2}) (\hat{\mathbf{Q}}_{v,i} - \hat{\mathbf{Q}}_{v,i-1}) \right]. \quad (\text{F.8})$$

With the forward and backward difference operators δ^+ and δ^- defined as $\delta^+ \psi_i = \psi_{i+1} - \psi_i$ and $\delta^- \psi_i = \psi_i - \psi_{i-1}$, respectively, the dissipation term can in compact form be expressed as

$$\mathbf{D}_{v,nc,i} = \frac{1}{2\Delta\xi} \delta^- \left(|A_{\Gamma_{v,\xi}}|_{i+1/2} \delta^+ \hat{\mathbf{Q}}_{v,i} \right). \quad (\text{F.9})$$

If this formulation is used, the artificial dissipation terms have to be added to the convective residual vector after the latter has been multiplied with the inverse preconditioning matrix. The use of this formulation would be disadvantageous for flows with shocks since the dissipation terms are written in a non-conservative form [277]. As can be seen from Eq. (F.7), the convective fluxes are multiplied with the inverse of the preconditioning matrix, which is varying from cell to cell, while the dissipation terms are not. To ensure conservativity of the discretization and to achieve a cancellation of the dissipation terms and the centrally discretized convective fluxes to yield full upwinding, the dissipation terms must be formulated as a part of the convective

fluxes. For the sake of achieving a discretization that is accurate when the flow variables are subject to strong variations, the formulation of the dissipation scheme should be such that when preconditioning is shut off (at supersonic conditions), the dissipation terms are effectively constructed from differences of the conservative variables. The choice of the variables used for the construction of the artificial dissipation terms will be discussed in the next section.

To attain a conservative formulation, Eq. (F.6) is multiplied by the preconditioning matrix Γ_v ; afterwards both the central and the dissipation terms are written in a non-linear representation to yield the following system

$$\Gamma_{v,i} \frac{\partial \hat{\mathbf{Q}}_{v,i}}{\partial t} + \frac{1}{2\Delta\xi} (\hat{\mathbf{E}}_{v,i+1} - \hat{\mathbf{E}}_{v,i-1}) = \frac{1}{2\Delta\xi} \delta^- \left(\Gamma_{v,i+1/2} |A_{\Gamma,\xi}|_{i+1/2} \delta^+ \hat{\mathbf{Q}}_{v,i} \right). \quad (\text{F.10})$$

Summing up the contributions of the convective fluxes and the artificial dissipation yields

$$\Gamma_{v,i} \frac{\partial \hat{\mathbf{Q}}_{v,i}}{\partial t} + \frac{1}{2\Delta\xi} \left[(\hat{\mathbf{E}}_{v,i+1} - \hat{\mathbf{E}}_{v,i-1}) - \delta^- \left(\Gamma_{v,i+1/2} |A_{\Gamma,\xi}|_{i+1/2} \delta^+ \hat{\mathbf{Q}}_{v,i} \right) \right] = \mathbf{0}. \quad (\text{F.11})$$

Introducing the flux vector at the interface $i + 1/2$ of the dual mesh as the contribution of both the convective and the dissipative fluxes as

$$\hat{\mathbf{F}}_{v,i+1/2} = \hat{\mathbf{E}}_{v,i+1/2} - \frac{1}{2} \Gamma_{v,i+1/2} |A_{\Gamma,\xi}|_{i+1/2} \delta^+ \hat{\mathbf{Q}}_{v,i} \quad (\text{F.12})$$

with $\hat{\mathbf{E}}_{v,i+1/2} = \frac{1}{2} (\hat{\mathbf{E}}_{v,i+1} + \hat{\mathbf{E}}_{v,i})$, Eq. (F.11) can also be written as

$$\Gamma_{v,i} \frac{\partial \hat{\mathbf{Q}}_{v,i}}{\partial t} + \frac{1}{\Delta\xi} \left(\hat{\mathbf{F}}_{v,i+1/2} - \hat{\mathbf{F}}_{v,i-1/2} \right) = \mathbf{0}. \quad (\text{F.13})$$

The fact that the dissipation term can be written as a part of the convective fluxes, shows the conservativity of the formulation of the dissipative fluxes in Eq. (F.10).

F.2 The use of conservative versus non-conservative solution variables

In order to obtain a formulation, for which effectively flux differences of conserved quantities are taken (when preconditioning is shut off), the Euler equations without preconditioning

$$\frac{\partial \hat{\mathbf{Q}}}{\partial t} + \frac{\partial \hat{\mathbf{E}}_c}{\partial \xi} = 0 \quad (\text{F.14})$$

are used as a starting point for the following analysis. Preconditioning is introduced by multiplying the temporal term with the preconditioning matrix Γ_k , which is defined as

$$\Gamma_k = \Gamma_v \Gamma_e^{-1}, \quad \Gamma_e = \frac{\partial \hat{\mathbf{Q}}}{\partial \hat{\mathbf{Q}}_v}. \quad (\text{F.15})$$

When preconditioning is shut off, $\Gamma_v = \Gamma_e$, and the matrix Γ_k equals the identity matrix. A linearization of these equations around an averaged state $\hat{\mathbf{Q}}$ yields the following equations

$$\frac{\partial \hat{\mathbf{Q}}}{\partial t} + \hat{A}_{\Gamma_k, \xi} \Big|_{\hat{\mathbf{Q}}} \cdot \frac{\partial \hat{\mathbf{Q}}}{\partial \xi} = \mathbf{0}, \quad \hat{A}_{\Gamma_k, \xi} = \Gamma_k^{-1} \hat{A}_{\xi, c}, \quad \hat{A}_{\xi, c} = \frac{\partial \hat{\mathbf{E}}_c}{\partial \hat{\mathbf{Q}}} \quad (\text{F.16})$$

and a successive multiplication with the left eigenvector matrix $L_{\xi, k}$ of the flux Jacobian $\hat{A}_{\Gamma_k, \xi}$ yields the following system of decoupled equations

$$L_{\xi, k} \frac{\partial \hat{\mathbf{Q}}}{\partial t} + \underbrace{L_{\xi, k} \hat{A}_{\Gamma_k, \xi} L_{\xi, k}^{-1}}_{\Lambda_{\xi, k}} L_{\xi, k} \frac{\partial \hat{\mathbf{Q}}}{\partial \xi} = \mathbf{0}, \quad (\text{F.17})$$

where $\Lambda_{\xi, k} = L_{\xi, k} \hat{A}_{\Gamma_k, \xi} L_{\xi, k}^{-1} = \text{Diag.} (\lambda'_{1, k}, \dots, \lambda'_{5, k})$ represents a diagonal matrix of the eigenvalues of the preconditioned, conservative flux Jacobian matrix. With the characteristic variable $\hat{\phi}_k$ now defined as $\hat{\phi} = L_{\xi, k} \hat{\mathbf{Q}}$, the last system of equations can be written as

$$\frac{\partial \hat{\phi}}{\partial t} + \Lambda_{\xi, k} \frac{\partial \hat{\phi}}{\partial \xi} = \mathbf{0}, \quad (\text{F.18})$$

which in a semi-discrete upwind formulation yields

$$\frac{\partial \hat{\phi}_i}{\partial t} + \Lambda_{\xi, k} \frac{\hat{\phi}_{i+1} - \hat{\phi}_{i-1}}{2\Delta\xi} = |\Lambda_{\xi, k}| \frac{\hat{\phi}_{i+1} - 2\hat{\phi}_i + \hat{\phi}_{i-1}}{2\Delta\xi}. \quad (\text{F.19})$$

Transformation back by multiplying with the inverse of the left eigenvector matrix yields

$$\frac{\partial \hat{\mathbf{Q}}_i}{\partial t} + \hat{A}_{\Gamma_k, \xi} \cdot \frac{\hat{\mathbf{Q}}_{i+1} - \hat{\mathbf{Q}}_{i-1}}{2\Delta\xi} = |\hat{A}_{\Gamma_k, \xi}| \frac{\hat{\mathbf{Q}}_{i+1} - 2\hat{\mathbf{Q}}_i + \hat{\mathbf{Q}}_{i-1}}{2\Delta\xi}, \quad (\text{F.20})$$

where the absolute Jacobian $|\hat{A}_{\Gamma_k, \xi}|$ is given by

$$|\hat{A}_{\Gamma_k, \xi}| = L_{\xi, k}^{-1} |\Lambda_{\xi, k}| L_{\xi, k}. \quad (\text{F.21})$$

Multiplying from the left with the preconditioning matrix Γ_k and treating the central term non-linearly yields

$$\Gamma_k \frac{\partial \hat{\mathbf{Q}}_i}{\partial t} + \frac{\hat{\mathbf{E}}_{i+1} - \hat{\mathbf{E}}_{i-1}}{2\Delta\xi} = \Gamma_k |\hat{A}_{\Gamma_k, \xi}| \frac{\hat{\mathbf{Q}}_{i+1} - 2\hat{\mathbf{Q}}_i + \hat{\mathbf{Q}}_{i-1}}{2\Delta\xi}. \quad (\text{F.22})$$

This formulation of the dissipation term is conservative but it has the disadvantage that it can not be used for the simulation of incompressible flows, as in this case the density variations vanish identically and consequently no dissipation would be added to the continuity equation. To be able to simulate both compressible and incompressible flow it would be preferable to use the

vector $\hat{\mathbf{Q}}_v$ of primitive viscous variables to construct the artificial dissipation. With $\delta\mathbf{Q} = \Gamma_e \delta\mathbf{Q}_v$ the last equation is transformed to

$$\Gamma_k \Gamma_e \frac{\partial \hat{\mathbf{Q}}_{v,i}}{\partial t} + \frac{\hat{\mathbf{E}}_{i+1} - \hat{\mathbf{E}}_{i-1}}{2\Delta\xi} = \Gamma_k |\hat{A}_{\Gamma_k, \xi}| \Gamma_e \frac{\hat{\mathbf{Q}}_{v,i+1} - 2\hat{\mathbf{Q}}_{v,i} + \hat{\mathbf{Q}}_{v,i-1}}{2\Delta\xi}. \quad (\text{F.23})$$

This formulation is still conservative and has the advantage that the artificial dissipation is constructed using differences of the primitive, viscous state variables. Thus, this formulation should be suited for the simulation of incompressible or compressible, low Mach number flows as well as flows containing shocks provided that the matrix $\Gamma_k |\hat{A}_{\Gamma_k, \xi}| \Gamma_e$ scales correctly.

To show that the formulation of the artificial dissipation in either Eq. (F.22) or (F.23) on the linear level is equivalent to the conservative formulation (F.10) used in the previous section, the absolute Jacobian $|\hat{A}_{\Gamma_k, \xi}|$ in the last equation has to be related to the absolute Jacobian $|\hat{A}_{\Gamma_v, \xi}|$. In Hirsch [118] the validity of $L_{\xi, k} \Gamma_e = L_{\xi, v}$ is shown. If it is also exploited, that the eigenvalues of the preconditioned flow equations do not change with a transformation of the independent variables, i.e., $\Lambda_{\xi, v} = \Lambda_{\xi, k}$, then the following relation follows

$$\Gamma_e^{-1} |\hat{A}_{\Gamma_k, \xi}| \Gamma_e = \Gamma_e^{-1} L_{\xi, k}^{-1} |\Lambda_{\xi, k}| L_{\xi, k} \Gamma_e = L_{\xi, v}^{-1} |\Lambda_{\xi, k}| L_{\xi, v} = L_{\xi, v}^{-1} |\Lambda_{\xi, v}| L_{\xi, v} = |\hat{A}_{\Gamma_v, \xi}|. \quad (\text{F.24})$$

Using this relation to substitute the conservative absolute Jacobian $|\hat{A}_{\Gamma_k, \xi}|$ in Eq. (F.23) with the absolute Jacobian $|\hat{A}_{\Gamma_v, \xi}|$ together with the equality $\Gamma_v = \Gamma_k \Gamma_e$ yields

$$\Gamma_v \frac{\partial \hat{\mathbf{Q}}_{v,i}}{\partial t} + \frac{\hat{\mathbf{E}}_{i+1} - \hat{\mathbf{E}}_{i-1}}{2\Delta\xi} = \Gamma_v |\hat{A}_{\Gamma_v, \xi}| \frac{\hat{\mathbf{Q}}_{v,i+1} - 2\hat{\mathbf{Q}}_{v,i} + \hat{\mathbf{Q}}_{v,i-1}}{2\Delta\xi}. \quad (\text{F.25})$$

This equation corresponds on the linear level to Eq. (F.10), which was to be demonstrated.

F.3 The principle of Roe-averaging

The absolute Jacobians, which are needed in the calculation of the dissipative terms in the Roe scheme, may be based on the arithmetic average of the left and right states of the interface for which the Jacobian is to be determined. However, this procedure will not lead to a full upwinding. In this section it will be briefly explained, which properties the averages must have in order to obtain a scheme that leads to full upwinding.

The starting point of the analysis is the following system of transport equations

$$\frac{\partial \mathbf{U}}{\partial t} + \frac{\partial \mathbf{F}(\mathbf{U})}{\partial x} = \mathbf{0}, \quad (\text{F.26})$$

where \mathbf{U} represent an arbitrary state vector and \mathbf{F} represents a convective flux vector.

On a one-dimensional, equidistant grid $\Pi : x_1, \dots, x_i, \dots, x_N$ with $x_i = i \cdot \Delta x$; $i \in \mathbb{N}$, $\Delta x > 0$ the semi-discrete form of these equations can be written as

$$\frac{\partial \mathbf{U}_i}{\partial t} V_i + \mathbf{H}_{i+1/2} - \mathbf{H}_{i-1/2} = \mathbf{0} \quad (\text{F.27})$$

where $\mathbf{H}_{i+1/2}$ and $\mathbf{H}_{i-1/2}$ represents the numerical flux terms at the interfaces $n_{i+1/2}$ and $n_{i-1/2}$ of the volume V_i enclosing node i . The numerical flux can be determined as the sum of a central and a dissipative part:

$$\mathbf{H}_{i+1/2} = \frac{1}{2} (\mathbf{F}_i + \mathbf{F}_{i+1}) n_{i+1/2} - \frac{1}{2} B (\mathbf{U}_{i+1} - \mathbf{U}_i) n_{i+1/2}. \quad (\text{F.28})$$

By introducing the interface flux Jacobian $A_{i+1/2}$ as

$$A_{i+1/2} = \begin{cases} \frac{\mathbf{F}_{i+1} - \mathbf{F}_i}{\mathbf{U}_{i+1} - \mathbf{U}_i}, & \mathbf{U}_{i+1} \neq \mathbf{U}_i \\ \frac{\partial \mathbf{F}}{\partial \mathbf{U}}, & \mathbf{U}_{i+1} = \mathbf{U}_i \end{cases} \quad (\text{F.29})$$

and setting the coefficient matrix B for the dissipative terms to the absolute Jacobian $B := |A|$, the following equation is obtained

$$\begin{aligned} \mathbf{H}_{i+1/2} &= \mathbf{F}_i n_{i+1/2} + \frac{1}{2} (\mathbf{F}_{i+1} - \mathbf{F}_i) n_{i+1/2} - \frac{1}{2} B (\mathbf{U}_{i+1} - \mathbf{U}_i) n_{i+1/2} \\ &= \mathbf{F}_i n_{i+1/2} + \frac{1}{2} (A - |A|)_{i+1/2} (\mathbf{U}_{i+1} - \mathbf{U}_i) n_{i+1/2}. \end{aligned} \quad (\text{F.30})$$

Using the definition of the absolute Jacobian $|A| = L^{-1} |\Lambda| L$, where L represents the matrix of left eigenvectors of the Jacobian A , the last relation can be expressed as

$$\mathbf{H}_{i+1/2} = \mathbf{F}_i n_{i+1/2} + \frac{1}{2} [L^{-1} (\Lambda - |\Lambda|)]_{i+1/2} (\phi_{i+1} - \phi_i) n_{i+1/2}. \quad (\text{F.31})$$

For positive values of the eigenvalues $\lambda_j, j = 1, \dots, 5$ the last relation reduces to $\mathbf{H}_{i+1/2} = \mathbf{F}_i n_{i+1/2}$. In the opposite case that all eigenvalues are negative, the last term on the right hand side in Eq. (F.31) equals $(\mathbf{F}_{i+1} - \mathbf{F}_i) n_{i+1/2}$ and the flux vector $\mathbf{H}_{i+1/2}$ becomes $\mathbf{H}_{i+1/2} = \mathbf{F}_{i+1} n_{i+1/2}$. In both of these cases the flux vector $\mathbf{H}_{i+1/2}$ is solely determined from the states lying upwind of the interface. In the case that the eigenvalues have a mixed set of signs, full upwinding is ensured for each of the individual characteristic variables $\phi_j, j = 1, \dots, 5$.

From this analysis it follows, that to ensure a full upwinding for the characteristic upwind scheme, the flux Jacobian $A(\mathbf{U}_i, \mathbf{U}_{i+1})$ should possess the following properties:

1. $A_{i+1/2}(\mathbf{U}_{i+1} - \mathbf{U}_i) = \mathbf{F}_{i+1} - \mathbf{F}_i; \quad \forall \mathbf{U}_i, \mathbf{U}_{i+1}$.
2. For $\mathbf{U}_i = \mathbf{U}_{i+1}$ the flux Jacobian should correspond to the analytical value: $A_{i+1/2}(\mathbf{U}, \mathbf{U}) = \frac{\partial \mathbf{F}(\mathbf{U})}{\partial \mathbf{U}} \Big|_{\mathbf{U}}$.
3. The Jacobian A should only possess real eigenvalues and should have linearly independent eigenvectors.

If an averaging technique due to Roe is used, the aforementioned properties can be fulfilled for the unscaled Euler equations. If the Jacobian matrix A is based on the Roe-averaged quantities

$$\begin{aligned}
 \tilde{\varrho}_{i+1/2} &= \sqrt{\varrho_i \varrho_{i+1}}, \\
 \tilde{\mathbf{v}}_{i+1/2} &= \frac{\sqrt{\varrho_i} \mathbf{v}_i + \sqrt{\varrho_{i+1}} \mathbf{v}_{i+1}}{\sqrt{\varrho_i} + \sqrt{\varrho_{i+1}}}, \\
 \tilde{h}_{0,i+1/2} &= \frac{\sqrt{\varrho_i} h_{0,i} + \sqrt{\varrho_{i+1}} h_{0,i+1}}{\sqrt{\varrho_i} + \sqrt{\varrho_{i+1}}}, \\
 \tilde{a}_{i+1/2} &= (\gamma - 1) \left(\tilde{h}_{0,i+1/2} - \frac{1}{2} \tilde{\mathbf{v}}_{i+1/2}^2 \right)
 \end{aligned} \tag{F.32}$$

then condition (1) above is fulfilled [274] for ideal gas flow. Condition (2) is fulfilled with a consistent derivation of the flux Jacobian, and condition (3) is given by the Euler equations for ideal gas flow [118].

In the current work the Roe-averaging procedure given in Eq. (F.32) was applied in conjunction with preconditioning for the determination of the interface states $\mathbf{Q}_{v,i+1/2}$ in the simulation of ideal gas flow. For the simulation of incompressible fluids flow the interface states were determined by simple arithmetic averaging of the left and right states of each cell interface.

F.4 Eigenvector and absolute Jacobian matrices

The system matrix $\hat{A}_{\Gamma_v, \xi} = \Gamma_v^{-1} \hat{A}_\xi = \Gamma_v^{-1} \frac{\partial \hat{\mathbf{E}}}{\partial \hat{\mathbf{Q}}_v}$ can be determined as [6]:

$$\hat{A}_{\Gamma_v, \xi} = \begin{bmatrix} [\varrho'_T(1 - \varrho h_p) + \varrho \varrho_p h'_T] \frac{\hat{w}_\xi}{d'} & \frac{\varrho^2 h'_T \xi_x}{d'} & \frac{\varrho^2 h'_T \xi_\phi}{d'} & \frac{\varrho^2 h'_T \xi_r}{d'} & \frac{\varrho \hat{w}_\xi}{d'} (\varrho_T h'_T) \\ \frac{\xi_x}{\varrho} & \hat{w} & 0 & 0 & -h_T \varrho'_T \\ \frac{\xi_\phi}{\varrho} & 0 & \hat{w} & 0 & 0 \\ \frac{\xi_r}{\varrho} & 0 & 0 & \hat{w} & 0 \\ \frac{\hat{w}_\xi}{d'} [\varrho_p h'_p - \varrho'_p(1 - \varrho h_p)] & \frac{\varrho h'_p \xi_x}{d'} & \frac{\varrho h'_p \xi_\phi}{d'} & \frac{\varrho h'_p \xi_z}{d'} & \frac{\hat{w}_\xi}{d'} (\varrho \varrho'_p h_T + \varrho_T h'_p) \end{bmatrix}, \tag{F.33}$$

where the contravariant velocity \hat{w}_ξ is given by Eq. (3.8). With the assumption that preconditioning variables ϱ'_T , h'_p and h'_T are set to their physical values, (i. e., only ϱ'_p is used as an active preconditioning parameter), the matrix $L_\xi = [\mathbf{l}_1(\lambda_{\xi,1}), \dots, \mathbf{l}_5(\lambda_{\xi,5})]$ of left eigenvectors becomes

$$L_\xi = \begin{bmatrix} -\frac{1 - \varrho h_p}{\varrho h_T} & 0 & 0 & 0 & 1 \\ 0 & \tilde{l}_x & \tilde{l}_\phi & \tilde{l}_r & 0 \\ 0 & \tilde{m}_x & \tilde{m}_\phi & \tilde{m}_r & 0 \\ 1 & \varrho \tilde{\lambda}_{\xi,4}^w \tilde{\xi}_x & \varrho \tilde{\lambda}_{\xi,4}^w \tilde{\xi}_\phi & \varrho \tilde{\lambda}_{\xi,4}^w \tilde{\xi}_r & 0 \\ 1 & \varrho \tilde{\lambda}_{\xi,5}^w \tilde{\xi}_x & \varrho \tilde{\lambda}_{\xi,5}^w \tilde{\xi}_\phi & \varrho \tilde{\lambda}_{\xi,5}^w \tilde{\xi}_r & 0 \end{bmatrix} \tag{F.34}$$

with $\tilde{\lambda}_{\xi,4}^w = (\tilde{\lambda}_{\xi,4} - \tilde{w} \frac{d}{dt})$ and $\tilde{\lambda}_{\xi,5}^w = (\tilde{\lambda}_{\xi,5} - \tilde{w} \frac{d}{dt})$. The left eigenvectors $\mathbf{l}_i, i = 1, \dots, 5$ are defined as the vectors fulfilling $(\mathbf{l}_i)^T (\hat{A}_\Gamma - \lambda_{\xi,i} I) = \mathbf{0}$ with the eigenvalues $\lambda_{\xi,i}$ defined according to Eq. (3.6). The quantities denoted by a "~" are normalized with $\|\nabla\xi\|$, for instance the normalized contravariant velocity \tilde{w}_ξ is defined as

$$\tilde{w}_\xi = \frac{\hat{w}}{\sqrt{\xi_x^2 + \xi_\phi^2 + \xi_r^2}} = \frac{\mathbf{w} \cdot \mathbf{S}_\xi}{\|\mathbf{S}_\xi\|}. \quad (\text{F.35})$$

The vectors $[\tilde{l}_x, \tilde{l}_\phi, \tilde{l}_r]$ and $[\tilde{m}_x, \tilde{m}_\phi, \tilde{m}_r]$ represent two mutually orthogonal unit vectors which both are orthogonal to the normalized grid projection vector $[\tilde{\xi}_x, \tilde{\xi}_\phi, \tilde{\xi}_r]$. Due to the orthogonality of the left \mathbf{l}_i and right eigenvectors \mathbf{r}_i , the matrix of right eigenvectors $R_\xi = [\mathbf{r}^R(\lambda_{\xi,1}), \dots, \mathbf{r}^R(\lambda_{\xi,5})]$ equals the inverse of the Matrix L_ξ , i. e., $R_\xi = L_\xi^{-1}$. Thus, this matrix reads as

$$R_\xi = \begin{bmatrix} 0 & 0 & 0 & \frac{\tilde{\lambda}_{\xi,5} - \tilde{w} \frac{d}{dt}}{\tilde{\lambda}_{\xi,5} - \tilde{\lambda}_{\xi,4}} & \frac{\tilde{\lambda}_{\xi,4} - \tilde{w} \frac{d}{dt}}{\tilde{\lambda}_{\xi,4} - \tilde{\lambda}_{\xi,5}} \\ 0 & \tilde{l}_x & \tilde{m}_x & \frac{\tilde{\xi}_x}{\varrho(\tilde{\lambda}_{\xi,4} - \tilde{\lambda}_{\xi,5})} & \frac{\tilde{\xi}_x}{\varrho(\tilde{\lambda}_{\xi,5} - \tilde{\lambda}_{\xi,4})} \\ 0 & \tilde{l}_\phi & \tilde{m}_\phi & \frac{\tilde{\xi}_\phi}{\varrho(\tilde{\lambda}_{\xi,4} - \tilde{\lambda}_{\xi,5})} & \frac{\tilde{\xi}_\phi}{\varrho(\tilde{\lambda}_{\xi,5} - \tilde{\lambda}_{\xi,4})} \\ 0 & \tilde{l}_r & \tilde{m}_r & \frac{\tilde{\xi}_r}{\varrho(\tilde{\lambda}_{\xi,4} - \tilde{\lambda}_{\xi,5})} & \frac{\tilde{\xi}_r}{\varrho(\tilde{\lambda}_{\xi,5} - \tilde{\lambda}_{\xi,4})} \\ 1 & 0 & 0 & \frac{1 - \varrho h_p}{\varrho h_T} \frac{\tilde{\lambda}_{\xi,5} - \tilde{w} \frac{d}{dt}}{\tilde{\lambda}_{\xi,5} - \tilde{\lambda}_{\xi,4}} & \frac{1 - \varrho h_p}{\varrho h_T} \frac{\tilde{\lambda}_{\xi,4} - \tilde{w} \frac{d}{dt}}{\tilde{\lambda}_{\xi,4} - \tilde{\lambda}_{\xi,5}} \end{bmatrix}. \quad (\text{F.36})$$

By defining the volume weighted diagonal matrix to

$$|\Lambda_\xi^V| = \text{Diag}(|\lambda_{\xi,1}^V|, |\lambda_{\xi,2}^V|, |\lambda_{\xi,3}^V|, |\lambda_{\xi,4}^V|, |\lambda_{\xi,5}^V|) \quad (\text{F.37})$$

with the volume weighted eigenvalues given by

$$\begin{aligned} \lambda_{\xi,1,2,3}^V &= \mathbf{w} \cdot \mathbf{S}_\xi = w_x S_{\xi,x} + w_\phi S_{\xi,\phi} + w_r S_{\xi,r}, \\ \lambda_{\xi,4,5}^V &= \frac{1}{2} \mathbf{w} \cdot \mathbf{S}_\xi \left(1 + \frac{d}{dt}\right) \pm \frac{1}{2} \sqrt{(\mathbf{w} \cdot \mathbf{S}_\xi)^2 \left(1 - \frac{d}{dt}\right)^2 + 4 \frac{\varrho h_T}{dt}} \end{aligned} \quad (\text{F.38})$$

the product $|A_{\Gamma,\xi}| \cdot \delta \mathbf{Q}_v = L_\xi \cdot |\Lambda_\xi| \cdot L_\xi^{-1} \cdot \delta \mathbf{Q}_v = \delta \pi$ after some algebra reduces to

$$\begin{aligned} \delta \pi_1 &= c_{11} \cdot \delta p + \varrho c_{12} \cdot (\delta \Upsilon)_\xi, \\ \delta \pi_2 &= |\lambda_1^V| \cdot \delta u + S_{\xi,x} \left[c_{21} \cdot \delta p - \frac{|\lambda_1^V| + |\lambda_{45}^V|}{\|\mathbf{S}_\xi\|^2} \cdot (\delta \Upsilon)_\xi \right], \\ \delta \pi_3 &= |\lambda_1^V| \cdot \delta v + S_{\xi,y} \left[c_{21} \cdot \delta p - \frac{|\lambda_1^V| + |\lambda_{45}^V|}{\|\mathbf{S}_\xi\|^2} \cdot (\delta \Upsilon)_\xi \right], \\ \delta \pi_4 &= |\lambda_1^V| \cdot \delta w + S_{\xi,z} \left[c_{21} \cdot \delta p - \frac{|\lambda_1^V| + |\lambda_{45}^V|}{\|\mathbf{S}_\xi\|^2} \cdot (\delta \Upsilon)_\xi \right], \\ \delta \pi_5 &= b_p \cdot \delta \pi_1 + |\lambda_1^V| (\delta T - b_p \cdot \delta p) \end{aligned} \quad (\text{F.39})$$

with $\delta\mathbf{Q}_v = [\delta p, \delta u, \delta v, \delta w, \delta T]^T$ and the terms $(\delta\Upsilon)_\xi$, b_p , c_{11} , c_{12} , c_{21} , λ_{45}^V given by

$$\begin{aligned}
 (\delta\Upsilon)_\xi &= S_{\xi,x}\delta u + S_{\xi,y}\delta v + S_{\xi,z}\delta w, & b_p &= \frac{(1 - \varrho h_p)}{\varrho h_T}, \\
 c_{11} &= \frac{|\lambda_5^V|(\lambda_4^V - U^V \frac{d}{d'}) - |\lambda_4^V|(\lambda_5^V - U^V \frac{d}{d'})}{\lambda_4^V - \lambda_5^V}, & c_{21} &= \frac{|\lambda_4^V| - |\lambda_5^V|}{\varrho(\lambda_4^V - \lambda_5^V)}, \\
 c_{12} &= \frac{(|\lambda_5^V| - |\lambda_4^V|)(\lambda_5^V - U^V \frac{d}{d'})(\lambda_4^V - U^V \frac{d}{d'})}{(\lambda_4^V - \lambda_5^V) \cdot \|\mathbf{S}_\xi\|^2}, \\
 \lambda_{45}^V &= \frac{|\lambda_5^V|(\lambda_5^V - U^V \frac{d}{d'}) - |\lambda_4^V|(\lambda_4^V - U^V \frac{d}{d'})}{(\lambda_4^V - \lambda_5^V)}.
 \end{aligned} \tag{F.40}$$

Appendix G

The influence of the geometrical parameters of the labyrinth seal

In the work of Anker et al. [14], steady-state simulations were carried out using the preconditioned solution scheme to study the influence of the geometrical parameters of the labyrinth seal on the leakage flow in the Bochum turbine. In that study, using the same geometry and the same operating point as described above (Ch. 6.1) as a basis ($s_{cl}, s_w = 3$ mm, $s_a, s_e = 6$ mm), the clearance height ($s_{cl}/\text{mm} = 1, 2, 3, 5$), the width of the fins of the labyrinth seals ($s_w/\text{mm} = 3, 6, 9$), the width of the inlet gap of the labyrinth seal ($s_e/\text{mm} = 3, 6, 12$) and the width of the labyrinth outlet gap ($s_a/\text{mm} = 3, 6, 12$) were changed independently of each other. Figure G.1 illustrates the geometrical variations that were subject to investigation. The purpose of the study was to calibrate a numerical model of the labyrinth seal which replaces a discretization of the details of the sealing arrangements.

The study showed that the clearance height is the most influential parameter of those investigated. For the geometrical configurations examined, the simulations predicted a nearly linear increase in the leakage mass flow rate with an increase in the seal leakage height (Fig. G.2a). The effect of varying this parameter from $s_{cl} = 0$ mm to $s_{cl} = 3$ mm has been described in previous chapters and shall not be repeated here. In the aforementioned study [14] it

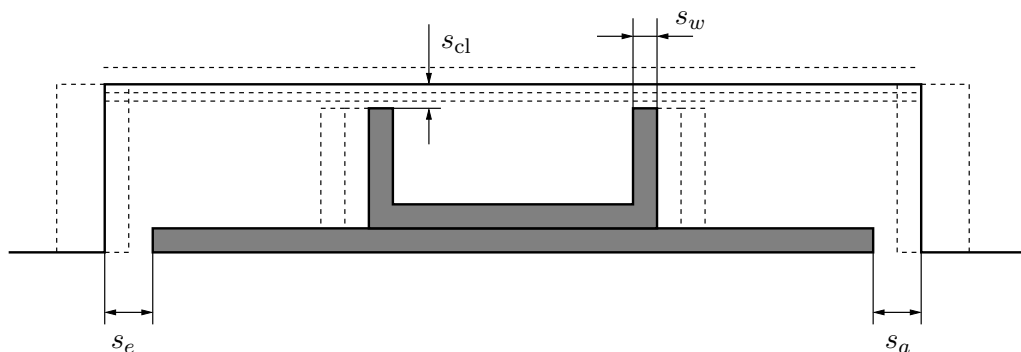


Figure G.1: Variations in the geometry of the labyrinth seal in the work of Anker et al. [14]

was however discovered that the difference Δv_ϕ in the circumferential velocity v_ϕ of the leakage flow between its entry in the first cavity of the labyrinth seal rotor to its re-injection in the main flow after the rotor is strongly dependent on the clearance height of the seal. In Fig. G.2b the change in the circumferential velocity Δv_ϕ is displayed in dependence of the clearance height. The swirl of the leakage flow increases from the entry in the seal to its re-injection in the main flow for low values of the clearance height s_{cl} , for which the mass flow rates are small. For low clearance heights more near-wall flow with a low circumferential velocity enters the labyrinth seal. For large clearance heights more fluid of the main flow, which has the circumferential velocity of the rotor, enters the labyrinth seal. While the leakage flow for large clearance heights passes through the labyrinth seal with a high swirl and without much deflection, for low clearance heights it enters the labyrinth seal with a low circumferential velocity and is accelerated to the half of the circumferential speed of the rotor through friction. This result is of importance since it implies that as long as the leakage flow rate is low, it is principally possible to extract fluid of the boundary layer with a low exergy and thus to avoid that fluid with high values of the kinetic energy is flowing through the labyrinth seal without doing work on the rotor blade.

The dependence of the leakage mass flow rate on the width of the inlet (s_e) or the outlet (s_a) gap of the labyrinth seal is much smaller than that of the clearance height (s_{cl}). The leakage mass flow rate \dot{m}_{cl} and the difference in the swirl of the leakage flow Δv_ϕ change only marginally with a variation in the width of the inlet or the outlet gap of the labyrinth seal. A variation in the size of the inlet gap does not qualitatively change the flow field in the inlet plane of the labyrinth seal, whereas a variation in the size of the outlet gap significantly changes the structure of the flow field at the outlet plane of the labyrinth seal (cf. Fig. G.3). With a larger width of the outlet gap, the relative area in which fluid enters the labyrinth seal increases significantly. However this does not lead to a noticeable impact on the main or the secondary flow in the measurement plane M2.

A change in the width of the labyrinth fins does not change the leakage flow rate, but leads to a slight increase in the swirl of the reentering leakage flow [14]. As with a change in the width of the inlet and the outlet gap, a variation of this parameter does not lead to a noticeable impact on the downstream flow field.

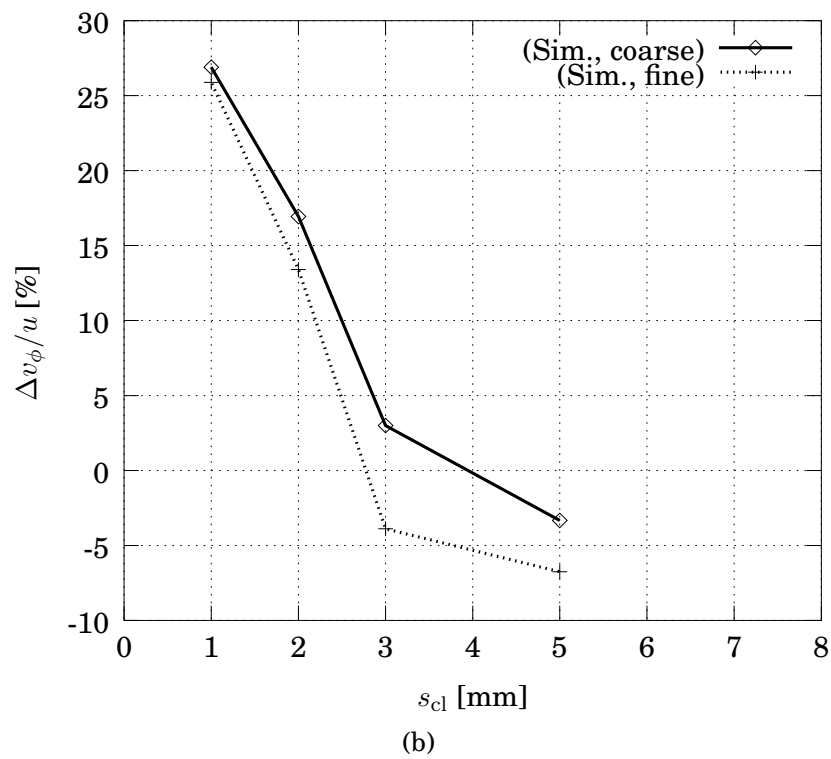
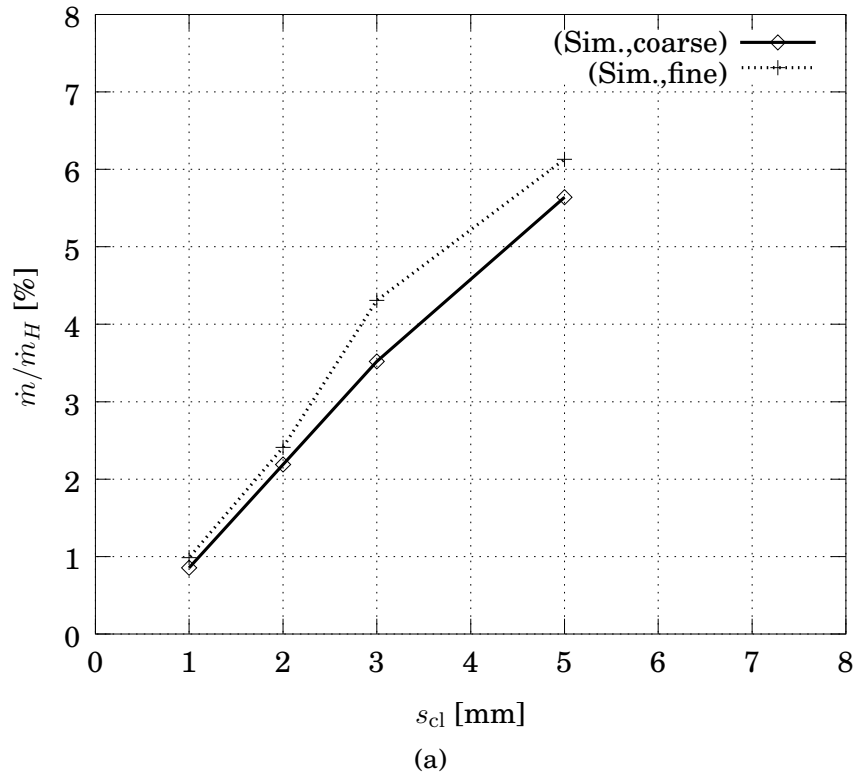
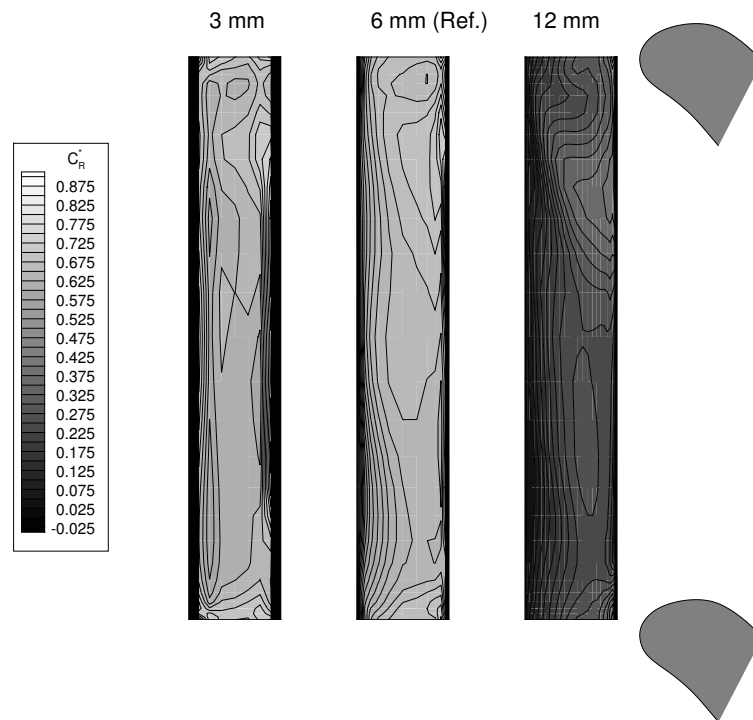
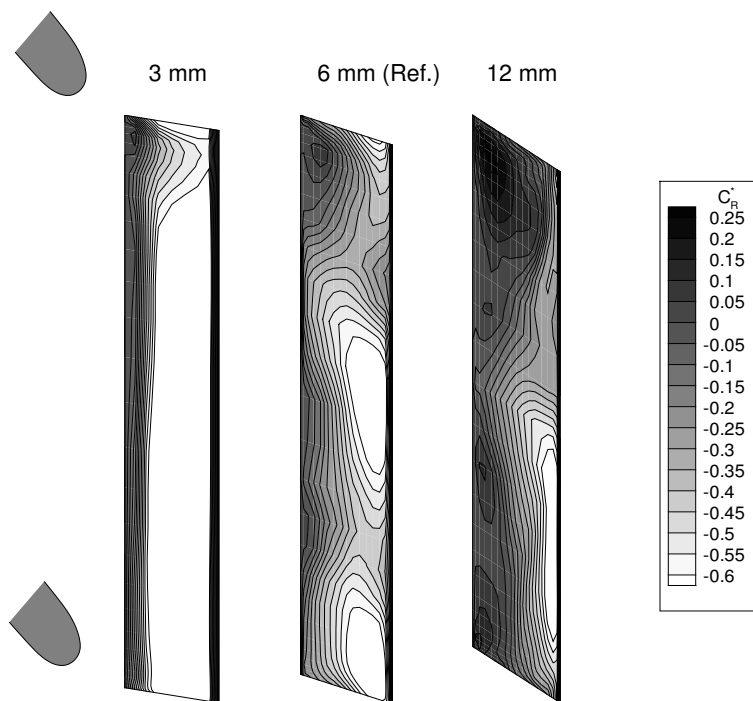


Figure G.2: (a) Percentage of the flow passing through the labyrinth seal, (b) change in the circumferential velocity of the leakage flow Δv_ϕ in dependence of the clearance height s_{cl} of the labyrinth seal



(a)



(b)

Figure G.3: Simulated radial velocities at the inlet plane (a) and the outlet plane (b) of the labyrinth seal in dependence of the width of the inlet and outlet gap. The width was scaled in the pictures.

Appendix H

Development and use of numerical labyrinth seal models

In the work of Anker et al. [14] a numerical model for labyrinth seals was developed by which a discretization of the labyrinth seal can be avoided in the simulation of shrouded turbines. The mass flow through the labyrinth seal is determined applying an approach suggested by Denton and Johnson [75] where it is assumed that the flow after each labyrinth chamber is fully mixed out. The development of the circumferential velocity of the leakage flow was determined using an approach suggested by Benckert [34], in which the labyrinth seal is subdivided in discrete segments and the change in the circumferential velocity is determined by balancing the angular momentum in consecutive segments through the labyrinth seal. The labyrinth model was calibrated with the results of the parameter study described in Appendix G.

To avoid that the use of a homogeneous boundary conditions for the numerical extraction and injection of leakage flow in the simplified model leads to an unrealistic prediction of the flow in the adjacent blade channels, the first and last cavity in a sealing arrangement need to be discretized, as shown in the work of Anker et al. [14]. A comparison of the computational results where the labyrinth seal was discretized and results which were obtained using the labyrinth model, showed that the labyrinth model qualitatively leads to a correct prediction of the impact of the leakage flow.

Even though the model is not suited for the detailed simulation of leakage flow effects and needs calibration to deliver accurate results, the approximate model is better used than to completely neglecting the leakage flow. Since the model only contains few parameters that need to be adapted to the specific turbine geometry, it is expected that the model delivers comparably good results, if it is used to account for the leakage flow effects in simulations of industrial turbines.

Appendix I

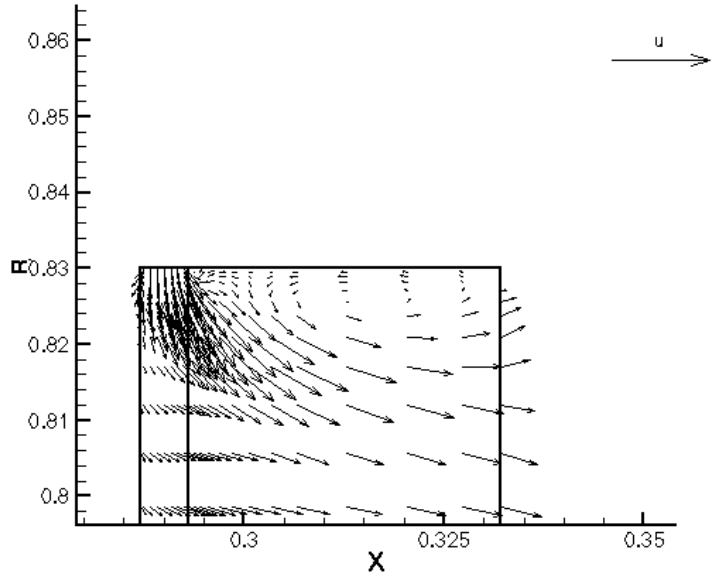
Unsteadiness of leakage flow effects and necessary level of numerical modelling

In a previous study of Anker et al. [14] it was investigated whether the time-averaged solution of an unsteady simulation differs from the corresponding solution of a steady-state simulation for a clearance height of $s_{cl} = 3$ mm for the shrouded Bochum turbine. While the rotor and stator systems are directly coupled in an unsteady simulation, the rotor and stator rows are linked via mixing planes in a steady-state simulation. The method of coupling stator and rotor systems is of importance in the current case, since the reentering leakage flow causes a recirculation behind the rotor row and the use of mixing planes, which does not allow reverse flow, potentially can degrade the accuracy of the predicted flow field. In the following a few results of the aforementioned study of Anker et al. [14] will be shown.

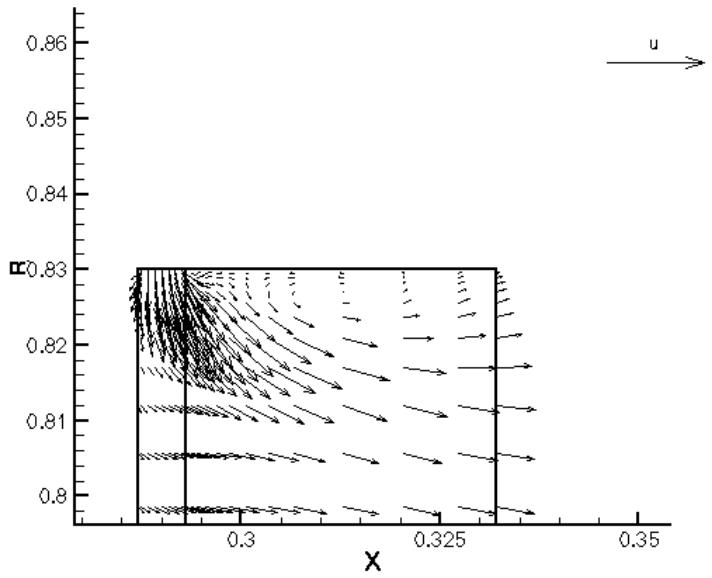
Representative for other circumferential positions, in Fig. I.1a and I.1b the velocity vectors of the steady-state simulations and the time-averaged velocity vectors of the unsteady simulations are plotted in the meridional plane after the trailing edge of the rotor, respectively. The solutions differ only slightly through vanishing velocity vectors on the right border of the domain close to the wall in the steady-state results due to the presence of a mixing plane. Otherwise, there are only minor differences between both velocity fields visible and the position of the vortex core is the same in both simulations.

In Figs. I.2 and I.3 the magnitude of the main and secondary flow vectors of the steady-state simulations and the time-averaged unsteady computations are compared in the measurement plane M2. The comparison shows a good agreement between the solutions.

From the presented excerpt of results of the work of Anker et al. [14] it can for the Bochum turbine be concluded that the steady-state results can be used to predict the time-averaged effects of the interaction between the leakage and the main flow.

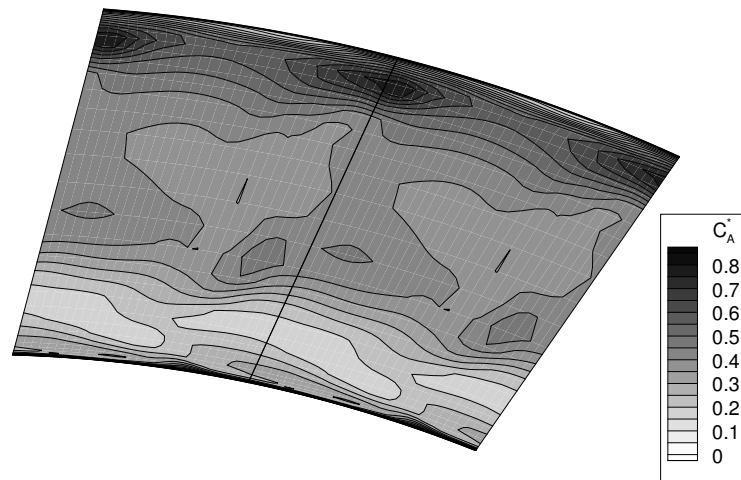


(a) Steady-state

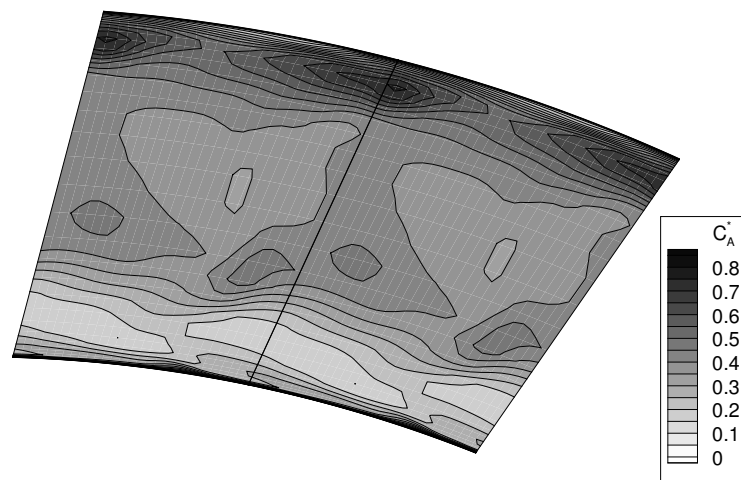


(b) Unsteady (time-averaged)

Figure I.1: Computed velocity vectors in the meridional plane after the trailing edge of the rotor for a clearance height of $s_{cl} = 3$ mm (Reference vector u - Circumferential velocity of the rotor at midspan). The results originate from the report of Anker et al. [14].

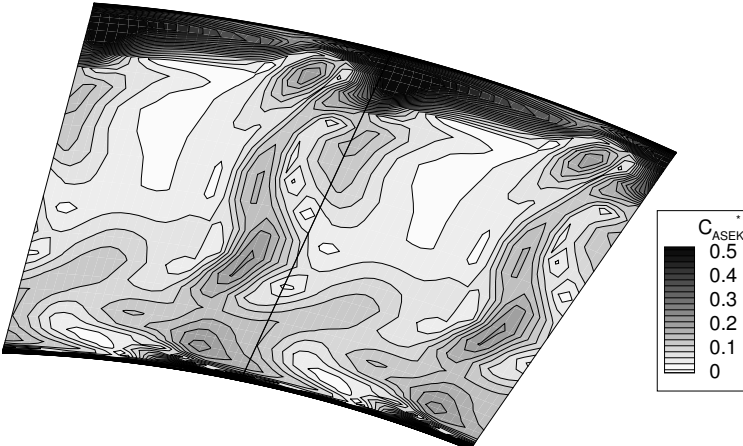


(a) Steady-state

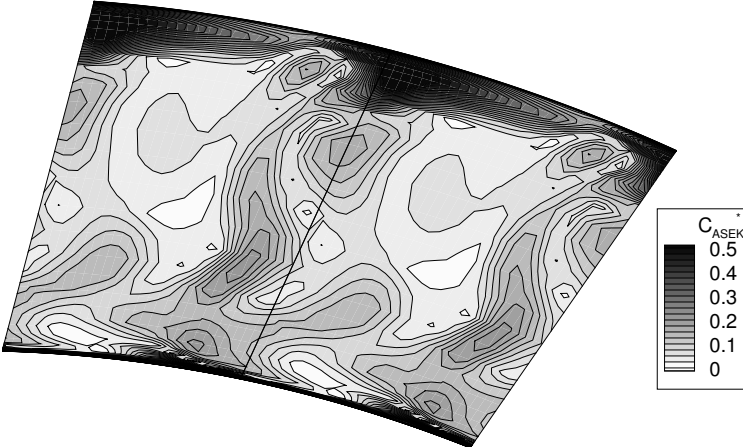


(b) Unsteady (time-averaged)

Figure I.2: Computed normalized magnitude of the velocity vectors in the absolute system for a clearance height of $s_{cl} = 3$ mm. The results originate from the report of Anker et al. [14].



(a) Steady-state



(b) Unsteady (time-averaged)

Figure I.3: Normalized magnitude of the vectors of the secondary flow for a clearance height of $s_{cl} = 3$ mm. The results originate from the report of Anker et al. [14].

Bibliography

- [1] Abu-Ghannam, B.J.; Shaw, R.: Natural transition of boundary layers – The effects of turbulence pressure gradient, and flow history, *Journal of Mechanical Engineering Science*, 22(5):213–228, October 1980
- [2] Adamczyk, J.J.: Model Equation for Simulating Flows in Multistage Turbomachinery, *ASME Paper 85-GT-226*, 1985
- [3] Adami, P.; Martelli, F.; Cecchi, S.: Analysis of the Shroud Leakage Flow and Mainflow Interactions in High-pressure Turbines using an Unsteady Computational Fluid Dynamics Approach, *Proceedings of the Institution of Mechanical Engineers, Part A: Journal of Power and Energy*, 221(6):837 pp., 2007
- [4] Anker, J.E.: *Entwicklung eines Finite-Volumen-Verfahrens zur Lösung der zwei- und dreidimensionalen Navier-Stokes-Gleichungen auf unstrukturierten Rechengittern*, Diplomarbeit, Institut für Thermische Strömungsmaschinen und Maschinenlaboratorium, Universität Stuttgart, 1997
- [5] Anker, J.E.: *Note on time derivative preconditioning and issues concerning the simulation of low Mach number flow*, Tech. Rep., 2010
- [6] Anker, J.E.; Breisig, V.; Giboni, A.; Lerner, C.; Mayer, J.; Peters, P.; Pfof, H.; Stetter, H.: *Deckbandströmungseinfluss I*, Abschlussbericht des FVV-Vorhabens Nr. 706, Forschungsvereinigung Verbrennungskraftmaschinen e. V. (FVV), 2001
- [7] Anker, J.E.; Breisig, V.; Pfof, H.; Stetter, H.: Deckbandströmungseinfluss, in: *FVV-Heft R 504, Informationstagung Turbinen*, Forschungsvereinigung Verbrennungskraftmaschinen e. V., Frankfurt a. M., S. 125–154, 1999
- [8] Anker, J.E.; Casey, M.V.; Pfof, H.; Wolter, K.: Deckbandströmungseinfluss III, Abschlussbericht des FVV-Vorhabens Nr. 801, in: *FVV-Heft R 527, Informationstagung Turbinen*, 2004
- [9] Anker, J.E.; Giboni, A.; Mayer, J.F.; Pfof, H.; Stetter, H.: Deckbandströmungseinfluss, in: *FVV-Heft R 509, Informationstagung Turbinen*, Forschungsvereinigung Verbrennungskraftmaschinen e. V., Frankfurt a. M., 2000

- [10] Anker, J.E.; Giboni, A.; Mayer, J.F.; Pfof, H.; Stetter, H.: Deckbandströmungseinfluss II, in: *FVV-Heft R 518, Informationstagung Turbinen*, Forschungsvereinigung Verbrennungskraftmaschinen e. V., Frankfurt a. M., 2002
- [11] Anker, J.E.; Mayer, J.F.: Computational Study of the Flow in Axial Turbine with Emphasis on the Interaction of Labyrinth Seal Leakage Flow and Main Flow, in: *High Performance Computing in Science and Engineering 2001*, Transactions of the High Performance Computing Center Stuttgart (HLRS) 2001, Springer-Verlag, 2002
- [12] Anker, J.E.; Mayer, J.F.: Simulation of the Interaction of Labyrinth Seal Leakage Flow and Main Flow in an Axial Turbine, *ASME Paper GT-2002-30348*, 2002
- [13] Anker, J.E.; Mayer, J.F.: A Preconditioned Solution Scheme for the Simulation of Turbomachinery Flow at Arbitrary Mach Numbers, *AIAA Paper 2004-0762*, 2004
- [14] Anker, J.E.; Mayer, J.F.; Casey, M.: *Deckbandströmungseinfluss III*, Abschlussbericht des FVV-Vorhabens Nr. 801, Teil 2: Numerische Arbeiten, Forschungsvereinigung Verbrennungskraftmaschinen e. V. (FVV), 2005
- [15] Anker, J.E.; Mayer, J.F.; Casey, M.V.: The Impact of Rotor Labyrinth Seal Leakage Flow on the Loss Generation in an Axial Turbine Stage, *Journal of Power and Energy, Special Issue on Turbomachinery*, 219 A6:481–490, 2005
- [16] Anker, J.E.; Mayer, J.F.; Stetter, H.: Computational Study of the Interaction of Labyrinth Seal Leakage Flow and Main Flow in an Axial Turbine, in: [38], pp. 641–652, 2001
- [17] Anker, J.E.; Mayer, J.F.; Stetter, H.: A Preconditioned Solution Scheme for the Computation of Compressible Flow in Turbomachinery at Arbitrary Mach Numbers, in: *Seminar / Summer School on CFD for Turbomachinery Applications*, Vol. 1 & 2, Polish Society of Computer Simulation, 1-3 September 2001, Gdansk, Poland, September 2001
- [18] Anker, J.E.; Mayer, J.F.; Stetter, H.: A Preconditioned Solution Scheme for the Computation of Compressible Flow in Turbomachinery at Arbitrary Mach Numbers, *Task Quarterly*, 6(1):143–176, 2002
- [19] Anker, J.E.; Mayer, J.F.; Stetter, H.: *Deckbandströmungseinfluss II*, Abschlussbericht des FVV-Vorhabens Nr. 756, Teil 2: Numerische Arbeiten, Forschungsvereinigung Verbrennungskraftmaschinen e. V. (FVV), 2003

- [20] Anker, J.E.; Schrader, B.; Sebold, U.; Mayer, J.F.; Casey, M.V.: A Three-dimensional Non-reflecting Boundary Condition Treatment for Steady-state Flow Simulations, *AIAA Paper 2006-1275*, 2006
- [21] Anker, J.E.; Seybold, U.: *Theorie für die nichtreflektierende Behandlung von Ein- und Austrittsrändern bei stationären Strömungssimulationen basierend auf den dreidimensionalen Euler-Gleichungen*, Interner Bericht, Institut für Thermische Strömungsmaschinen und Maschinenlaboratorium, Universität Stuttgart, 2004
- [22] Arnone, A.; Benvenuti, E.: Three-Dimensional Navier-Stokes Analysis of a Two-Stage Gas Turbine, *ASME Paper 94-GT-88*, 1994
- [23] Arnone, A.; Liou, M.S.; Povinelli, L.A.: Integration of Navier-Stokes Equations Using Dual Time Stepping and a Multigrid Method, *AIAA J.*, 33(6):985–990, 1995
- [24] Balasubramanian, R.; Chen, J.P.: Preconditioned Algorithms with a General Equation of State for Rotating Machinery Flows, *AIAA Paper 2010-4862*, 2010
- [25] Baldwin, B.S.; Barth, T.J.: *A One-Equation Turbulence Transport Model for High Reynolds Number Wall-Bounded Flows*, Tech. Rep. NASA/TM-102847, NASA, 1990
- [26] Baldwin, B.S.; Barth, T.J.: A One-Equation Turbulence Transport Model for High Reynolds Number Wall-Bounded Flows, *AIAA Paper 91-0610*, 29th Aerospace Sciences Meeting, January 7-10, 1991, Reno, Nevada, 1991
- [27] Baldwin, B.S.; Lomax, H.: Thin Layer Approximation and Algebraic Model for Separated Turbulent Flows, *AIAA Paper 78-257*, 1978
- [28] Bardina, J.E.; Huang, P.G.; Coakley, T.J.: *Turbulence Modeling Validation, Testing and Development*, NASA Technical Memorandum NASA TM-110446, NASA, 1997
- [29] Bauer, H.; Mayer, J.F.; Stetter, H.: Unsteady Flow Simulations for Turbomachinery Applications on Dynamic Grids, in: *High Performance Computing in Science and Engineering 2000*, edited by Krause, E.; Jäger, W., Transactions of the High Performance Computing Center Stuttgart (HLRS) 2000, pp. 349–355, Springer-Verlag, 2001
- [30] Bauer, H.; Urban, B.; Stetter, H.: *Aerodynamische Anregung von transsonisch durchströmten Turbinenstufen*, Abschlussbericht, HTGT-Turbotech-II-Vorhaben, Teilprojekt 1.221, 1999
- [31] Bauer, H.; Urban, B.; Stetter, H.; Vortmeyer, N.: Experimentelle und numerische Untersuchungen selbsterregter Stoßschwingungen in Turbomaschinengittern mit oszillierenden Schaufeln, in: *Tagungsband 7*.

- Statusseminar der Arbeitsgemeinschaft „Hochtemperatur-Gasturbine“, 7.-8. Dezember 2000, DLR Köln Porz, 2000*
- [32] Beam, R.M.; Warming, R.F.: An Implicit Finite-Difference Algorithm for Hyperbolic Systems in Conservation Law Form, *J. Comp. Phys.*, 22:87–110, 1976
- [33] Belluchi, V.; Bruno, C.: Numerical simulation of low-speed non-premixed combustion using a preconditioning technique, *AIAA Paper 1998-2980*, 1998
- [34] Benckert, H.: *Strömungsbedingte Federkennwerte in Labyrinthdichtungen*, Dissertation, Institut für Thermische Strömungsmaschinen und Maschinenlaboratorium, Universität Stuttgart, 1980
- [35] Bijl, H.: *Computation of flow at all speeds with a staggered scheme*, PhD Thesis, TU Delft, The Netherlands, 1999
- [36] Bilanceri, M.; Beux, F.; Salvetti, M.V.: An implicit low-diffusive HLL scheme with complete time linearization: Application to cavitating barotropic flows, *Computers & Fluids*, 2010:1990–2006, 39
- [37] Bindon, J.P.; Morphis, G.: The Development of Axial Turbine Leakage Loss for Two Profiled Tip Geometries Using Linear Cascade Data, *ASME Journal of Turbomachinery*, 114:198–203, 1992
- [38] Bois, G.; Decuyper, R.; Martelli, F. (eds.): *4th European Conference on Turbomachinery, Fluid Dynamics and Thermodynamics*, 2001
- [39] Borhani, N., *ERCOFTAC Bulletin 80, September, 2009*
- [40] Boudier, G.; Gicquel, L.Y.M.; Poinso, T.; Bissieres, D.; Berat, C.: Comparison of LES, RANS and experiments in an aeronautical gas turbine combustion chamber, *Proceedings of the Combustion Institute*, 31:3075–3082, 2007
- [41] Boussinesq, J. : Théorie de l'Écoulement Tourbillant, *Mém. Acad. Sci.*, 23 :46–50, 1877
- [42] Breisig, V.: *Experimentelle und numerische Untersuchung der Leitradströmungen in einem 1.5-stufigen Axialturbinenprüfstand*, Dissertation (PhD Thesis), Ruhr-Universität Bochum, 2000
- [43] Briley, W.R.; McDonald, H.; Shamroth, S.: A Low Mach Number Euler Formulation and Application to Time-Iterative LBI Schemes, *AIAA J.*, 21(10):1467–1469, 1983
- [44] Brodersen, O., *Untersuchung einer Matrix-Dissipation in einem Zelleneckpunkt-Finite-Volumen-Schema zur Lösung der Navier-Stokes-Gleichungen*, DLR-FB 92-33, 1992

- [45] Brown, D.: Leakage Flow Modelling of Two Shrouded Compressor Stator Configurations Using a 3D Structured Mesh Flow Solver, in: *5th European Conference on Turbomachinery, Fluid Dynamics and Thermodynamics*, edited by Št'astný, M.; Sieverding, C.H.; Bois, G., pp. 313–322, 2003
- [46] Buelow, P.E.O.: *Convergence Enhancement of Euler- and Navier-Stokes Computations*, PhD Thesis, Department of Mechanical Engineering, Penn State University, 1995
- [47] Buelow, P.E.O., *Preconditioning Methods at the Propulsion Engineering Center*, Penn State University, 1998
- [48] Buelow, P.E.O.; Schwer, D.; Feng, J.; Merkle, C.; Choi, D.: A Preconditioned Dual-Time Diagonalized ADI Scheme for Unsteady Computations, *AIAA Paper 97-2101*, 1997
- [49] Bunge, U.; Mockett, C.; Auxpoix, B.; Haase, W.; Menter, F.; Schwamborn, D.; Weinmann, K.: Summary of experience (of the FLO-MANIA project), in: [106], pp. 405–420, 2006
- [50] Cebeci, T.; Smith, A.M.O.: *Analysis of Turbulent Boundary Layers*, Academic Press, Inc. Ltd., London, 1974
- [51] Celestina, M.L.; Turkel, E.: Matrix Viscosity and Preconditioning for Rotating Turbomachinery, in: *9th Int. Symp. on Transport Phenomena and Dynamics of Rotating Machinery*, edited by Tsujimoto, Y., 2002
- [52] Celik, A.; Hirschel, E.H.: Comparison of Eddy-Viscosity Turbulence Models in Flows with Adverse Pressure Gradient, *AIAA J.*, 44(10):2156–2169, 2006
- [53] Chen, C.J.; Jaw, S.Y.: *Fundamentals of Turbulence Modeling*, Taylor & Francis, 1997
- [54] Chen, Y.G.; Price, W.G.: Numerical simulation of liquid sloshing in a partially filled container with inclusion of compressibility effects, *Physics of Fluids*, 21, 2009
- [55] Childs, D.: *Turbomachinery Rotordynamics: Phenomena, Modeling, and Analysis*, John Wiley & Sons, 1993
- [56] Chima, R.V.; Yokota, J.W.: *Numerical Analysis of Three-Dimensional Viscous Internal Flows*, Tech. Rep. NASA TM-100878, NASA, National Aeronautics and Space Administration, Lewis Research Center, Cleveland, Ohio 44135-3191G, 1988
- [57] Cho, J.R.; Chung, M.: A $k - \epsilon - \gamma$ Equation Turbulence Model, *J. Fluid Mech.*, 237:301–322, 1992

- [58] Choi, D.; Merkle, C.L.: Application of Time-Iterative Schemes to Incompressible Flow, *AIAA Paper 84-1638*, 1984
- [59] Choi, D.; Merkle, C.L.: Application of Time-Iterative Schemes to Incompressible Flow, *AIAA J.*, 23(10):1518–1524, 1985
- [60] Choi, Y.H.; Merkle, C.L.: The Application of Preconditioning in Viscous Flows, *J. Comp. Phys.*, 105:207–223, 1993
- [61] Chorin, A.J.: A Numerical Method for Solving Incompressible Viscous Flow Problems, *J. Comp. Phys.*, 2:12–26, 1967
- [62] Clauser, F.H.: The Turbulent Boundary Layer, *Advances in Applied Mechanics*, IV:1–51, 1956
- [63] Contreras, J.; Corral, R.: Quantitative Influence of the Steady Non-Reflecting Boundary Conditions on Blade-to-Blade Computations, *ASME Paper 2000-GT-0515*, 2000
- [64] Corrsin, S.; Kistler, A.L., *Natl. Advisory Comm. Aeronaut. Tech. Notes 3133*, 1954
- [65] Coutier-Delgosha, O.; Fortes-Patella, R.; Reboud, J.L.; Hakimi, N.; Hirsch, C.: Numerical simulation of cavitating flow in 2D and 3D geometries, *Int. J. Numer. Meth. Fluids*, 48:135–167, 2005
- [66] Darmofal, D.L.: *Eigenmode Analysis of Boundary Conditions for the One-dimensional Preconditioned Euler Equations*, NASA Contractor Report NASA CR-208741, NASA, Institute for Computer Applications in Science and Engineering, NASA Langley Research Center, Hampton, VA 23681-0001, ICASE Report No. 98-51, November 1998
- [67] Darmofal, D.L.; Moinier, P.; Giles, M.B.: Eigenmode Analysis of Boundary Conditions for the One-dimensional Preconditioned Euler Equations, *J. Comp. Phys.*, 160(1):369–384, 2000
- [68] Darmofal, D.L.; Schmid, P.J.: The Importance of Eigenvectors for Local Preconditioners of the Euler Equations, *J. Comp. Phys.*, 127:346–362, 1996
- [69] Darmofal, D.L.; van Leer, B.: Local Preconditioning: Manipulating Mother Nature to fool Father Time, in: *Computing the Future II: Advances and Prospects in Computational Aerodynamics*, edited by Hafez, M.; A., C.D., John Wiley and Sons, 1998
- [70] Darwish, M.; Moukalled, F.: TVD schemes for unstructured grids, *Int. J. for Heat and Mass Transfer*, 46:599–611, 2003
- [71] de Groot, S.R.; Mazur, P.: *Non-Equilibrium Thermodynamics*, Dover Publications Inc., 1985

- [72] Denton, J.D.: The Calculation of Three-Dimensional Viscous Flow Through Multistage Turbomachines, *ASME Journal of Turbomachinery*, 114:18–26, 1992
- [73] Denton, J.D.: Loss Mechanisms in Turbomachines, *Journal of Turbomachinery*, 115(4):621–656, October 1993
- [74] Denton, J.D.; Dawes, W.N.: Computational fluid dynamics for turbomachinery, *IMECHE Proc. Part C*, 213(C2):107–124, 1999
- [75] Denton, J.D.; Johnson, C.G.: *The Tip Leakage of Turbine Blades - A Review and A Theory For Shrouded Blades*, Tech. Rep. CEGB Report No. R/M/N627, Marchwood Engineering Laboratories, 1972
- [76] Dietz, M.; Kessler, M.; Krämer, E.; Wagner, S.: Tip Vortex Conservation on a Helicopter Main Rotor Using Vortex-Adapted Chimera Grids, *AIAA J.*, 45(8):2062–2074, 2007
- [77] Dunham, J.; Came, P.M.: Improvements to the Ainley-Mathieson Method of Turbine Performance Prediction, *Trans. ASME, J. of Engrg. for Power*, 92:252–256, July 1970
- [78] Edwards, J.; Liou, M.S.: Low Diffusion Flux Splitting Methods for Flows at All Speeds, *AIAA Paper 97-1862*, 17th AIAA CFD Conference, Snowmass, CO, 1997
- [79] Edwards, J.; Liou, M.S.: Low-diffusion Flux-splitting Methods for Flows at all Speeds, *AIAA J.*, 36:1610–1617, 1998
- [80] Edwards, J.R.: Towards Unified CFD Simulations of Real Fluid Flows, *AIAA Paper 2001-2524*, 2001
- [81] Edwards, J.R.; Roy, C.J.: Preconditioned Multigrid Methods for Two-Dimensional Combustion Calculations at All Speeds, *AIAA J.*, 36(2):185–192, February 1998
- [82] Engquist, B.; Majda, A.: Absorbing Boundary Conditions for the Numerical Simulation of Waves, *Mathematics of Computation*, 31:629–651, 1977
- [83] Engquist, B.; Majda, A.: Radiation Boundary Conditions for Acoustic and Elastic Wave Calculations, *Communications on pure and applied mathematics*, 32:313–357, 1979
- [84] Esfahanian, V.; Akbarzadeh, P.: Numerical investigation on a new local preconditioning method for solving the incompressible inviscid, non-cavitating and cavitating flows, *J. Franklin Inst.*, 348:1208–1230, 2011

- [85] Fan, S.; Lakshminarayana, B.: Time Accurate Euler Simulation of Interaction of Nozzle Wake and Secondary Flow with Rotor Blade in an Axial Turbine Stage Using Nonreflecting Boundary Conditions, *ASME Paper 95-GT-230*, pp. 1–20, September 1995
- [86] Fatsis, A.; van den Braembussche, R.: Evaluation of an Euler Code with Non-reflecting Boundary Conditions for the Analysis of 3D Flow in Radial Impellers, *ASME Paper 94-GT-147*, 1994
- [87] Ferziger, J.H.; Peric, M.: *Computational Methods for Fluid Dynamics*, Springer-Verlag, 1997
- [88] Fluent, Inc., *Fluent User's Guide V6.3*, 2010
- [89] Fritsch, G.; Giles, M.B.: An Asymptotic Analysis of Mixing Loss, *Trans. ASME, J. Turbomachinery*, 117(3):367–374, July 1995
- [90] Gatski, T.B.; Hussaini, M.Y.; Lumley, J.L. (eds.): *Simulation and Modeling of Turbulent Flows*, Oxford University Press, 1996
- [91] Gerlinger, P.; Stoll, P.; Brüggemann, D.: An Implicit Multigrid Method for the Simulation of Chemically Reacting Flows, *J. Comp. Phys.*, 146:322–345, 1998
- [92] Giboni, A.: *Experimentelle und numerische Untersuchung der instationären Wechselwirkung zwischen Deckbandströmung und Hauptströmung einer 1,5-stufigen Axialturbine*, Dissertation, Ruhr-Universität Bochum, 2002
- [93] Giboni, A.; Menter, J.R.; Peters, P.; Wolter, K.; Pfof, H.; Breisig, V.: Interaction of Labyrinth Seal Leakage Flow and Main Flow in an Axial Turbine, *ASME Paper GT2003-38722*, 2003
- [94] Giboni, A.; Wolter, K.; Menter, J.R.; Pfof, K.: Experimental and Numerical Investigation into the Unsteady Interaction of Labyrinth Seal Leakage Flow and Main Flow in a 1.5-Stage Axial Turbine, *ASME Paper GT2004-53024*, 2004
- [95] Gier, J.; Engel, K.; Stubert, B.; Wittmaack, R.: Modelling and Analysis of Main Flow - Shroud Leakage Flow Interactions in LP Turbines, *ASME Paper GT2006-90773*, 2006
- [96] Gier, J.; Stubert, B.; Brouillet, B.; de Vito, L.: Interaction of Shroud Leakage Flow and Main Flow in a Three-Stage LP Turbine, *ASME Paper 2003GT-38025*, 2003
- [97] Giles, M.B.: Developments in the Calculation of Unsteady Turbomachinery Flow, in: *Proceedings of the Conference on Numerical Methods for Fluid Dynamics*, Oxford University, 1988

- [98] Giles, M.B.: *Non-Reflecting Boundary Conditions for the Euler Equations*, TR-88-1, MIT Computational Fluid Dynamics Laboratory, 1988
- [99] Giles, M.B.: *UNSFLO: A Numerical Method For Unsteady Inviscid Flow In Turbomachinery*, GTL Report 195, MIT Gas Turbine Laboratory, 1988
- [100] Givoli, D.: Non-reflecting Boundary Conditions, *Journal of Computational Physics*, 94:1–29, 1991
- [101] Godunov, S.K.: A Difference Method for Numerical Calculation of Discontinuous Solution of the Equations of Hydrodynamics, *Math. Sbornik*, 47:271–306, 1959
- [102] Godunov, S.K.; Ryabenki, V.S.: *Difference Schemes*, Elsevier Publishing Company, Amsterdam, 1987
- [103] Greitzer, E.M.; Tan, C.S.; Graf, M.: *Internal Flow – Concepts and Applications*, Cambridge University Press, 2004
- [104] Guerra, J.; Gustafsson, B.: A Numerical Method for Incompressible Flow Problems with Smooth Solutions, *J. Comp. Phys.*, 63:377–397, 1986
- [105] Guillard, H.; Viozat, C.: On the behaviour of upwind schemes in the low Mach number limit, *Computers & Fluids*, 28:63–86, 1999
- [106] Haase, W.; Aupoix, B.; Bunge, U.; Schwamborn, D. (eds.): *FLOMANIA - A European Initiative on Flow Physics Modelling*, Springer-Verlag, Heidelberg, Germany, 2006
- [107] Haase, W.; Braza, M.; Revell, A. (eds.): *DESider - A European Initiative on Hybrid RANS-LES modeling*, Springer-Verlag, Heidelberg, Germany, 2009
- [108] Hakimi, N.: *Preconditioning methods for time dependent Navier-Stokes equations*, PhD Thesis, Vrije Universiteit Brussels, Belgium, 1997
- [109] Hall, M.G.: Cell-Vertex Multigrid Scheme for Solution of the Euler Equations, in: *Proc. Conf. on Numerical Methods for Fluid Dynamics*, Reading, UK, 1985
- [110] Hanjalić, K.; Jakirlic, S.: Contribution towards the second-moment closure modeling of separated turbulent flows, *Computers and Fluids*, 27(2):137–156, 1998
- [111] Hanjalić, K.; Launder, B.E.: A Reynolds Stress Model of Turbulence and its Application to Thin Shear flows, *J. Fluid Mech.*, 52(4):609–638, 1972

- [112] Hanjalić, K.; Launder, B.E.: Contribution Towards a Reynolds-Stress Closure for Low-Reynolds-Number Turbulence, *J. Fluid Mech.*, 54(4):593–610, 1976
- [113] Harten, A.: High Resolution Schemes for Hyperbolic Conservation Laws, *J. Comp. Phys.*, 49:357–393, 1983
- [114] Hartland, J.C.; Gregory-Smith, D.G.; Harvey, N.W.; Rose, M.G.: Nonaxisymmetric Turbine End Wall Design: Part II - Experimental Validation, *Trans. ASME, J. Turbomachinery*, 122(2):286–293, April 2000
- [115] Hedstrom, G.W.: Nonreflecting Boundary Conditions for Nonlinear Hyperbolic Systems, *J. Comp. Phys.*, 30:222–237, 1979
- [116] Hinze, J.O.: *Turbulence*, Classic Textbook Reissue (Mechanical Engineering), McGraw-Hill, 2nd edn., 1975
- [117] Hirsch, C.: *Numerical Computation of Internal and External Flows, vol. 1: Fundamentals of Internal and External Flows*, Wiley Interscience Series in Numerical Methods in Engineering, John Wiley & Sons Ltd., Chichester, 1988
- [118] Hirsch, C.: *Numerical Computation of Internal and External Flows, vol. 2: Computational Methods for Inviscid and Viscous Flows*, Wiley Interscience Series in Numerical Methods in Engineering, John Wiley & Sons Ltd., Chichester, 1990
- [119] Hirsch, C.: *Numerical Computation of Internal and External Flow – Fundamentals of Computational Fluid Dynamics*, Butterworth-Heinemann, 2nd edn., 2007
- [120] Housman, J.; Kiris, C.; Hafez, M.: Time-Derivative Preconditioning Methods for Multicomponent Flows – Part I: Riemann Problems, *J. Appl. Mech.*, March 2009
- [121] Housman, J.; Kiris, C.; Hafez, M.: Time-Derivative Preconditioning Methods for Multicomponent Flows – Part II: Two-Dimensional Applications, *J. Appl. Mech.*, May 2009
- [122] Hunter, S.; Orkwis, P.: Endwall Cavity Flow Effects on Gaspath Aerodynamics in an Axial Flow Turbine: Part 2 – Source Term Development, *ASME Paper 2000-GT-513*, 2000
- [123] Höhn, W.; Gombert, R.; Kraus, A.: Unsteady Aerodynamical Blade Row Interaction in a New Multistage Research Turbine. Part II: Numerical Investigation, *ASME Paper 2001-GT-0307*, 2001
- [124] Ihm, S.W.; Hong, S.W.; Han, S.; Kim, C.: Numerical Simulation of Homogeneous Equilibrium Two-Phase Flows with Shock-Stable Schemes, *ASME Paper 2007-4457*, 2007

- [125] Imanari, K.; Kodama, H.: Application of Non-Reflecting Boundary Conditions to Three-Dimensional Euler Equation Calculations for Thick Strut Cascades, *AIAA Paper 92-3045*, 1992
- [126] Irmisch, S.: *Numerische Simulation der Turbinenschaufelströmung mit Kühlluftausblasung unter Einbeziehung der Kühlluftkanäle*, Dissertation, Universität Stuttgart, 1995
- [127] Ivey, P.C.; Swoboda, M.: Leakage Effects in the Rotor Tip-Clearance Region of a Multistage Axial Compressor, Part I: Innovative Experiments, *ASME Paper 98-GT-591*, 1998
- [128] Jameson, A.: Artificial Diffusion, Upwind Biasing, Limiters and Their Effect on Accuracy and Multigrid Convergence in Transonic and Hypersonic Flow, *AIAA Paper 93-3359*, 1993
- [129] Jameson, A.: Analysis and Design of Numerical Schemes for Gas Dynamics, 1: Artificial Diffusion, Upwind Biasing, Limiters and their Effect on Accuracy and Multigrid Convergence, *International Journal of Computational Fluid Dynamics*, 4:171–218, 1995
- [130] Jameson, A.: Analysis and Design of Numerical Schemes for Gas Dynamics, 2: Artificial Diffusion and Discrete Shock Structure, *International Journal of Computational Fluid Dynamics*, 5:1–38, 1995
- [131] Jameson, A.; Schmidt, W.; Turkel, E.: Numerical Solutions of the Euler Equations by Finite Volume Methods Using Runge Kutta Time-Stepping Schemes, *AIAA Paper 81-1259*, 1981
- [132] Jameson, A.; Turkel, E.: Implicit Schemes and LU-Decomposition, *Mathematical Computations*, 1981
- [133] Johnson, D.A.; King, L.S.: A Mathematically Simple Turbulence Closure Model for Attached and Separated Turbulent Boundary Layers, *AIAA J.*, 23(11):1684–1692, November 1985
- [134] Johnson, F.T.; Tinoco, E.N.; Yu, N.J.: Thirty Years of Development and Application of CFD at Boeing Commercial Airplanes, Seattle, *AIAA Paper 2003-3439*, 2003
- [135] Jones, W.P.; Musonge, P.: Closure of the Reynolds stress and scalar flux equations, *Phys. Fluids*, 31:3589–3604, 1988
- [136] Jung, A.: *Berechnung der Stator-Rotor-Wechselwirkung in Turbomaschinen*, Dissertation, Universität Stuttgart, 2000
- [137] Jung, A.R.; Mayer, J.F.; Stetter, H.: Simulation of 3D-Unsteady Stator/Rotor Interaction in Turbomachinery Stages of Arbitrary Pitch Ratio, *ASME Paper 96-GT-69*, 1996

- [138] Kacker, S.C.; Okapuu, U.: A Mean Line Prediction Method for Axial Flow Turbine Efficiency, *Trans. ASME, J. of Engrg. for Power*, 104(1):111–119, January 1982
- [139] Kermani, M.; Plett, E.: Roe Scheme in Generalized Coordinates; Part II – Application to Inviscid and Viscous Flow, *AIAA Paper AIAA-2001-87*, 2001
- [140] Kermani, M.J.; Gerber, A.G.; Stockie, J.M.: Thermodynamically Based Moisture Prediction Using Roe’s Scheme, in: *The 4th Conference of Iranian AeroSpace Society, Amir Kabir University of Technology, Teheran, Iran*, 2003
- [141] Kitamura, K.; Fujimoto, K.; Shima, E.; Wang, Z.J.: Performance of Low-Dissipation Euler Fluxes and Preconditioned Implicit Schemes in Low Speeds, *AIAA Paper 2010-1272*, 2010
- [142] Klebanoff, P.S.: Characteristics of Turbulence in a Boundary Layer with Zero Pressure Gradient, *NACA TN 3178*, 1956
- [143] Klein, J.A.: *Experimentelle und numerische Untersuchung des Einflusses örtlich begrenzt abdichtender Deckbänder an einer Axialturbinen-Laufschaufelreihe*, Dissertation, Ruhr-Universität Bochum, 2006
- [144] Korschunov, B.A.; Döhler, S.W.: Einfluss von Leckageströmungen an der Laufradspitze auf die aerodynamischen Charakteristiken des folgenden Leitgitters, *BWK - Brennstoff, Wärme, Kraft*, 48(7/8), 1996
- [145] Kreiss, H.O.: Initial Boundary Value Problems for Hyperbolic Systems, *Comm. Pure Appl. Math.*, 23:277–298, 1970
- [146] Krückels, J.: *Auswirkungen der Spaltströmung auf die Strömung in der letzten Turbinenstufe und im Diffusor*, Abschlussbericht Vorhaben Nr. 578, Forschungsvereinigung Verbrennungskraftmaschinen e. V. (FVV), 1995
- [147] Krückels, J.: *Numerische Berechnung der spaltbeeinflussten Strömung in Axialturbinen mit Diffusoren*, Dissertation, Universität Stuttgart, 1996
- [148] Krückels, J.; Mayer, J.F.; Stetter, H.: Simulation of Diffuser Flow Using an Euler Solver with a Distributed Loss Model, *ASME Paper 93-GT-257*, 1993
- [149] Krückels, J.; Merz, R.; Mayer, J.F.; Stetter, H.: Flow Calculation of a Steam Turbine Last Stage with Diffuser, in: *Rotating Machinery – 1996, Proc. ISROMAC-6, Honolulu, Hawaii*, Vol. II, pp. 170–179, 1996

- [150] Kunz, R.F.; Bogner, D.A.; Stinebring, D.R.; Chyczewinski, T.S.; Lindau, J.W.; Gibeling, H.J.; Venkateswaran, S.; Govindan, T.R.: A preconditioned Navier-Stokes Method for Two-phase Flows with Application to Cavitation Prediction, *Computers & Fluids*, 29(8):849–875, 2000
- [151] Kunz, R.F.; Lakshminarayana, B.; Basson, A.H.: Investigation of Tip Clearance Phenomena in an Axial Compressor Cascade Using Euler and Navier-Stokes Procedures, *ASME Paper 92-GT-299*, 1992
- [152] Lakshminarayana, B.: *Fluid Dynamics and Heat Transfer of Turbomachinery*, John Wiley & Sons, 1996
- [153] Langtry, R.B.: *A Correlation-Based Transition Model using Local Variables for Unstructured Parallelized CFD Codes*, PhD Thesis, Universität Stuttgart, Germany, 2006
- [154] Langtry, R.B.; Menter, F.R.: Transition Modeling for General CFD Applications in Aeronautics, *AIAA Paper 2005-522*, 2005
- [155] Launder, B.E.; Reece, G.J.; Rodi, W.: Progress in the development of a Reynolds-stress turbulence closure, *J. Fluid Mech.*, 68(part 3):537–566, 1975
- [156] Launder, B.E.; Sharma, B.I.: Application of the Energy-Dissipation Model of Turbulence to the Calculation of Flow near a Spinning Disc, *Letters in Heat and Mass Transfer*, 1(2):131–138, 1974
- [157] Launder, B.E.; Spalding, D.B.: *Lectures in Mathematical Models of Turbulence*, Academic Press, 1972
- [158] Lee, D.: *Local Preconditioning of the Euler and Navier-Stokes Equations*, PhD Thesis, University of Michigan, 1996
- [159] Lee, D.; Leer, B.v.; Lynn, J.F.: A Local Navier-Stokes Preconditioner for all Mach and Cell Reynolds Numbers, *AIAA Paper 97-2024*, 1997
- [160] Leer, B.v.; Lee, W.T.; Roe, P.: Characteristic Time-Stepping or Local Preconditioning of the Euler Equations, *AIAA Paper 91-1552-CP*, 1991
- [161] LeVeque, R.: *Numerical Methods for Conservation Laws*, Birkhäuser Verlag, Basel, Boston, Berlin, 1992
- [162] Lewis, K.L.: *The Aerodynamics of Shrouded Multistage Turbines*, Dissertation (PhD Thesis), Cambridge University Engineering Department, November 1993
- [163] Li, X.S.; Gu, C.W.: An All-Speed Roe-type scheme and its asymptotic analysis of low Mach number behaviour, *J. Comp. Phys.*, 227:5144–5159, 2008

- [164] Lindau, J.W.; Venkateswaran, S.; Kunz, R.; Merkle, C.L.: Computation of Compressible Multiphase Flows, *AIAA Paper 2003-1285*, 2003
- [165] Liou, M.S.: *A Continuing Search for a Near-Perfect Numerical Flux Scheme-Part 1: AUSM+*, Tech. Rep. NASA TM-106524, NASA, March 1994
- [166] Liou, M.S.: A Sequel to AUSM: AUSM+, 129:364–382, 1996
- [167] Liou, M.S.: A Sequel to AUSM, Part II: AUSM⁺-up for all speeds, *J. Comp. Phys.*, 214:137–170, 2006
- [168] Liou, M.S.; Kao, K.H.; Ajmani, K.: Computation of Internal/Rotating Flows Using Recent CFD Techniques, *ASME Paper 96-GT-30*, 1996
- [169] Liou, M.S.; Steffen, C.: A New Flux Splitting Scheme, *J. Comp. Phys.*, 107(1):23–39, 1993
- [170] Lodato, G.; Domingo, P.; Vervisch, L.: Three-dimensional boundary conditions for direct and large-eddy boundary conditions of compressible viscous flow, *J. Comp. Phys.*, 227:5105–5143, 2008
- [171] Luo, H.; Baum, J.D.; Löhner, R.: Extension of Harten-Lax-van Leer Scheme for Flows at All Speeds, *AIAA J.*, 43(6):1160–1166, 2005
- [172] Luo, H.; Baum, J.D.; Löhner, R.: On the computation of multi-material flows using ALE formulation, *J. Comp. Phys.*, 194:304–328, 2004
- [173] Lynn, J.F.: *Multigrid solution of the Euler equations with local preconditioning*, Dissertation (PhD Thesis), University of Michigan, 1995
- [174] Lynn, J.F.; van Leer, B.: Multi-Stage Schemes for the Euler and Navier-Stokes Equations with Optimal Smoothing, *AIAA Paper 93-3355*, pp. 1–15, 1993
- [175] Lynn, J.F.; van Leer, B.: Multigrid Euler Solutions with Semi-Coarsening and Local Preconditioning, in: *Fourteenth International Conference on Numerical Methods in Fluid Dynamics*, edited by Deshpande, S.M.; Desai, S.S.; Narasimha, R., Vol. 453 of *Lecture Notes in Physics*, pp. 161–165, Springer, 1994
- [176] Mahle, I.: Improving the Interaction between Leakage Flows and Main Flow in a Low Pressure Turbine, *ASME Paper GT2010-22448*, 2010
- [177] Martinelli, L.: *Calculations of Viscous Flows with a Multigrid Method*, PhD Thesis, MAE Department, Princeton University, 1987
- [178] Martini, P.; Schulz, A.; Bauer, H.J.; Whitney, C.F.: Detached Eddy Simulation of Film Cooling Performance on the Trailing Edge Cutback of Gas Turbine Airfoils, *Trans. ASME, J. Turbomachinery*, 128:292–299, 2006

- [179] Mavriplis, D.J.: Accurate Multigrid Solution of the Euler Equations on Unstructured and Adaptive Meshes, *AIAA Paper 88-3706-CP*, 1988
- [180] Mayle, R.E.: The Role of Laminar-Turbulent Transition in Gas Turbine Engines, *Trans. ASME, J. Turbomachinery*, 113(4):509–537, October 1991
- [181] Medic, G.; Kalitzin, G.; You, D.; van der Weyde, E.; Alonso, J.; Pitsch, H.: Integrated RANS/LES Computations of an Entire Gas Turbine Jet Engine, *AIAA Paper 2007-1117*, 2007
- [182] Meister, A.; Struckmeier, J.: *Hyperbolic Partial Differential Equations*, Vieweg, 2002
- [183] Menter, F.R.: Performance of Popular Turbulence Models for Attached and Separated Adverse Pressure Gradient Flows, *AIAA J.*, 30(8):2066–2072, 1992
- [184] Menter, F.R.: Two-Equation Eddy-Viscosity Turbulence Models for Engineering Applications, *AIAA J.*, 32(8):1598–1605, August 1994
- [185] Menter, F.R.; Langtry, R.B.; Likki, S.R.; Suzen, Y.B.; Huang, P.G.; Völker, S.: A correlation-based transition model using local variables Part I – Model formulation, *ASME Paper GT2004-53452*, 2004
- [186] Merkle, C.L.: Preconditioning Methods for Viscous Flow Calculations, in: *Computational Fluid Dynamics Review 1995*, edited by Hafez, M.; Oshima, K., pp. 419–436, Wiley, Chichester, England, 1995
- [187] Merkle, C.L.; Choi, Y.H.: Computation of Low-speed Compressible Flows with Time-marching Procedures, *Internat. J. Numer. Methods Engrg.*, 25:293–311, 1988
- [188] Merkle, C.L.; Sullivan, J.A.; Buelow, P.E.O.; Venkateswaran, S.: Computations of Flows with Arbitrary Equations of State, *AIAA J.*, 36(4):515–521, 1998
- [189] Merkle, C.L.; Venkateswaran, S.; Deshpande, M.: Convergence Acceleration of the Navier-Stokes Equations through Time-Derivative Preconditioning, in: *Progress and Challenges in CFD Methods and Algorithms*, AGARD-CP-578, pp. 20.1–20.10, NATO, 1995
- [190] Merz, R.: *Entwicklung eines Mehrgitterverfahrens zur numerischen Lösung der dreidimensionalen, kompressiblen Navier-Stokes-Gleichungen in mehrstufigen Turbomaschinen*, Dissertation (PhD Thesis), Universität Stuttgart, 1998
- [191] Merz, R.; Krückels, J.; Mayer, J.F.; Stetter, H.: Computation of Three-Dimensional Viscous Transonic Turbine Stage Flow Including Tip Clearance Effects, *ASME Paper 95-GT-76*, 1995

- [192] Merz, R.; Krückels, J.; Mayer, J.F.; Stetter, H.: Simulation of Three-Dimensional Viscous Flow in a Three-Stage Steam Turbine with Tip Leakage, in: *Rotating Machinery – 1996, Volume II Transport Phenomena, Proc. ISROMAC-6, Honolulu, Hawaii, USA*, pp. 297–305, 1996
- [193] Michelassi, V.; Giangiaco, P.; Martelli, F.: On the choice of variables and matching criteria for the steady simulation of transonic axial turbine stages, in: [38], pp. 151–163, 2001
- [194] Müller, B., *Low Mach Number Asymptotics of the Navier-Stokes Equations and Numerical Implications*, von Karman Institute for Fluid Dynamics, Lecture Series 1999-03, 1999
- [195] Neaves, M.D.; Edwards, J.R.: All-Speed Time-Accurate Underwater Projectile Calculations Using a Preconditioning Algorithm, *Trans. ASME, J. Fluids Engrg.*, 128:284–296, March 2006
- [196] Nemec, M.; Zingg, D.W.: Aerodynamic Computations Using The Convective Upstream Split Pressure Scheme With Local Preconditioning, *AIAA Paper 98-2444*, June 1998
- [197] Özdemir, H.: *Experimentelle und numerische Untersuchungen zur Analyse und Modellierung der Leckageströmung an Deckbändern von Turbinenschaukeln*, Dissertation (PhD Thesis), Ruhr-Universität Bochum, 2006
- [198] Paillère, H.; Corre, C.; Cascales, J.R.G.: On the extension of the AUSM+ scheme to compressible two-fluids models, *Computers & Fluids*, 32:891–916, June 2003
- [199] Park, S.H.; Lee, J.E.; Kwon, J.H.: Preconditioned HLLE Method for Flows at All Mach Numbers, *AIAA J.*, 44(11), 2006
- [200] Patankar, S.V.: *Numerical Heat Transfer and Fluid Flow*, McGraw-Hill, New York, 1980
- [201] Patel, A.: *Développement d'un solveur RANS adaptif sur maillages non-structurés hexaédriques*, PhD Thesis, ULB, Brussels, 2003
- [202] Peters, P.: *Experimentelle und numerische Untersuchungen des Einflusses der Deckbandströmung auf das nachfolgende Leitgitter in einer Axialturbine*, Dissertation (PhD Thesis), Ruhr-Universität Bochum, 2001
- [203] Peters, P.; Breisig, V.; Giboni, A.; Lerner, C.; Pfof, H.: The Influence of the Clearance of Shrouded Rotor Blades on the Development of the Flowfield and Losses in the Subsequent Stator, *ASME Paper 2000-GT-478*, 2000
- [204] Peters, P.; Giboni, A.; Wolter, K.; Menter, J.R.; Pfof, H.: Unsteady Interaction of Labyrinth Seal Leakage Flow and Downstream Stator Flow in a Shrouded 1.5 Stage Axial Turbine, *ASME Paper GT2005-68065*, 2005

- [205] Peyret, R.; Taylor, T.D.: *Computational Methods for Fluid Flow*, Springer-Verlag, New York, 1983
- [206] Pfau, A.; Schlienger, J.; Rausch, D.; Kalfas, A.I.; Abhari, R.S.: Unsteady Flow Interactions within the Inlet Cavity of a Turbine Rotor Tip Labyrinth Seal, *ASME Paper GT2003-38271*, 2003
- [207] Pfof, H.; Giboni, A.; Breisig, V.; Peters, P.; Wolter, K.: *Deckbandströmungseinfluss II*, Abschlussbericht des FVV-Vorhabens Nr. 756, Teil 1: Experimentelle Arbeiten, Forschungsvereinigung Verbrennungskraftmaschinen e. V. (FVV), 2003
- [208] Pfof, H.; Wolter, K.; Breisig, V.; Giboni, A.; Lerner, C.; Peters, P.: *Deckbandströmungseinfluss III*, Abschlussbericht des Vorhabens Nr. 801, Teil 1: Experimentelle Arbeiten, Forschungsvereinigung Verbrennungskraftmaschinen e. V. (FVV), 2004
- [209] Pieringer, P.: *Implementieren von nichtreflektierenden Randbedingungen in Finite-Volumen-Strömungsrechenverfahren*, Diplomarbeit (MSc Thesis), TU Graz, 1999
- [210] Pieringer, P.; Gehrler, A.; Sanz, W.: Calculation of the Stator-Rotor Interaction of a Transonic Turbine Stage using an Innovative Unsteady Flow Solver, in: *Proc. of the 4th European Conference on Turbomachinery*, pp. 1009–1020, 2001
- [211] Poinso, T.J.; Lele, S.K.: Boundary Conditions for Direct Simulations of Compressible Viscous Flows, *J. Comp. Phys.*, 101:104–129, 1992
- [212] Pope, S.B.: *Turbulent Flows*, Cambridge University Press, 2000
- [213] Praisner, T.; Clark, J.: Predicting Transition in Turbomachinery: Part I – A Review and New Model Development, *Journal of Turbomachinery*, pp. 1–13, 129
- [214] Prandtl, L.: Über die ausgebildete Turbulenz, *Z. angew. Math. Mech.*, 5:136–139, 1925
- [215] Press, W.H.; Flannery, B.P.; Teukolsky, S.A.; Vetterling, W.T.: *Numerical Recipes*, Cambridge University Press, 2nd edn., 1992
- [216] Radespiel, R.; Kroll, N.: Accurate Flux Vector Splitting for Shocks and Shear Layers, *J. Comp. Phys.*, 121, 1995
- [217] Radespiel, R.; Rossow, C.C., *A Cell Vertex Finite Volume Scheme for the Two-Dimensional Navier-Stokes Equations*, DFVLR-IB 129-87/40, 1987
- [218] Radespiel, R.; Rossow, C.C.; Swanson, R.C.: An Efficient Cell-Vertex Multigrid Scheme for the Three-Dimensional Navier-Stokes Equations, *AIAA Paper 89-1953*, 1989

- [219] Radespiel, R.; Swanson, R.C.: An Investigation of Cell Centered and Cell Vertex Multigrid Schemes for the Navier-Stokes Equations, *AIAA Paper 89-548*, 1989
- [220] Radespiel, R.; Turkel, E.; Kroll, N.: *Assessment of Preconditioning Methods*, Forschungsbericht 95-29, DLR, Institut für Entwurfsaerodynamik, Braunschweig, 1995
- [221] Raif, M.: *Berechnung der dreidimensionalen Strömung in Turbomaschinen mittels TVD-Upwind-Verfahren höherer Ordnung*, Dissertation, Institut für Thermische Strömungsmaschinen und Maschinenlaboratorium, Universität Stuttgart, 1998
- [222] Rehm, R.G.; Baum, H.R.: The Equations of Motion for Thermally Driven, Buoyant Flows, *Journal of Research of the National Bureau of Standards*, 83:297–308, 1978
- [223] Rhode, D.; Johnson, J.: Flow Visualisation and Leakage Measurements of Stepped Labyrinth Seals; Part 1: Annular Groove, *ASME Paper 96-GT-136*, 1996
- [224] Riedel, U.: Numerical Simulation of Reactive Flows with Detailed Reaction Schemes on Unstructured Grids, *AIAA Paper 98-2970*, 1998
- [225] Rieper, F.: A low-Mach number fix for Roe's approximate Riemann solver, *J. Comp. Phys.*, 230:5263–5287, 2011
- [226] Rizzi, A.; Viviani, H.: Numerical Methods for the Computation of Inviscid Transonic Flows with Shock Waves, *Notes on Numerical Fluid Mechanics*, GAMM Workshop, 1981
- [227] Rodi, W.: *Turbulence Models and their Application in Hydraulics – A state of the Art Review*, International Association for Hydraulic Research, Delft, Niederlande, 2nd edn., 1984
- [228] Rodi, W.: Simulation of Turbulence in Practical Flow Calculations, in: *ECCOMAS 2000, Barcelona, Spain*, 2000
- [229] Roe, P.L.: Approximate Riemann Solvers, Parameter Vectors, and Difference Schemes, *J. Comp. Phys.*, 43:357–372, 1981
- [230] Rogers, S.E.; Kwak, D.; Kiris, C.: Numerical Solution of the Incompressible Navier-Stokes Equations for Steady-State and Time-Dependent Problems, *AIAA Paper 89-0463*, 1989
- [231] Rosic, B.; Denton, J.D.: The Control of Shroud Leakage Loss by Reducing Circumferential Mixing, *ASME Paper GT2006-90946*, 2006

- [232] Rosic, B.; Denton, J.D.; Curtis, E.M.: The Influence of Shroud and Cavity Geometry on Turbine Performance – An Experimental and Computational Study, Part 1: Shroud Geometry, *ASME Paper GT2007-27769*, 2007
- [233] Rosic, B.; Denton, J.D.; Curtis, E.M.; Peterson, A.T.: The Influence of Shroud and Cavity Geometry on Turbine Performance – An Experimental and Computational Study, Part 2: Exit Cavity Geometry, *ASME Paper GT2007-27770*, 2007
- [234] Rosic, B.; Denton, J.D.; Pullan, G.: The Importance of Shroud Leakage Modelling in Multistage Turbine Flow Calculations, *ASME Paper GT2005-68459*, 2005
- [235] Rossow, C.C.: *Berechnung von Strömungsfeldern durch Lösung der Euler-Gleichungen mit einer erweiterten Finite-Volumen Diskretisierungsmethode*, Dissertation (PhD Thesis), Technische Universität Braunschweig, 1988
- [236] Rossow, C.C.: A flux splitting scheme for compressible and incompressible flow, *J. Comp. Phys.*, 164:104–122, 2000
- [237] Rossow, C.C.: Extension of a Compressible Code Towards the Incompressible Limit, *AIAA J.*, 41(12):2379–2386, 2003
- [238] Roy, C.J.; Blottner, F.G.: Assessment of One-and Two-Equation Turbulence Models for Hypersonic Transitional Flows, *Journal of Spacecraft and Rockets*, 38(5):699–710, 2001
- [239] Rumsey, C.L.: Apparent transition behaviour of widely-used turbulence models, *Int. J. of Heat and Fluid Flow*, 28(6):1460–1471, 2007
- [240] Rung, T.; Bunge, U.; Schatz, M.; Thiele, F.: Restatement of the Spalart-Allmaras Eddy-Viscosity Model in Strain-Adaptive Formulation, *AIAA J.*, 41(7):1396–1399, 2003
- [241] Sankaran, V.; Oefelein, J.: Advanced Preconditioning Strategies for Chemically Reacting Flow, *AIAA Paper 2007-1432*, 2007
- [242] Saxer, A.P.: *A Numerical Analysis of 3-D Inviscid Stator/Rotor Interactions Using Non-Reflecting Boundary Conditions*, PhD Thesis, MIT Gas Turbine Laboratory, 1992
- [243] Saxer, A.P.; Giles, M.B.: Quasi-3-D Non-Reflecting Boundary Conditions for Euler Equations Calculations, *AIAA Paper 91-1603-CP*, 1991
- [244] Schlienger, J.; Pfau, A.; Kalfas, A.I.; Abhari, R.S.: Effects of Labyrinth Seal Variation on Multistage Axial Turbine Flow, *ASME Paper GT2003-38270*, 2003

- [245] Schlienger, J.P.: *Evolution of Unsteady Secondary Flows in a Multistage Shrouded Axial Turbine*, Dissertation (PhD Thesis), ETH Zürich, 2003
- [246] Schrader, B.: *Dreidimensionale nichtreflektierende Randbehandlung von Ein- und Austrittsrändern bei der Simulation stationärer Strömungen*, Studienarbeit (Thesis), Institut für Thermische Strömungsmaschinen und Maschinenlaboratorium, Universität Stuttgart, 2005
- [247] Seybold, U.: *Untersuchung verschiedener Randbedingungen bei der Berechnung von Turbomaschinenströmungen*, Studienarbeit (Thesis), Institut für Thermische Strömungsmaschinen und Maschinenlaboratorium, Universität Stuttgart, 2002
- [248] Seybold, U.; Anker, J.E.; Kämmerer, S.; Mayer, J.F.; Casey, M.: A Comparison of Different Boundary Conditions for Turbomachinery Flow Simulation, in: *ECCOMAS 2004 Proceedings*, edited by Neittaanmäki, P.; Rossi, T.; Korotov, S.; Oñate, E.; Périaux, J.; Knörzer, D., Jyväskylä, Finland, July 2004
- [249] Seybold, U.; Mayer, J.F.; Casey, M.: *2D-Studie zum Einfluss von Turbulenzmodell und Rechengitter auf die Strömung durch das Labyrinth einer Axialturbine*, Interner Bericht, Institut für Thermische Strömungsmaschinen und Maschinenlaboratorium, Universität Stuttgart, 2004
- [250] Shih, T.H.; Liou, W.W.; Shabbir, A.; Yang, Z.; Zhu, J.: A New $k-\varepsilon$ Eddy Viscosity Model for High Reynolds Number Turbulent Flows, *Computers Fluids*, 24(3):227–238, 1995
- [251] Shin, B.R.; Yamamoto, S.; Yuan, X.: Application of Preconditioning Method to Gas-Liquid Two-Phase Flow Computations, *Trans. ASME, J. Fluids Engrg.*, 126:605–612, July 2004
- [252] Shur, M.L.; Strelets, M.K.; Travin, A.K.; Spalart, P.: Turbulence Modeling in Rotating and Curved Channels: Assessing the Spalart-Shur Correction, *AIAA J.*, 38(5):784–792, 2000
- [253] Sieverding, C.H.: Experimental Data on Two Transonic Turbine Blade Sections and Comparison with Various Theoretical Methods, in: *Lecture Series 59: Transonic Flows in Turbomachines*, von Karman Institute for Fluid Dynamics, 1973
- [254] Singh, J.P.: Evaluation of Jameson-Schmidt-Turkel dissipation scheme for hypersonic flow computations, in: *13th AIAA Applied Aerodynamics Conference, San Diego, CA, USA*, 1995
- [255] Smith, A.M.O.; Cebeki, T.: *Numerical Solution of Turbulent Boundary-Layer Equations*, Tech. Rep., Douglas Aircraft Division Report, DAC 33735, 1967

- [256] Sögüt, S.: *Numerische Berechnung und Analyse des Strömungsfeldes in einer 1.5-stufigen Axialturbine mit Deckbandgeometrie*, Studienarbeit (Thesis), Institut für Thermische Strömungsmaschinen und Maschinenlaboratorium, Universität Stuttgart, 2005
- [257] Spalart, P.; Schur, M.: On the sensitiviation of turbulence models to rotation and curvature, *Aerospace Science and Technology*, 1(5):297–302, 1997
- [258] Spalart, P.R.; Allmaras, S.R.: A One-Equation Turbulence Model for Aerodynamic Flows, *AIAA Paper 92-0439*, 30th Aerospace Sciences Meeting & Exhibit, January 6-9, 1992, Reno, Nevada, 1992
- [259] Speziale, C.G.; Sarkar, S.; Gatski, T.B.: Modelling the pressure-strain correlation of turbulence – An invariant dynamical systems approach, *J. Fluid Mech.*, 227:245–272, 1991
- [260] Steelant, J.; Dick, E.: Modelling of Bypass Transition with Conditioned Navier-Sokes Equations Coupled to an Intermittency Transport Equation, *Internat. J. Numer. Methods in Fluids*, 23:193–220, 1996
- [261] Steelant, J.; Dick, E.: Modelling of Laminar-Turbulent Transition for High Freestream Turbulence, *Trans. ASME, J. Fluids Engrg.*, 123:22–30, 2001
- [262] Stetter, H.; Jung, A.R.; Mayer, J.F.: Numerical Studies of Unsteady Flow Phenomena in Multi-Blade Row Environment, in: *Latest Advances in the Aerodynamics of Turbomachinery, IMechE Seminar S461*, Rugby, UK, 1996
- [263] Stoll, P.; Gerlinger, P.; Brüggemann, D.: Implicit Preconditioning Method for Turbulent Reacting Flows, in: *ECCOMAS 98*, pp. 205–212, John Wiley & Sons, 1998
- [264] Storteig, E.: *Dynamic Characteristics and Leakage Performance of Liquid Annular Seals in Centrifugal Pumps*, Doktoravhandling (PhD Thesis), Institutt for Marint Maskineri, NTNU, Trondheim, Norway, 2000
- [265] Subramanian, S.V.; Bozzola, R.: Numerical Simulation of Three-Dimensional Flow Fields in Turbomachinery Blade Rows Using the Compressible Navier-Stokes Equations, *AIAA Paper 87-1314*, 1987
- [266] Suzen, Y.B.; Huang, P.G.: Modeling of Flow Transition Using an Intermittency Transport Equation, *Trans. ASME, J. Fluids Engrg.*, 122(2):273–284, June 2000
- [267] Swanson, R.C.; Radespiel, R.; Turkel, E.: *Comparison of Several Dissipation Algorithms for Central Difference Schemes*, ICASE Report No. 97-40, ICASE, 1997

- [268] Swanson, R.C.; Turkel, E.: On Central-Difference and Upwind Schemes, *J. Comp. Phys.*, 101:292–306, 1992
- [269] Sweby, P.K.: High Resolution Schemes Using Flux Limiters for Hyperbolic Conservation Laws, *SIAM J. Numer. Anal.*, 21(45):995–1011, 1984
- [270] Tatsumi, S.; Martinelli, L.; Jameson, A.: A New High Resolution Scheme for Compressible Viscous Flow with Shocks, *AIAA Paper 95-0466*, January 1995
- [271] Tennekes, H.; Lumley, J.L.: *A First Course in Turbulence*, MIT Press, 1972
- [272] Thieleke, G.: *Experimentelle und theoretische Untersuchung der Strömungskräfte in Labyrinthdichtungen von Turbomaschinen*, Dissertation, Universität Stuttgart, 1991
- [273] TNF Workshop, *Proceedings of the International Workshops on Measurement and Computation of Turbulent Non-premixed Flames (TNF)*, URL: <http://www.sandia.gov/TNF/abstract.html>, 2006-2010 (TNF8-10)
- [274] Toro, E.F.: *Riemann Solvers and Numerical Methods for Fluid Dynamics*, Springer-Verlag, 2nd edn., 1999
- [275] Traupel, W.: *Thermische Turbomaschinen*, Springer-Verlag, 1966
- [276] Turkel, E.: Preconditioned Methods for Solving the Incompressible and Low Speed Compressible Equations, *J. Comp. Phys.*, 72:277–298, 1987
- [277] Turkel, E.; Radespiel, R.; Kroll, N.: Assessment of Two Preconditioning Methods for Aerodynamic Problems, *Computers & Fluids*, 26(6):613–634, 1997
- [278] Turkel, E.; Vatsa, V.N.; Radespiel, R.: Preconditioning Methods for Low-Speed Flows, *AIAA Paper 96-2460-CP*, 1996
- [279] Tweedt, D.L.; Chima, R.V.; Turkel, E.: Preconditioning for Numerical Simulation of Low Mach Number Three-Dimensional Viscous Turbomachinery Flows, *AIAA Paper 97-1828*, June 1997
- [280] van Albada, G.D.; van Leer, B.; Roberts, W.W.: A Comparative Study of Computational Methods in Cosmic Gas Dynamic, *Astron. Astrophysics*, 108:76–84, 1982
- [281] van Driest, E.R.: On turbulent Flow near a Wall, *J. of the Aeronautical Sciences*, 23:1007–1011 and 1036, November 1956
- [282] van Leer, B.: Towards the Ultimate Conservative Difference Scheme. Part V: A Second-Order Sequel to Godunov's Method, *J. Comp. Phys.*, 32:101–136, 1979

- [283] Venkatakrishnan, V.; Chakravarthy, S.R.: Towards Higher-Order Accuracy on Arbitrary Grids, in: *Fifteenth International Conference on Numerical Methods in Fluid Dynamics*, edited by Kutler, P.; Flores, J.; Chattot, J.J., Vol. 490 of *Lecture Notes in Physics*, pp. 249–254, Springer, 1996
- [284] Venkateswaran, S.; Buelow, P.E.O.; Merkle, C.L.: Development of Linearized Preconditioning Methods for Enhancing Robustness and Efficiency of Euler and Navier-Stokes Computations, *AIAA Paper 97-2030*, 13th AIAA CFD Conference, Snowmass, CO, 1997
- [285] Venkateswaran, S.; Li, D.; Merkle, C.L.: Influence of Stagnation Regions on Preconditioned Solutions at Low Speeds, *AIAA Paper 2003-435*, 2003
- [286] Venkateswaran, S.; Merkle, C.L.: Dual Time-Stepping and Preconditioning for Unsteady Computations, *AIAA Paper 95-0078*, 1995
- [287] Venkateswaran, S.; Merkle, C.L.: Evaluation of Artificial Dissipation Models and their Relationship to the Accuracy of the Euler and Navier-Stokes Computations, in: *16th International Conference on Numerical Methods in Fluid Dynamics, July 6-10, Arcachon, France*, 1998
- [288] Venkateswaran, S.; Merkle, C.L.; Zeng, X.Q.; Li, D.: Influence of Large-Scale Pressure Changes on Preconditioned Solutions at Low Speeds, *AIAA J.*, 42(12):2490–2498, 2004
- [289] Venkateswaran, S.; Merkle, L., *Analysis of Preconditioning Methods for the Euler and Navier-Stokes Equations*, von Karman Institute for Fluid Dynamics, Lecture Series 1999-03, 1999
- [290] Viviand, H.: Pseudo-Unsteady Systems for Steady Inviscid Flow Calculation, in: *Numerical Methods for the Euler Equations of Fluid Dynamics*, edited by Angrand, F., pp. 334–368, Society for Industrial and Applied Mathematics (SIAM), 1985
- [291] Volpe, G.: Performance of Compressible Flow Codes at Low Mach Numbers, *AIAA J.*, 31(1), 1993
- [292] Wallis, A.M.; Denton, J.D.; Demargne, A.A.J.: The Control of Shroud Leakage Flows to Reduce Aerodynamic Losses in an Low Aspect Ratio, Shrouded Axial Flow Turbine, *ASME Paper 2000-GT-475*, 2000
- [293] Walraevens, R.: *Turbinenleitradströmung hinter einem Laufrad mit Radialspalt*, Techn. Ber., Informationstagung Turbinen Frankfurt, Institut für Strahlantriebe und Turboarbeitsmaschinen RWTH Aachen, 1995

- [294] Walraevens, R.E.; Gallus, H.E.; Jung, A.R.; Mayer, J.F.; Stetter, H.: Experimental and Computational Study of the Unsteady Flow in a 1.5 Stage Axial Turbine with Emphasis on the Secondary Flow in the Second Stator, *ASME Paper 98-GT-254*, 1998
- [295] Walters, D.; Cokljat, D.: A Three-Equation Eddy-Viscosity Model for Reynolds-Averaged Navier-Stokes Simulations of Transitional Flow, *Journal of Fluids Engineering*, 130:121401.1–14, December 2008
- [296] Walters, D.; Leylek, J.H.: A New Model for Boundary Layer Transition Using a Single-Point RANS Approach, *ASME J. Turbomach.*, 126:193–202, 2004
- [297] Wang, C.; Perot, B.: Prediction of Turbulent Transition in Boundary Layers Using the Turbulent Potential Model, *J. Turbul.*, 3, 2002
- [298] Wang, X.: *A Preconditioned Algorithm for Turbomachinery Viscous Flow Simulation*, PhD Thesis, Mississippi State University, Mississippi, USA, 2005
- [299] Weiss, J.M.; Maruszewski, J.P.; Smith, W.A.: Implicit Solution of the Preconditioned Navier-Stokes Equations Using Algebraic Multigrid, *AIAA J.*, 37(1):29, 1999
- [300] Weiss, J.M.; Murthy, J.: Computation of Reacting Flowfields Using Unstructured Adaptive Meshes, *AIAA Paper 95-0870*, 1995
- [301] Weiss, J.M.; Smith, W.A.: Preconditioning Applied to Variable and Constant Density Time-Accurate Flows on Unstructured Meshes, *AIAA Paper 94-2209*, 1994
- [302] Wesseling, P.: *Principles of Computational Fluid Dynamics*, Springer Verlag, 2010
- [303] Westin, K.J.A.; Henkes, R.A.W.M.: Application of Turbulence Models to Bypass Transition, *Journal of Fluids Engineering*, 119(4):859–866, 1997
- [304] Whitham, G.B.: *Linear and Nonlinear Waves*, John Wiley & Sons, 1974
- [305] Wilcox, D.C.: Reassessment of the Scale-Determining Equation for Advanced Turbulence Models, *AIAA J.*, 26(11):1299–1310, November 1988
- [306] Wilcox, D.C.: *Turbulence Modeling for CFD*, DCW Industries, Inc., La Cañada, California, 2nd edn., 1993
- [307] Wilcox, D.C.: Simulation of Transition with a Two-Equation Model, *AIAA J.*, 32:247–255, 1994
- [308] Wilcox, D.C.: *Turbulence Modeling for CFD*, DCW Industries, Inc., La Cañada, California, 2nd edn., 1998

- [309] Witchington, J.P.; Shuen, J.S.; Yang, V.: A Time-Accurate Implicit Method for Chemically Reacting Flows at All Mach Numbers, *AIAA Paper 91-0581*, 1991
- [310] Wolter, K.: *Experimentelle und numerische Untersuchung der stationären Strömung über dem Deckband einer 1,5-stufigen Axialturbinen*, Dissertation (PhD Thesis), Fakultät der Maschinenbau der Ruhr-Universität Bochum, 2004
- [311] Wolter, K.; Giboni, A.; Peters, P.; Menter, J.; Pfof, H.: Experimental and Numerical Investigation of the Unsteady Leakage Flow Through the Rotor Tip Labyrinth of a 1.5-Stage Turbine, *ASME Paper GT2005-68156*, 2005
- [312] Wölfel, C.: *Berechnung des stationären Strömungsfeldes in einer Gasturbine*, Studienarbeit, Institut für Luftfahrtantriebe und Turbomaschinen; Universität Stuttgart, 1999
- [313] Yakhot, A.; Staroselsky, I.; Orszag, S.A.: Asymptotic Behaviour of Solutions of the Renormalization Group $k\text{-}\varepsilon$ Turbulence Model, *AIAA J.*, 32(5):1087–1089, 1993
- [314] Yoo, C.; Im, H.: Characteristic Boundary Conditions for Simulations of Compressible Reacting Flows with Multi-Dimensional, Viscous and Reaction Effects, *Combustion Theory and Modelling*, 11(2):259–286, 2007
- [315] Yoo, C.; Wang, Y.; Trouvé, A.; Im, H.: Characteristic Boundary Conditions for Direct Simulations of Turbulent Counterflow Flames, *Combustion Theory and Modelling*, 9(4):617–646, 2005
- [316] You, D.; Wang, M.; Moin, P.; Mittal, R.: Effect of tip-gap size on the tip-leakage flow in a turbomachinery cascade, *Physics of Fluids*, 18:105102.1–14, 2006